

# Highly radiation-resistant 3D pixel semiconductor detectors for experiments in future accelerators

## *Detectores semiconductores 3D pixelados altamente resistentes a la radiación para experimentos en futuros aceleradores*

Dissertation submitted in fulfillment of the requirements for the Degree of Doctor of Philosophy in Physics at the University of Cantabria.

*Tesis presentada en cumplimiento de los requisitos para optar al título de Doctora en Física por la Universidad de Cantabria.*

Author / Autora:

**Clara Lasaosa García**

Thesis supervisors / Supervisores de tesis:

**Gervasio Gómez Gramuglio**

**Jordi Duarte Campderrós**

Thesis tutor / Tutor de tesis:

**Iván Vila Álvarez**

---

October 2025 - Octubre 2025





## Acknowledgments

Gracias a Gervasio, Iván y Jordi por todas las oportunidades que me han brindado en estos cinco años, así como por la confianza que han depositado en mí. Gracias, en general, al grupo de Altas Energías del IFCA por haber hecho cada día de trabajo más ameno. Siempre recordaré la cita diaria a las once de la mañana con notas de *Ojalá que llueva café*. Gracias a todos los estudiantes de doctorado que me han acompañado en este camino, desde quienes ya lo han terminado hasta quienes acaban de empezar. En especial, gracias a Agustín, Cristian y Pablo, con quienes he tenido la suerte de compartir cubículo durante estos años. Gracias por escucharme siempre que lo he necesitado, así como por los momentazos que hemos vivido juntos.

Many thanks to everyone in the CMS tracker group for placing your trust in me and valuing my work. A special thank you to all the colleagues who participated in the test beam campaigns and made them a memorable experience, despite the lack of sleep. It was a real pleasure to meet and work with all of you. Thanks also to Marcos, whose kindness and positive energy turned even the most intense laser-based campaigns into a wonderful experience.

Grazie al gruppo di Alte Energie di INFN-Firenze per avermi accolta come parte del vostro gruppo durante un breve periodo del mio dottorato. Antonio, Marco, Rudy: è stato un vero piacere lavorare con voi. Un grazie speciale ad Antonio, per tantissime cose, senza le quali non sarei la ricercatrice che sono oggi. Grazie mille per il tuo sostegno e il tuo aiuto in questi anni, non sarebbe stato lo stesso senza di te.

Gracias a mis amigos de Santander por ser hogar, por abrirme las puertas de su casa y por convertir esta ciudad en un lugar entrañable. En especial, gracias a Jaime, Carmen, Iván y Asael por estar presentes en cada etapa de este camino, por sacarme una sonrisa cuando lo he necesitado y por los planes de desconexión tan necesarios. Me siento muy afortunada de tenerlos en mi vida.

Un gracias inmenso a mi familia: Antonio, Araceli, Elena y Guille. Gracias por haber estado siempre ahí para absolutamente todo, por confiar plenamente en mí, apoyar todas mis decisiones y celebrar cada uno de mis logros. A vosotros os dedico esta tesis.



# Abstract

The upcoming high-luminosity phase of the CERN Large Hadron Collider (LHC) imposes stringent requirements on the Compact Muon Solenoid (CMS) experiment, which must operate under unprecedented radiation levels and collision rates. To maintain high performance in such demanding conditions, the tracking system will be completely replaced. The upgraded system requires sensors that combine high radiation tolerance, minimal power dissipation, increased granularity to improve spatial resolution, and high single-hit detection efficiency. While planar silicon pixel sensors will be installed throughout most of the inner tracking system, 3D pixel sensors are the only viable option for the layer closest to the interaction point, owing to their superior radiation hardness and lower power dissipation.

This thesis presents the characterization of 3D pixel sensors—interconnected with full-size prototype readout chips—and their qualification for deployment in the upgraded CMS tracking system. The performance of these detectors was evaluated in test beam experiments before and after irradiation. The results demonstrate that 3D pixel sensors meet the CMS requirements, confirming their suitability for installation in the innermost layer of the tracking system.

System-level tests were also performed to fully validate the pixel detectors developed for the upgrade. In particular, their performance and specific functionalities of the readout chip were assessed under the power distribution scheme planned for the inner tracking system. Additionally, following a successful qualification program, initial quality control tests of the sensor-readout interconnects were carried out, marking the beginning of the production phase at one of the designated assembly centers.

Beyond the high-luminosity LHC upgrade, 3D pixel sensors are also being explored for timing applications in next-generation experiments, where high radiation tolerance and precise time resolution are required. This thesis investigates their timing performance, with particular focus on the effects of electric field non-uniformities and the influence of pixel cell geometry. Laser-based measurements reveal a significant impact of pixel cell layout, highlighting the importance of sensor design optimization for future timing applications.

**Key words:** LHC, CMS experiment, high luminosity, tracking detectors, timing detectors, 3D pixel silicon sensors, radiation hardness, laser-based characterization, test beam characterization, electrical characterization.

## Resumen

La fase de alta luminosidad del Large Hadron Collider (LHC) del CERN plantea exigencias técnicas al experimento Compact Muon Solenoid (CMS), que deberá operar bajo niveles de radiación y tasas de colisión sin precedentes. Para garantizar un rendimiento óptimo en estas condiciones, se ha previsto la sustitución completa del sistema de reconstrucción de trazas. El nuevo sistema requiere sensores que combinen alta tolerancia a la radiación, bajo consumo energético, mayor granularidad para mejorar la resolución espacial, y una alta eficiencia de detección. Si bien la mayor parte del sistema interno de trazas utilizará sensores con píxeles planares de silicio, los sensores con píxeles 3D constituyen la única opción viable para la capa más próxima al punto de interacción, gracias a su superior resistencia a la radiación y menor consumo energético.

Esta tesis presenta la caracterización de sensores con píxeles 3D—interconectados con prototipos a escala real del chip de lectura—y su validación para ser implementados en el nuevo sistema de trazas de CMS. El rendimiento de estos detectores se evaluó en experimentos con haces de prueba, tanto antes como después de ser irradiados. Los resultados obtenidos demuestran que los sensores de píxeles 3D cumplen con los requisitos establecidos por CMS, confirmando su idoneidad para ser instalados en la capa más interna del sistema de trazas.

Asimismo, se realizaron pruebas a nivel de sistema para validar integralmente los nuevos detectores de píxeles. En particular, se evaluaron su rendimiento y funciones específicas del chip de lectura bajo el esquema de distribución de potencia previsto para el sistema interno de trazas. Además, tras un exitoso programa de validación, se realizaron las primeras pruebas de control de calidad de las interconexiones entre el sensor y el chip de lectura, marcando así el inicio de la fase de producción de módulos en uno de los centros de ensamblado.

Más allá de la actualización para la fase de alta luminosidad del LHC, los sensores con píxeles 3D se están explorando para aplicaciones de medición temporal en experimentos de próxima generación, donde se requiere alta tolerancia a la radiación y resolución temporal precisa. En esta tesis también se investiga su rendimiento en este contexto, con especial atención a los efectos de las no uniformidades del campo eléctrico y la influencia de la geometría de la celda píxel. Las mediciones realizadas con técnicas láser revelan un impacto significativo del diseño de la celda, lo que resalta la importancia de optimizar la arquitectura de los sensores para este tipo de aplicaciones.

**Palabras clave:** LHC, experimento CMS, alta luminosidad, detectores de trazas, detectores temporales, sensores de silicio con píxeles 3D, resistencia a la radiación, caracterización con láser, caracterización con haz de partículas, caracterización eléctrica.

# Contents

Acknowledgments . . . . .	i
Abstract . . . . .	ii
Resumen . . . . .	iii
List of figures . . . . .	vii
List of tables . . . . .	xv
List of acronyms . . . . .	xvi
<b>1 Introduction</b>	<b>1</b>
1.1 Motivation . . . . .	1
1.2 The Large Hadron Collider . . . . .	3
1.2.1 The high-luminosity phase . . . . .	8
1.3 The Compact Muon Solenoid . . . . .	9
1.3.1 Upgrade for the high-luminosity phase . . . . .	15
<b>2 Silicon particle detectors</b>	<b>22</b>
2.1 Semiconductor detectors. Silicon . . . . .	22
2.1.1 Crystalline structure . . . . .	22
2.1.2 Energy band configuration . . . . .	24
2.1.3 Intrinsic and extrinsic semiconductors . . . . .	27
2.1.4 Charge carrier transport . . . . .	31
2.1.5 The pn-junction in thermal equilibrium . . . . .	33
2.1.6 The pn-junction under bias voltage . . . . .	37
2.1.7 Electrical characteristics of the pn-junction . . . . .	39
2.2 Signal formation . . . . .	42
2.2.1 Ionizing radiation . . . . .	43
2.2.2 Shockley-Ramo theorem . . . . .	47
2.3 Radiation damage in silicon . . . . .	48
2.3.1 Impact on the sensor properties . . . . .	50
2.3.2 Annealing . . . . .	54
2.4 State-of-the-art in silicon-based detectors . . . . .	54
2.4.1 Hybrid detectors . . . . .	59

2.4.2	Monolithic detectors . . . . .	68
<b>3</b>	<b>Performance evaluation of 3D pixel detectors via test beam characterization</b>	<b>72</b>
3.1	3D pixel detectors under test . . . . .	73
3.1.1	Description of the readout electronics . . . . .	73
3.1.2	Description of the sensors . . . . .	79
3.1.3	Detector calibration procedure . . . . .	81
3.2	Facilities and experimental setups . . . . .	92
3.2.1	Irradiation facilities and setups . . . . .	92
3.2.2	Test beam facilities and setups . . . . .	94
3.3	Test beam measurements . . . . .	98
3.3.1	Data analysis procedure . . . . .	100
3.3.2	Definition of observables . . . . .	108
3.3.3	Performance of non-irradiated devices . . . . .	118
3.3.4	Performance of irradiated devices . . . . .	130
3.4	Comparison between test beam measurements and simulation . . . . .	144
3.5	Summary . . . . .	149
<b>4</b>	<b>System-level testing and integration quality control</b>	<b>151</b>
4.1	Bump-bond quality control . . . . .	151
4.1.1	Evaluation with an X-ray method . . . . .	152
4.1.2	Evaluation with an electrical method . . . . .	157
4.1.3	Comparison between methods . . . . .	162
4.2	System-level tests . . . . .	164
4.2.1	Power distribution scheme . . . . .	164
4.2.2	Performance in a serial-power chain . . . . .	167
4.2.3	Performance under system failure . . . . .	171
4.3	Summary . . . . .	176
<b>5</b>	<b>Performance evaluation of 3D pixel sensors via laser characterization</b>	<b>177</b>
5.1	3D pixel sensors under test . . . . .	178
5.2	Electrical measurements . . . . .	179
5.3	Laser-based measurements . . . . .	180
5.3.1	Experimental setup . . . . .	182
5.3.2	Definition of observables . . . . .	185
5.3.3	Timing performance of square 3D pixel sensors . . . . .	187
5.3.4	Timing performance of hexagonal 3D pixel sensors . . . . .	192
5.4	Summary . . . . .	198
<b>6</b>	<b>Conclusions</b>	<b>199</b>
	<b>References</b>	<b>202</b>

---

<b>Appendix</b>	<b>215</b>
A.1 Test beam measurements across a multi-pixel grid . . . . .	215
A.1.1 Performance of non-irradiated devices . . . . .	215
A.1.2 Performance of irradiated devices . . . . .	218

# List of Figures

1.1	Elementary particles of the Standard Model of particle physics . . . . .	2
1.2	Schema of the CERN accelerator complex . . . . .	4
1.3	Images of the four main detector experiments at the CERN LHC . . . . .	6
1.4	Integrated luminosity delivered by the LHC and recorded by the CMS experiment for proton-proton collisions and lead-lead collisions. Distribution of the average number of interactions per bunch crossing for proton-proton collisions . . . . .	7
1.5	Complete LHC and HL-LHC schedule . . . . .	9
1.6	Layout and coordinate system of the CMS detector . . . . .	10
1.7	Layout of one quarter of the Phase-1 CMS tracking system in the longitudinal view . . . . .	11
1.8	Monte Carlo simulation of the 1 MeV neutron equivalent fluence and the absorbed dose in the Phase-2 CMS tracker for an integrated luminosity of $4000 \text{ fb}^{-1}$ from proton-proton collisions at a beam energy of 7 TeV . . . . .	17
1.9	Layout of one quarter of the Phase-2 CMS tracking system in the longitudinal view . . . . .	18
1.10	Hit occupancy as a function of pseudorapidity in the Phase-2 CMS tracking system . . . . .	20
2.1	Diamond and zinc blende crystal structures. Basic lattice planes in a cubic crystal with their corresponding orientations . . . . .	23
2.2	Simplified energy-band diagram of an insulator, conductor and semiconductor material at absolute zero . . . . .	25
2.3	Simplified energy-band structure in the crystal momentum space for gallium arsenide, a direct band gap semiconductor, and silicon, an indirect band gap semiconductor . . . . .	26
2.4	Schematic bond representation and simplified energy band diagram of intrinsic silicon, $p$ -type silicon and $n$ -type silicon at absolute zero . . . . .	27
2.5	Simplified illustration of a pn-junction and its energy band diagram in thermal equilibrium . . . . .	35



2.6	Distribution of space-charge density, electric field and electric potential as a function of space in the abrupt junction approximation . . . . .	36
2.7	Simplified illustration of a pn-junction and its energy band diagram under reverse and forward bias . . . . .	38
2.8	Characteristic <i>IV</i> and <i>CV</i> curves for a pn-junction diode . . . . .	39
2.9	Inverse capacitance squared as a function of voltage . . . . .	42
2.10	Mass stopping power for positively charged muons in copper as a function of the relativistic $\beta\gamma$ product and muon momentum . . . . .	44
2.11	Photon interaction cross-section in carbon as a function of photon energy. Dominant interaction mechanism as a function of photon energy for different atomic number values . . . . .	46
2.12	Variation of the linear absorption coefficient and absorption length in silicon at room temperature as a function of photon wavelength . . . . .	48
2.13	Schematic representation of point-like and clustered defects produced in the collision of an incident particle with a silicon lattice atom . . . . .	50
2.14	Displacement damage function of several particles, normalized to the displacement damage produced by a 1 MeV neutron, as a function of the particle energy . . . . .	51
2.15	Variation in leakage current per unit volume for several silicon sensors as a function of the 1 MeV-equivalent particle fluence . . . . .	52
2.16	Effective doping concentration and depletion voltage as a function of the 1 MeV-equivalent particle fluence for an <i>n</i> -type silicon detector . . . . .	53
2.17	Schematic representation of a <i>p</i> -in- <i>n</i> detector with different electrode segmentation: pad detector, strip detector, and pixel detector . . . . .	57
2.18	Sketches of the methods used in hybrid detectors for connection between the sensor and the readout electronics: wire-bonding and bump-bonding techniques. . . . .	58
2.19	Schematic front-view representation of a <i>p</i> -in- <i>n</i> planar pixel sensor. . . . .	60
2.20	Schematic front-view representation of a single-sided and a double-sided <i>p</i> -in- <i>n</i> 3D pixel sensor. Top view of two rectangular pixel cells featuring columnar and trench electrode geometries. . . . .	62
2.21	Schematic representation of an <i>n</i> -in- <i>p</i> APD. . . . .	64
2.22	Schematic representation of several <i>n</i> -in- <i>p</i> LGAD variants. . . . .	66
2.23	Schematic representation of MAPS and DMAPS detectors. . . . .	68
2.24	Schematic representation of a DEPFET detector. . . . .	70
2.25	Schematic representation of a SOI detector. . . . .	71
3.1	Picture of a CROCv1 3D pixel module mounted on a single-chip card for testing. . . . .	74
3.2	Schematic and block diagram of the CROCv1 linear analog front-end. . . . .	75

3.3	Ph2-ACF DAQ system for tuning and characterization of the CROCv1 front-end. . . . .	78
3.4	Schematic front-view layout of a CNM and an FBK 3D pixel sensor. . .	80
3.5	Top-view layout of a CNM and an FBK 3D pixel sensor, along with close-up views of four adjacent $25 \times 100 \mu\text{m}^2$ pixel cells. . . . .	81
3.6	Schematic representation of an S-Curve, illustrating the definition of threshold and noise for a single pixel. Tuning status of a digital module tuned to a threshold of 2000 electrons, before equalization. . . . .	84
3.7	TDAC distribution and tuning status of a digital module tuned to a threshold of 2000 electrons, after equalization. . . . .	86
3.8	Map of masked pixels and tuning status of a digital module tuned to a threshold of 2000 electrons, after equalization and noisy pixel masking. . . . .	87
3.9	Map of masked pixels and tuning status of a digital module tuned to a threshold of 1000 electrons, after the masking of noisy and stuck pixels. . . . .	88
3.10	Superimposed gain curves of all pixels in a digital module tuned to a threshold of 1000 electrons. . . . .	89
3.11	Map of masked pixels in two hybrid pixel modules tuned to a threshold of 1000 electrons following a complete set of calibrations. . . . .	90
3.12	Tuning status of two hybrid pixel modules, both tuned to a threshold of 1000 electrons following a complete set of calibrations. . . . .	91
3.13	Layout of the CERN PS IRRAD facility and components used for the irradiation setup. . . . .	94
3.14	Images of the experimental setups at the CERN SPS and DESY test beam facilities. Schematic of the test beam setup with the EUDET-type telescope. . . . .	96
3.15	Block diagram of the data reconstruction and analysis chain. . . . .	100
3.16	Schematic representation of cluster formation and residuals in track reconstruction. . . . .	103
3.17	Distribution of residuals in the $x$ and $y$ coordinates for one of the telescope planes, as well as the track $\chi^2$ distribution over the degrees of freedom after the final alignment. . . . .	105
3.18	Distribution of residuals along both coordinates for two fully depleted, non-irradiated DUTs after the final alignment: one with a pixel size of $25 \times 100 \mu\text{m}^2$ and another with $50 \times 50 \mu\text{m}^2$ . . . . .	106
3.19	Bunch crossing and track isolation criteria for the timing-reference plane. . . . .	107
3.20	Definition of tests performed at normal beam incidence and under a rotation angle. . . . .	108
3.21	Residual distributions from a toy Monte Carlo simulation for a module with $25 \times 100 \mu\text{m}^2$ pixel size, assuming no charge sharing and perfect telescope resolution. . . . .	111

3.22	Residual distributions from a toy Monte-Carlo simulation for a module with $25 \times 100 \mu\text{m}^2$ pixel size, illustrating the individual effects of charge sharing and telescope resolution, as well as their combination. . . . .	113
3.23	Residual distributions along the long pixel pitch for a non-irradiated DUT with $25 \times 100 \mu\text{m}^2$ pixel size, fitted to the difference of two Gaussian CDFs. . . . .	114
3.24	Residual distributions along the short pixel pitch for a non-irradiated DUT with $25 \times 100 \mu\text{m}^2$ pixel size, divided into subsets of events and fitted with the sum of a Gaussian and a constant term. . . . .	116
3.25	Residual distributions along the short pixel pitch for a non-irradiated DUT with $25 \times 100 \mu\text{m}^2$ pixel size, divided into subsets of events and fitted with the sum of two Gaussian functions. . . . .	117
3.26	Hit detection efficiency at normal incidence as a function of bias voltage for several non-irradiated modules. . . . .	118
3.27	Hit detection efficiency cell maps for several non-irradiated modules at different bias voltages and normal incidence. . . . .	119
3.28	Hit detection efficiency profiles along the long pixel pitch for non-irradiated modules at normal incidence. . . . .	120
3.29	Hit detection efficiency cell map for a non-irradiated module at normal incidence and rotated by $5^\circ$ . . . . .	121
3.30	Cluster charge distributions for non-irradiated FBK modules. . . . .	122
3.31	Cluster charge MPV cell maps for a non-irradiated module at different bias voltages and normal incidence. . . . .	123
3.32	Average cluster size as a function of bias voltage for non-irradiated modules at normal incidence. . . . .	124
3.33	Cluster size cell maps for several non-irradiated modules at different bias voltages and normal incidence. . . . .	125
3.34	One-dimensional cluster size distributions for several non-irradiated modules at normal incidence, showing the total cluster size as well as separately in the $x$ and $y$ directions. . . . .	126
3.35	Average cluster size as a function of the rotation angle for all non-irradiated FBK modules. . . . .	127
3.36	Cluster size cell maps for a non-irradiated FBK module at several rotation angles. . . . .	128
3.37	One-dimensional cluster size distributions for a non-irradiated module at different rotation angles, showing the total cluster size as well as separately in the $x$ and $y$ directions. . . . .	129
3.38	DUT spatial resolution along the short pixel pitch as a function of the rotation angle for all non-irradiated FBK modules. . . . .	130

3.39	Percentage of masked pixels as a function of bias voltage for irradiated modules. . . . .	131
3.40	Hit detection efficiency at normal incidence as a function of bias voltage for several irradiated modules, with and without the acceptance correction. . . . .	132
3.41	Hit detection efficiency cell map at normal incidence for modules irradiated to different fluences and biased at different bias voltages. . . . .	133
3.42	Hit detection efficiency as a function of the rotation angle for modules irradiated to $1 \times 10^{16} \text{ n}_{\text{eq}}\text{cm}^{-2}$ . . . . .	134
3.43	Hit detection efficiency cell maps for a module irradiated to $1 \times 10^{16} \text{ n}_{\text{eq}}\text{cm}^{-2}$ at normal incidence and under different rotation angles. . . . .	134
3.44	Hit detection efficiency profiles along the long pixel pitch for a module irradiated to $1 \times 10^{16} \text{ n}_{\text{eq}}\text{cm}^{-2}$ at different bias voltages and rotation angles. . . . .	135
3.45	Hit detection efficiency at normal incidence as a function of the average pixel threshold for several irradiated modules. . . . .	136
3.46	Cluster charge MPV as a function of bias voltage for irradiated modules. . . . .	137
3.47	Cluster charge distributions for irradiated modules. . . . .	138
3.48	Cluster charge MPV cell maps for modules irradiated to $1 \times 10^{16} \text{ n}_{\text{eq}}\text{cm}^{-2}$ at different bias voltages and normal incidence. . . . .	139
3.49	Cluster charge MPV cell maps for modules irradiated to $1 \times 10^{16} \text{ n}_{\text{eq}}\text{cm}^{-2}$ at different bias voltages and normal incidence. . . . .	139
3.50	Average cluster size as a function of bias voltage for irradiated modules at normal incidence. . . . .	140
3.51	Average cluster size as a function of the rotation angle for modules irradiated to $1 \times 10^{16} \text{ n}_{\text{eq}}\text{cm}^{-2}$ . . . . .	141
3.52	Cluster size cell maps for a module irradiated to $1 \times 10^{16} \text{ n}_{\text{eq}}\text{cm}^{-2}$ at several rotation angles. . . . .	142
3.53	Average cluster size as a function of the average pixel threshold for irradiated modules. . . . .	143
3.54	DUT spatial resolution along the short pixel pitch as a function of the rotation angle for modules irradiated to $1 \times 10^{16} \text{ n}_{\text{eq}}\text{cm}^{-2}$ . . . . .	144
3.55	Hit detection efficiency cell maps and profiles for a non-irradiated module at normal incidence, comparing test beam data and simulation. . . . .	146
3.56	Average cluster size cell maps and profiles for a non-irradiated module rotated by $8^\circ$ , comparing test beam data and simulation. . . . .	147
3.57	Residual distributions for a non-irradiated module rotated by $8^\circ$ , comparing test beam data and simulation. . . . .	148
3.58	DUT spatial resolution along the short pixel pitch as a function of the rotation angle, comparing test beam data and simulation. . . . .	149

4.1	X-ray setup used for bump-bond quality control and X-ray spectrum for a tungsten target. . . . .	152
4.2	Map of masked pixels in two hybrid pixel modules tuned to a threshold of 2000 electrons. . . . .	153
4.3	Tuning status of the hybrid pixel modules under test for bump-bond quality control using a method based on X-rays. . . . .	154
4.4	Map and one-dimensional distribution of hits per pixel for two hybrid pixel modules, obtained with the X-ray method for bump-bond quality control. . . . .	155
4.5	Map of defective bump-bonds for two hybrid pixel modules, identified using the X-ray quality control method. . . . .	156
4.6	Tuning status of the first hybrid pixel module under test for bump-bond quality control using an electrical method. . . . .	159
4.7	Tuning status of the second hybrid pixel module under test for bump-bond quality control using an electrical method. . . . .	160
4.8	Threshold and noise shift distributions for defective bump-bond identification using the electrical quality control method. . . . .	161
4.9	Map of defective bump-bonds for two hybrid pixel modules, identified using the electrical quality control method. . . . .	162
4.10	Schematic representation of the power distribution system in a serial-power chain. . . . .	165
4.11	Simplified SLDO model and ideal VI curve in either the analog or digital domain of the CROC chip. . . . .	166
4.12	Experimental setup of a serial-power chain with ten modules. . . . .	168
4.13	VI characteristics of a CROCv1 connected to a CNM 3D pixel sensor. . . . .	170
4.14	Threshold and noise distributions for a 3D pixel module placed at different positions along a serial-power chain. . . . .	171
4.15	Experimental setup with four digital CROCv1 SCCs connected in parallel to emulate a quad module. . . . .	172
4.16	VI characteristics of four CROCv1 chips connected in parallel to emulate a quad module. . . . .	173
4.17	VI characteristics of three CROCv1 chips in an emulated quad module under a failure scenario. . . . .	174
4.18	VI characteristic for the three working CROCv1 chips in an emulated quad module under a failure scenario, using different input resistors for the analog and digital SLDO circuits. . . . .	175
5.1	Simulated electric field maps for 3D pixel sensors with square and hexagonal cell geometries. . . . .	178
5.2	Layout of the square and hexagonal 3D pixel sensors used for timing performance studies. . . . .	178

5.3	Probe station used for the electrical characterization of 3D pixel sensors with square and hexagonal cell geometries. . . . .	180
5.4	IV characteristics of the 3D pixel sensor under test with square and hexagonal cell geometry. . . . .	181
5.5	Schematic of the TPA-TCT setup at the CERN SSD laser facility. . . . .	182
5.6	Beam radius at the illuminated surface as a function of the focus depth inside the sensor. Schematic of the beam profile and the excitation volume in TPA-TCT. . . . .	184
5.7	Image of one of the samples mounted and wire-bonded to a PCB compatible with the TPA-TCT setup. . . . .	184
5.8	Example of ToA extraction using the constant-fraction discrimination technique. . . . .	185
5.9	Schematic representation of time walk and sensor time jitter. . . . .	186
5.10	ToA distribution across the square pixel cell at two different depths. . .	188
5.11	MAD of the ToA distribution across the square pixel cell as a function of bias voltage. . . . .	189
5.12	ToA across the square pixel cell for several bias voltages. One-dimensional distributions for the inner and outer regions of the pixel cell. . . . .	190
5.13	Inverse ToA profiles for various bias voltages along the horizontal and diagonal axes of the square pixel cell. . . . .	191
5.14	ToA as a function of depth at different positions within the square pixel cell. . . . .	192
5.15	ToA distribution across the hexagonal pixel cell at two different depths.	193
5.16	Inverse ToA profiles along the horizontal and vertical axes of the hexagonal pixel cell. . . . .	193
5.17	MAD of the ToA distribution across the hexagonal pixel cell as a function of bias voltage. . . . .	194
5.18	ToA across one quarter of the hexagonal pixel cell for several bias voltages. One-dimensional distributions for the inner and outer regions of the pixel cell. . . . .	195
5.19	ToA as a function of depth at different positions within the hexagonal pixel cell. . . . .	196
5.20	Sensor time jitter as a function of the constant-fraction discrimination threshold used for the evaluation of ToA differences. . . . .	197
A.1	Hit detection efficiency maps for a $2 \times 2$ pixel grid from several non-irradiated modules at different bias voltages and normal incidence. . .	216
A.2	Cluster charge MPV maps for a $2 \times 2$ pixel grid from a non-irradiated module at normal incidence. . . . .	216
A.3	Cluster size maps for a $2 \times 2$ pixel grid from several non-irradiated modules at different bias voltages and normal incidence. . . . .	217

A.4	Cluster size maps for a $2 \times 2$ pixel grid from a non-irradiated module at different rotation angles. . . . .	218
A.5	Hit detection efficiency maps for a $2 \times 2$ pixel grid from a module irradiated to $1 \times 10^{16} \text{ n}_{\text{eq}}\text{cm}^{-2}$ . Measurements were performed at normal incidence and different bias voltages. . . . .	219
A.6	Cluster size maps for a $2 \times 2$ pixel grid from a module irradiated to $1 \times 10^{16} \text{ n}_{\text{eq}}\text{cm}^{-2}$ at different rotation angles. . . . .	220
A.7	Cluster charge MPV maps for a $2 \times 2$ pixel grid from a module irradiated to $1 \times 10^{16} \text{ n}_{\text{eq}}\text{cm}^{-2}$ . Measurements were performed at normal incidence and different bias voltages. . . . .	221



# List of Tables

1.1	Radiation exposure of the tracker's innermost layer in terms of particle fluence and TID for different levels of integrated luminosity during the high-luminosity phase. . . . .	17
3.1	CMS requirements for 3D pixel detectors to be installed in the innermost layer of the IT. . . . .	72
3.2	Summary of digital and hybrid pixel modules for laboratory tests. . . .	82
3.3	Comparison of results from the front-end tuning in single-chip digital and hybrid pixel modules. . . . .	92
3.4	Particle beams used to irradiate CROCv1 3D pixel modules at the CERN PS and KIT irradiation facilities. . . . .	93
3.5	Particle beams used to evaluate the performance of CROCv1 3D pixel modules at the CERN SPS and DESY test beam facilities. . . . .	95
3.6	Summary of single-chip 3D pixel modules tested in beam for the Phase-2 CMS tracker upgrade. . . . .	99
3.7	Overview of beam tests for the single-chip 3D pixel modules before and after irradiation, including irradiation facilities and particle fluences. . .	99
4.1	Classification of defective bump-bonds in the hybrid pixel modules under test, using the X-ray quality control method. . . . .	157
4.2	Classification of defective bump-bonds in the hybrid pixel modules under test, using the electrical quality control method. . . . .	162
4.3	Comparison of defective pixel classification from X-ray and electrical methods. . . . .	163
4.4	Details of the hybrid pixel module tested in a serial-power chain. . . . .	169
4.5	Comparison of results from the front-end tuning in a hybrid pixel module at different positions along a serial-power chain. . . . .	171



# List of Acronyms

<b>ALICE</b>	A Large Ion Collider Experiment
<b>ASIC</b>	Application-Specific Integration Circuit
<b>ATLAS</b>	A Toroidal LHC Apparatus
<b>CDF</b>	Cumulative Distribution Function
<b>CERN</b>	European Laboratory for Nuclear Research
<b>CFD</b>	Constant-Fraction Discrimination
<b>CMOS</b>	Complementary Metal-Oxide-Semiconductor
<b>CMS</b>	Compact Muon Solenoid
<b>CMSSW</b>	CMS Software
<b>CNM</b>	Centro Nacional de Microelectrónica
<b>CoG</b>	Center-of-Gravity
<b>DAC</b>	Digital-to-Analog Converter
<b>DAQ</b>	Data Acquisition
<b>DESY</b>	Deutsches Elektronen-Synchrotron
<b>DUT</b>	Device Under Test
<b>ECAL</b>	Electromagnetic Calorimeter
<b>FBK</b>	Fondazione Brunno Kessler
<b>FCC</b>	Future Circular Collider
<b>FPGA</b>	Field-Programmable Gate Array
<b>HCAL</b>	Hadronic Calorimeter
<b>HL-LHC</b>	High-Luminosity LHC
<b>IT</b>	Inner Tracker

---

<b>KIT</b>	Karlsruhe Institute of Technology
<b>LDO</b>	Low-DropOut
<b>LHC</b>	Large Hadron Collider
<b>LHCb</b>	Large Hadron Collider beauty
<b>MAD</b>	Median Absolute Deviation
<b>MIP</b>	Minimum Ionizing Particle
<b>MPV</b>	Most Probable Value
<b>MTD</b>	MIP Timing Detector
<b>NIEL</b>	Non-Ionizing Energy Loss
<b>OT</b>	Outer Tracker
<b>PCB</b>	Printed Circuit Board
<b>PMT</b>	Photon-Multiplier Tube
<b>PS</b>	Proton Synchrotron
<b>RMS</b>	Root Mean Square
<b>ROC</b>	Readout Chip
<b>R&amp;D</b>	Research & Development
<b>SCC</b>	Single-Chip Card
<b>SLDO</b>	Shunt LDO
<b>SNR</b>	Signal-to-Noise Ratio
<b>SPA-TCT</b>	Single-Photon Absorption Transient Current Technique
<b>SPS</b>	Super Proton Synchrotron
<b>TBPX</b>	Tracker Barrel Pixel
<b>TID</b>	Total Ionizing Dose
<b>TLU</b>	Trigger Logic Unit
<b>ToA</b>	Time-of-Arrival
<b>ToT</b>	Time-over-Threshold
<b>TPA-TCT</b>	Two-Photon Absorption Transient Current Technique

# Chapter 1

## Introduction

This thesis focuses on the characterization of 3D pixelated silicon detectors and their qualification for deployment in the upgraded tracking system of the Compact Muon Solenoid (CMS) at the Large Hadron Collider (LHC). The introductory chapter presents the motivation for this work within the broader context of high-energy physics and the challenges posed by extreme radiation environments, and provides a detailed description of the LHC and the CMS experiment.

Chapter 2 reviews the fundamental principles in semiconductor physics and the state-of-the-art in silicon detector technologies, with particular emphasis on 3D pixel sensors and their suitability for high-radiation applications. Chapter 3 presents test beam measurements used to evaluate the performance of 3D pixel detectors before and after irradiation, assessing their compliance with CMS specifications. Chapter 4 focuses on integration and system-level testing of the pixel detectors developed for the upgraded CMS tracking system, including the evaluation of the sensor-readout interconnect integrity and the performance under final powering conditions. Beyond the CMS upgrade, Chapter 5 investigates the timing capabilities of 3D pixel sensors using laser-based measurements, with particular focus on the influence of pixel cell layout on timing performance. Finally, Chapter 6 summarizes the main findings of this thesis and outlines possible directions for future research.

### 1.1. Motivation

The Standard Model (SM) [1] of particle physics is the currently accepted theory that describes the fundamental particles constituting visible matter in the universe and their interactions. These particles, called fermions, may interact through the electromagnetic, weak and strong forces. All fermions undergo weak interactions, while only charged particles suffer the electromagnetic force. Fermions are classified as quarks if they

interact via the strong force and as leptons if they do not. Due to the nature of the strong interaction, quarks are never found as free particles but are always bound in composite states called hadrons. For example, a proton is a hadron made up of three quarks.

The SM describes the forces as interactions mediated by other particles called gauge bosons. The bosons that mediate the electromagnetic and strong interactions are the photon and gluon, respectively. The weak interaction might be mediated by the neutral Z boson or the charged W bosons. The model is completed with the Higgs boson, a particle introduced in the theory to provide the mechanism by which all other particle acquire their mass. Its existence was not confirmed until its discovery in 2012 at the LHC by the ATLAS and CMS experiments. Figure 1.1 summarizes the fundamental particles of the SM.

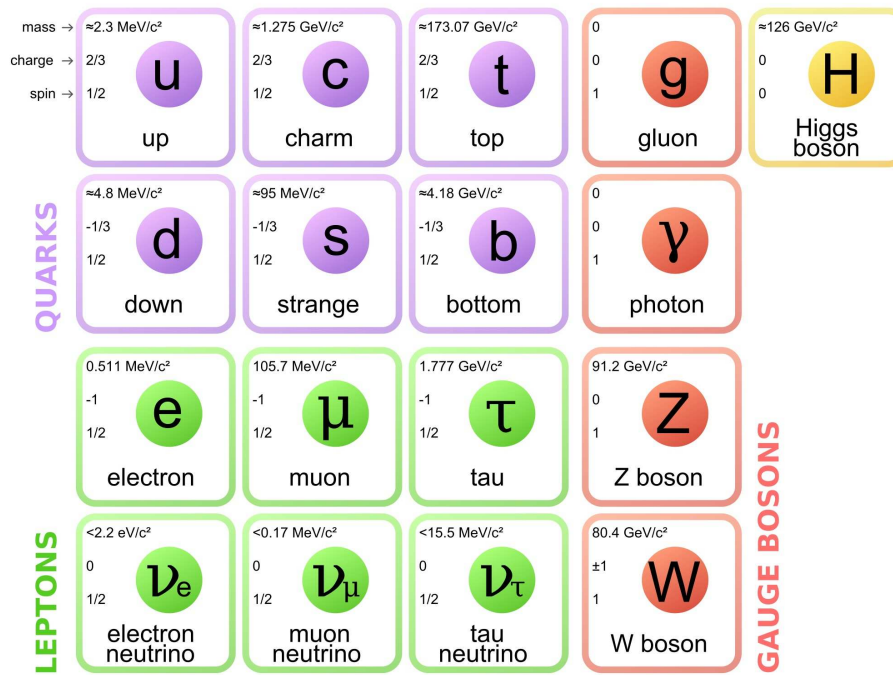


**Figure 1.1:** Elementary particles of the Standard Model of particle physics. Image from [2].

While the SM has been incredibly successful, it leaves several fundamental questions unanswered, such as the origin of the matter-antimatter asymmetry in the universe and the nature of dark matter. To explore new physics beyond the SM, a higher level of sensitivity than what the LHC currently offers is needed. In the past decade, new technological solutions have been investigated to significantly enhance the LHC potential and the detection capabilities of its experiments.

The High-Luminosity LHC (HL-LHC), as discussed in Section 1.2.1, is a planned upgrade of the LHC expected to become operational in the coming years. It will increase statistical precision while maintaining operation at the same energy scale as the current LHC, greatly expanding its physics potential. This will enable direct searches for new physics through the study of rare SM and beyond SM processes, as well as precise measurements of known particles to detect deviations from predictions that may uncover new phenomena. The Future Circular Collider (FCC) [3], on the other hand, is a proposed next-generation accelerator at CERN. Its tentative program envisions a first stage of electron-positron collisions, offering even better statistical significance for precision measurements, followed by a second stage of proton-proton collisions at much higher energies, enabling the exploration of physics beyond the energy reach of the LHC. Similar goals are shared by other proposed electron-positron colliders, such as the Circular Electron-Positron Collider (CEPC) [4] in China and the International Linear Collider (ILC) [5] in Japan. Both aim to deliver high-precision measurements of SM processes, thereby complementing the physics reach of the HL-LHC.

## 1.2. The Large Hadron Collider

The Large Hadron Collider (LHC) [6] is the largest circular particle accelerator in the world. It is located in a tunnel 100 m underground at the European Laboratory for Nuclear Research (CERN) near Geneva, Switzerland. This machine comprises a 27-km ring equipped with superconducting magnets and radiofrequency cavities that accelerate and guide particles along their way. These components are integrated with a cryogenic system of liquid helium that maintains superconducting temperatures, enabling operation with zero electrical resistance.

The radiofrequency cavities are metallic chambers containing an electromagnetic field. They are designed to resonate at specific frequencies and increase the intensity of the radio waves. Each time a beam passes through a cavity, some energy is transferred to the particles, accelerating them. In addition, these cavities group particles into synchronized tight packets, known as bunches. The LHC features 16 radiofrequency cavities operating at a frequency of 400 MHz and delivering a maximum voltage of 2 MV.

Several types of electromagnets are used to guide particles around a circular accelerator. Dipole magnets generate strong magnetic fields that bend the trajectory of the particle beam, ensuring it follows a circular orbit rather than a straight line. The more energetic the particles, the stronger the magnetic field required to maintain a stable orbit, which poses a limiting factor. Quadrupole magnets, on the other hand, focus the beam, preventing divergence and keeping the bunches tight. These are arranged in pairs,

with one quadrupole controlling beam width and the other beam height. The LHC contains 1232 main dipoles, each capable of producing a maximum magnetic field of 8.3 T, and 392 quadrupole magnets. Additional types of magnets are used for functions such as further squeezing the particles before collision or correcting imperfections in the beam deflection and focusing.

The CERN accelerator complex, depicted in Figure 1.2, is a chain of machines intended to progressively accelerate particles to higher energies [7, 8]. In the final stage, the particle beams are injected into the LHC through two separate metal pipes maintained at ultrahigh vacuum. These beams travel in opposite directions at close to the speed of light before colliding. The LHC accelerates two types of particles: protons and heavy lead ions. Protons are boosted to an energy of 6.8 TeV <sup>1</sup>, resulting in proton collisions at a center-of-mass energy of 13.6 TeV. Conversely, lead ions reach an energy of 6.8 TeV <sup>1</sup> per proton, leading to collisions at a center-of-mass energy of 5.36 TeV per nucleon pair.

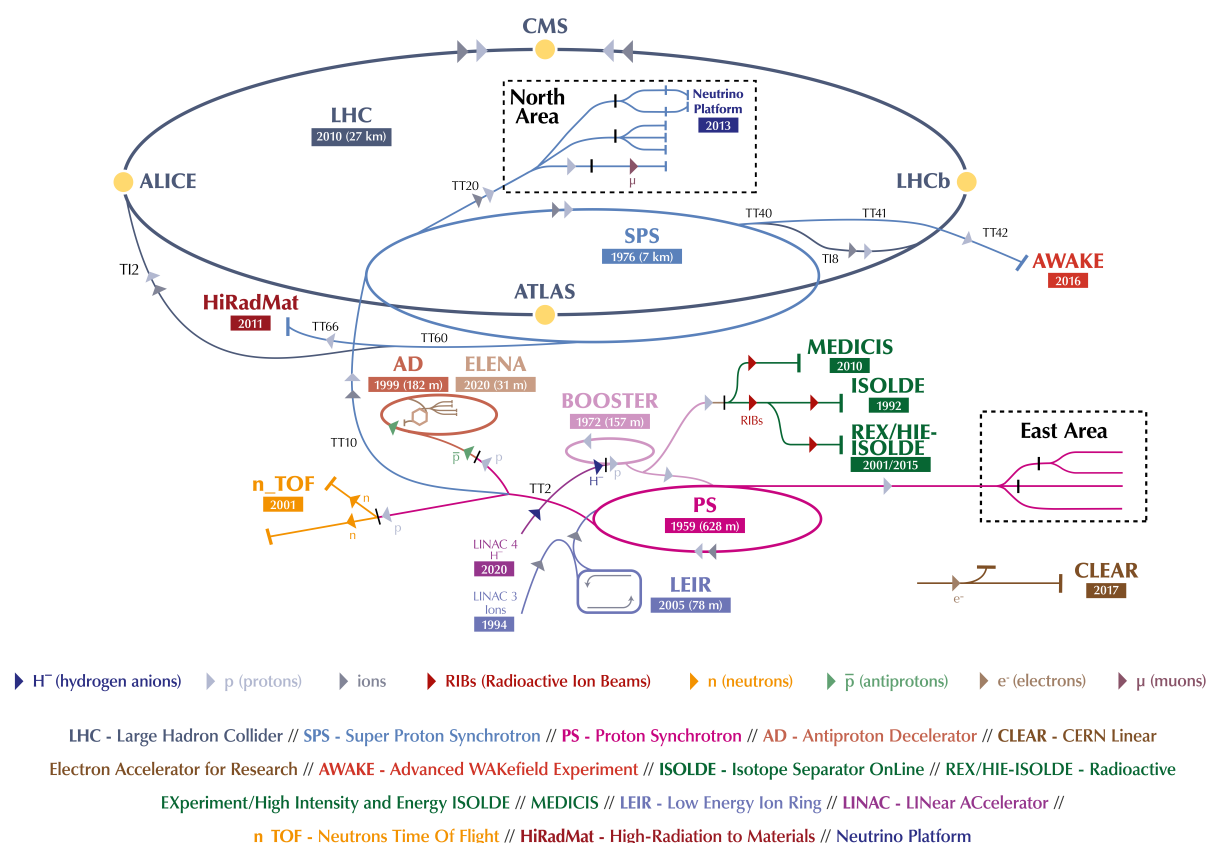


**Figure 1.2:** Schema of the CERN accelerator complex. Image from [9].

The starting point for providing proton beams within the CERN accelerator complex is Linear accelerator 4 (Linac4), which accelerates negative hydrogen ions to an energy of

<sup>1</sup>This is the energy level established for the current operation program, known as LHC Run 3 (2022-2026). The maximum proton energy that the LHC design allows is 7 TeV.

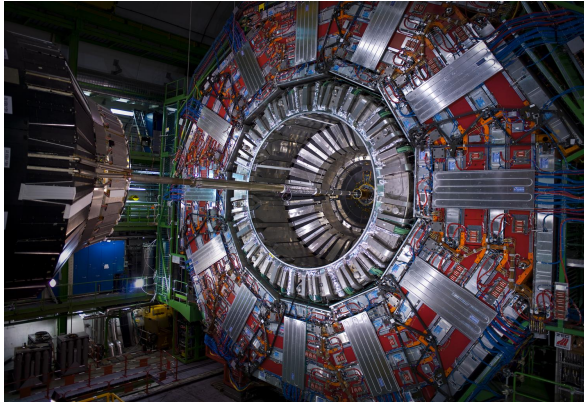
160 MeV. During their injection into the Proton Synchrotron Booster (PSB), these ions are stripped of their electrons, converting them into protons. The PSB then accelerates the protons up to 2 GeV and transfers them to the Proton Synchrotron (PS), where their energy increases to 26 GeV. Finally, the protons are sent to the Super Proton Synchrotron (SPS), reaching a maximum energy of 450 GeV prior to injection into the LHC.

Heavy-ion beams follow a different acceleration chain before reaching the PS. This process begins with Linear accelerator 3 (Linac3), which supplies lead ions to the CERN accelerator complex. The lead atoms are ionized at several stages during the acceleration sequence, achieving a fully ionized state just before injection into the PS. Initially, Linac3 accelerates the lead ions to 4.2 MeV per nucleon and sends them to the Low Energy Ion Ring (LEIR), where their energy is increased to approximately 72 MeV per nucleon. From this stage, the ion beams follow the same path as the protons: they are accelerated up to 6 GeV per nucleon in the PS and further to 177 GeV per nucleon in the SPS before their final injection into the LHC.

The accelerator complex also serves many facilities and experiments that do not belong to the LHC and require lower beam energies. For instance, the PS and the SPS feature an extraction beam line to feed the so-called East Area [10] and North Area [11], respectively. These experimental areas provide beams of various particle types and energies for fixed-target experiments, irradiation, and test-beam purposes. In particular, some of the devices analyzed for this thesis were irradiated at the IRRAD facility, which is accommodated in the East Area, and tested in beam at the North Area. More details on these irradiation and test beam campaigns will be provided in Chapter 3.

There are currently nine experiments operating at the LHC, each using sophisticated detectors to record the particles produced in the collisions. The main experiments positioned at the four collision points are: ATLAS (A Toroidal LHC ApparatuS) [12], CMS (Compact Muon Solenoid) [13], ALICE (A Large Ion Collider Experiment) [14] and LHCb (Large Hadron Collider beauty) [15]. Figure 1.3 shows an image of each of these experiments. ATLAS and CMS employ general-purpose detectors to explore a wide range of physics, from probing the Standard Model to searching for particles that could constitute dark matter. Although ATLAS and CMS share the same scientific goals, they use different technical solutions and designs, which is crucial for cross-confirming any new discoveries. In contrast, ALICE and LHCb employ specialized detectors to investigate specific phenomena. ALICE focuses on strongly interacting matter by studying the quark-gluon plasma produced in heavy-ion collisions, while LHCb examines the differences between matter and antimatter through studies of beauty quarks.

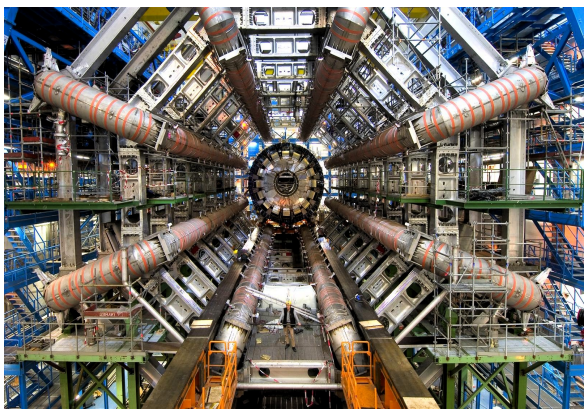




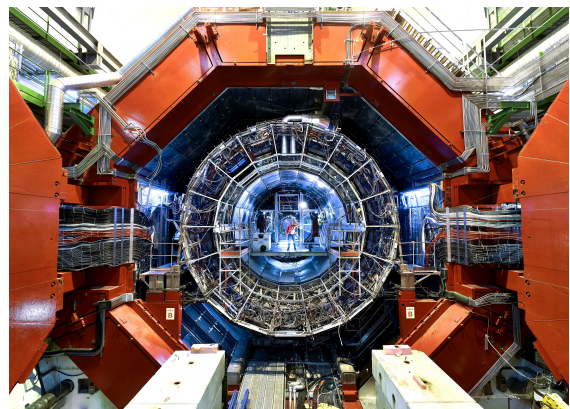
(a) CMS. Image from [16].



(b) LHCb. Image from [17].



(c) ATLAS. Image from [18].



(d) ALICE. Image from [19].

**Figure 1.3:** Images of the four main detector experiments at the CERN LHC.

The beams are divided into discrete bunches, each containing up to approximately  $1.6 \times 10^{11}$  protons with a 25 ns bunch spacing or  $2.4 \times 10^8$  lead ions with a 50 ns bunch spacing<sup>2</sup>. This configuration can result in multiple simultaneous collisions per bunch crossing, especially in proton beams. The term pile-up refers to the average number of interactions produced per bunch crossing, which increases with the instantaneous luminosity. A high pile-up environment complicates the reconstruction and identification of individual events, posing a significant challenge for data analysis. Figure 1.4c illustrates the pile-up distribution for proton-proton collisions recorded by the CMS experiment during LHC Run 2 (2015-2018) and the first years of LHC Run 3 (2022-2026). Although several interaction vertices can be reconstructed, only the most energetic interaction, known as the primary vertex, is typically considered of interest.

Luminosity [6, 21] is an important indicator of the accelerator performance. The instantaneous luminosity,  $\mathcal{L}$ , is defined as the number of particle crossings or potential

<sup>2</sup>Peak beam intensity per bunch and bunch spacing achieved in 2024 as part of the LHC Run 3 (2022-2026), based on available data at the time of writing.



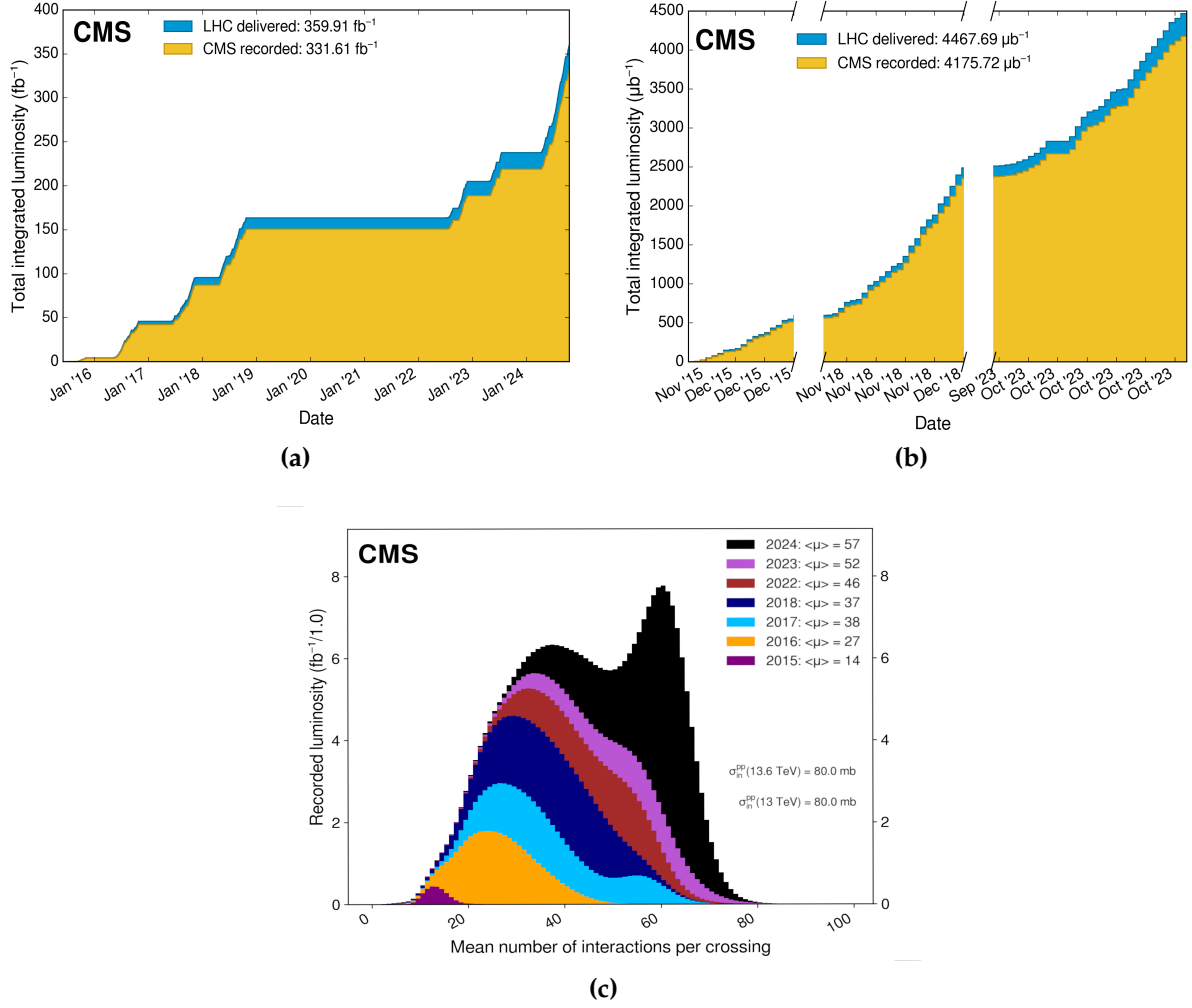


**Figure 1.4:** Integrated luminosity delivered by the LHC and recorded by the CMS experiment for (a) proton-proton collisions and (b) lead-lead collisions. The dataset includes the full Run 2 (2015-2018) and the partial Run 3 (2022-2026) available at the time of writing. (c) Distribution of the average number of interactions per bunch crossing for proton-proton collisions during the same period, with histograms for each year stacked on top of one another. Images from [20].

collisions that are produced per unit area and time. It depends on several beam parameters and can be expressed as:

$$\mathcal{L} = \gamma \frac{N_b^2 n_b f}{4\pi \epsilon_n \beta^*} F \quad (1.1)$$

where  $\gamma$  is the relativistic gamma factor,  $N_b$  the number of particles per bunch,  $n_b$  the number of colliding bunches per beam,  $f$  the revolution frequency,  $\beta^*$  the beta function at the interaction point,  $\epsilon_n$  the normalized transverse emittance, and  $F$  a geometric reduction factor from the crossing angle at the collision point.

The event rate in a particle collider,  $dR/dt$ , quantifies how often a specific process or event occurs. It depends on the instantaneous luminosity and the production cross-section  $\sigma$ , which represents the probability of that process happening. The relationship between these quantities is given in equation 1.2. A higher luminosity increases the probability of collisions, leading to a greater event rate for a particular interaction or process. This is especially important for studying rare events with a small cross-section.

$$\frac{dR}{dt} = \mathcal{L}(t)\sigma \quad (1.2)$$

The integrated luminosity,  $L$ , is the ultimate figure of merit, as it directly relates to the total number of recorded events over a given period. It is defined in equation 1.3 as the integral of the instantaneous luminosity over time. Figures 1.4a and 1.4b shows the cumulative integrated luminosity during LHC Run 2 (2015-2018) and the first years of LHC Run 3 (2022-2026) for proton-proton and lead-lead collisions, respectively.

$$L = \int \mathcal{L}(t)dt \quad (1.3)$$

### 1.2.1. The high-luminosity phase

The High-Luminosity Large Hadron Collider (HL-LHC) [22] project aims to significantly enhance the performance of the LHC in order to increase its discovery potential. The HL-LHC is designed to achieve instantaneous peak luminosities up to  $5 \times 10^{34} \text{ cm}^{-2}\text{s}^{-1}$ , with the potential to reach  $7.5 \times 10^{34} \text{ cm}^{-2}\text{s}^{-1}$  in the ultimate performance scenario. This enhancement will enable the ATLAS and CMS experiments to collect an integrated luminosity of up to  $3000 \text{ fb}^{-1}$  during the project lifetime, roughly ten times the LHC nominal design value. If the ultimate scenario is achieved, this integrated luminosity could increase further to  $4000 \text{ fb}^{-1}$ . The upgraded machine will operate at a center-of-mass energy of 14 TeV, with a bunch spacing of 25 ns. It is expected to run for a period longer than 10 years, beginning in 2030. Figure 1.5 shows the complete schedule for both the LHC and HL-LHC.

To achieve the desired luminosity, the particle beams need to be more intense and focused than in the current LHC configuration. Additionally, the higher luminosities impose unprecedented demands on vacuum, cryogenics and machine protection. The development of the necessary equipment involved over ten years of dedicated research. The project is now in the industrialization phase, with series production underway for all major components. The deployment and commissioning phase is scheduled to start in 2026, during a non-collision period known as Long Shutdown 3 (LS3). The HL-LHC relies on new operation modes and innovative technologies, including leveled luminosity operation with dynamic optics adjustments, more powerful superconducting magnets, and high-current superconducting links with almost zero energy dissipation.

It also incorporates compact, ultra-precise superconducting radiofrequency cavities for beam rotation, along with cutting-edge technologies for beam collimation.

While the increase in luminosity brings substantial benefits, it also presents the challenge of higher pile-up. For an instantaneous luminosity of  $5 \times 10^{34} \text{ cm}^{-2} \text{ s}^{-1}$ , an average of 140 interactions per bunch crossing is expected, rising to 200 in the ultimate luminosity scenario. Consequently, the experiments will be exposed to unprecedented radiation levels, requiring a comprehensive upgrade to maintain excellent detection performance under these more demanding operating conditions.



**Figure 1.5:** Complete LHC and HL-LHC schedule, as available at the time of writing. The collision center-of-mass energy, the peak instantaneous luminosity relative to the nominal value, and the cumulative integrated luminosity are indicated for each operation period. Image adapted from [23].

### 1.3. The Compact Muon Solenoid

CMS [13, 24] is a large cylindrical particle detector composed of several concentric layers that employ different sensor technologies to detect and identify the stable particles produced in each collision. The complete detector extends 21 meters in length and 15 meters in diameter, with a total weight of 14 000 tons. Figure 1.6a shows the overall layout of the CMS experiment with the following components from the innermost to the outermost region: tracker, electromagnetic calorimeter, hadron calorimeter, superconducting solenoid and muon system.

The global coordinate system used by CMS to define the direction of particles produced in the collisions is represented in Figure 1.6b. The origin is centered at the collision

point inside the detector, with the  $z$ -axis aligned along the beam direction. The  $y$ -axis points vertically upward and the  $x$ -axis is directed radially toward the center of the accelerator. The direction of a particle is determined by its momentum vector,  $\vec{p}$ , and its projection onto the plane transverse to the beam is denoted as  $\vec{p}_T$ . The azimuthal angle,  $\phi$ , is the angle between the  $x$ -axis and the transverse momentum, while the polar angle,  $\theta$ , is the angle between the  $z$ -axis and the total momentum. The pseudorapidity,  $\eta$ , is defined in terms of the polar angle as:

$$\eta = -\ln \left( \tan \left( \frac{\theta}{2} \right) \right) \quad (1.4)$$

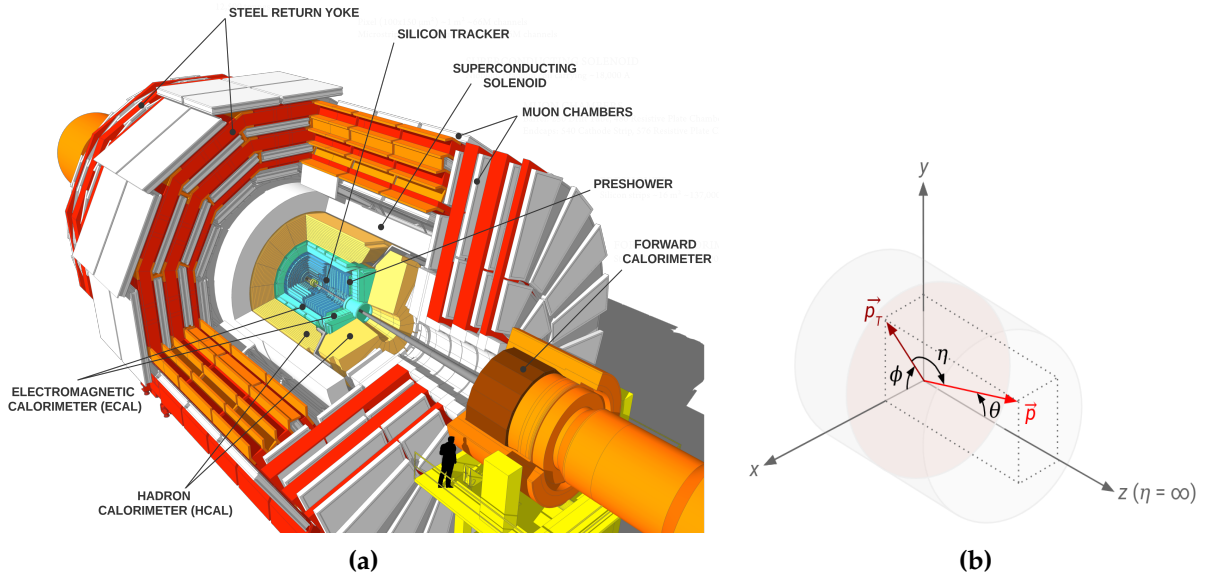


**Figure 1.6:** (a) Layout of the CMS detector. Image adapted from [25]. (b) Coordinate system of the CMS detector.

A description of each subdetector, along with the trigger system for data selection and the software infrastructure for data processing and analysis, is provided below. Particular attention is given to the tracker, since the topic of this thesis is closely related to this component.

## Tracker

The tracker [26, 27] is designed to accurately and efficiently reconstruct the trajectories of charged particles, as well as to identify those originating from primary, secondary or pile-up vertices. Combined with a homogeneous magnetic field that bends the particle trajectories, the tracker allows to measure the momentum of the particles: a higher curvature indicates lower particle momentum.

Being exposed to the highest intensity of particles, the tracking system is subject to severe radiation damage. For this reason, the detector technology is carefully chosen to feature high granularity, fast response and radiation hardness. Moreover, the tracker must be lightweight in order to disturb the particles as little as possible, thus reducing multiple scattering, bremsstrahlung, photon conversion and nuclear interactions. A compromise among all these requirements leads to a tracker entirely based on silicon detector technology.

The tracker consists of a pixel detector, which is closest to the interaction region, surrounded by a strip detector, as shown in Figure 1.7. The CMS Phase-1 pixel detector supersedes the original design and is composed of four concentric barrel layers and three disks on each side of the barrel. Similarly, the strip detector features ten barrel layers and twelve disks at each end, providing tracking coverage up to pseudorapidities of  $|\eta| = 2.5$ .

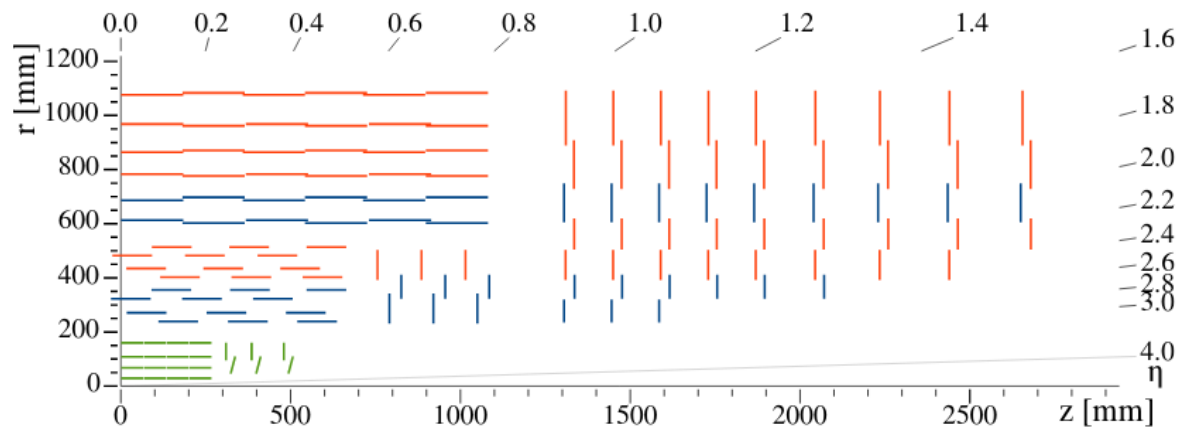


**Figure 1.7:** Layout of one quarter of the Phase-1 CMS tracker in the longitudinal view. The pixel detector with planar pixel modules is shown in green. The strip detector, consisting of single and double back-to-back modules, is depicted in red and blue, respectively. Image from [28].

The CMS Phase-1 pixel detector comprises 1856 modules, with approximately 124 million channels in total. Each module consists of a planar silicon sensor with  $160 \times 416$  pixels connected to an array of  $2 \times 8$  readout chips (ROCs) that are segmented into channels for reading out the pulse height information of each pixel. The sensors adopt the double-sided  $n$ -in- $n$  configuration, with strongly  $n$ -doped ( $n^+$ ) pixelated implants in an  $n$ -doped bulk and a uniform  $p^+$  backside implant. The sensor thickness is  $285 \mu\text{m}$ , and the standard pixel size is  $100 \times 150 \mu\text{m}^2$ . However, since two ROCs can only be placed at some minimum distance from each other, the pixels along the ROC boundaries and at the corners have twice and four times the area of a standard pixel, respectively. The sensor surface is oriented such that the long side of the pixel is

parallel to the beam line in the barrel modules and to the radial direction in the disk modules.

The strip detector is composed of 15 148 modules, some arranged in pairs mounted back-to-back, with a strip inclination of 100 mrad relative to each other for coarse two-dimensional position measurements. Each module carries either one thin sensor of 320  $\mu\text{m}$  thickness or two sensors of 500  $\mu\text{m}$  thickness each. These sensors follow a single-sided  $p$ -in- $n$  configuration, with  $p^+$  strip-shaped implants in an  $n$ -doped bulk and a uniform  $n^+$  implant on the backside. Each module features 512 or 768 strips connected to 4 or 6 ROCs, with 128 readout channels per chip. The sensor surface is generally oriented such that the strips are parallel to the beam line in the barrel and radial in the disks, although the inclination of some modules leads to different orientations. A wide variety of sensor designs exist, resulting not only from differences in thickness and number of strips, but also from variations in strip pitch and length depending on the region. All sensors maintain a ratio of  $p^+$  implant width over strip pitch of 0.25, ensuring uniform strip capacitance per unit length across all sensor geometries.

As high-energy charged particles pass through the tracker, they lose energy through ionization, producing charge carriers that generate tiny electric signals in the silicon sensors. These signals are detected and amplified by the ROCs, providing detailed information about the particle's trajectory at multiple points.

### Electromagnetic calorimeter

The electromagnetic calorimeter (ECAL) [29] consists of scintillating lead-tungstate crystals designed to precisely measure the energy of electrons, positrons and photons. When these high-energy particles interact with the dense crystal material, they initiate an electromagnetic shower, where secondary particles are produced in a cascade through processes like bremsstrahlung or pair production. The energy from these particles is transferred to the crystal lattice, causing the emission of scintillation light. This light is then captured and amplified by photodetectors: avalanche silicon photodiodes attached to the crystals in the barrel section and vacuum phototriodes glued to the crystals in the endcap regions.

A preshower detector is placed in front of the endcap to enhance the spatial resolution in this region. This is crucial for distinguishing single photons from closely-spaced photon pairs produced by the decay of neutral pions. The preshower is a sampling calorimeter with two layers of lead absorbers, which initiate electromagnetic showers, followed by silicon sensors that measure the energy deposition and the transverse shower profiles.

### Hadron calorimeter

The hadron calorimeter (HCAL) [30, 31] is designed to measure the energy of hadrons<sup>3</sup>. The barrel and endcap sections consist of alternating layers of dense absorber material, mainly brass or steel, and plastic scintillator tiles. When hadrons interact with the dense absorber, they initiate a hadronic shower of secondary particles, which produce the emission of light in their passage through the scintillator material. The scintillator tiles are instrumented with optic fibers that guide the scintillation light to silicon photomultipliers for signal detection and amplification.

The forward region serves to detect particles emerging from collisions at shallow angles relative to the beam line. Located far from the rest of the calorimeter in a high-rate environment, it uses radiation-hard quartz fibers embedded in a steel absorber structure, enabling fast collection of Cherenkov light. This light is then transmitted to photomultiplier tubes for detection.

### Superconducting solenoid

The superconducting solenoid [32] is a powerful magnet formed by a cylindrical niobium-titanium coil cooled to superconducting temperatures. This allows the circulation of approximately 19 000 A with zero electrical resistance, generating a magnetic field of up to 4 T. A steel return yoke surrounds the coil, confining the magnetic field to the detector volume while also providing structural support to the whole experiment. A strong magnetic field is crucial for bending the path of charged particles as they move away from the collision point. Combined with high-precision position measurements from the tracking and muon detectors, this enables the determination of both the charge and momentum of the particles.

### Muon system

The muon system [33, 34] integrates four types of muon chambers with diverse gaseous technologies: Drift Tubes Chambers (DTCs), Cathode Strip Chambers (CSCs), Resistive Plate Chambers (RPCs) and Gas Electron Multipliers (GEMs). Their functions are muon identification, momentum measurement and triggering. Unlike most particles, muons are highly penetrating, so they can traverse big amounts of material with little energy loss. For this reason, the muon chambers can be interleaved within the layers of the return yoke structure. The barrel section features DTCs and RPCs, while the two endcap regions incorporate RPCs, CSCs and GEMs.

### Trigger system

The LHC provides collisions at extremely high interaction rates. For instance, the 25 ns

---

<sup>3</sup>The hadrons are composite particles made up of quarks and gluons.



bunch spacing in proton beams corresponds to a crossing frequency of 40 MHz. These high rates, combined with significant pile-up, make it impossible to process and store the vast amount of generated data. CMS employs a two-stage trigger system [35] that reduces the data volume by selecting events of potential physics interest.

The first processing stage is the Level-1 (L1) Trigger, a hardware-based system implemented in custom-designed electronics. For flexibility and speed, the L1 Trigger mainly employs Field-Programmable Gate Array (FPGA) technology. It performs fast filtering based on simplified event reconstruction using the data from the calorimeters and muon chambers. The L1 Trigger reduces the data transfer rate to the second trigger level from 40 MHz to 110 kHz, with a latency of 3.8  $\mu$ s.

The second processing stage is the High-Level Trigger (HLT), an entirely software-based system that runs on a farm of commercial computers, including Central Processing Units (CPUs) and Graphical Processing Units (GPUs). The HLT accesses data from the full detector, including the tracker, and performs sophisticated event reconstruction using advanced algorithms. It ensures that the most relevant events are stored for subsequent offline analysis, with a standard data storage rate reduced to about 5 kHz.

### **CMS software**

The CMS software collection, referred to as CMSSW [36], provides a comprehensive toolkit to process and select data recorded by the CMS experiment, as well as to process data simulated through Monte Carlo techniques. The software is built around a framework, an event data model and several services required by the simulation, calibration, alignment, and reconstruction modules. These elements enable data analysis at every stage of the processing chain.

The event data model is centered around the concept of an `EVENT`, which serves as a container for data related to a specific collision from either the detector or simulation. During processing, the `EVENT` passes through a sequence of modules, each encapsulating a different functionality. As the data is processed, the products from these modules are stored in the `EVENT` as reconstructed objects, with metadata describing the configuration used for reconstruction to ensure reproducibility.

The CMSSW simulation program relies on the GEANT4 [37] toolkit to provide an accurate model of the CMS experiment. This model offers a detailed representation of the detector, including its geometry, materials, and alignment corrections. It is essential for simulating the detector response to interactions with particles produced in high-energy collisions, and it serves as the primary mechanism for comparing detector data with theoretical predictions.

The CMSSW processing chain consists of several stages, resulting in different data formats. The main stages are generation, simulation, digitization, and reconstruction.



While the first three stages apply only to simulated data, reconstruction is applied to both simulated and real detector data.

- **Generation:** high-energy physics events are created using Monte Carlo generators. General-purpose generators offer a detailed description of high-energy collisions by simulating the interaction between two incoming particles, which results in a set of outgoing particles. Additionally, there are simpler tools called particle guns that can be used to generate specific particles with user-defined kinematics, typically for software testing or specialized simulation studies.
- **Simulation:** the GEANT4 toolkit provides an accurate model of the CMS experiment and simulates the physics processes governing the interaction of generated particles with matter as they traverse the detector. The results of these interactions, such as energy loss in the sensitive volume of a subdetector, are recorded as simulated hits.
- **Digitization:** the detector response to simulated hits, as modeled by the readout electronics and data acquisition systems, is reproduced. The results closely resemble real detector data and preserve the Monte Carlo information from the generation stage. Different digitization algorithms are applied to each subdetector technology to model their specific responses.
- **Reconstruction:** this stage is divided into three phases. In the local reconstruction, individual subdetector modules reconstruct hits that provide information on energy deposition and particle positions. The global phase combines reconstructed hits from different modules within a subdetector to produce more accurate and complex objects, such as charged particle tracks in the tracker or candidate muon tracks in the muon system. The final reconstruction phase merges objects from multiple subdetectors to create higher-level objects suitable for further physics analysis, such as refined muon candidates obtained by matching tracks from the tracker and muon system.

### 1.3.1. Upgrade for the high-luminosity phase

The CMS experiment needs substantial upgrades to maintain its excellent performance in detection efficiency, resolution, and background rejection during the HL-LHC operation, as anticipated in Section 1.2.1. The so-called CMS Phase-2 Upgrade [38] addresses key challenges arising from the expected high luminosity. These include severe radiation damage to detector materials and on-board readout electronics, which could degrade the detector performance, and extremely high pile-up, which could interfere with the triggering system or hinder event reconstruction. To meet these challenges, the detector design must incorporate technologies offering high radiation hardness, improved spatial granularity and timing precision, extended coverage, increased band-

width to accommodate higher data rates, and enhanced trigger capabilities.

The upgrade of the two-stage trigger system is crucial for preserving and expanding the physics sensitivity under HL-LHC conditions. It will feature an output rate limited to 750 kHz at L1 and 7.5 kHz at the HLT. In addition, the information from the tracker will be included at the L1 stage of event selection, improving background rejection. For this reason, the L1 latency will be increased up to 12.5  $\mu$ s, providing enough time for track reconstruction and matching with calorimeter and muon chamber information. The new L1 requirements drive the upgrade of readout electronics in most subdetectors, which will also allow to improve their radiation tolerance, readout speed, and time resolution.

The muon system will implement additional stations with enhanced RPC and GEM detectors, boosting the trigger and reconstruction performance, adding redundancy, and extending the acceptance coverage. The tracker and endcap calorimeters are reaching the end of their lifetime, so they need to be fully replaced for the high-luminosity period. The large-scale hardware upgrades, including complete renovation of subdetectors or deployment of entirely new detection systems, are described in more detail below, with particular focus on the tracker upgrade.

In parallel, significant effort has been made to adapt the CMS software and computing model to new detector geometries and technologies. To address higher pile-up while minimizing the computational needs both at the online and offline levels, the algorithms for data reconstruction, analysis and storage have been optimized.

## Tracker upgrade

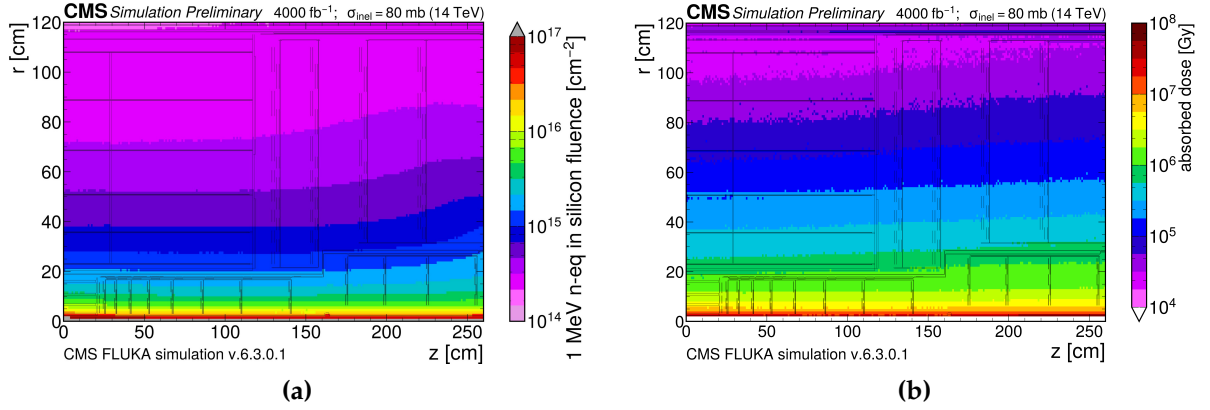
The tracker is the CMS component that will be exposed to the highest radiation levels foreseen during the high-luminosity phase. Monte Carlo simulations with the FLUKA [39] package are used to predict the magnitude of radiation as a function of luminosity. Predictions of both particle fluence<sup>4</sup> and absorbed dose—using proton-proton collisions as the primary source of radiation—are shown in Figure 1.8 for the ultimate performance scenario.

Table 1.1 reports the particle fluence and Total Ionizing Dose (TID) received by the layer closest to the interaction point for different levels of integrated luminosity accumulated during the high-luminosity phase<sup>5</sup>. The radiation damage varies across subdetectors. An overview of its main effects on silicon detectors is given in Section 2.3.

---

<sup>4</sup>Particle fluence refers to the non-ionizing energy loss per unit area, expressed as the neutron equivalent fluence for 1 MeV neutron energy (see Section 2.3). Two notations are used interchangeably throughout this thesis:  $\Phi_{\text{eq}}$  [ $\text{cm}^{-2}$ ] and  $\Phi$  [ $\text{n}_{\text{eq}}\text{cm}^{-2}$ ].

<sup>5</sup> This classification is preferred over referencing specific operational periods as the exact timing of these runs is subject to change, while the fluence and TID are tied to the achieved integrated luminosity.



**Figure 1.8:** Monte Carlo simulation of (a) the 1 MeV neutron equivalent fluence and (b) the absorbed dose in the Phase-2 CMS tracker for an integrated luminosity of  $4000 \text{ fb}^{-1}$  from proton-proton collisions at a beam energy of 7 TeV. The inelastic collision cross-section used for normalization is 80 mb. The geometry shown in black represents the longitudinal view of one quarter of the tracking system. Images from [39].

**Table 1.1:** Radiation exposure of the tracker’s innermost layer in terms of particle fluence ( $\Phi$ ) and TID for different levels of integrated luminosity expected during the high-luminosity phase.

Integrated luminosity [ $\text{fb}^{-1}$ ]	$\Phi[\text{n}_{\text{eq}}\text{cm}^{-2}]$	TID [MGy]
2100	$1.8 \times 10^{16}$	9.3
3000	$2.6 \times 10^{16}$	13.4
4000	$3.4 \times 10^{16}$	17.8

To withstand this unprecedented radiation environment and maintain good performance under more demanding operational conditions, the tracking system needs to be completely replaced. The main requirements for the upgrade include high radiation tolerance, increased granularity for better spatial resolution, high single-hit detection efficiency, minimal power dissipation, reduced material budget, and extended tracking acceptance. The Phase-2 CMS tracker [28] is specifically designed to meet these criteria. It consists of an Inner Tracker (IT) based on silicon pixel modules, which extends the tracking coverage up to pseudorapidities of  $|\eta| = 4.0$ , and an Outer Tracker (OT) made from silicon modules with strip and macro-pixel sensors, which implements the L1 trigger functionality. Figure 1.9 shows the longitudinal view of one quarter of the optimized tracker layout. The material budget in the tracking volume is reduced through the use of thinner sensors and a two-phase  $\text{CO}_2$  cooling system. Additionally, thinner sensors contribute to lower power dissipation.

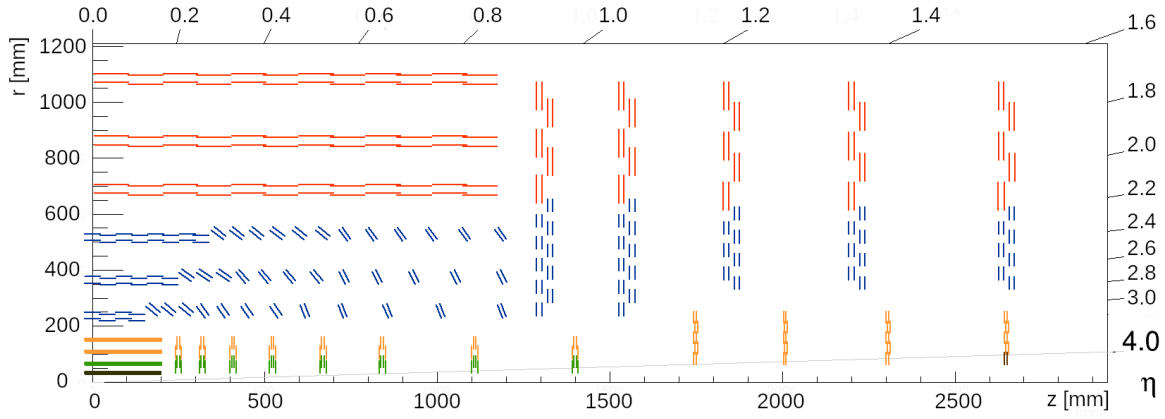


**Figure 1.9:** Layout of one quarter of the Phase-2 CMS tracking system in the longitudinal view. Planar pixel modules with two and four readout chips are depicted in green and orange, respectively. 3D pixel modules with two readout chips are shown in black. The innermost ring of the last disk, depicted in brown, has modules with four readout chips and sends data to the beam luminosity system. PS and 2S modules are shown in blue and red, respectively. More details are given in the text. Image from [40].

The OT system consists of six barrel layers, complemented by five endcap double-disks at both ends. It provides information to the L1 trigger through the so-called  $p_T$  modules. Each  $p_T$  module features two closely spaced sensors, read out by common front-end electronics. These electronics correlate the signals from both sensors and select the hit pairs, called stubs, that are compatible with particles exceeding a specific  $p_T$  threshold. The target  $p_T$  threshold of 2 GeV ensures effective background rejection at the earliest stage of event selection.

There are two types of  $p_T$  modules: 2S modules and PS modules. The 2S modules incorporate two strip sensors, each with 2032 strips that are parallel to each other and connected to 16 ROCs. The strip length in these modules is 5 cm, and the strip pitch is 90  $\mu\text{m}$ . In contrast, the PS modules combine a macro-pixel sensor with a strip sensor, each connected to 16 ROCs specific to each sensor type. The PS modules feature 1920 strips and 30 720 pixels. The strips have a length of 2.4 cm and a pitch of 100  $\mu\text{m}$ , while the pixels have a pitch of 1.5 mm. The macro-pixels in these modules are responsible for measuring the  $z$  coordinate in the barrel and the  $r$  coordinate in the endcap. Both types of modules use single-sided  $n$ -in- $p$  sensors with an active thickness of 290  $\mu\text{m}$ .

The OT system is divided into three substructures: the Tracker Barrel with PS modules (TBPS), comprising the three inner barrel layers; the Tracker Barrel with 2S modules (TB2S), which are deployed in the three outer barrel layers; and the Tracker Endcap with Double-Disks (TEDD), where the inner and outer rings are populated with 2S and PS modules, respectively.

The IT system is also divided into three substructures: the Tracker Barrel Pixel (TBPX) with four cylindrical layers, the Tracker Forward Pixel (TFPX) featuring eight small double-disks at both ends of the barrel, and the Tracker Extended Pixel (TEPX) with four large double-disks on each side. Given the expected high radiation in this region, the mechanical design of the IT system emphasizes accessibility, enabling easy maintenance and module replacement when necessary.

The IT includes 3892 hybrid pixel modules, with a total of approximately 2 billion channels. Each module features an array of either  $1 \times 2$  or  $2 \times 2$  ROCs, called double and quad modules, respectively. Each ROC is connected to 145 152 pixels. The baseline design incorporates single-sided  $n$ -in- $p$  sensors. This configuration is chosen mainly because the main source of induced charge is electrons, which have a higher mobility than holes. Moreover, this sensor type does not undergo type-inversion of the bulk after irradiation, and its fabrication process is more cost-effective than the double-sided processing used for Phase-1 pixel sensors. The standard pixel size is  $25 \times 100 \mu\text{m}^2$ , and the nominal active thickness is  $150 \mu\text{m}$ . These dimensions are six times smaller in area and about twice as thin compared to the Phase-1 pixel sensors. The sensor surface is oriented such that the long pitch of the pixel is parallel to the beam line in TBPX modules and to the radial direction in TFPX/TEPX modules.

Planar pixel sensors will be used for the entire IT, except for the innermost barrel layer, where 3D pixel sensors have been chosen due to their high radiation tolerance and lower power consumption. A detailed description of these sensor technologies is presented in Section 2.4. Extensive simulations have been conducted to assess the thermal properties of both planar and 3D pixel sensors under several particle fluences for the innermost layer of the barrel. These simulations show that the temperature needed to prevent thermal runaway<sup>6</sup> in planar pixel sensors is significantly lower than the minimum CO<sub>2</sub> temperature, whereas 3D pixel sensors offer a safety margin in this regard.

The entire Phase-2 CMS tracker provides increased sensor granularity, ensuring efficient tracking performance even with high levels of pile-up. This is achieved by maintaining the hit occupancy, defined as the fraction of channels with signal above threshold, near or below the per cent level across all regions of the tracking system. The simulated hit occupancy shown in Figure 1.10 demonstrates that the optimized tracker layout meets these requirements.

---

<sup>6</sup>Thermal runaway refers to uncontrolled heat generation that occurs when the coolant temperature is insufficient to dissipate the heat produced by the sensor, leading to a steep increase in temperature.

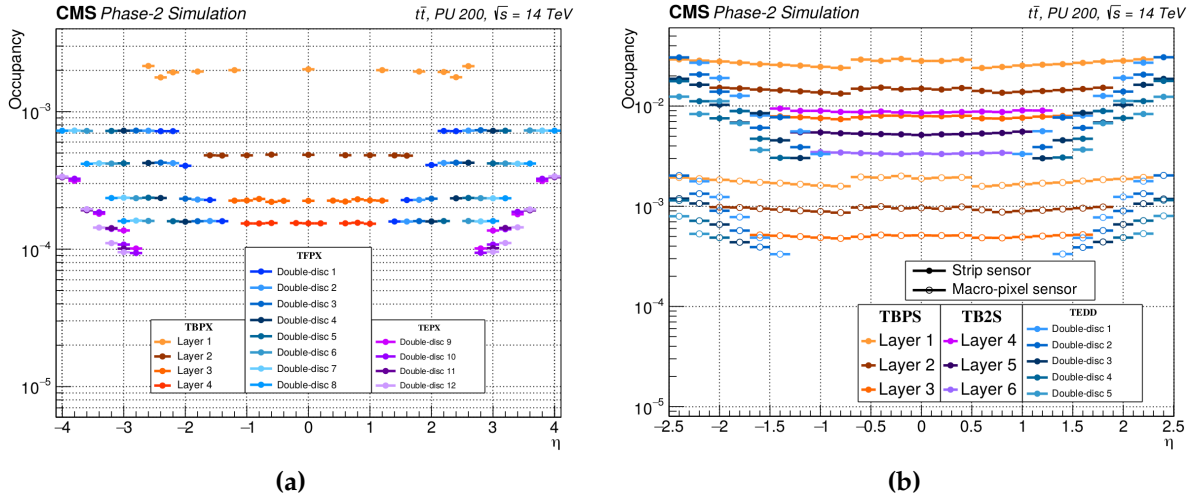


**Figure 1.10:** Hit occupancy as a function of pseudorapidity,  $\eta$ , for the (a) IT and (b) OT systems. The occupancy in the OT is shown separately for strip and macro-pixel sensors by filled and open markers, respectively. The simulation uses  $t\bar{t}$  events with an average pile-up of 200 collisions per bunch crossing. Images from [28].

## High Granularity Calorimeter

The High Granularity Calorimeter (HGCAL) [41] is an upgrade of the endcap calorimeters that integrates both the electromagnetic and hadronic components. It offers an unprecedented level of transverse and longitudinal segmentation, enabling measurements of the three-dimensional topology of energy deposits in particle showers, along with precise time-stamping of neutral particles. These features enhance particle identification, energy resolution, and pile-up rejection.

The electromagnetic section comprises 26 layers of hexagonal modules based on silicon pad detectors, interleaved with absorber structures made of copper, copper-tungsten and lead. The hadronic section consists of 21 layers of active material interleaved with steel absorber; it combines silicon pad sensors in the inner, high-radiation region and plastic scintillator tiles readout by silicon photomultipliers in the lower-radiation region farther from the beam line.

## MIP Timing Detector

The MIP Timing Detector (MTD) [42] is a new component for the CMS experiment designed to precisely measure the production time of charged minimum ionizing particles (MIPs), aiming to mitigate the impact of high pile-up on reconstruction performance. It exploits the fact that interactions within a bunch crossing occur at slightly different times due to the longitudinal extent of the bunches, with a spread of approximately 190 ps. The MTD not only improves the track-vertex assignments

by associating tracks with their corresponding timestamps, but it also provides new capabilities for charge hadron identification and the search for long-lived particles.

The MTD design consists of barrel and endcap sections, limited by the available space between the tracker and the calorimeters. The Barrel Timing Layer (BTL) is a thin cylindrical detector made of small scintillating LYSO crystals, read out by pairs of silicon photomultipliers. The Endcap Timing Layer (ETL) features a pair of double disks at each end, using silicon pad low-gain avalanche detectors for better radiation tolerance. These technologies are expected to provide a time resolution of 30–40 ps per track at the beginning of the HL-LHC operation, degrading to 50–60 ps by the end of the high-luminosity phase.



# Chapter 2

## Silicon particle detectors

Solid-state detectors have largely replaced gas-based and liquid-based detectors in many areas of experimental physics. This transition has been driven by two main advantages of semiconductor detectors: lower ionization energy and faster response time. The lower ionization energy results in more charge generation, which improves the energy resolution. At the same time, the high electric fields achievable in crystalline structures enable fast and efficient signal collection. These characteristics allow for detectors with high precision, fast readout and compact design, which are essential features for applications such as particle tracking and imaging.

Silicon represents the material of choice for most solid-state detectors in modern high-energy physics. It offers the best compromise between electrical performance, material availability and technological maturity. Silicon is abundant in nature and benefits from decades of development in the microelectronics industry, leading to reliable, high-quality and cost-effective fabrication processes. Although degradation of its properties due to radiation damage is not fully understood and remains under active investigation, it can be minimized through careful sensor design. While alternative materials such as germanium or gallium arsenide may be preferred for specific applications, silicon remains the standard for large-scale, high-resolution detectors.

### 2.1. Semiconductor detectors. Silicon

#### 2.1.1. Crystalline structure

Single-crystal materials exhibit a high degree of order throughout their volume, enhancing their electrical properties. The unit cell refers to a small set of atoms that, when repeated at regular intervals in all three dimensions, forms the lattice [43]. The most basic unit cell is the simple cubic (sc) crystal, where each vertex of the cube is occupied by an atom. The body-centered cubic (bcc) crystal features an additional atom



positioned at the center of the cube, while the face-centered cubic (fcc) crystal includes an additional atom at the center of each face. More complex configurations based on cubic crystals are present in the most commonly used semiconductors. For instance, classic single-element semiconductors, such as silicon or germanium, crystallize in the diamond structure. This structure can be described as two interpenetrating fcc sublattices, offset by one-quarter of the cube's body diagonal. In a diamond lattice, all atoms are identical, and each atom is bonded to the four equidistant nearest neighbors, forming a tetrahedral arrangement. Many compound semiconductors, such as gallium arsenide and silicon carbide, exhibit a zinc blende structure, which is similar to the diamond structure except that the fcc sublattices are composed of different atomic species. Figure 2.1a shows both the diamond and zinc blende crystal structures.

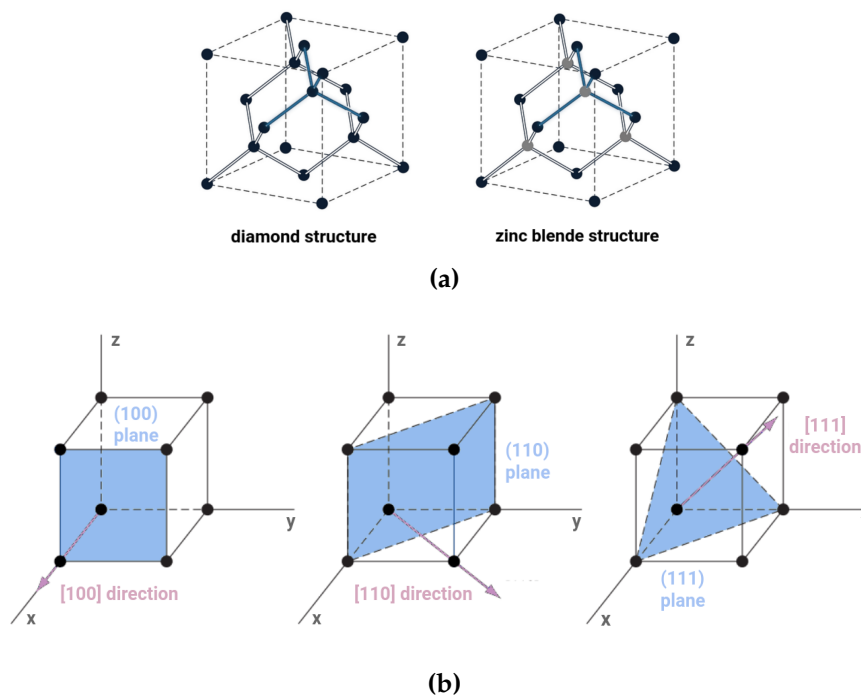


**Figure 2.1:** (a) Diamond and zinc blende crystal structures. Different atomic species are represented by different colors. The tetrahedral arrangement of an atom and its four nearest neighbors is highlighted using blue bonds. (b) Basic lattice planes in a cubic crystal with their corresponding orientations. The planes are shown in blue and the orientations are indicated by pink vectors.

Since semiconductor devices are fabricated on or near the surface of the crystal, the orientations and properties of the surface crystal planes significantly influence the electrical characteristics of the devices. The Miller indices are a notation system used to describe crystal planes and directions within the lattice, denoted as  $(hkl)$  and  $[hkl]$ , respectively. These indices are determined by taking the reciprocals of the intercepts that a plane makes with the three basis axes defining the lattice. Silicon detectors

are typically produced using three wafer orientations: (100), (110) and (111). The preferred option depends on the intended application of the device. Figure 2.1b illustrates these basic crystallographic directions and planes for the sc crystal structure.

### 2.1.2. Energy band configuration

Electrons within an atom are organized into discrete energy levels [43]. According to Pauli exclusion principle, each orbital can accommodate a maximum of two electrons with opposite spins. The so-called valence electrons, located in the outermost shell of the atom, are less tightly bound to the nucleus and readily participate in chemical reactions. When multiple atoms are brought together to form a crystal, their outer shells overlap and interact leading to an energy band structure. These energy bands actually consist of many discrete levels so slightly separated from each other that can be considered as a continuum. In particular, a silicon atom contains fourteen electrons and belongs to group IV of the periodic table, which means it has four valence electrons. The outermost shell features two subshells: 3s and 3p. The 3s subshell contains two allowed quantum states, both occupied by a pair of valence electrons. In contrast, the 3p subshell has six quantum states and only two of them are occupied by the remaining valence electrons. When  $N$  silicon atoms come close enough for their electron wavefunctions to overlap and interact, they form covalent bonds with neighboring atoms and two energy bands with  $4N$  quantum states each.

The valence band consists of the highest energy levels fully occupied by electrons at absolute zero temperature. Above the valence band lies the conduction band, where electrons are free to move through the crystal. These two bands may be separated by a forbidden energy range, known as the band gap, where no electron states can exist. The band gap, which is temperature-dependent, is defined as the difference in energy between the bottom of the conduction band and the top of the valence band. Any process that promotes an electron into the conduction band leaves behind a vacancy, or hole, in the valence band. The hole, acting as a net positive charge carrier, also moves in an electric field, but in a direction opposite to that of the electron. Therefore, the motion of both electrons in the conduction band and holes in the valence band can contribute to the electrical conductivity of a solid. The configuration of these bands, shown in Figure 2.2, determines the electrical properties of a material, leading to the following classification.

- **Insulator:** In the absence of thermal excitation, the valence band is fully occupied and the conduction band completely empty, leading to no electrical conductivity. At room temperature, the probability of electrons being thermally excited across the large band gap is very low. Consequently, insulators exhibit little to no current flow even when an electric field is applied. Typical insulators have a band gap energy ranging from 5 to 10 eV at room temperature.

- **Conductor:** The valence and conduction bands partially overlap, resulting in a nonexistent band gap. This allows electrons to move freely throughout the material, facilitating the flow of electrical current. Therefore, conductors exhibit excellent electrical conductivity, even with a minimal applied electric field.
- **Semiconductor:** At absolute zero, semiconductors behave like insulators. However, their band gap is small enough that some electrons can be thermally excited at room temperature, allowing electrical conductivity in the presence of an electric field. The typical band gap energy for semiconductors ranges from 0.5 to 3.5 eV at room temperature. In particular, the band gap energy in silicon is approximately 1.12 eV at room temperature, and its temperature dependence is described by the semi-empirical Varshni equation [44]:

$$E_g(T) = 1.1692 - \frac{(4.9 \pm 0.2) \cdot 10^{-4} \cdot T^2}{T + (655 \pm 40)} \text{ [eV]} \quad (2.1)$$

where  $E_g$  is the band gap energy and  $T$  is the temperature in Kelvin.

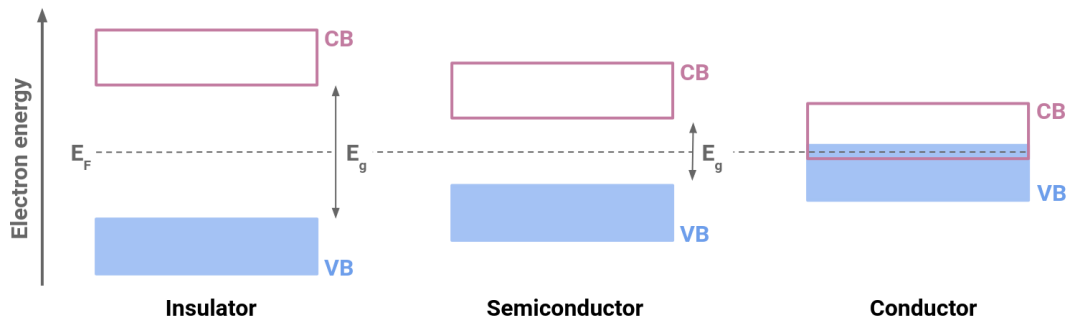


**Figure 2.2:** Simplified energy-band diagram of an insulator, conductor and semiconductor material at absolute zero.  $VB$  and  $CB$  represent the valence band and conduction band, respectively. The band gap energy,  $E_g$ , and the Fermi level,  $E_F$ , are also indicated.

The energy-momentum relation in crystalline solids, often referred to as the  $E - k$  relation, describes the energy bands in the crystal momentum space (or  $k$ -space) and is essential for understanding electron behavior in a crystal lattice. This relation expresses the electron energy  $E$  as a function of the wavevector  $k$ , which indicates the direction of the electron wavefunction within the crystal. Although crystal momentum is related to electron motion, it does not represent the actual momentum of the electron. Instead, it is a quantity that accounts for the electron interaction with the periodic potential of the crystal. Since the energy band structure varies with crystal orientation,  $E - k$  diagrams are typically plotted along several directions. In diamond and zinc blende structures, the most important orientations are  $[111]$  and  $[100]$ , as the maximum in the valence band and the minimum in the conduction band occur either at  $k=0$  or along one of these two directions.

In direct band gap semiconductors, such as gallium arsenide, the valence band maximum and the conduction band minimum are at the same  $k$ -value, usually  $k=0$ . This allows electrons to transition between these bands through the absorption or emission of photons without a change in crystal momentum. On the other hand, in indirect band gap semiconductors, such as silicon or germanium, the valence band maximum and the conduction band minimum lie at different  $k$ -values. In silicon, the minimum of the conduction band occurs along the  $[100]$  direction, while in germanium, it is along the  $[111]$  direction. In both semiconductors, the maximum of the valence band is at  $k=0$ . As a result, electron transitions between the two bands require interaction with the crystal lattice to conserve momentum, typically involving both a photon and a phonon. Figures 2.3a and 2.3b illustrate the  $E - k$  diagrams for gallium arsenide and silicon, respectively.

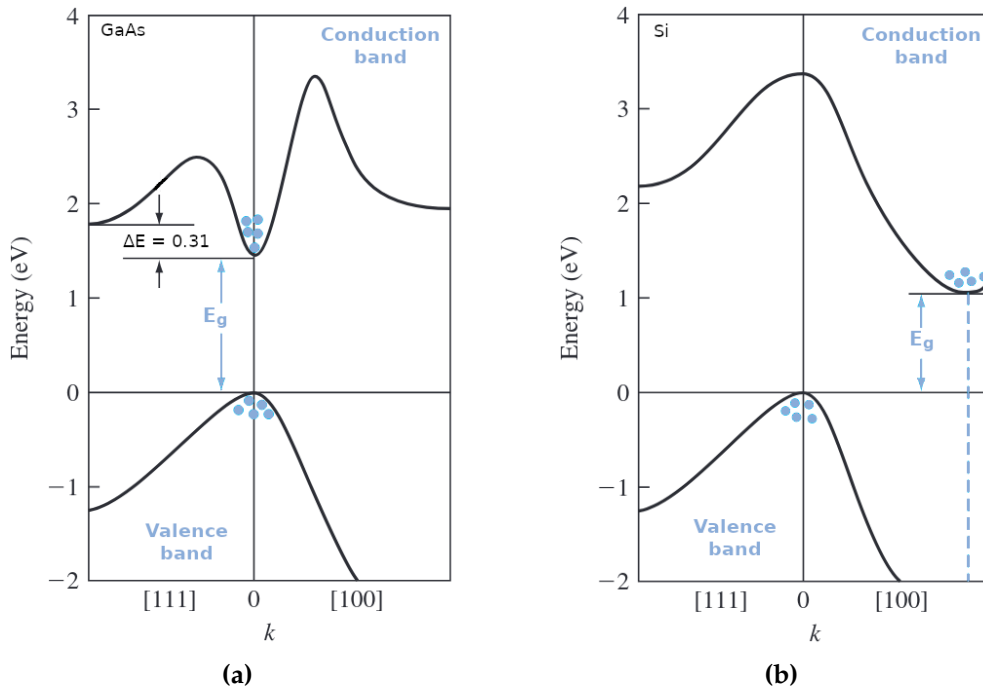


**Figure 2.3:** Simplified energy-band structure in the crystal momentum space for (a) gallium arsenide, a direct band gap semiconductor, and (b) silicon, an indirect band gap semiconductor. The  $E - k$  diagram is shown along the  $[111]$  and  $[100]$  crystal directions. The band gap is labeled as  $E_g$ . Images adapted from [43].

The Fermi-Dirac distribution,  $f(E)$ , gives the probability of an electron occupying a specific energy level  $E$  in thermal equilibrium. It is expressed as:

$$f(E) = \frac{1}{\exp \left[ \frac{E - E_F}{k_B T} \right] + 1} \quad (2.2)$$

where  $E_F$  is the Fermi level or chemical potential,  $T$  is the absolute temperature and

$k_B$  is the Boltzmann constant. The Fermi level represents the energy at which, if an electronic state were available, the occupation probability at thermal equilibrium would be exactly one-half. Temperature plays a crucial role because, as it rises, the probability that an electron is thermally excited and occupies an energy state above the Fermi level increases.

At energies that are several  $k_B T$  above or below the Fermi level, the exponential term in equation 2.2 becomes much greater than one. In this limit, the Fermi-Dirac probability function can be approximated by the Maxwell-Boltzmann distribution as follows:

$$f(E) \approx \exp \left[ -\frac{E - E_F}{k_B T} \right] \quad (2.3)$$

### 2.1.3. Intrinsic and extrinsic semiconductors

Since both electrons in the conduction band and holes in the valence band contribute to the current in a semiconductor, the density of these charge carriers is an important characteristic of the material. Semiconductors are classified as intrinsic or extrinsic based on the ratio of electron to hole concentrations at thermal equilibrium [43]. Figure 2.4 shows the schematic bond representation and simplified energy band diagram for each category. A more detailed explanation follows below.

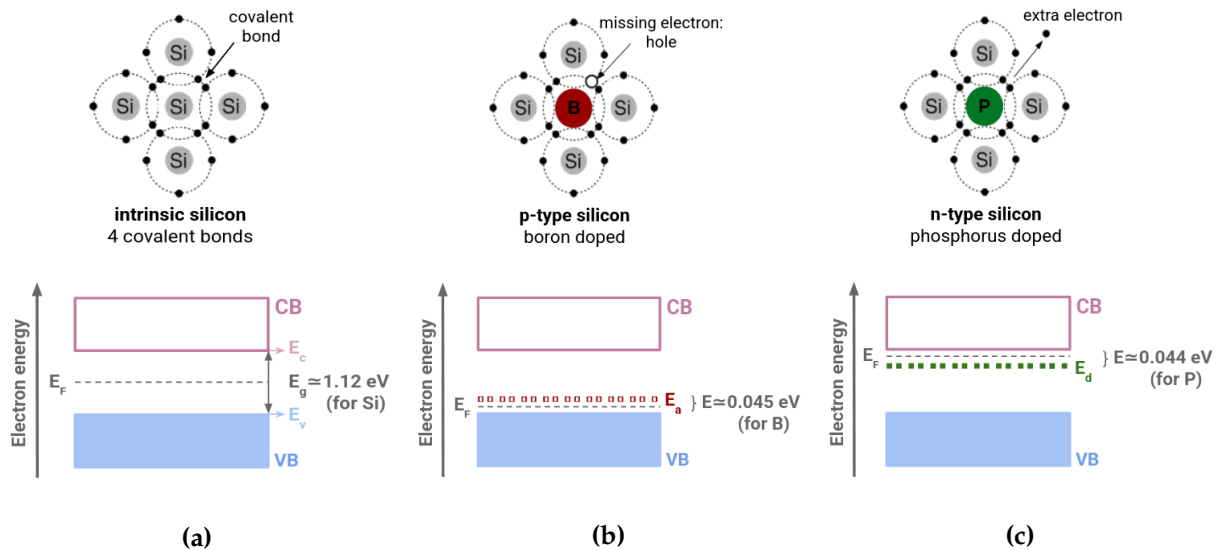


**Figure 2.4:** Schematic bond representation and simplified energy band diagram of (a) intrinsic silicon, (b) *p*-type silicon and (c) *n*-type silicon at absolute zero. The valence band, conduction band, Fermi level and band gap energy are indicated.  $E_c$  and  $E_v$  denote the energy levels at the bottom of the conduction band and the top of the valence band, respectively. The dashed red and green lines represent the new energy states,  $E_a$  and  $E_d$ , introduced by the acceptor and donor dopants, respectively.

### Intrinsic semiconductors

An ideal intrinsic semiconductor is a pure material without impurity atoms or lattice defects. As explained above, the valence band is full and the conduction band is empty at absolute zero. As the temperature increases, electrons and holes are created in pairs by thermal energy, so the number of electrons in the conduction band and holes in the valence band is the same. Thus, the Fermi level in intrinsic semiconductors, often called intrinsic Fermi level, is located somewhere between the bottom of the conduction band,  $E_c$ , and the top of the valence band,  $E_v$ .

If the intrinsic Fermi level is near the middle of the band gap, the Boltzmann approximation to the Fermi-Dirac distribution holds for energy states in both the conduction and valence bands. As a result, the thermal-equilibrium electron and hole concentrations,  $n$  and  $p$ , are given by:

$$n = N_c \exp \left[ -\frac{E_c - E_F}{k_B T} \right] \quad \text{with} \quad N_c = 2 \left( \frac{2\pi m_n k_B T}{h^2} \right)^{3/2} \quad (2.4)$$

$$p = N_v \exp \left[ -\frac{E_F - E_v}{k_B T} \right] \quad \text{with} \quad N_v = 2 \left( \frac{2\pi m_p k_B T}{h^2} \right)^{3/2} \quad (2.5)$$

where  $N_c$  and  $N_v$  are the effective density of states in the conduction and valence bands, respectively. These values are constant for a given semiconductor material at a fixed temperature. The parameters  $m_n$  and  $m_p$  represent the effective mass<sup>1</sup> of electrons and holes, and  $h$  denotes the Planck constant.

The intrinsic Fermi level is determined by setting equations 2.4 and 2.5 equal to each other, given that the electron and hole concentrations are equal in an intrinsic semiconductor. Equation 2.6 shows that the Fermi level is located slightly above or below the center of the band gap due to the different effective masses of electrons and holes. Only if these effective masses were equal would the intrinsic Fermi level lie exactly at the middle of the band gap.

$$E_F = \frac{1}{2}(E_c - E_v) + \frac{3}{4}k_B T \ln \left( \frac{m_p}{m_n} \right) \quad (2.6)$$

Since the electron and hole concentrations are equal, they are typically represented by a single parameter—the intrinsic carrier concentration  $n_i$ —such that  $n = p = n_i$ . The product of the electron and hole concentrations leads to the so-called mass action law:

$$n_i^2 = np = N_c N_v \exp \left[ -\frac{E_c - E_v}{k_B T} \right] = N_c N_v \exp \left[ -\frac{E_g}{k_B T} \right] \quad (2.7)$$

<sup>1</sup>The motion of an electron in a crystal lattice differs from that in vacuum. The concept of effective mass accounts for the interaction with the periodic potential of the lattice and its influence on the motion of electrons and holes, allowing them to be treated as free particles with a modified mass.

where  $E_g$  is the band gap energy. This equation states that, for a given semiconductor material at a fixed temperature, the intrinsic carrier concentration is constant and independent of the Fermi level.

### Extrinsic semiconductors

The electrical properties of a semiconductor can be favorably altered by adding controlled amounts of specific impurity atoms. This process, known as doping, involves swapping some of the atoms in the crystal lattice for atoms of another element. The resulting doped material, called an extrinsic semiconductor, is essential for fabricating particle detectors. These semiconductors exhibit a predominant type of charge carrier, leading to different electron and hole concentrations under thermal equilibrium.

In non-degenerate semiconductors, the impurity concentration is low compared to the concentration of host atoms, and the impurities are spread far enough apart to prevent interaction with one another. Consequently, the impurities introduce discrete energy states instead of forming a new energy band.

There are two kinds of impurities: donor and acceptor atoms. Semiconductors doped with donor atoms contain an excess of negative charge carriers and are called *n*-type semiconductors. On the contrary, semiconductors doped with acceptor atoms feature a deficit of negative charge carriers and are called *p*-type semiconductors.

In the case of silicon, impurity atoms are typically elements from either group V or III of the periodic table. A group V element, such as phosphorus, has five valence electrons. Four of these electrons participate in covalent bonds with the silicon atoms, while the fifth electron remains loosely bound to the donor atom, creating a new energy state close to the conduction band. The energy required to promote an electron from the donor energy state,  $E_d$ , to the conduction band is lower than that required for electrons involved in covalent bonding. Since these electrons do not create holes in the valence band upon excitation, the electron concentration exceeds that of holes. Therefore, in *n*-type semiconductors, electrons are the majority carriers, while holes are the minority carriers. On the other hand, a group III element, such as boron, has only three valence electrons, which are insufficient to complete all the covalent bonds with neighboring silicon atoms. This electron deficiency introduces a new energy state near the valence band. An electron from the valence band may gain a small amount of thermal energy and occupy the acceptor energy state,  $E_a$ , generating a hole in the valence band without an electron entering the conduction band. As a result, in *p*-type semiconductors, the density of holes surpasses that of electrons, making holes the majority carriers and electrons the minority carriers. Figure 2.4c and 2.4b illustrate the simplified energy band diagram at absolute zero for *n*-type and *p*-type silicon, respectively.



The electron and hole concentrations can be determined using the same expressions derived for intrinsic semiconductors in equations 2.5 and 2.4, with the key difference that the Fermi level is no longer at the intrinsic Fermi level. The addition of impurities shifts the Fermi level from near the middle of the band gap to a higher energy in  $n$ -type semiconductors and a lower energy in  $p$ -type semiconductors.

An alternative method for determining the carrier concentrations involves using the impurity concentrations. In thermal equilibrium, the crystal remains electrically neutral, meaning the net charge density is zero. This condition of charge neutrality is satisfied when the density of negative charges equals the density of positive charges. Assuming all impurity atoms are ionized, the charge-neutrality condition can be expressed as:

$$n + N_a = p + N_d \quad (2.8)$$

where  $N_a$  and  $N_d$  are the acceptor and donor concentrations, respectively. Note that in  $n$ -type semiconductors, the acceptor concentration is zero, while in  $p$ -type semiconductors, the donor concentration is zero. The mass action law from equation 2.7, along with the charge-neutrality condition, provides the electron concentration in the conduction band for an  $n$ -type semiconductor as:

$$n = \frac{N_d}{2} + \left[ \left( \frac{N_d}{2} \right)^2 + n_i^2 \right]^{1/2} \approx N_d \quad (2.9)$$

Similarly, for a  $p$ -type semiconductor, the hole concentration in the valence band is:

$$p = \frac{N_a}{2} + \left[ \left( \frac{N_a}{2} \right)^2 + n_i^2 \right]^{1/2} \approx N_a \quad (2.10)$$

When the impurity concentration is significantly larger than the intrinsic carrier concentration, the majority carrier density approximates the impurity concentration:  $N_d$  for an  $n$ -type semiconductor, and  $N_a$  for a  $p$ -type semiconductor. Once the majority carrier density is known, the minority carrier concentration can be determined using the mass action law.

The position of the Fermi level in extrinsic semiconductors depends on both impurity concentration and temperature. For  $n$ -type semiconductors, the Fermi level can be determined from equations 2.4 and 2.9 as follows:

$$E_c - E_F = k_B T \ln \left( \frac{N_c}{n} \right) \approx k_B T \ln \left( \frac{N_c}{N_d} \right) \quad (2.11)$$

As the donor concentration increases, the Fermi level moves closer to the conduction band. Similarly, for  $p$ -type semiconductors, the Fermi level can be determined using



equations 2.5 and 2.10 as follows:

$$E_F - E_v = k_B T \ln \left( \frac{N_v}{p} \right) \approx k_B T \ln \left( \frac{N_v}{N_a} \right) \quad (2.12)$$

In this case, as the acceptor concentration increases, the Fermi level moves closer to the valence band.

#### 2.1.4. Charge carrier transport

The net flow of electrons and holes in a semiconductor crystal generates currents. There are two main mechanisms for charge carrier transport: drift and diffusion [43].

##### Drift

An electric field applied to a semiconductor produces a force on electrons and holes, causing them to experience a net acceleration and movement, known as drift. This drift of charge carriers leads to the generation of a drift current.

In thermal equilibrium, charge carriers in a semiconductor move randomly in all directions due to thermal energy. However, in the absence of an electric field, their net displacement over time is zero. There are two main collision mechanisms that alter the thermal velocity of charge carriers: phonon scattering and ionized impurity scattering. The former involves interactions between charge carriers and lattice atoms that vibrate due to temperature, while the latter arises from the Coulomb interaction between charge carriers and ionized impurities. The average distance a charge carrier travels between collisions is known as the mean free path, and the average time between collisions is called the mean free time—denoted as  $\tau_n$  for electrons and  $\tau_p$  for holes.

In the presence of an electric field, the net motion of charge carriers is, therefore, a combination of the drift velocity and the random thermal velocity influenced by scattering processes. The average drift velocities for electrons,  $v_{n|drf}$ , and holes,  $v_{p|drf}$ , can be expressed as:

$$v_{n|drf} = -\mu_n E \quad \text{with} \quad \mu_n = q \frac{\tau_n}{m_n} \quad (2.13)$$

$$v_{p|drf} = \mu_p E \quad \text{with} \quad \mu_p = q \frac{\tau_p}{m_p} \quad (2.14)$$

where  $q$  is the magnitude of the elementary charge. The carrier mobilities,  $\mu_n$  for electrons and  $\mu_p$  for holes, indicate how well carriers move in response to an electric field. It should be noted that hole mobility is lower than electron mobility mostly due to the lower effective mass of electrons. Since holes are positively charged, their average drift velocity aligns with the direction of the electric field, while the drift of electrons occurs in the opposite direction.

The linear relation between average drift velocity and electric field holds only at low field strengths. In the regime of high electric fields, the drift velocity behavior deviates significantly from the linear relation and saturates, primarily due to increased scattering. This velocity saturation leads to field-dependent mobility, commonly represented by the Caughey-Thomas model, which is detailed in [45, 46].

Carrier mobility is also affected by temperature. As temperature decreases, lattice vibrations diminish, which in turn reduces the probability of phonon scattering. In lightly-doped semiconductors, this scattering mechanism predominates, making temperature a limiting factor for the mobility achievable. On the other hand, carrier mobility decreases with increasing impurity concentration, provided that the impurities are ionized at the given temperature. However, at high temperatures, the velocity of charge carriers increases, reducing the effect of Coulomb interactions due to less time spent near the ionized impurities.

The drift current densities for negatively charged carriers,  $J_{n|drf}$ , and positively charged carriers,  $J_{p|drf}$ , are given by:

$$J_{n|drf} = -qn v_{n|drf} = qn \mu_n E \quad (2.15)$$

$$J_{p|drf} = qp v_{p|drf} = qp \mu_p E \quad (2.16)$$

Since both electrons and holes contribute to the drift current, the total drift current density is the sum of the individual electron and hole drift current densities:

$$J_{drift} = J_{n|drf} + J_{p|drf} = q(\mu_n n + \mu_p p)E \quad (2.17)$$

The proportionality factor in equation 2.17 represents the conductivity,  $\sigma$ , of the semiconductor material. The reciprocal of conductivity is resistivity,  $\rho$ , expressed as:

$$\rho = \frac{1}{\sigma} = \frac{1}{q(\mu_n n + \mu_p p)} \quad (2.18)$$

In extrinsic semiconductors, both conductivity and resistivity primarily depend on the concentration and mobility of the majority carrier. High-resistivity semiconductors require a lower bias voltage to become fully depleted of charge carriers.

## Diffusion

The second mechanism that may induce current in a semiconductor is diffusion. This process drives charge carriers in random thermal motion to flow from regions of high concentration to regions of low concentration until equilibrium is reached. The net flow of charge due to this concentration gradient generates a diffusion current. The electron and hole diffusion currents, denoted as  $J_{n|dif}$  and  $J_{p|dif}$ , are given by:

$$J_{n|dif} = qD_n \nabla n \quad \text{with} \quad D_n = l_n v_{n|th} = l_n \left[ \frac{3k_B T}{m_n} \right]^{1/2} \quad (2.19)$$

$$J_{p|dif} = -qD_p \nabla p \quad \text{with} \quad D_p = l_p \nu_{p|th} = l_p \left[ \frac{3k_B T}{m_p} \right]^{1/2} \quad (2.20)$$

where  $D_n$  and  $D_p$  are the electron and hole diffusion coefficients, respectively, indicating how easily carriers move due to a density gradient. These coefficients depend on the carrier mean free path— $l_n$  for electrons and  $l_p$  for holes—and the thermal velocity of the carriers— $\nu_{n|th}$  for electrons and  $\nu_{p|th}$  for holes. The diffusion coefficients are related to the carrier mobility through the Einstein relation:

$$D_n = \frac{k_B T}{q} \mu_n \quad (2.21)$$

$$D_p = \frac{k_B T}{q} \mu_p \quad (2.22)$$

The total diffusion current density is the sum of the individual electron and hole diffusion current densities:

$$J_{diffusion} = J_{n|dif} + J_{p|dif} = q(D_n \nabla n - D_p \nabla p) \quad (2.23)$$

### 2.1.5. The pn-junction in thermal equilibrium

A pn-junction is formed when a  $p$ -type and an  $n$ -type semiconductor are brought into contact [43]. The interface separating these regions is known as the metallurgical junction. Most semiconductor devices contain at least one pn-junction, typically with one region more heavily doped than the other.

Initially, a large carrier concentration gradient exists at the metallurgical junction, leading to majority carrier diffusion. Electrons from the  $n$ -side diffuse into the  $p$ -side, while holes from the  $p$ -side diffuse into the  $n$ -side, as illustrated in Figure 2.5a. As diffusion occurs, electrons and holes recombine near the interface, leaving behind fixed ionized donor atoms on the  $n$ -side and acceptor atoms on the  $p$ -side. These ions create positive and negative space-charge regions, respectively, and induce an electric field directed from the  $n$ -side to the  $p$ -side. This electric field generates a drift of charge carriers in the direction opposite to diffusion. Equilibrium is eventually reached when the diffusion and electric field forces balance each other, as shown in Figure 2.5b. Since the space-charge region is depleted of mobile charge carriers, it is also referred to as the depletion region. The boundaries of the depletion region are denoted as  $x_n$  on the  $n$ -side and  $x_p$  on the  $p$ -side.

Figure 2.5c shows the energy band diagram of a pn-junction in thermal equilibrium. Since the Fermi level is constant throughout the system and the position of the conduction and valence bands with respect to it changes for  $n$ -type and  $p$ -type semiconductors, as discussed in section 2.1.3, the bands must bend along the space-charge region. The

potential barrier that electrons in the conduction band of the  $n$ -type region find when trying to move into the conduction band of the  $p$ -type region is known as the built-in potential,  $\phi_{bi}$ , whose expression is:

$$\phi_{bi} = \frac{k_B T}{q} \ln \left( \frac{N_a N_d}{n_i^2} \right) \quad (2.24)$$

For simplicity, the derivation of the electric field and potential assumes complete ionization of impurities and a uniform doping concentration within each region of the pn-junction. The abrupt junction approximation is also applied, assuming a sharp transition at the interface and no gradual variation in space-charge density between the depletion and neutral regions. Therefore, the space-charge density  $\rho(x)$  in the depletion region is:

$$\rho(x) = \begin{cases} -qN_a & , -x_p \leq x \leq 0 \\ qN_d & , 0 \leq x \leq x_n \end{cases} \quad (2.25)$$

where the boundaries,  $x_p$  and  $x_n$ , are positive quantities. In a pn-junction with the  $p$ -type region more heavily doped than the  $n$ -type region, the concentration of acceptor atoms is much larger than that of donor atoms:  $N_a \gg N_d$ . The space-charge density distribution is graphically represented in Figure 2.6a.

The electric field created in the depletion region by the separation of positively and negatively ionized impurities is determined from Poisson's equation, which, for a one-dimensional analysis, is:

$$\frac{d^2 \phi(x)}{dx^2} = -\frac{\rho(x)}{\epsilon} \quad \text{with } \epsilon = \epsilon_r \epsilon_0 \quad (2.26)$$

where  $\epsilon$ ,  $\epsilon_r$  and  $\epsilon_0$  are the permittivity of the semiconductor, the relative permittivity and the permittivity in vacuum, respectively. The electric potential is denoted as  $\phi(x)$ .

The integration of Poisson's equation, with null electric field at  $x = x_n$  and  $x = -x_p$  as boundary condition, leads to the expression of the electric field  $E(x)$ :

$$E(x) = -\frac{d\phi(x)}{dx} = \begin{cases} -\frac{qN_a}{\epsilon}(x + x_p) & , -x_p \leq x \leq 0 \\ -\frac{qN_d}{\epsilon}(x_n - x) & , 0 \leq x \leq x_n \end{cases} \quad (2.27)$$

For the uniformly doped pn-junction, the electric field is a linear function of distance through the space-charge region, as shown in Figure 2.6b. It reaches its maximum magnitude  $E_{\max}$  at the metallurgical junction or  $x = 0$ , so that:

$$E_{\max} = -\frac{qN_a}{\epsilon}x_p = -\frac{qN_d}{\epsilon}x_n \quad (2.28)$$

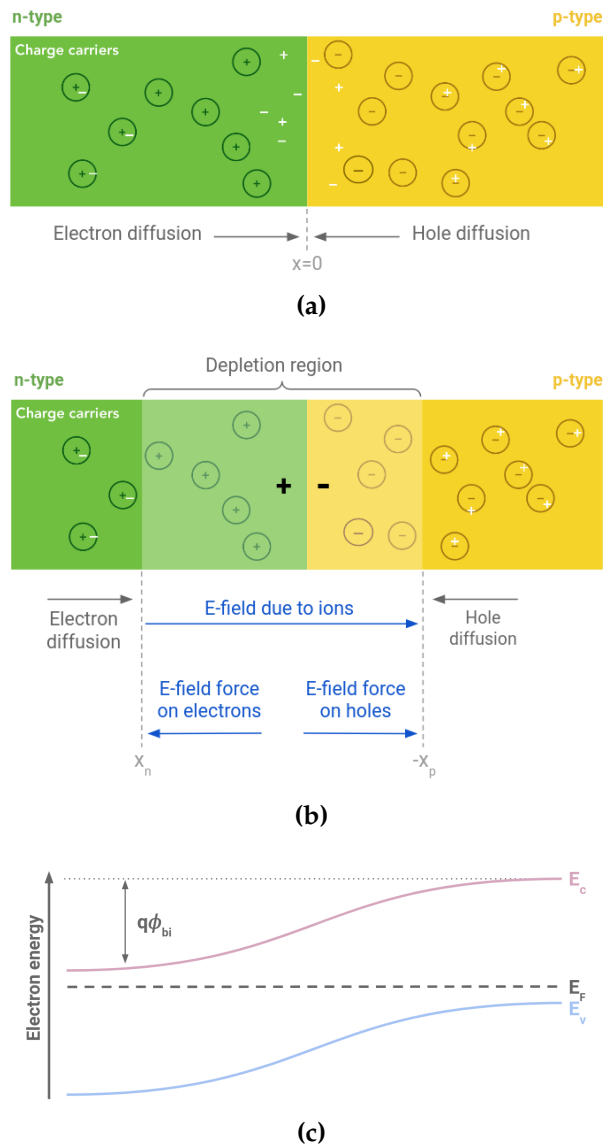


**Figure 2.5:** Simplified illustration of a pn-junction: (a) immediately after contact between the *n*-type region in green and the *p*-type region in yellow, and (b) at equilibrium. The depletion region boundaries are  $x_n$  on the *n*-side and  $x_p$  on the *p*-side. Ionized donor and acceptor atoms are represented by circles with a plus and minus sign, respectively. Charge carriers are shown as white plus signs for holes and white minus signs for electrons. (c) Energy band diagram of a pn-junction in thermal equilibrium. The potential energy of an electron is indicated as the product of the built-in potential,  $\phi_{bi}$ , and the elementary charge,  $q$ . Top images adapted from [47].

Moreover, since the electric field is a continuous function, the expressions for each region should be equal at the metallurgical junction. This results in the charge-neutrality condition given by equation 2.29, which states that the number of negative charges per unit area in the *p*-side is the same as the number of positive charges per

unit area in the  $n$ -side.

$$N_a x_p = N_d x_n \quad (2.29)$$

The integration of the electric field provides the expression of the electric potential, which is also a continuous function. To obtain this expression, the potential on one of the two boundaries is arbitrarily set to zero, since the potential difference across the junction is the magnitude of interest, rather than the absolute potential. In particular, the expressions of the electric potential in equation 2.30 are derived choosing the potential to be zero at  $x = -x_p$ .

$$\phi(x) = \begin{cases} \frac{qN_a}{2\epsilon}(x + x_p)^2 & , -x_p \leq x \leq 0 \\ \frac{qN_d}{2\epsilon}(2x_n x - x^2) + \frac{qN_a}{2\epsilon}x_p^2 & , 0 \leq x \leq x_n \end{cases} \quad (2.30)$$

The quadratic dependence of the electric potential with distance through the junction is shown in Figure 2.6c. Based on the previous choice, the magnitude of the electric potential at  $x = x_n$  corresponds to the built-in potential barrier, which takes the form:

$$\phi_{bi} = \frac{q}{2\epsilon}(N_d x_n^2 + N_a x_p^2) \quad (2.31)$$

As a result, the potential energy, which is the product of the electric potential and the electronic charge, also exhibits a quadratic dependence on distance, as anticipated in Figure 2.5c.

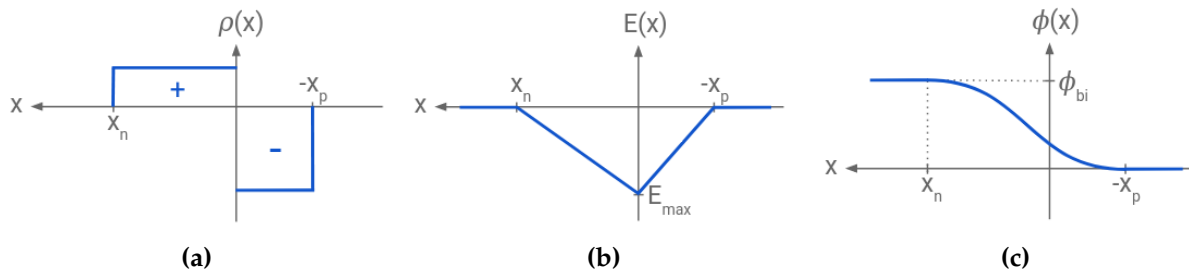


**Figure 2.6:** Distribution of (a) space-charge density  $\rho$ , (b) electric field  $E$  and (c) electric potential  $\phi$  as a function of space  $x$  in the abrupt junction approximation. The depletion region boundaries are denoted as  $x_n$  on the  $n$ -side and  $x_p$  on the  $p$ -side. The maximum electric field,  $E_{max}$ , and the built-in potential,  $\phi_{bi}$ , are also indicated.

The boundaries  $x_n$  and  $x_p$  represent the width of the space-charge region extending from the metallurgical junction into the  $n$ -side and  $p$ -side, respectively. The expressions for these parameters are derived from the built-in potential in combination with the charge-neutrality condition, given in equation 2.29, and take the form:

$$x_n = \left[ \frac{2\epsilon\phi_{bi}}{q} \frac{N_a}{N_d(N_a + N_d)} \right]^{1/2} \quad (2.32)$$

$$x_p = \left[ \frac{2\epsilon\phi_{bi}}{q} \frac{N_d}{N_a(N_a + N_d)} \right]^{1/2} \quad (2.33)$$

It might be noted that the width of the space-charge region depends on the impurity concentration in such a way that the lightly-doped side exhibits a larger depletion.

The total depletion width,  $w$ , is the sum of the two components. If the  $p$ -type region is more heavily doped ( $N_a \gg N_d$ ), the approximation shown in equation 2.34 indicates that the main contribution to the total depletion width comes from the lightly-doped side—in this case, the  $n$ -type region.

$$w = x_n + x_p = \left[ \frac{2\epsilon\phi_{bi}}{q} \frac{(N_a + N_d)}{N_a N_d} \right]^{1/2} \approx \left[ \frac{2\epsilon\phi_{bi}}{q N_d} \right]^{1/2} \quad (2.34)$$

### 2.1.6. The pn-junction under bias voltage

If an external potential is applied between the  $p$ -type and  $n$ -type regions, the junction is no longer in equilibrium and, therefore, the Fermi level is not constant through the system anymore [43]. The external potential can be either a reverse-bias voltage,  $\phi_R$ , or a forward-bias voltage,  $\phi_F$ . The pn-junction and the simplified energy band diagram for each scenario are shown in Figure 2.7.

A forward-bias voltage has the opposite sign of the built-in potential, which means that a positive voltage is applied to the  $p$ -side with respect to the  $n$ -side. Its application to the pn-junction reduces the potential barrier, and the net electric field in the depletion region also decreases. This smaller electric field allows charge carriers to diffuse across the space-charge region, so that electrons from the  $n$ -side flow into the  $p$ -side and holes from the  $p$ -side flow into the  $n$ -side, generating a diffusion current. These electrons and holes become minority charge carriers in the new regions and eventually recombine with majority carriers. The external power supply sustains the diffusion current by maintaining the forward bias across the pn-junction, which enables a continuous injection of charge carriers into the depletion region.

On the other hand, a reverse-bias voltage has the same sign as the built-in potential, which means that a negative voltage is applied to the  $p$ -side with respect to the  $n$ -side. Its application to the pn-junction enlarges the potential barrier, and the net electric field in the depletion region increases. This higher electric field pulls charge carriers further away from the metallurgical junction, leaving behind more ionized impurities and causing the width of the depletion region to increase. As a result, the pn-junction in reverse bias exhibits essentially no charge flow and, therefore, no current.

The expressions for the width of the  $n$ -type and  $p$ -type space-charge regions, as well as for the total depletion width in thermal equilibrium, remain valid when an external

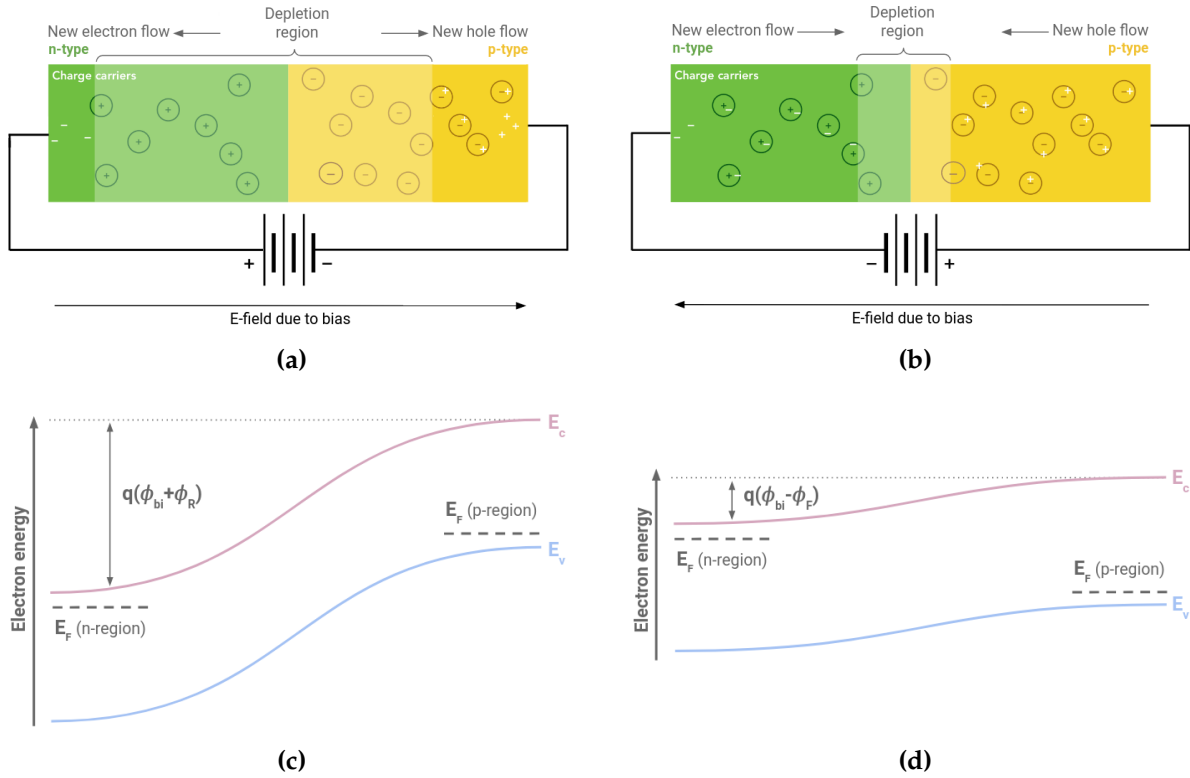


**Figure 2.7:** Simplified illustration of a pn-junction under (a) reverse-bias voltage and (b) forward-bias voltage. The  $n$ -type region is depicted in green, while the  $p$ -type region in yellow. Ionized donor and acceptor atoms are represented by circles with a plus and minus sign, respectively. Charge carriers are shown as white plus signs for holes and white minus signs for electrons. Energy band diagram of a pn-junction under (c) reverse-bias voltage,  $\phi_R$ , and (d) forward-bias voltage,  $\phi_F$ . The built-in potential is denoted as  $\phi_{bi}$ . Top images adapted from [47].

potential  $\phi_{bias}^2$  is applied. The only difference is that the built-in potential barrier is now replaced by the total potential barrier  $\phi_{bi} + \phi_{bias}$ . For instance, the total depletion width, given by equation 2.34 in thermal equilibrium, is modified under bias as:

$$w = \left[ \frac{2\epsilon(\phi_{bi} + \phi_{bias})}{q} \frac{(N_a + N_d)}{N_a N_d} \right]^{1/2} \approx \left[ \frac{2\epsilon(\phi_{bi} + \phi_{bias})}{q N_d} \right]^{1/2} \quad (2.35)$$

In reverse bias, the depletion region grows with the external potential until the lightly-doped region is fully depleted of charge carriers. At this point, the depletion region is considered to cover the entire sensor volume, providing the most efficient configuration for particle detection as it will be explained in section 2.2. Therefore, the external

<sup>2</sup>Note that  $\phi_{bias}$  may represent either  $\phi_F$  or  $\phi_R$ .



voltage to reach full depletion is derived from equation 2.35 as:

$$\phi_{\text{dep}} = \frac{q}{2\epsilon} \frac{N_a N_d}{(N_a + N_d)} d^2 - \phi_{\text{bi}} \approx \frac{q N_d}{2\epsilon} d^2 \quad (2.36)$$

where  $\phi_{\text{bias}}$  representing the full depletion voltage is denoted as  $\phi_{\text{dep}}$ , and  $w$  indicating the full thickness of the sensor is denoted as  $d$ . Furthermore, the approximation considers the built-in potential to be negligible compared to the full depletion voltage:  $\phi_{\text{dep}} \gg \phi_{\text{bi}}$ .

### 2.1.7. Electrical characteristics of the pn-junction

The current-voltage (IV) and capacitance-voltage (CV) characteristics are essential for the electrical analysis of a pn-junction under bias. Figure 2.8 presents typical curves illustrating these relationships. The equations for the IV and CV characteristics are provided below, with detailed derivations available in [43, 48].

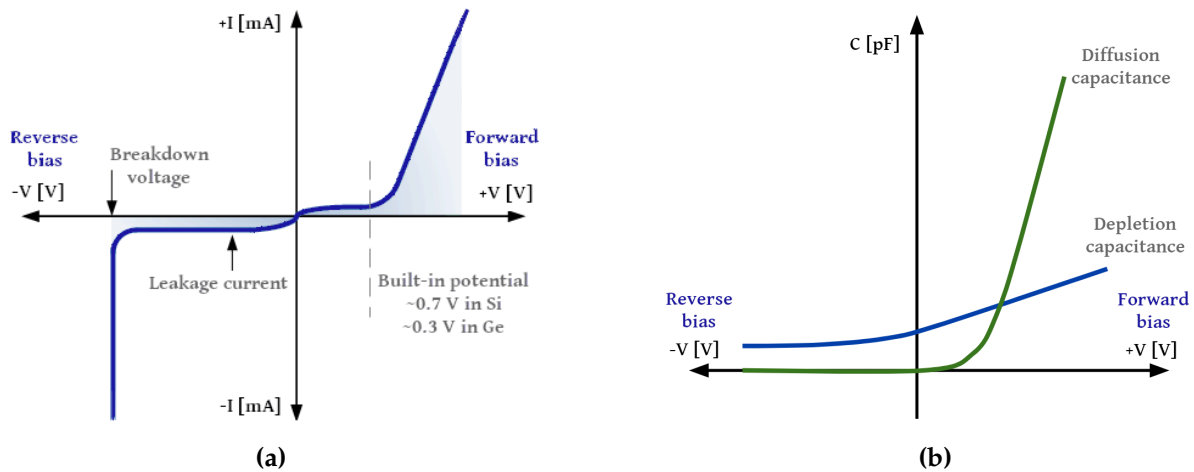


**Figure 2.8:** Characteristic curves for a pn-junction diode: (a) current-voltage,  $IV$ , and (b) capacitance-voltage,  $CV$ . The regimes for both forward and reverse bias are indicated. Left image adapted from [49].

#### Current-voltage or IV relation

The ideal IV characteristic follows the Shockley equation:

$$I = I_s \left( \exp \left[ \frac{q\phi_{\text{bias}}}{k_B T} \right] - 1 \right) \quad \text{with} \quad I_s = A \left( \frac{q D_p n_i^2}{L_p N_d} + \frac{q D_n n_i^2}{L_n N_a} \right) \quad (2.37)$$

where  $I_s$  is the reverse saturation current, and  $A$  denotes the cross-sectional area of the pn-junction.  $L_p$  and  $L_n$  represent the minority carrier diffusion lengths for holes and electrons, respectively. The large current in forward bias results from the diffusion

of majority charge carriers across the junction, which become minority carriers upon entering the opposite region. Conversely, the small current in reverse bias arises from the diffusion of minority carriers that drift to the opposite side as they enter the space-charge region.

Equation 2.37 assumes, among other ideal conditions, the absence of generation-recombination currents within the depletion region. However, in practical devices, deviations from the ideal behavior occur due to imperfections in the crystal surface and volume, which are often introduced during fabrication. These defects in the space-charge region act as generation-recombination centers, introducing new energy states within the band gap.

Under forward bias, the dominant generation-recombination process within the depletion region is carrier capture. The generation-recombination centers may trap some carriers, which eventually recombine with other carriers diffusing through the depletion region. This recombination is balanced by a continuous injection of charge carriers, resulting in an additional recombination current. Therefore, the total current in forward bias,  $I_F$ , is:

$$I_F = I + A \frac{qwn_i}{2\tau_r} \exp \left[ \frac{q\phi_{\text{bias}}}{2k_B T} \right] \quad (2.38)$$

where  $I$  is the ideal current given by the Shockley equation and  $\tau_r$  is called the recombination lifetime.

In reverse bias, the dominant generation-recombination process within the depletion region is carrier emission. The generation-recombination centers facilitate the creation of electron-hole pairs due to thermal excitation. These carriers drift influenced by the electric field, resulting in an additional generation current known as dark current or leakage current<sup>3</sup>. Thus, the total reverse current,  $I_R$ , is:

$$I_R = I + I_{\text{dark}} \quad \text{with} \quad I_{\text{dark}} = A \frac{qwn_i}{\tau_g} \quad (2.39)$$

where  $I$  refers to the ideal current given by the Shockley equation,  $I_{\text{dark}}$  is the dark current, and  $\tau_g$  is called the generation lifetime. The generation rate is proportional to the width of the depletion region, which grows with the square root of the bias voltage. Therefore, this current keeps increasing with bias rather than saturating.

The dark current strongly depends on temperature, especially after irradiation. This dependence is governed by the concentration and position of generation-recombination centers, the likelihood of charge carriers interacting with them, and the temperature dependence of the band gap itself. The standard parameterization for this relationship,

---

<sup>3</sup>Leakage current includes both dark current from bulk generation and surface currents. While technically distinct, the terms are often used interchangeably in the literature.

as described in [50], is:

$$I_{\text{dark}} \propto T^2 \exp \left[ -\frac{E_{\text{eff}}}{2k_{\text{B}}T} \right] \quad (2.40)$$

where  $E_{\text{eff}}$  is the effective band gap energy that accounts for the energy difference between the generation-recombination centers and the intrinsic Fermi level. The most efficient generation current occurs when these centers are near the intrinsic Fermi level.

An important feature of reverse bias at sufficiently high voltages is the junction breakdown, where the current sharply increases, potentially damaging the device. The main breakdown mechanism is avalanche multiplication. This happens when charge carriers, moving through the depletion region, gain enough energy from the electric field to create additional electron-hole pairs by colliding with lattice atoms. These new carriers not only contribute to the existing current but may also acquire enough energy to ionize more atoms, leading to an avalanche effect. The voltage at which this multiplication begins is known as the breakdown voltage.

### Capacitance-voltage or CV relation

The electrical capacitance of a pn-junction increases with forward-bias voltages and decreases with reverse-bias voltages. This behavior results from two contributions: depletion capacitance and diffusion capacitance. The former is present under both reverse and forward bias, while the latter is only present in forward bias.

The depletion capacitance,  $C$ , arises from the charge stored in the depletion region of the pn-junction and is given by:

$$C = \frac{dQ}{dV} \quad (2.41)$$

where  $dQ$  represents the variation of space-charge on either side of the depletion region due to a change in voltage,  $dV$ . This capacitance can be approximated as that of a parallel-plate capacitor:

$$C = \frac{A\epsilon}{w} \approx A \left[ \frac{qN_{\text{d}}\epsilon}{2(\phi_{\text{bi}} + \phi_{\text{bias}})} \right]^{1/2} \quad (2.42)$$

where the depletion width represents the distance between the two plates. This capacitance decreases as the magnitude of the reverse-bias voltage increases, which enlarges the depletion width and reduces the charge storage ability. On the contrary, under forward bias, the capacitance increases with the applied voltage, reducing the depletion width and enhancing charge storage.

Equation 2.42 is often rearranged to give:

$$\frac{1}{C^2} \approx \frac{2(\phi_{\text{bi}} + \phi_{\text{bias}})}{qN_{\text{d}}\epsilon A^2} \quad (2.43)$$

which shows a linear relationship with the applied voltage, valid up to full depletion. Once full depletion is reached, the capacitance approaches a constant value. Thus, the full depletion voltage is conventionally defined to be at the turning point of this curve, as shown in Figure 2.9. The magnitude of the built-in potential can also be experimentally determined by extrapolating the curve to the point where the inverse capacitance squared equals zero.

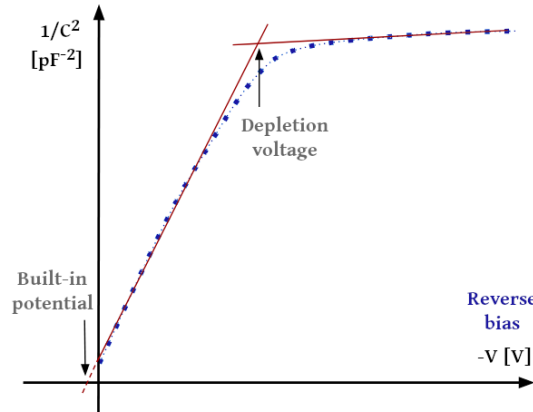


**Figure 2.9:** Inverse capacitance squared as a function of voltage. The red lines indicate the linear regimes used to empirically determine the full depletion voltage and the built-in potential magnitude. More details are provided in the text.

The diffusion capacitance,  $C_d$ , is due to a completely different mechanism, associated with the diffusion and recombination of charge carriers on each side of the junction. The significant injection of minority carriers across the junction in forward bias leads to considerable charge storage. This capacitance is an exponential function of voltage, expressed as:

$$C_d = \frac{q}{2k_B T} (I_p \tau_p + I_n \tau_n) \quad \text{with} \quad I_p, I_n \propto \exp \left[ \frac{q\phi_{\text{bias}}}{k_B T} \right] \quad (2.44)$$

where  $\tau_p$  and  $\tau_n$  are the excess minority carrier lifetimes for holes and electrons, respectively.  $I_p$  and  $I_n$  represent the hole and electron diffusion currents, which together constitute the ideal IV relation as expressed in equation 2.37. Diffusion capacitance dominates over depletion capacitance at high forward-bias voltages.

## 2.2. Signal formation

Silicon detectors are operated under reverse bias, and must be fully depleted for efficient particle detection. Ionizing particles deposit some or all of their energy when they traverse a silicon detector, generating free electron-hole pairs in the bulk material. These excess charge carriers do not recombine in the depleted medium. Instead, they

drift influenced by the electric field across the detector, inducing an electrical signal at the collecting electrodes. The mechanisms that lead to charge carrier generation and signal measurement are discussed below.

### 2.2.1. Ionizing radiation

The basis for the detection of particles is their interaction with the sensor material. They can interact with matter in many different ways, losing energy through ionizing and non-ionizing processes. In the frame of this thesis, the interactions leading to electron-hole pair generation are of the greatest importance. The interactions of particles with matter can be classified in two broad categories: charge particle interactions and neutral particle interactions.

#### Charged particles

As charged particles travel through a sensor, they continuously lose energy along their path due to interactions with the orbital electrons and nuclei of the medium. When sufficient energy is transferred to these electrons, they can be promoted to the conduction band, leading to ionization and the generation of electron-hole pairs. The mass stopping power, measured as the average energy loss per unit distance divided by the material density, depends on both the particle and material properties. Figure 2.10 shows the total mass stopping power for positively charged muons in copper as a function of the muon momentum and the relativistic  $\beta\gamma$  product, where  $\beta$  is the velocity of the traversing particle in units of the speed of light in vacuum and  $\gamma$  is the Lorentz factor.

For heavy charged particles in the range of  $0.1 \leq \beta\gamma \leq 1000$ , the average energy loss  $dE$  per unit length  $dx$ , which leads to ionization, is described by the Bethe-Bloch formula. Its expression, including correction terms for shell ( $C/Z$ ) and density ( $\delta$ ) effects, which are important at low and high energies as discussed in [52], is given by:

$$-\left\langle \frac{dE}{dx} \right\rangle = 2\pi r_e^2 m_e c^2 \rho N_A \frac{Z}{A} \frac{z^2}{\beta^2} \left( \ln \left[ \frac{2m_e c^2 \beta^2 \gamma^2 T_{\max}}{I^2} \right] - 2\beta^2 - \delta - 2\frac{C}{Z} \right) \quad (2.45)$$

where  $r_e$  is the classical electron radius,  $m_e$  is the electron mass,  $c$  is the speed of light in vacuum, and  $N_A$  is the Avogadro's number. This formula is a function of the material density  $\rho$ , the atomic number  $Z$  and atomic weight  $A$  of the medium, the effective ionization potential  $I$ , the charge of the traversing particle  $z$ , and the relativistic functions  $\beta$  and  $\gamma$ .  $T_{\max}$  represents the maximum energy that can be transferred to an electron by the traversing particle and is defined as:

$$T_{\max} = \frac{2m_e c^2 \beta^2 \gamma^2}{1 + 2\gamma m_e / M + (m_e / M)^2} \quad (2.46)$$

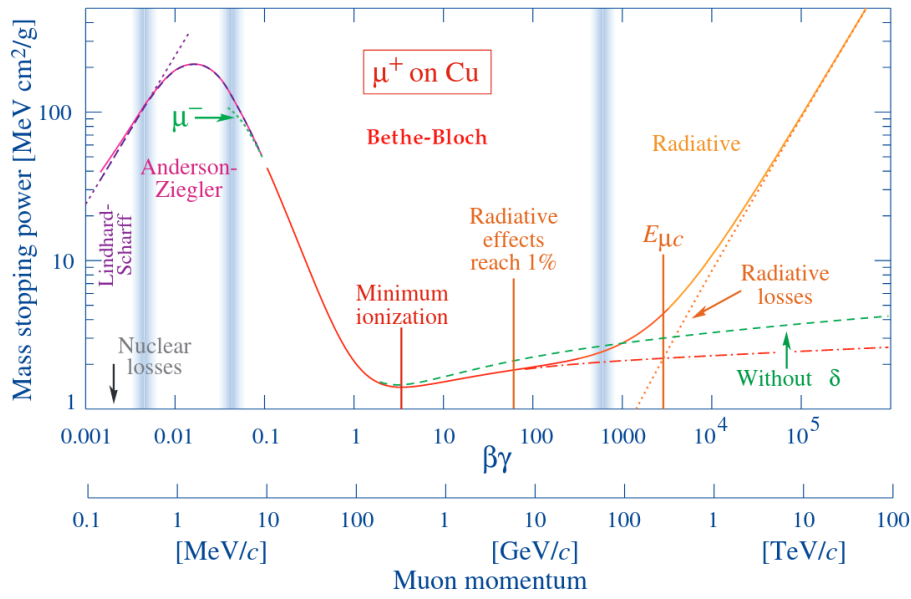


**Figure 2.10:** Mass stopping power for positively charged muons in copper as a function of  $\beta\gamma$  and muon momentum. The vertical lines indicate boundaries between different approximations. The ionization region, described by the Bethe-Bloch formula, spans the range  $0.1 \leq \beta\gamma \leq 1000$ . Image adapted from [51].

where  $M$  is the mass of the incident particle [52].

Within the Bethe-Bloch domain, the energy loss of particles in a given material decreases as  $\beta^{-2}$  and reaches a broad minimum typically positioned in the range  $3 \leq \beta\gamma \leq 4$ , depending on  $Z$ . In practical cases, most relativistic particles have an energy loss near this minimum and are referred to as Minimum Ionizing Particles (MIPs). The minimum is followed by a slow increase due to the logarithmic term, which is partially canceled by the density correction. In general, particles exhibit similar energy loss rates in different materials, although there is a slight decrease in the rate with increasing  $Z$ .

In the lower energy regime, a theoretical description is missing, and phenomenological approximations are used instead. Moreover, non-ionizing energy loss due to nuclear interactions becomes significant at very low energies. On the other hand, in the higher energy regime, the energy loss is dominated by Bremsstrahlung radiation, emitted when the traversing particle is decelerated in the Coulomb field of a nucleus. This process becomes the primary mechanism above the critical energy  $E_C$ , where ionization energy loss equals radiative energy loss. Nevertheless, these energy regimes are beyond the focus of this thesis.

The Bethe-Bloch formula in equation 2.45 provides accurate estimates for muons, pions, protons, and other charged particles of similar mass. However, it requires modifications for the much lighter fast electrons and positrons. This is due to the fact that these particles have identical mass as the orbital electrons with which they interact, and

also because scattering between indistinguishable particles must be accounted for in the mathematical treatment. Furthermore, the low mass of electrons and positrons causes Bremsstrahlung to dominate over ionization at much lower energies compared to heavier particles. The radiative energy loss for these particles increases linearly with particle energy and quadratically with  $Z$ , while the ionization energy loss decreases logarithmically with particle energy and increases linearly with  $Z$ . More details can be found in [53].

It is important to note that the Bethe-Bloch formula provides only the average ionization energy loss, but the actual energy loss of individual charged particles in matter is subject to statistical fluctuations. These fluctuations arise from variations in both the number of interactions with orbital electrons and the energy transferred in each interaction. A rare but significant event is the production of the so-called  $\delta$ -electrons, orbital electrons that gain enough energy from the incident particle to become ionizing particles themselves. The probability distribution function of energy loss in thick detectors typically follows a Gaussian distribution, while in thin detectors, where fewer interactions occur, it follows a Landau distribution, with the most probable energy loss shifted relative to the mean. Smaller energy transfers are more common, but the Landau distribution has a characteristic long tail on the high-energy side caused by rare interactions, such as the generation of  $\delta$ -electrons and, in the case of fast electrons or positrons, significant Bremsstrahlung radiation in one single interaction. As a result of this asymmetry, the mean energy loss exceeds the most probable value.

In addition, since the resolution of experimental measurement devices is typically Gaussian, the distribution of charge carriers generated by the energy loss of charged particles is best described by the convolution of a Landau distribution with a Gaussian distribution. For a MIP, the energy deposited in a 150  $\mu\text{m}$ -thick silicon absorber corresponds to approximately 11 000 electrons [52]. Moreover, the mean ionization energy required to generate an electron-hole pair in silicon is approximately 3.6 eV [54], which is more than three times larger than the silicon band gap. This energy difference is converted into phonons, which eventually dissipate as thermal energy.

### Neutral particles

The behavior of photons and neutrons with matter differs significantly from that of charged particles due to the absence of electric charge, which prevents the Coulomb interactions with orbital electrons and nuclei so characteristic of charged particles. Neutrons are usually detected through the production and detection of secondary charged particles. They interact primarily with nuclei via the strong force and can undergo a variety of nuclear processes depending on its energy, as discussed in [53]. Since photons are the most relevant neutral particles in the context of this thesis, their main interactions with matter are detailed below.



Photon interactions with matter are strongly dependent on photon energy and the electron density of the medium. The primary processes involving energy transfer are the photoelectric effect, Compton scattering and pair production [53]. Figure 2.11a shows their interaction cross-sections in carbon as a function of photon energy.

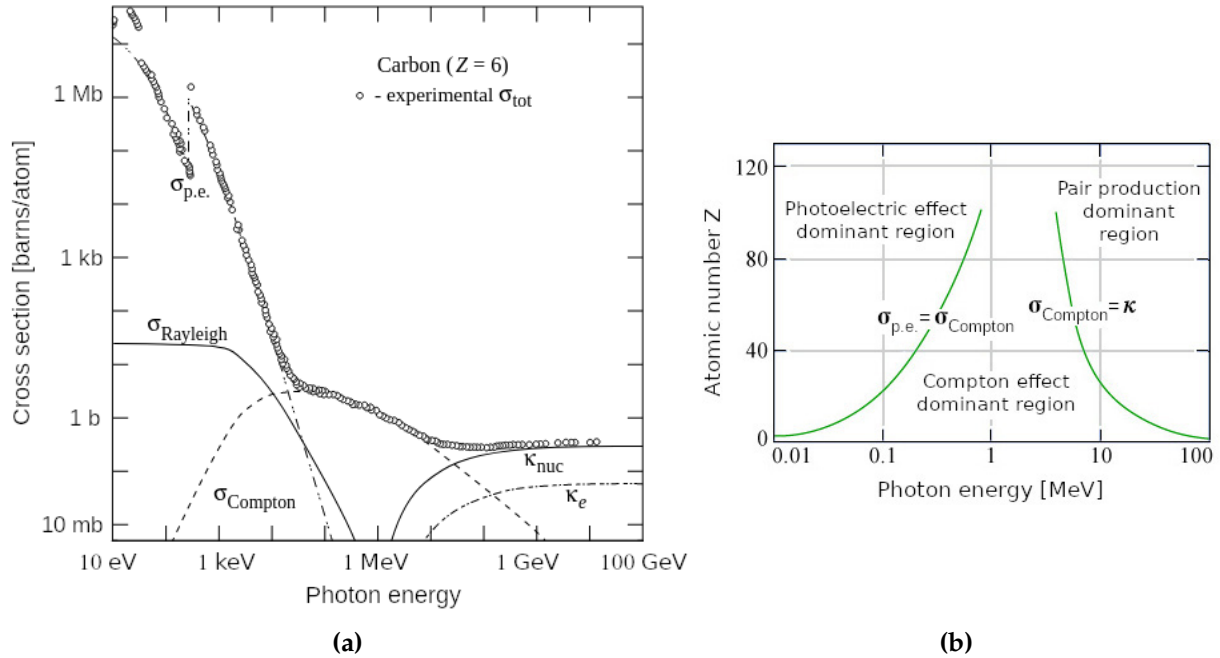


**Figure 2.11:** (a) Photon interaction cross-section in carbon as a function of photon energy. The contributions from photoelectric effect ( $\sigma_{\text{p.e.}}$ ), Rayleigh scattering ( $\sigma_{\text{Rayleigh}}$ ), Compton scattering ( $\sigma_{\text{Compton}}$ ), and electron-positron pair production in the field of a nucleus ( $\kappa_{\text{nuc}}$ ) and in the field of an orbital electron ( $\kappa_e$ ) are indicated. Image adapted from [51]. (b) Dominant interaction mechanism as a function of photon energy for different atomic number values (Z). The green curves indicate regions where the interaction cross-sections of two mechanisms are equal. Image adapted from [55].

The Compton effect involves the inelastic scattering of photons with loosely bound electrons, transferring some of the photon energy to the electron and resulting in a lower-energy scattered photon. The cross-section for this process is directly proportional to Z. When the photon energy exceeds twice the electron rest mass<sup>4</sup>, interactions with the electric field of either an atomic nucleus or an electron may lead to photon conversion into matter, creating an electron-positron pair. Its cross-section varies quadratically with Z.

The photoelectric effect, which occurs at lower photon energies, involves the photon absorption by a bound electron, resulting in the ejection of the electron from the atom. If the photon energy is high enough to promote the electron to the conduction band

<sup>4</sup>The electron rest mass is about 0.511 MeV



but not eject it from the material, the process is referred to as the photovoltaic effect. The cross-section for the photoelectric effect depends strongly on  $Z$ , varying between the fourth and fifth power depending on photon energy. Rayleigh scattering is another mechanism that occurs in the same energy range as the photoelectric effect, but it has a lower cross-section and does not involve energy transfer. For this thesis, the photovoltaic effect is the most relevant process, since it describes the generation of excess charge carriers from light.

Figure 2.11b illustrates the dominant photon interaction mechanisms as a function of photon energy for different  $Z$  values. Overall, the photoelectric effect dominates at low energies, the Compton effect at intermediate energies, and pair production at high energies.

In the interaction of photons with matter, a photon is removed from the beam after a single interaction, either through total absorption or scattering at a large angle. Unlike charged particles, a monochromatic photon beam is not degraded in energy as it passes through a material. Instead, it is attenuated in intensity according to the following equation:

$$I = I_0 e^{-\mu x} \quad \text{with} \quad \mu = N (\sigma_{\text{p.e.}} + \sigma_{\text{Compton}} + \sigma_{\kappa}) \quad (2.47)$$

where  $I_0$  and  $I$  represent the beam intensity before and after traversing a medium of thickness  $x$ ,  $N$  is the density of atoms, and  $\sigma$  represents the interaction cross-section of each relevant process per atom. The absorption coefficient,  $\mu$ , represents the probability of an interaction occurring per unit length. It is a material property that varies with photon energy and characterizes how the medium absorbs or attenuates the photon beam. Figure 2.12 shows the variation of the absorption coefficient in silicon as a function of photon wavelength, along with the corresponding attenuation length or absorption depth, which is inversely proportional. At very low photon energies, materials typically become transparent.

### 2.2.2. Shockley-Ramo theorem

Electron-hole pairs generated by ionizing radiation in the depleted region of a sensor drift towards the collecting electrodes under the influence of the electric field. Electrons are collected at the  $n^+$  electrode, while holes are collected at the  $p^+$  electrode. The movement of these charge carriers through the bulk induces a current on the collecting electrode:  $I_e$  for electrons and  $I_h$  for holes. The total induced current,  $I$ , is described by the Shockley-Ramo theorem [57] as follows:

$$I(t) = I_e(t) + I_h(t) = qN(\vec{v}_{n|\text{drf}} + \vec{v}_{p|\text{drf}}) \cdot \vec{E}_W \quad (2.48)$$

where  $q$  is the elementary charge and  $N$  is the number of electron-hole pairs. The drift velocities for electrons,  $v_{n|\text{drf}}$ , and holes,  $v_{p|\text{drf}}$ , are defined in equations 2.13 and 2.14,

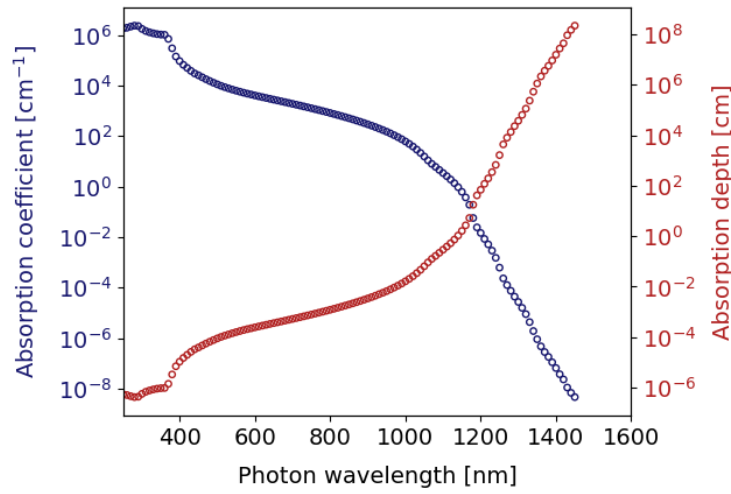


**Figure 2.12:** Variation of the linear absorption coefficient (blue) and absorption length (red) in silicon at room temperature as a function of photon wavelength. Data from [56].

respectively. The weighting field,  $E_W$ , determines how the charge motion couples to a specific electrode to induce a signal, and it depends on the geometry and configuration of the electrodes. In contrast, the electric field governs the direction and velocity of charge carriers and is influenced by factors such as electrode geometry, bias voltage and radiation damage.

The time dependence,  $t$ , in Shockley-Ramo theorem accounts for the variation of both the electric field and weighting field as a function of the position of charge carriers as they move. To calculate the total charge induced on the collecting electrode, equation 2.48 has to be integrated over the collection time. Assuming the charge carriers are generated at a position  $x_0$ , the total collected charge  $Q$  is:

$$Q = \int I(t)dt = qN(\phi_W(x_n) - \phi_W(x_0)) + qN(\phi_W(x_p) - \phi_W(x_0)) \quad (2.49)$$

where  $x_n$  and  $x_p$  are the positions of the  $n^+$  and  $p^+$  electrodes, respectively, and  $\phi_W$  is the weighting potential evaluated at different positions. The weighting field and potential are obtained by solving the Laplace equation, after applying a unit potential to the sensing electrode and zero potential to all other electrodes in the system.

## 2.3. Radiation damage in silicon

The performance of detectors degrades when exposed to a continuous flux of high-energy particles, making efficient operation challenging. Radiation-induced effects vary depending on the detector type. In silicon detectors, radiation damage is usually divided into surface and bulk defects. It is worth noting that, although defects are most commonly associated with radiation damage, they are also present in non-irradiated

devices due to imperfections in the crystal lattice. The purity of the silicon wafer and its processing influence the type and concentration of these crystalline defects. However, their concentration is significantly lower than that of radiation-induced defects.

Surface damage occurs in the covering dielectric and its interface with silicon, primarily due to ionization of the silicon oxide layer. Ionization in silicon oxide is not fully reversible and leads to the accumulation of charges at the interface. This can generate surface currents, contributing to the overall leakage current, and high local electric fields, which may lead to breakdown or avalanche effects. However, advanced detector design techniques, such as *p*-stop or *p*-spray isolation, are employed to minimize these effects, ensuring that surface damage has a limited impact on the operational lifetime of silicon detectors. More details on this type of damage can be found in [58].

In contrast, bulk damage arises from the displacement of atoms within the silicon crystal lattice. These defects significantly alter the electrical and optical properties of the material, becoming an important limiting factor for the use of silicon detectors in high-radiation environments. A detailed discussion of bulk damage and its impact on detector performance is provided below, based on [59].

The interaction of high-energy particles with the nuclei of the silicon lattice can result in energy loss through non-ionizing processes. These interactions can damage the device by displacing silicon atoms from their regular lattice positions. To displace a silicon atom, a minimum recoil energy of approximately 25 eV must be transferred. If the so-called primary knock-on atom gains enough energy during its collision with the incident particle, it can cause further displacement of neighboring atoms, creating a cluster of defects. The energy threshold for the formation of a cluster is approximately 5 keV. Figure 2.13 shows a schematic representation of point-like and clustered defects in a silicon lattice. Each defect or Frenkel pair consists of a vacancy, which is the empty lattice site left by the displaced atom, and an interstitial, which is the displaced atom located at a non-periodical position. The interactions between these defects, or between defects and impurity atoms, along with their electrical properties, are responsible for the macroscopic deterioration of the detector performance.

The Non-Ionizing Energy Loss (NIEL) quantifies the energy deposit of the incident particle that does not result in ionization of the material. The fraction of this energy that leads to displacement damage rather than dissipation in phonons depends on the particle energy. The NIEL hypothesis assumes that any radiation-induced effect in the macroscopic sensor properties is proportional to the amount of energy transferred in the collision, independently of the defect spatial distribution. Therefore, the radiation damage produced by different particle species or the same particle with different energies can be scaled under this assumption. Figure 2.14 shows the NIEL cross-section or displacement damage function for several types of radiation as a function of

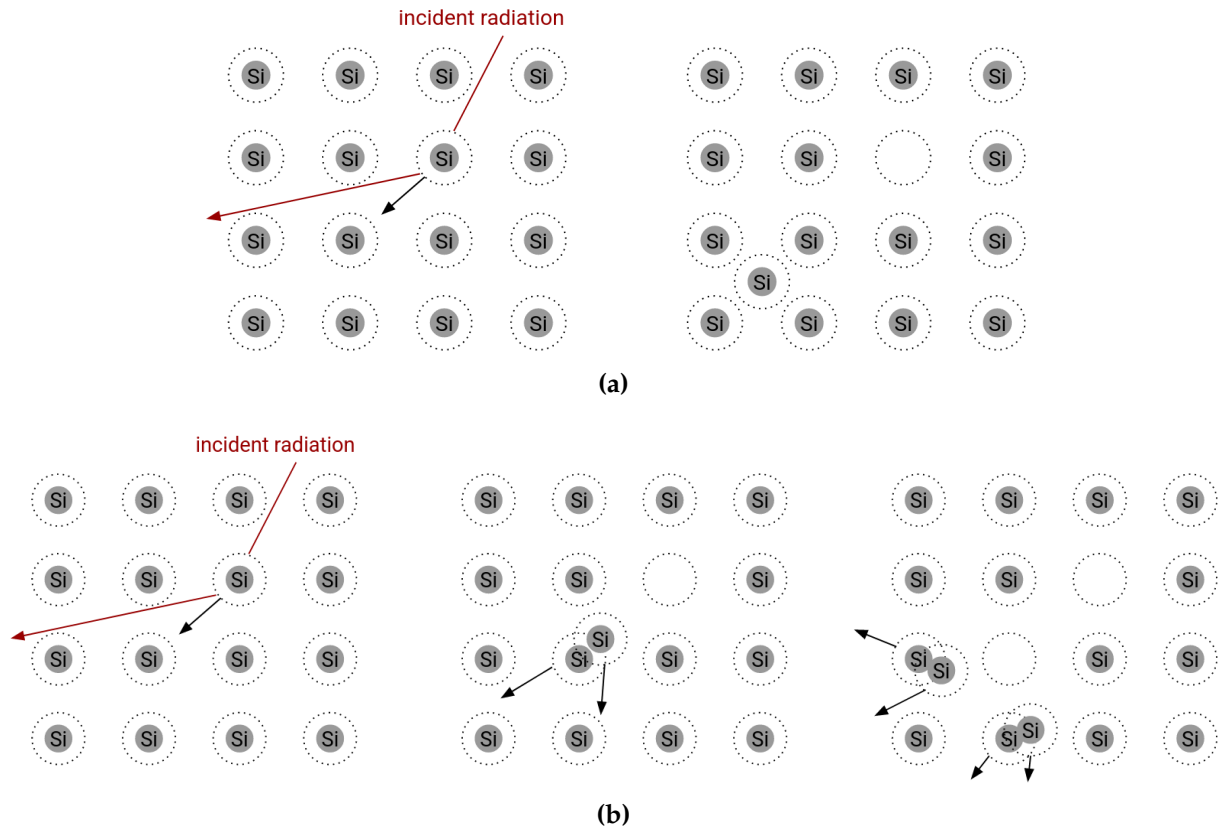


**Figure 2.13:** Schematic representation of (a) a point-like defect and (b) a clustered defect produced in the collision of an incident particle with an atom of the silicon lattice. The displacement damage leads to vacancies and interstitial atoms.

the particle energy. The displacement damage is typically normalized to a reference value, which by convention is the displacement damage of a 1 MeV neutron.

In line with the scaling hypothesis, the hardness factor,  $\kappa$ , defines the amount of displacement damage caused by a particle with energy  $E$  relative to the damage produced by a 1 MeV neutron. This factor enables comparisons between irradiation facilities that use different radiation sources, by converting the particle fluence,  $\Phi_p$ , into an equivalent 1 MeV neutron fluence,  $\Phi_{eq}$ . The conversion is expressed as:

$$\Phi_{eq} = \kappa \Phi_p(E) \quad (2.50)$$

### 2.3.1. Impact on the sensor properties

Displacement damage can introduce additional energy levels within the band gap, modifying the electrical characteristics of the bulk material. These energy levels mainly lead to increased leakage current, variations in depletion voltage, and reduced charge collection [59]. Although these effects are not mutually exclusive, the position of the energy levels causes some defects to affect specific characteristics more than others.

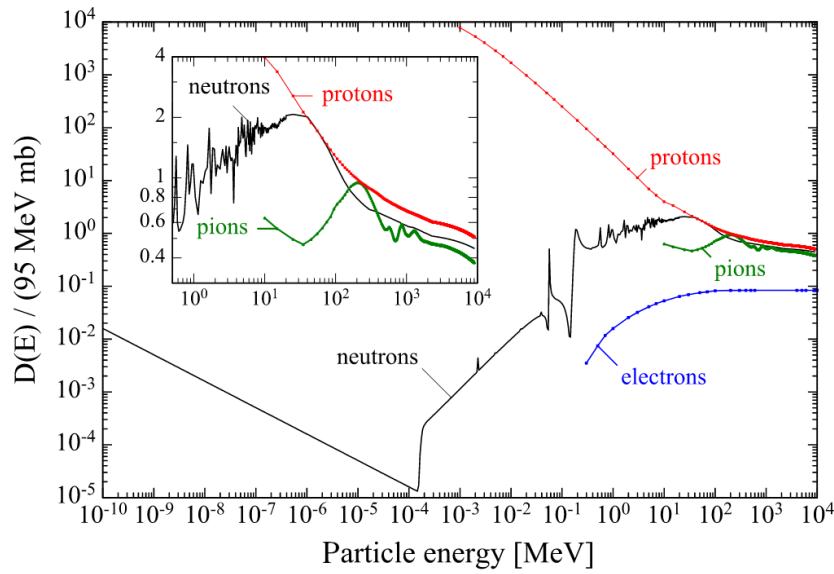


**Figure 2.14:** Displacement damage function,  $D$ , of several particles, normalized to the displacement damage produced by a 1 MeV neutron, as a function of the particle energy. The reference value used for normalization is 95 MeVmb. Image from [59].

### Leakage current

Defect energy levels near the middle of the band gap are the most efficient generation centers, since they provide a shortcut for electron-hole pair generation through thermal excitation. This leads to an increase in leakage current,  $\Delta I$ , which scales linearly with fluence, as described by:

$$\Delta I = \alpha V \Phi_{eq} \quad (2.51)$$

where  $V$  is the depleted volume contributing to the leakage current, and  $\alpha$  is the current-related damage factor. Figure 2.15 shows the leakage current increase per unit volume as a function of  $\Phi_{eq}$  for several silicon devices with different doping types, resistivity, and growth techniques.

An increase in leakage current is undesirable because it introduces additional noise in the readout electronics and results in higher power consumption, increasing the risk of thermal runaway. The strong temperature dependence of the leakage current, as indicated in equation 2.40, makes device cooling an effective strategy to counterbalance its increase during operation.

### Charge Trapping

Defects with deep energy levels typically act as trapping centers, capturing charge carriers as they drift toward the electrodes. If the time required to release the trapped carriers exceeds the charge collection time, this results in charge collection inefficiency and a reduction in the measured signal. Assuming that the charge loss depends solely

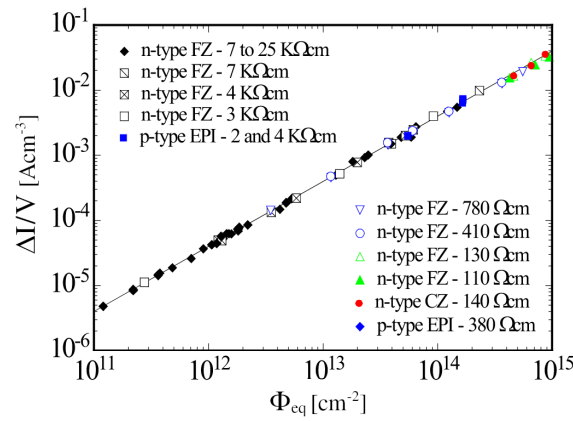


**Figure 2.15:** Variation in leakage current per unit volume,  $\Delta I/V$ , for several silicon sensors as a function of the 1 MeV-equivalent particle fluence,  $\Phi_{eq}$ . Measurements were conducted at room temperature after exposure to 60 °C for 80 min. Image adapted from [59].

on the transport time,  $t$ , of the charge carriers within the sensor, the collected charge in the presence of trapping is given by:

$$Q(t) = Q_0 \exp \left[ -\frac{t}{\tau_{eff}} \right] \quad \text{with} \quad \frac{1}{\tau_{eff}} = \frac{1}{\tau_{eff,0}} + \beta \Phi_{eq} \quad (2.52)$$

where  $Q_0$  is the charge generated by ionizing radiation that would be collected in the absence of trapping,  $\tau_{eff}$  is the effective trapping time,  $\tau_{eff,0}$  is the effective carrier lifetime before irradiation, and  $\beta$  is the effective trapping damage constant, which differs for electrons and holes. The effective trapping time is inversely proportional to the defect concentration and, consequently, also to the fluence.

The negative impact of trapping on detector performance can be mitigated through optimization of the device design, specifically by shortening the charge collection distances. Moreover, collecting electrons rather than holes is advantageous due to the higher mobility of electrons.

### Effective space-charge and depletion voltage

Defects with shallow energy levels can act as either donor or acceptor impurities, contributing to the space-charge density with positive and negative charges, respectively. To account for varying doping concentrations within the bulk material, the concept of effective doping concentration,  $N_{eff}$ , is introduced. It is defined as:

$$N_{eff} = |N_d - N_a| \quad (2.53)$$

where  $N_d$  and  $N_a$  are the donor and acceptor concentrations, respectively. Changes in the space-charge density influence the electric field distribution and the depletion voltage of the device, with their linear relationship discussed in sections 2.1.5 and 2.1.6.

The space-charge density can either increase or decrease depending on the material type and the nature of the defects. Figure 2.16 shows the evolution of the effective doping concentration and depletion voltage in an  $n$ -type silicon sensor as a function of fluence. In this case, radiation-induced defects are predominantly acceptor-like, leading to the formation of negative space-charge that compensates the initial positive space-charge. The effective doping concentration decreases with increasing fluence and, at a certain point, the net space-charge becomes negative. This results in type inversion, transforming the bulk into a  $p$ -type material. With further increases in fluence, the effective doping concentration rises, making it progressively harder to deplete the sensor. Eventually, the depletion voltage reaches a level that cannot be sustained without causing breakdown, forcing the detector to operate in an underdepleted state with the subsequent signal loss. Although type inversion from negative to positive space-charge is rare, it has been observed in some non-standard silicon materials at much higher fluences.

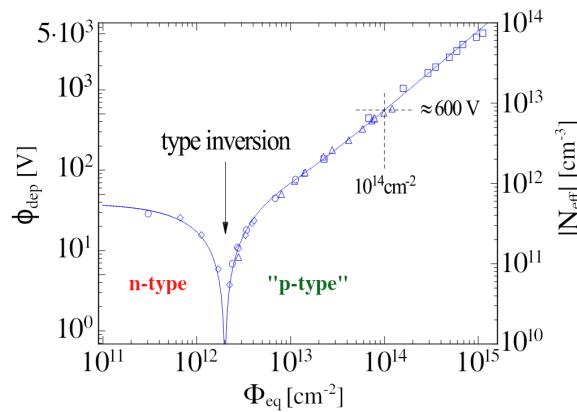


**Figure 2.16:** Effective doping concentration,  $N_{\text{eff}}$ , and depletion voltage,  $\phi_{\text{dep}}$ , as a function of the 1 MeV-equivalent particle fluence,  $\Phi_{\text{eq}}$ , for an  $n$ -type silicon detector. Image adapted from [59].

Furthermore, deep energy levels can lead to a double-peak electric field structure due to the formation of inhomogeneous space-charge regions. These defects, acting as trapping centers, accumulate negative and positive space-charges at the  $n^+$  and  $p^+$  contacts, respectively. This results in a double-junction effect that alters the electric field distribution. More details on this phenomenon can be found in [60].

As reported in [59], several studies have shown that the space-charge variation in silicon strongly depends on the impurity concentration and the type of incident radiation, suggesting that this effect does not directly scale with NIEL. Therefore, while the NIEL model is an effective tool for predicting displacement damage in complex radiation fields, it does have limitations.



### 2.3.2. Annealing

The radiation-induced defects, specifically vacancy-interstitial pairs, are not stationary at room temperature and can move through the crystal, potentially leading to the repair of some of the damage. This partial healing process, known as annealing, is temperature-dependent and can be accelerated by heat treatment. The primary processes involved in annealing are migration, complex formation, and complex dissociation. As temperature increases, defects become mobile and migrate through the silicon lattice. During this migration, defects can interact with other defects or impurities, forming stable defect complexes, recombining with their counterpart, or experiencing dislocation within the lattice. Additionally, defect complexes can dissociate into smaller components, which may migrate and undergo further recombination or complex formation themselves.

While annealing can repair some radiation-induced damage, it does not always have beneficial effects on the device properties. For instance, the current-related damage factor,  $\alpha$ , decreases with increasing annealing time, but the effective trapping damage constant,  $\beta$ , exhibits a different behavior for electrons and holes. For electrons,  $\beta$  decreases during annealing, while for holes, an increase in trapping is observed.

The impact of annealing on the effective doping concentration,  $N_{\text{eff}}$ , can be either beneficial or detrimental, depending on the duration of heat exposure. Short-term annealing reduces the effective doping concentration and repairs part of the damage, which can be advantageous for the device. However, after a prolonged period, the so-called reverse annealing becomes dominant, causing  $N_{\text{eff}}$  to increase until it reaches saturation. This long-term annealing can result in undesirable effects, such as an increase in the full depletion voltage. Short-term annealing is often used to extend the operational lifetime of silicon detectors. Further details on the parametrization of all these effects can be found in [59].

## 2.4. State-of-the-art in silicon-based detectors

Silicon-based detectors have become fundamental to modern high-energy physics due to their exceptional precision, compactness, radiation hardness, and fast signal collection. Their use began in the 1980s, driven by the need for vertex detectors with high spatial resolution to measure the lifetimes of short-lived particles by resolving secondary decay vertices. Only silicon detectors, with their fine electrode segmentation and rapid response, could meet the demands of such accuracy and handle the increasing data rates of modern particle accelerators. The technology evolved rapidly through continuous innovation and the development of new capabilities, allowing silicon sensors to expand beyond the vertex region and gradually cover larger volumes



of the tracking system. This enabled the detailed reconstruction of particle trajectories while reducing the overall detector size, establishing silicon as the core technology for tracking in current high-energy physics experiments.

Building on their success in tracking and vertexing, silicon detectors have been adopted for a broader range of applications within high-energy physics. They are now used in calorimetry for precise energy measurements. For example, the CMS ECAL and HCAL employ silicon-based photodetectors in their readout systems, while the HGCAL detector for the Phase-2 CMS upgrade implements silicon sensors as active elements. Their fast signal response makes them ideal for timing measurements, which are essential for accurate particle identification and pile-up rejection. In this context, the ATLAS and CMS upgrades for the HL-LHC include new dedicated timing detectors, called HGTD<sup>5</sup> and MTD, respectively. Furthermore, the radiation hardness of silicon detectors makes them well-suited for beam monitoring and luminosity measurements, as demonstrated by their integration into the CMS BRIL system<sup>6</sup>.

Beyond collider experiments, silicon detectors play a crucial role in direct searches for dark matter in underground experiments like DAMIC-M<sup>7</sup>. They are also employed in space-based experiments, such as AMS-02<sup>8</sup> aboard the International Space Station, where they track cosmic rays and contribute to indirect dark matter searches. In addition, silicon devices are widely used in medical imaging, detecting gamma photons in Positron Emission Tomography (PET) and X-rays in Computed Axial Tomography (CAT). This broad range of environments and applications—from underground to outer space, and from fundamental physics research to clinical diagnostics—highlights the versatility of silicon technology.

Given the wide range of applications and performance requirements, silicon detectors are designed in various configurations that optimize specific features. Two fundamental design aspects are the segmentation of their electrodes and the degree of integration between the sensing element (or sensor) and the readout electronics. These classifications, examined below, reflect engineering choices that determine a detector's spatial resolution, signal processing capabilities, and overall suitability for different experimental areas.

### Detector classification by electrode segmentation

Pad detectors, consisting of large-area diodes with parallel-plate electrodes, represent

<sup>5</sup> HGTD stands for High-Granularity Timing Detector [12].

<sup>6</sup> The BRIL system, which stands for Beam Radiation Instrumentation and Luminosity [61], includes independent sub-detectors for beam and radiation monitoring, as well as for luminosity measurement.

<sup>7</sup> DAMIC-M stands for DArk Matter In CCDs at Modane [62]. A Charge-Coupled Device (CCD) is a low-noise silicon detector sensitive to very faint signals, such as those expected from light dark matter.

<sup>8</sup> AMS stands for Alpha Magnetic Spectrometer [63].

the most basic form of silicon sensors. While their relatively large electrode size makes them unsuitable for use in tracking and vertexing systems, their straightforward geometry makes them ideal for material characterization and other applications where high spatial resolution is not required, but energy or timing precision is critical. For instance, both the HGCal and MTD detectors in the Phase-2 CMS upgrade plan to incorporate this sensor format in parts of their systems, as discussed in Section 1.3.1. Figure 2.17a shows the schematic representation of a pad detector. This detector format features a highly-doped readout implant on the frontside, covered with a metal layer for connection to the readout system, and a highly-doped ohmic implant on the backside, covered with a metal contact for applying the bias voltage. The ohmic implant, which has the same doping type as the bulk, serves the main purpose of forming a low-resistivity interface with the backside metallization.

The simplest position-sensitive detectors are strip and pixel sensors, which are essentially diodes with different electrode segmentation. Single-sided strip sensors were the first silicon devices used in vertexing and tracking systems [64]. They consist of a one-dimensional array of parallel strip-like implants, as illustrated in Figure 2.17b. Each strip is connected to an individual readout channel, allowing the sensor to provide position information along the coordinate perpendicular to the strip direction. However, determining position along only one coordinate is insufficient to reconstruct secondary vertices, since the decaying particles are isotropically emitted in all directions. To enable two-dimensional position measurements, double-sided strip sensors were developed, where both the frontside and backside are segmented into orthogonally oriented strips, each connected to a separate readout system. Although this configuration enables two-dimensional reconstruction, it can lead to ambiguities when multiple tracks traverse the detector simultaneously. Pixelated sensors mitigate this issue by providing unambiguous two-dimensional spatial information, making them suitable for applications in high particle density environments, such as those encountered at the LHC. Another advantage of pixel detectors is their inherently low capacitance, which enables fast signal shaping and very low noise, both essential for precise timing and efficient operation under high-rate conditions. Figure 2.17c shows the schematic representation of a pixel detector, where the frontside electrode is patterned along both directions into small discrete areas.

Strip detectors typically have fewer readout channels than pixel detectors, allowing the associated electronics to be placed on one side of the sensor. In contrast, pixel detectors consist of a dense matrix of channels, requiring pixel-by-pixel readout connections positioned directly on top of the sensor. This not only increases manufacturing costs and power consumption, but also adds to the material budget due to the dense electronics. For these reasons, the tracking system in some of the main LHC experiments, such as CMS and ATLAS, combines pixel detectors in the inner layers, where high

spatial resolution is essential for vertexing, with strip detectors in the outer layers for extended tracking coverage.

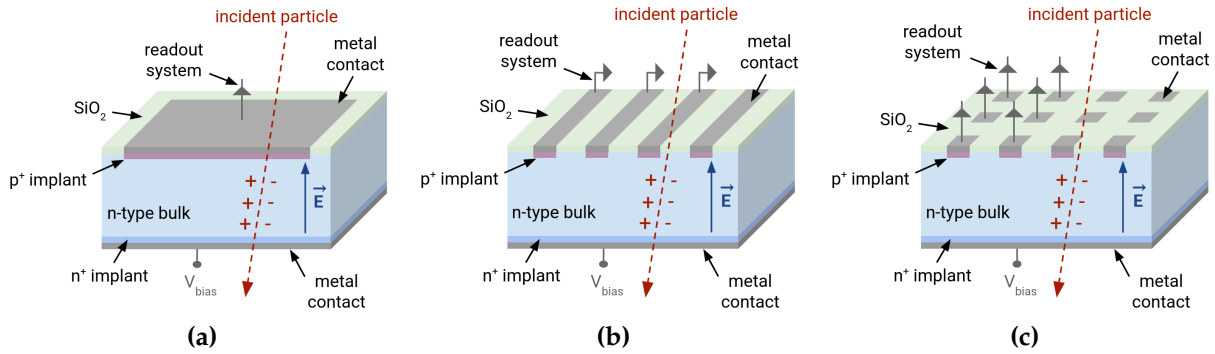


**Figure 2.17:** Schematic representation of a  $p$ -in- $n$  detector with different electrode segmentation: (a) pad detector, (b) strip detector, and (c) pixel detector. The  $p^+$  and  $n^+$  electrodes are indicated in pink and blue, respectively. The dielectric layer is shown in green, and the metal contacts are depicted in gray. The electric field,  $\vec{E}$ , is represented by a blue arrow.

### Detector classification by integration design

Detectors are commonly classified into two main categories based on the level of integration between the sensor and the readout electronics: hybrid and monolithic detectors.

In hybrid detectors, the sensor and readout electronics are fabricated on separate silicon substrates and later interconnected. This architecture offers significant design flexibility, as each component can be independently optimized. High-resistivity silicon substrates are used for the sensors to enhance charge collection efficiency, while the readout electronics are typically implemented in Complementary Metal-Oxide-Semiconductor (CMOS) technology and integrated into a dedicated front-end Application-Specific Integrated Circuit (ASIC). The ASIC, responsible for signal amplification, discrimination, digitization and potentially further data processing, must be physically connected to the sensor to ensure proper operation.

The interconnection technique depends largely on the electrode segmentation. In strip detectors, the ASIC is positioned at one end of the sensor and connected to each strip via wire-bonding. This cost-effective industry-standard process typically employs a thin gold or aluminum wire that is bonded onto aluminum pads using ultrasonic power. It is especially well-suited to geometries where electrical connections can be arranged in rows, such as in strip detectors or certain pixel detectors with projective readout. In contrast, regular pixel detectors require a much higher density of readout

channels due to their fine segmentation. To achieve a one-to-one connection between each pixel in the sensor and its corresponding readout cell in the ASIC, bump-bonding is used. This technique creates intermediate microscopic bumps, typically made from solder alloys or indium, that form direct electrical and mechanical contact at each pixel. Although more complex and expensive due to the need for wafer-level processing, bump-bonding is essential for achieving the fine granularity and high spatial resolution required in modern detection systems. Figure 2.18 illustrates the wire-bonding and bump-bonding techniques used in hybrid detectors.

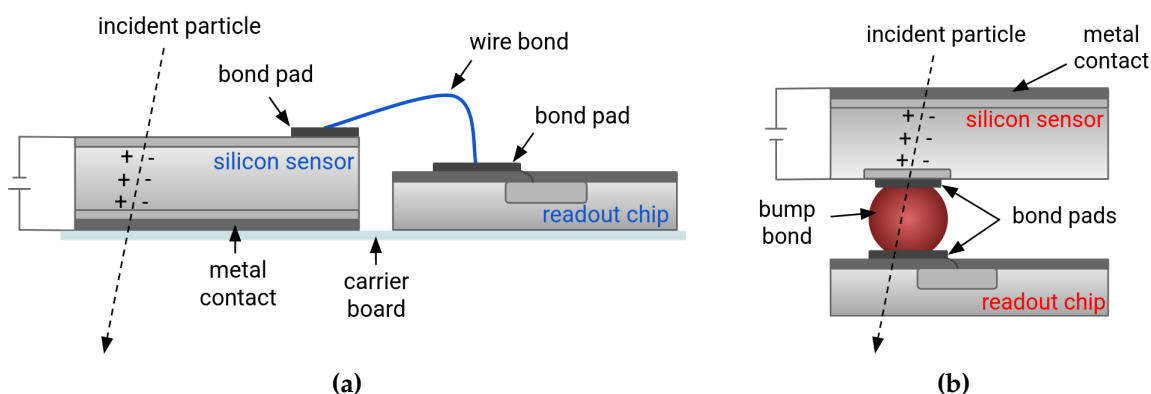


**Figure 2.18:** Sketches of a hybrid detector showing (a) the wire-bonding technique for a strip detector and (b) the bump-bonding technique for a pixel detector, both representing the connection between the sensor and the readout electronics.

On the other hand, monolithic detectors integrate both the sensor and all or part of the readout electronics onto a single silicon substrate, eliminating the need for complex interconnection techniques characteristic of hybrid architectures. This design was developed to overcome some of the limitations present in hybrid pixel detectors, including high material budget, complex and costly assembly, and constraints on pixel pitch imposed by the bump-bond size. By combining sensing and readout functions within a single layer of silicon, the monolithic design can achieve very thin detectors with low power consumption and simplified production. Furthermore, the absence of bump-bonding constraints enables smaller pixel sizes, leading to higher spatial resolution and reduced noise levels. However, these benefits come with trade-offs, since integrating all components on the same substrate often limits the complexity and performance of the readout circuitry. In addition, monolithic designs have historically exhibited lower radiation tolerance and rate capabilities compared to hybrid systems.

Both hybrid and monolithic detectors continue to evolve to mitigate their respective limitations. Hybrid detectors aim to reduce material, pixel size and cost through improved interconnection techniques, while monolithic designs focus on enhancing radiation tolerance and readout performance to meet the demands of more challenging

environments. An overview of selected silicon detector technologies relevant to current and future high-energy physics experiments is presented below, organized according to their architectural design. Particular emphasis is placed on hybrid detectors.

### 2.4.1. Hybrid detectors

In hybrid detectors, planar pixel sensors, fabricated using standard microelectronics processes, have long been the most widely adopted technology. Their well-established manufacturing techniques and reliability have made them the baseline choice for many high-energy physics experiments. More recently, 3D pixel sensors, which feature an innovative electrode geometry, have emerged as a compelling alternative for extreme radiation environments due to their superior radiation hardness. In parallel, avalanche sensors have gained increasing attention for their ability to provide internal signal amplification through controlled charge multiplication. This feature makes them particularly suitable for applications requiring enhanced timing resolution or sensitivity to very low signal levels. Complementing these sensor advancements, the Medipix/Timepix family of readout ASICs has become a cornerstone of hybrid pixel detector development. Their excellent per-pixel signal processing capabilities and compatibility with a wide range of sensor materials and technologies make them essential tools for a broad spectrum of applications.

#### Detectors with planar pixel sensors

As anticipated, planar sensor fabrication technologies have been well established for several decades, enabling large-scale production at low cost and with high yield. For this reason, planar technology remains the standard choice in current tracking systems. Planar pixel sensors typically consist of a high-resistivity silicon bulk with a matrix of segmented readout implants on the frontside and a uniform ohmic implant on the backside, as illustrated in the simplified representation of Figure 2.19. Additional implant structures, called guard rings, surround the active pixel matrix to control the electric field at the sensor edges and prevent breakdown at high bias voltages. The inter-electrode distance, defined as the separation between electrode implants of different doping type, equals the sensor thickness. Consequently, the electric field created by the applied bias voltage is oriented along the depth of the sensor, with field lines running mostly perpendicular to the surface and parallel to the sensor edge.

The first sensor configuration to be introduced was the  $p$ -in- $n$  pixel design, chosen for its fabrication simplicity due to single-sided processing and no need for isolation structures between the  $p$ -type segmented implants. To take advantage of the higher mobility and radiation hardness of electrons compared to holes,  $n$ -in- $n$  and  $n$ -in- $p$  pixel designs were later developed and adopted. These configurations require additional  $p$ -type implantations, using  $p$ -stop and  $p$ -spray techniques, to provide electrical

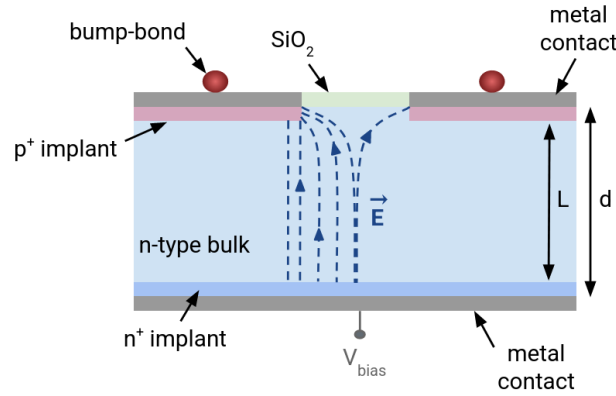


**Figure 2.19:** Schematic representation of a  $p$ -in- $n$  planar pixel sensor, showing the front view of two pixel cells. The  $p^+$  and  $n^+$  electrodes are indicated in pink and blue, respectively. The dielectric layer is shown in green, and the metal contacts are depicted in gray. Bump-bonds are represented as red circles. The parameters  $L$  and  $d$  denote the inter-electrode distance and the active sensor thickness, respectively. The electric field  $\vec{E}$  is illustrated with blue dashed lines.

isolation between the  $n$ -type electrodes and to suppress surface inversion effects.

Both ATLAS and CMS deploy  $n$ -in- $n$  pixel sensors in their Phase-1 tracking systems. In ATLAS,  $n$ -in- $n$  planar sensors with a thickness of  $250\text{ }\mu\text{m}$  and a standard pixel size of  $50 \times 400\text{ }\mu\text{m}^2$  are used, alongside  $200\text{ }\mu\text{m}$ -thick sensors with a smaller  $50 \times 250\text{ }\mu\text{m}^2$  pixel size for the innermost layer. These sensors are bump-bonded to the FE-I3 [65] and FE-I4 [66] front-end ASICs, respectively. The FE-I3 ROC is fabricated using  $250\text{ nm}$  CMOS process, while the FE-I4 chip employs a more advanced  $130\text{ nm}$  CMOS technology. CMS uses  $285\text{ }\mu\text{m}$ -thick sensors with standard pixel size of  $100 \times 150\text{ }\mu\text{m}^2$ , as described in Section 1.3. These sensors are bump-bonded to the PSI46dig chip [67], except in the innermost layer, where they are connected to the PROC600 chip [68], both of which are manufactured using the same  $250\text{ nm}$  CMOS technology.

The  $n$ -in- $n$  configuration, however, needs a double-sided processing that elevates the production cost and, moreover, suffers from type inversion of the bulk after irradiation. The alternative  $n$ -in- $p$  sensors with simpler single-sided technology is the baseline design for the Phase-2 upgrades of the ATLAS and CMS pixel detectors. The new planar sensors for ATLAS feature a pixel size of  $50 \times 50\text{ }\mu\text{m}^2$  and a thickness of either  $100\text{ }\mu\text{m}$  or  $150\text{ }\mu\text{m}$ , while those for CMS have a pixel size of  $25 \times 100\text{ }\mu\text{m}^2$  pixel size and a single thickness of  $150\text{ }\mu\text{m}$ . The RD53 Collaboration, a joint effort between ATLAS and CMS, developed a common front-end ASIC in  $65\text{ nm}$  CMOS technology, known as RD53A, which incorporates three different analog front-end designs for R&D purposes. The final ROC versions, referred to as ItkPixv2 (or RD53C-ATLAS) and CROCv2 (or RD53C-CMS), differ in dimensions and analog front-end flavor [69]. The excellent performance of planar  $n$ -in- $p$  pixel sensors for the Phase-2 CMS tracker



has been demonstrated through extensive test beam campaigns, both before and after irradiation, as reported in [70].

In addition to tracking applications, planar sensor technology is also employed in pad detectors for calorimetry systems. For instance, the CMS HGCAL detector for the Phase-2 upgrade features *n*-in-*p* planar sensors with a hexagonal geometry. Their thicknesses range from 120  $\mu\text{m}$  in the innermost region to 200  $\mu\text{m}$  and 300  $\mu\text{m}$  in the outer regions, with a cell size of approximately 0.5  $\text{cm}^2$  for the thinnest sensors and 1.1  $\text{cm}^2$  for the thicker ones.

### Detectors with 3D pixel sensors

The 3D pixel technology, proposed by S. Parker and collaborators in 1997 [71], consists of cylindrical electrodes etched into the substrate perpendicular to the sensor surface, as illustrated in Figure 2.20. These sensors require a more complex fabrication process than planar pixel technology, since they involve the formation of vertical columnar structures within the silicon bulk.

Unlike planar pixel detectors, this relatively novel design decouples the sensor thickness from the inter-electrode distance, resulting in a significantly lower depletion voltage and, consequently, reduced power consumption. Moreover, charge carriers generated by ionizing particles follow much shorter collection paths, improving charge collection efficiency after irradiation due to a lower probability of trapping. It is also worth noting that, while the collection path in planar pixel sensors can only be reduced by thinning the sensor at the expense of decreasing signal amplitude, 3D pixel sensors achieve shorter paths by reducing the inter-electrode spacing without compromising the signal. These advantages position 3D pixel sensors as a more radiation-tolerant technology and a compelling alternative for use in extremely high-radiation environments. However, 3D pixel sensors present some drawbacks compared to their planar counterparts. These include lower production yields and intrinsic inhomogeneities in the electric field, with regions of very low or even null field within the pixel cell that can degrade charge collection [72]. In addition, a slight reduction in hit detection efficiency at normal incidence is observed due to the electrodes passing through the bulk.

The Phase-1 ATLAS tracking system was the first detector in a large-scale high-energy physics experiment to deploy the 3D pixel technology [73]. These sensors, connected to the FE-I4 chip, are installed together with planar pixel sensors in the innermost layer of the detector. They feature an *n*-in-*p* configuration with a thickness of 230  $\mu\text{m}$  and a  $50 \times 250 \mu\text{m}^2$  pixel size. The pixel design features two *n*-type readout electrodes embedded along the 250  $\mu\text{m}$ -long pixel direction, surrounded by six *p*-type ohmic electrodes shared with the neighboring pixels. This architecture leads to an inter-electrode distance of 67.3  $\mu\text{m}$ . The sensors were fabricated by Fondazione Bruno

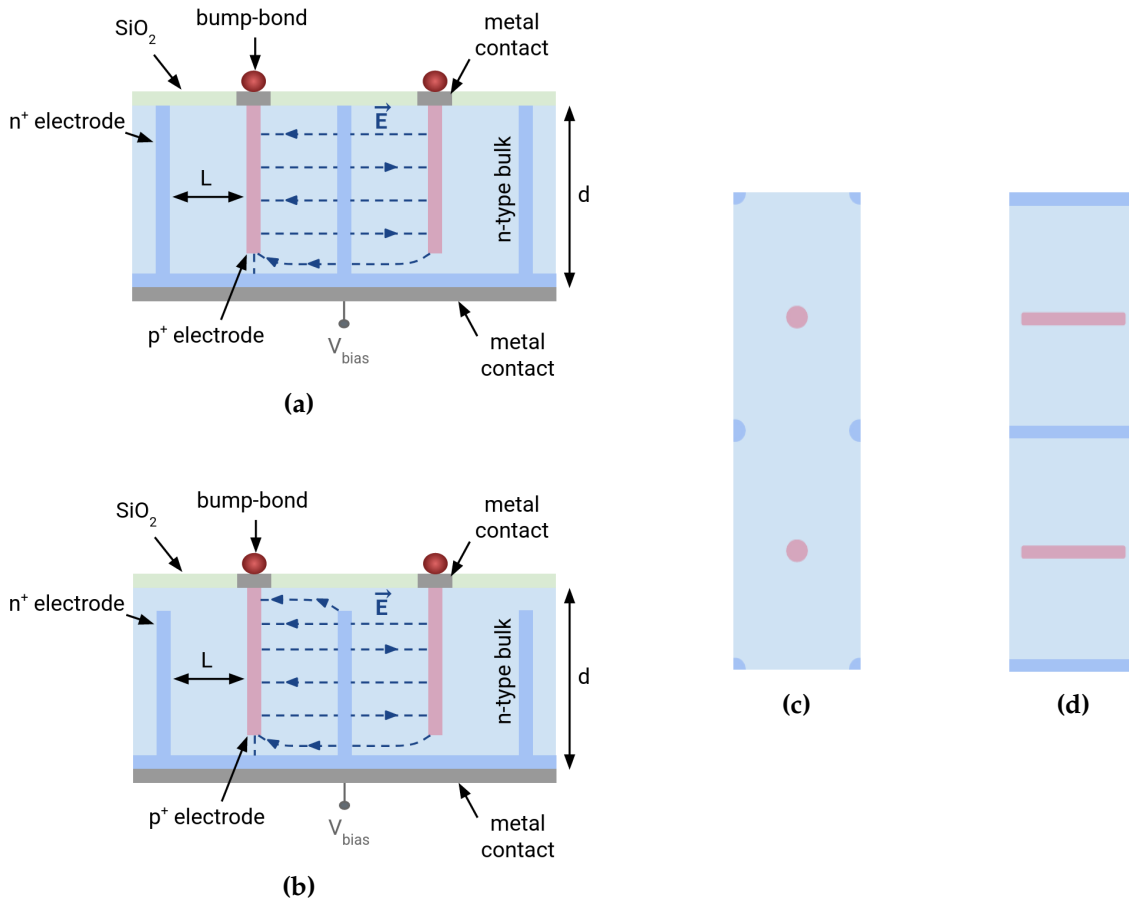


**Figure 2.20:** Schematic representation of (a) a single-sided and (b) a double-sided  $p$ -in- $n$  3D pixel sensor, showing the front view of two pixel cells. The  $p^+$  and  $n^+$  electrodes are indicated in pink and blue, respectively. The dielectric layer is shown in green, and the metal contacts are depicted in gray. Bump-bonds are represented as red circles. The parameters  $L$  and  $d$  denote the inter-electrode distance and the active sensor thickness, respectively. The electric field  $\vec{E}$  is illustrated with blue dashed lines. The top view of two rectangular pixel cells with (c) columnar and (d) trench electrode geometries is also shown.

Kessler (FBK) and Centro Nacional de Microelectrónica (CNM), both using a double-sided processing in which the  $n^+$  and  $p^+$  electrodes are etched from the frontside and backside, respectively. The overall sensor structure from both manufacturers is compatible, but there are some differences in the design. FBK sensors feature fully passing-through columns with  $p$ -spray isolation, whereas CNM sensors use  $210\text{ }\mu\text{m}$ -deep columns with  $p$ -stop isolation. To stop the lateral spread of the depletion region and shield the active area from edge effects, 3D pixel sensors typically display fences of ohmic columns surrounding the pixel matrix across a slim edge.

The CMS-TOTEM Precision Proton Spectrometer (CT-PPS) [74] and the ATLAS Forward Proton (AFP) [75] detectors were developed to study proton-proton collisions in the



forward physics region, complementing the physics programs of the LHC general-purpose experiments. Their tracking systems, designed to precisely measure the trajectories of protons that emerge from the interaction point at very small angles relative to the beam line, also employ 3D pixel technology. The sensors used in the AFP detector share a similar design with those of the Phase-1 ATLAS tracking system and are connected to the FE-I4 chip. In CT-PPS, the sensors bump-bonded to the PSI46dig chip feature an  $n$ -in- $p$  configuration with a  $230\text{ }\mu\text{m}$ -thick substrate and  $200\text{ }\mu\text{m}$ -deep electrodes. The pixel cell design includes two readout electrodes and six ohmic electrodes, with an inter-electrode distance of  $62.5\text{ }\mu\text{m}$  and a pixel size of  $150 \times 100\text{ }\mu\text{m}^2$  [76].

Following the successful operation of 3D pixel sensors in the aforementioned experiments, both ATLAS and CMS have decided to adopt this technology in their tracking systems for the Phase-2 upgrade. The new sensor designs incorporate a single readout electrode and four ohmic columns per pixel, with reduced dimensions to enhance spatial resolution and minimize the material budget. The sensors to be deployed in the CMS innermost barrel layer are  $150\text{ }\mu\text{m}$ -thick and have a pixel size of  $25 \times 100\text{ }\mu\text{m}^2$ , as detailed in Section 1.3.1. In contrast, ATLAS will implement  $150\text{ }\mu\text{m}$ -thick sensors with pixel sizes of  $25 \times 100\text{ }\mu\text{m}^2$  for the innermost barrel layer and  $50 \times 50\text{ }\mu\text{m}^2$  for the innermost rings. To fabricate such thin sensors, a single-sided processing in which all the columnar electrodes are etched from the frontside is used. While the ohmic columns penetrate the entire bulk, the readout columns have lengths of  $125\text{ }\mu\text{m}$  in ATLAS sensors and  $115\text{ }\mu\text{m}$  in CMS sensors. The selected manufacturers are FBK and SINTEF for ATLAS, and FBK alone for CMS. The front-end ASICs bump-bonded to these sensors are the same as those used in planar pixel detectors: ItkPixV2 for ATLAS and CROCv2 for CMS. The performance of 3D pixel detectors developed for ATLAS is reported in [77], while the R&D efforts and performance evaluation of the CMS 3D pixel detectors are presented and discussed in this thesis.

3D pixel sensors are also being explored for precision timing applications. In this context, the TIMESPOT R&D project has developed a new family of 3D pixel sensors featuring trench-shaped electrodes, which show excellent time resolution for MIP detection [78, 79]. This innovative electrode geometry was conceived to minimize the electric field inhomogeneities found in standard 3D pixel sensors, thus enhancing signal shape uniformity. These sensors, fabricated by FBK using single-sided processing, employ an  $n$ -in- $p$  configuration with a  $55\text{ }\mu\text{m}$  pitch and a  $150\text{ }\mu\text{m}$  thickness. The  $n$ -type readout electrodes extend  $135\text{ }\mu\text{m}$  into the bulk. Figures 2.20a and 2.20d show simplified front and top views of a 3D pixel sensor with trench-shaped electrodes. To accurately assess the performance of these sensors, TIMESPOT has also developed a dedicated ASIC using  $28\text{ nm}$  CMOS technology. The TIMESPOT devices are being considered for use in the upgraded Vertex Locator (VELO) detector for the Phase-2

LHCb upgrade [80], given their high spatial and time resolution. Nevertheless, the final decision between adopting columnar or trench electrodes remains under evaluation. The main disadvantage of the trench electrode geometry lies in the limited prior experience with this design and the lower production yield, due to the increased complexity of the fabrication process compared to conventional columnar electrodes.

### Detectors with avalanche sensors

Avalanche sensors follow a fabrication process similar to that of planar sensor technology, with the addition of a charge multiplication layer that enables internal signal amplification. This feature significantly increases their sensitivity to weak signals. A high Signal-to-Noise Ratio (SNR) is crucial to achieve the time resolution demanded by modern high-energy physics experiments, typically on the order of tens of picoseconds. The amplification capability of avalanche sensors is determined by the uniformity, thickness, area, and doping concentration of the multiplication layer.

The simplest sensor incorporating internal amplification is the Avalanche Photo-Diode (APD), which is optimized for light detection. In APDs, the multiplication layer is embedded within the sensor bulk near the readout implant where the electric field is the strongest. This layer shares the same doping type as the bulk but has a higher concentration to further enhance the electric field. Figure 2.21 shows a simplified representation of an  $n$ -in- $p$  APD and its electric field profile. When charge carriers generated by ionizing radiation reach the multiplication layer, they gain enough energy to cause impact ionization, producing additional electron-hole pairs in an avalanche process and increasing the collected charge.

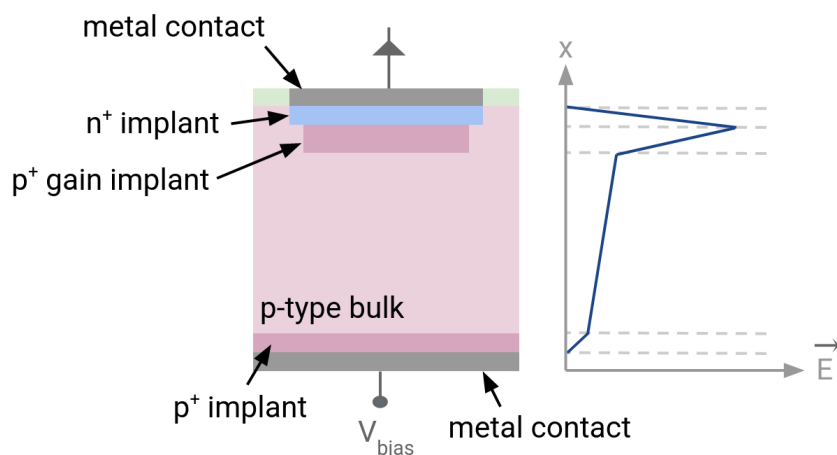


**Figure 2.21:** Schematic representation of an  $n$ -in- $p$  APD. The  $n^+$  electrode is indicated in blue, while the  $p^+$  gain layer is indicated in pink. The dielectric film is shown in green, and the metal contacts are depicted in gray. The electric field  $\vec{E}$  as a function of depth  $x$  is illustrated with blue solid lines.

APDs can operate in either linear or Geiger mode, depending on the applied bias voltage. In linear mode, the sensor is biased just below the breakdown voltage, ensuring an electric field strong enough to cause controlled multiplication without a diverging avalanche. The output signal in this mode is proportional to the number of incident photons. In contrast, operation in Geiger mode is achieved by biasing the sensor well above the breakdown voltage. This leads to a self-sustaining avalanche process that can only be limited through a quenching resistor. Although this mode offers high sensitivity to very low signals, it sacrifices the ability to resolve the number of incident photons.

A Silicon Photo-Multiplier (SiPM) consists of a matrix of micro-APDs operating in Geiger mode and connected in parallel. While the gain of an APD in linear mode is on the order of  $10^2$ , SiPMs and APDs operated in Geiger mode reach gains of about  $10^6$ , comparable to that of a traditional Photo-Multiplier Tube (PMT). SiPMs offer additional advantages such as compactness, low operation voltage, insensitivity to magnetic fields, and cost-effectiveness. For these reasons, SiPMs are increasingly replacing PMTs in low-light applications such as PET and high-energy physics detectors. For instance, SiPMs are used in the CMS HCAL to detect scintillation light and are key components in the HGCal and MTD-BTL detectors developed for the Phase-2 CMS upgrade.

Low-Gain Avalanche Diode (LGAD) technology provides some of the most promising results for precise timing measurements of MIPs in high-energy physics, achieving resolutions on the order of 30 picoseconds. LGADs are a variant of APDs operated in linear mode. They feature a lower gain, typically on the order of 10, to limit the noise. The electrodes can be patterned in strips or relatively large pixels. Figure 2.22a illustrates a standard *n-in-p* LGAD with segmented readout and gain implants. Electrical isolation between pixels is achieved using *p*-stop implants, while Junction Termination Extensions (JTEs) [81] at the implant edges—where the electric field is the strongest—help prevent early breakdown. This sensor technology, with a  $50\text{ }\mu\text{m}$  active thickness and a  $1.3 \times 1.3\text{ mm}^2$  pixel size, will be deployed for the first time in the MTD-ETL and HGTD detectors for the Phase-2 CMS and ATLAS upgrades, respectively. The sensors are bump-bonded to custom-designed ASICs: ETROC based on 65 nm CMOS technology for CMS [82], and ALTIROC fabricated using 130 nm CMOS technology for ATLAS [83, 84]. They integrate fast front-end electronics and dual time-to-digital converters to extract both Time-of-Arrival (ToA) and Time-over-Threshold (ToT), enabling precise per-hit timing measurements.

A limitation of standard LGADs is the presence of inter-pixel regions without gain, which reduce the fill factor—the fraction of pixel area that contributes to signal multiplication. While acceptable for large pixels, this limits their use in applications requiring fine pitch and high spatial resolution, making standard LGADs unsuitable for 4D tracking. To address the fill factor problem, several technological solutions were

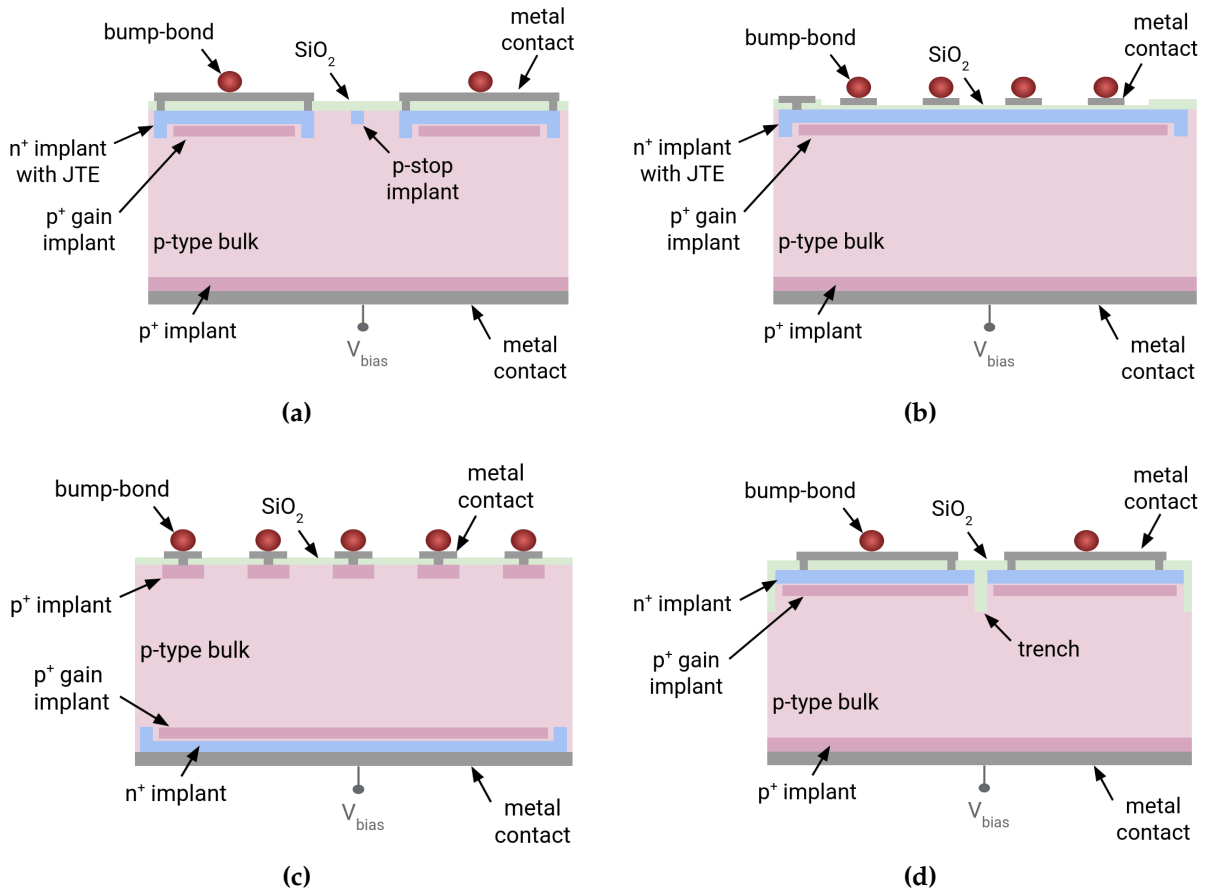


**Figure 2.22:** Schematic representation of several *n-in-p* avalanche detectors with low gain: (a) standard LGAD, (b) AC-LGAD, (c) iLGAD and (d) TI-LGAD. The  $n^+$  electrodes are indicated in blue, while the  $p^+$  electrodes and gain layers are indicated in pink. Bump-bonds are represented as red circles. The dielectric film and the metal contacts are shown in green and gray, respectively. Further details are given in the text.

proposed and are under active investigation.

The AC-coupled LGAD (AC-LGAD), shown in Figure 2.22b, was the first solution proposed. It features continuous readout implant and gain layer across the sensor area. Sensor segmentation is achieved via metal contacts AC-coupled to the underlying  $n^+$  implant through a thin dielectric layer, enabling almost 100% fill factor. However, this design can introduce signal cross-talk between adjacent pixels. The inverse LGAD (iLGAD), shown in Figure 2.22c, also has a continuous multiplication layer and  $n^+$  implant covering the entire sensor. Unlike standard LGADs, segmentation is applied only to the opposite-side implant, which does not form the junction and is connected to readout. This architecture also achieves full fill factor but requires double-sided processing, leading to thicker sensors and degraded timing performance. Another solution is the Trench-Isolated LGAD (TI-LGAD), illustrated in Figure 2.22d,

which uses narrow trenches filled with dielectric material to electrically isolate the pixels. These structures eliminate the need for *p*-stops and JTEs, reducing the no-gain region and improving the fill factor. However, this design can lower the charge sharing between pixels, limiting the spatial resolution and resulting in a more digital-like response.

Each LGAD variant presents trade-offs among timing precision, spatial resolution, fill factor, and fabrication complexity. Their suitability depends on the specific requirements of the application, with some designs better suited for high-energy physics and others for photonics. Further technical details on these and other variants under development, such as DC-LGAD and DJ-LGAD, can be found in [85].

### Detectors with Medipix and Timepix ASICs

The Medipix and Timepix family [86] comprises a series of hybrid pixel detector ASICs developed by the Medipix Collaboration. These chips were initially conceived to transfer the precision and advanced capabilities of high-energy physics detectors to the biomedical field. However, their highly versatile design makes them suitable for a broader range of applications, from medical imaging to space radiation monitoring and dosimetry [87]. Moreover, their modular architecture and compatibility with different sensor materials and technologies make them perfect tools for detector R&D.

Medipix chips operate in a photon-counting mode and are optimized mainly for X-ray and gamma-ray applications. The first generation, Medipix1, features a matrix of  $64 \times 64$  pixels with a  $170 \mu\text{m}$  pixel pitch. Successive generations were successfully developed and provide additional functionalities, smaller pixel sizes, and larger active areas. Medipix2 expanded the matrix to  $256 \times 256$  pixels with a reduced pitch of  $55 \mu\text{m}$ , while Medipix3 introduced user-adjustable energy thresholds at the pixel level for spectroscopic imaging.

The Timepix1 series builds upon the Medipix2 design by adding timing capabilities. Timepix1 can be configured to measure either ToA or ToT, providing insight into the particle arrival times or deposited charge. Timepix3 implements a data-driven readout mode that allows for simultaneous per-pixel ToA and ToT measurements, enabling precise time-resolved tracking. These capabilities led to the integration of Timepix-derived ASICs in major collider experiments. A notable example is the VELOpix ASIC, used in the LHCb VELO detector, which is based on Timepix3 and customized for the first operation period of the HL-LHC environment. The latest generation, Timepix4 [88], fabricated using 65 nm CMOS technology, features a  $448 \times 512$  pixel matrix with a  $55 \mu\text{m}$  pitch. This highly programmable ASIC delivers a time resolution down to 200 picoseconds and enhanced hit rate capabilities, making it a strong candidate for next-generation detectors with requirements of fast timing and high granularity.

### 2.4.2. Monolithic detectors

Monolithic detectors have seen significant advancements in recent years, largely driven by the evolution of CMOS-based technologies. Among these, MAPS and DMAPS stand out due to their low material budget, high granularity and cost-effective scalability for large-area coverage. Benefiting from the maturity of CMOS fabrication processes, these detectors deliver performance levels that are suitable for demanding applications, such as vertex tracking in high-energy physics experiments. In addition, alternative monolithic technologies, including DEPFET and SOI detectors, also offer promising capabilities, especially in applications requiring low noise or enhanced radiation tolerance.

#### MAPS and DMAPS detectors

Monolithic Active Pixel Sensors (MAPS) are fabricated using standard CMOS technology and feature a complete level of integration, with both the sensing element and front-end electronics implemented on the same silicon wafer. Their typical structure consists of a low-resistivity  $p$ -type substrate, which provides mechanical support and acts as the electrical backplane, and a thin  $p$ -type epitaxial layer of higher resistivity. This layer enables a limited depletion region around the collecting  $n^+$  electrodes and serves as the active volume where charge carriers are generated by ionizing radiation. Figure 2.23a shows a simplified schematic of a MAPS detector.

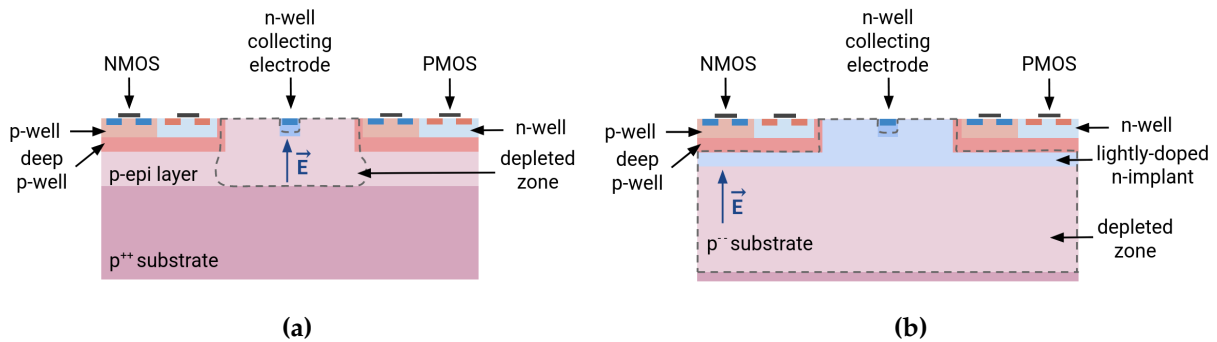


**Figure 2.23:** Schematic representation of (a) MAPS and (b) DMAPS detectors with  $n$ -in- $p$  configuration. The depleted region is outlined by a gray dashed line, and the electric field  $\vec{E}$  is shown in dark blue. The NMOS and PMOS transistors, characteristic of CMOS technology, are also indicated. Further details are provided in the text.

In MAPS, charge collection relies primarily on diffusion through the lightly-doped epitaxial layer. Once the charge carriers reach the small depleted region surrounding the readout electrodes, they are quickly collected by drift under the influence of the electric field. This architecture offers key advantages, such as very low material budget



and high spatial resolution, making MAPS ideal for applications like vertexing or tracking. However, the strong dependence on diffusion limits their timing performance and rate capability, reducing suitability for high-radiation or high-rate environments.

The MIMOSA family represents one of the first and most influential developments in MAPS technology, demonstrating the feasibility of monolithic detectors in high-energy physics. For example, the MIMOSA26 detectors [89], developed using a 350 nm CMOS process, are widely used in EUDET-type telescopes for beam tests and feature a 18.4  $\mu\text{m}$  pixel pitch. A more advanced implementation is found in the ALICE Inner Tracking System (ITS2) at the LHC, which is the first large-scale detector entirely based on MAPS technology. It uses ALPIDE detectors [90] fabricated in a 180 nm CMOS process. They feature a pixel pitch of 18  $\mu\text{m}$ , a spatial resolution of around 5  $\mu\text{m}$ , and a peaking time of around 2  $\mu\text{s}$ .

To overcome the limitations present in MAPS, Depleted Monolithic Active Pixel Sensors (DMAPS) were developed. These devices use modified CMOS processes that allow for high-resistivity substrates and the application of higher reverse-bias voltages. They also incorporate deep  $n$ -implants to isolate the readout electrodes and front-end electronics from the sensor active volume. This enables full or partial depletion of the active region, favoring charge collection by drift rather than diffusion. The resulting design improves charge collection speed, timing performance, and radiation tolerance. The simplified layout of a DMAPS detector is shown in Figure 2.23b.

A notable application of DMAPS is the planned upgrade of the Belle II vertex detector, which will employ the so-called OBELIX [91] detectors fabricated in a 180 nm CMOS technology with a pixel pitch of approximately 33  $\mu\text{m}$ . Another example is the planned upgrade of the ALICE Inner Tracking System (ITS3) [92], where DMAPS with a thickness of 50  $\mu\text{m}$  will be fabricated using a 65 nm CMOS process. Moreover, they will employ a novel stitching technology to interconnect individual sensors into a large, flexible structure that can be placed directly around the beam line in a truly cylindrical shape. In the longer term, DMAPS are under consideration for potential use in future collider experiments.

### DEPFET detectors

The DEPLETED Field-Effect Transistor (DEPFET) detector is a monolithic technology with a reduced level of integration, as it includes only the first amplification stage within the sensor substrate. While charge collection and amplification occur locally at the pixel level, subsequent processing is performed by an external ASIC. Figure 2.24 shows a simplified schematic of a DEPFET detector. Each pixel integrates a Metal-Oxide-Semiconductor Field-Effect Transistor (MOSFET) on a high-resistivity  $n$ -type substrate, providing in-pixel signal amplification. This local amplification results in a

high SNR even for thin detectors.

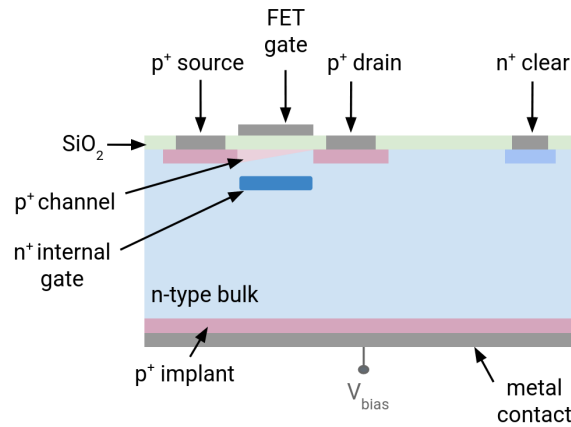


**Figure 2.24:** Schematic representation of a *p*-in-*n* DEPFET detector, showing the front view of one pixel. The  $p^+$  electrode and the  $p^+$  implants corresponding to the transistor are depicted in pink. The  $n^+$  implants for the internal gate and clear structure are depicted in blue. The dielectric film is shown in green, and the metal contacts are depicted in gray. Further details are provided in the text.

In addition to the external gate of the transistor, each DEPFET unit features an internal gate—an  $n^+$  implant located beneath the channel—which acts as a potential minimum for electrons and serves as the charge collection node. After signal readout, the charge stored in the internal gate is removed by applying a positive voltage to the so-called clear contact, thus resetting the pixel for the next event.

Combining in-pixel amplification with high granularity, DEPFET detectors are well-suited for applications requiring low noise and precise spatial resolution, such as X-ray imaging and particle tracking. For instance, DEPFET sensors are used in the innermost layers of the Belle II vertex detector [93].

### SOI detectors

The Silicon-On-Insulator (SOI) monolithic technology consists of a thick high-resistivity silicon substrate, where the active pixel matrix is formed, and a thin low-resistivity silicon layer hosting the front-end CMOS electronics, both bonded via a buried oxide layer (BOX). These two parts are interconnected by metal lines that pass through the BOX and reach the readout implants, as shown in Figure 2.25.

SOI detectors are fully depleted devices, enabling fast charge collection and reduced parasitic capacitance. While offering significant advantages, the technology faces some fabrication and signal integrity challenges. These are being addressed through new developments, such as Double SOI structures that incorporate an additional shielding layer. SOI detectors remain largely in the R&D phase, but they have shown promising



results in beam tests [94] and are being evaluated for application in high-energy physics and X-ray imaging.

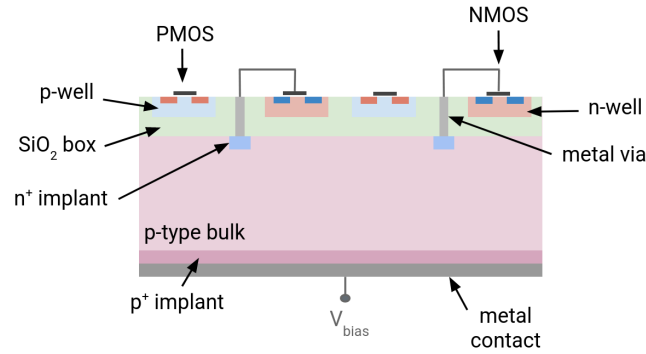


**Figure 2.25:** Schematic representation of a  $n$ -in- $p$  SOI detector, showing the front view. The green region represents the buried oxide layer, while  $n^+$  and  $p^+$  electrodes are shown in blue and pink, respectively. Metal vias and backplane contact are depicted in light and dark gray. CMOS technology elements, including NMOS and PMOS transistors, are also labeled. Further details are provided in the text.

## Chapter 3

# Performance evaluation of 3D pixel detectors via test beam characterization

3D pixel detectors were characterized in test beam experiments to evaluate their performance before and after irradiation. Their qualification for installation in the innermost layer of the CMS IT relies on the performance requirements summarized in Table 3.1. These specifications include post-irradiation measurements at fluences up to  $1.5 \times 10^{16} \text{ n}_{\text{eq}}\text{cm}^{-2}$ , corresponding to the radiation level expected after around six years of HL-LHC operation. Replacement of the innermost layer is foreseen at the end of this period.

**Table 3.1:** CMS requirements for 3D pixel detectors to be installed in the innermost layer of the IT, before and after exposure to radiation. The full depletion and breakdown voltages prior to irradiation are denoted by  $V_{\text{dep}}$  and  $V_{\text{bd}}$ , respectively. After irradiation,  $V_{\text{op}}$  indicates the minimum operational voltage at which the hit detection efficiency requirement is met. The particle fluence,  $\Phi$ , is expressed in units of  $\text{n}_{\text{eq}}\text{cm}^{-2}$ .

Parameter	Value	Irradiation status
Full depletion voltage ( $V_{\text{dep}}$ )	$< 10 \text{ V}$	non-irradiated
Breakdown voltage ( $V_{\text{bd}}$ )	$> V_{\text{dep}} + 25 \text{ V}$	non-irradiated
Leakage current at room temperature and $V_{\text{dep}} + 25 \text{ V}$	$< 2.5 \mu\text{A cm}^{-2}$	non-irradiated
Minimum operation voltage ( $V_{\text{op}}$ )	$< 200 \text{ V}$	$\Phi = 1.5 \times 10^{16}$
Leakage current at $-25^\circ\text{C}$ and $V_{\text{op}}$	$< 150 \mu\text{A cm}^{-2}$	$\Phi = 1.5 \times 10^{16}$
Hit detection efficiency at normal incidence	$\geq 96\%$	$\Phi = 1.5 \times 10^{16}$

Continued on next page

Continued from previous page

Hit detection efficiency at $10^\circ$ incidence	$\geq 97\%$	$\Phi = 1.5 \times 10^{16}$
Masked channels	$< 2\%$	$\Phi = 1.0 \times 10^{16}$

A detailed description of the 3D pixel detectors under test, the methodology for test beam data analysis, and a thorough evaluation of their performance before and after irradiation are presented below. A comparison between test beam results and simulation is also provided.

### 3.1. 3D pixel detectors under test

A general overview of 3D pixel technology and its comparison with planar pixel sensors was provided in Section 2.4.1. The Devices Under Test (DUTs) are hybrid detectors, consisting of a 3D pixel sensor bump-bonded to a dedicated front-end ASIC. Their main characteristics are described below, with the sensor and the readout electronics discussed separately.

While the experiment will use double 3D pixel modules—each comprising two sensors bump-bonded to two chips—the R&D prototypes evaluated in this thesis consist of a single sensor connected to a single chip. These single-chip modules are mounted on custom printed circuit boards (PCBs), known as Single-Chip Cards (SCCs), for testing purposes. Figure 3.1 shows an SCC with and without a light-proof cover, which protects the wire-bonds and helps minimize leakage current during operation. The metalized backside of the sensor is wire-bonded to the PCB to apply the reverse-bias voltage, while the chip is wire-bonded to enable tuning, monitoring, and communication. Power and full control of the chip are provided through several components soldered onto the PCB.

#### 3.1.1. Description of the readout electronics

The RD53 Collaboration is a joint effort between the ATLAS and CMS experiments to develop a pixel readout ASIC for their Phase-2 tracking system upgrades. The ASIC was developed using a 65 nm CMOS technology. This technology was chosen to meet the demanding requirements for granularity, hit rate, and radiation hardness necessary for operation during the HL-LHC phase. In particular, its design needs to handle hit rates up to  $3.5 \text{ GHz cm}^{-2}$  and withstand a TID of at least 10 MGy. The chosen readout cell has a  $50 \mu\text{m}$  pixel pitch, compatible with the sensor geometries planned by both experiments—either  $50 \times 50 \mu\text{m}^2$  or  $25 \times 100 \mu\text{m}^2$  pixel size.

The first demonstrator chip, known as RD53A [95], was submitted in 2017 as a half-

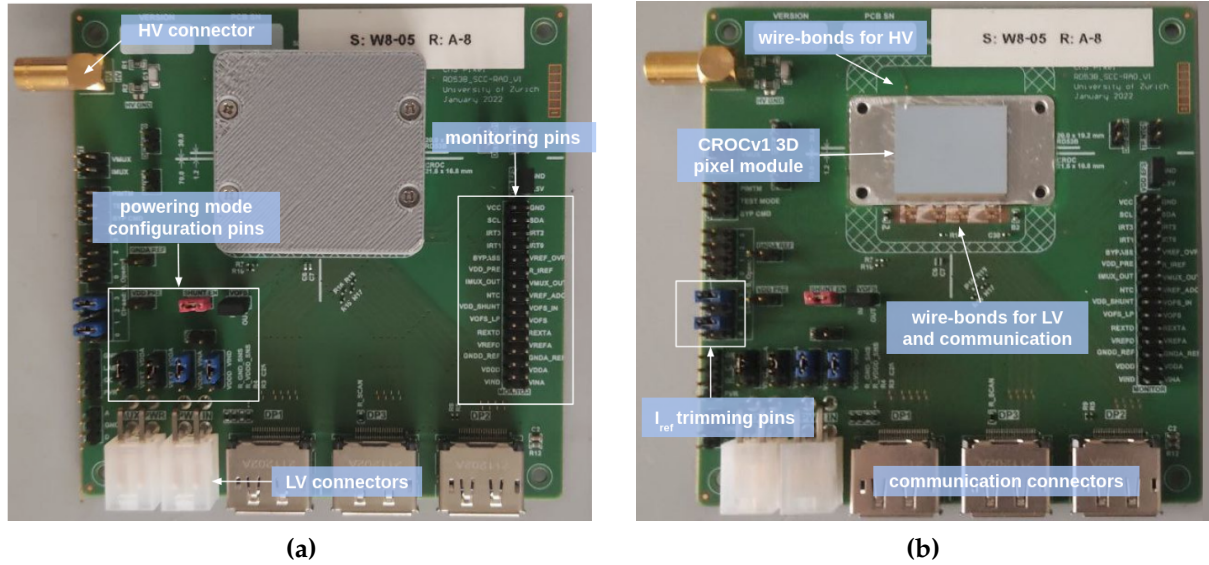


**Figure 3.1:** Hybrid pixel module mounted on a SCC, shown (a) with and (b) without the light-proof protective cover. The main components soldered onto the SCC for powering, monitoring, configuration, and communication are labeled.

scale prototype. It measures approximately  $20 \times 11.6 \text{ mm}^2$  and features a readout matrix of 76 800 pixel cells, arranged in 400 columns and 192 rows. For R&D purposes, RD53A incorporates three different analog front-end designs—synchronous, linear and differential—each implemented in roughly one-third of the pixel matrix. Following a detailed testing and characterization program, CMS selected the linear analog front-end [96], while ATLAS opted for the differential design.

The full-scale CMS-specific prototype, referred to as RD53B-CMS or CROCV1 [97], was submitted in 2021. It builds on the RD53A linear analog front-end and incorporates design optimizations tailored to CMS requirements. After extensive performance evaluation, the final version of the chip, known as RD53C-CMS or CROCV2, was submitted in 2023. This version introduces bug fixes and additional features in the digital domain. Both CROCV1 and CROCV2 include an enlarged readout matrix with 432 columns and 336 rows, totaling 145 152 pixel cells. The bottom of the chip houses the wire-bond pads along with all global analog and digital circuitry required to bias, configure, monitor, and read out the chip. The full-scale chip has approximate dimensions of 21.6 mm in width and 18.6 mm in height.

Figure 3.2 shows the schematic and block diagram of the CROCV1 linear analog front-end, which interfaces with both the input signal pathway and the digital domain. The pixel front-end includes a low-noise Charge-Sensitive Amplifier (CSA) with Krummenacher feedback, designed to comply with radiation-induced increases in detector leakage current and to provide a linear discharge of the feedback capacitor. The CSA

output is processed by a low-power threshold comparator, which drives a Time-over-Threshold (ToT) counter operating at 40 MHz for analog-to-digital conversion. This system provides 4-bit ToT charge information, with output codes ranging from 0 to 14 (code 15 is reserved for non-hit pixels). If the comparator output remains high when the counter saturates, the counting halts and the maximum ToT code is recorded.

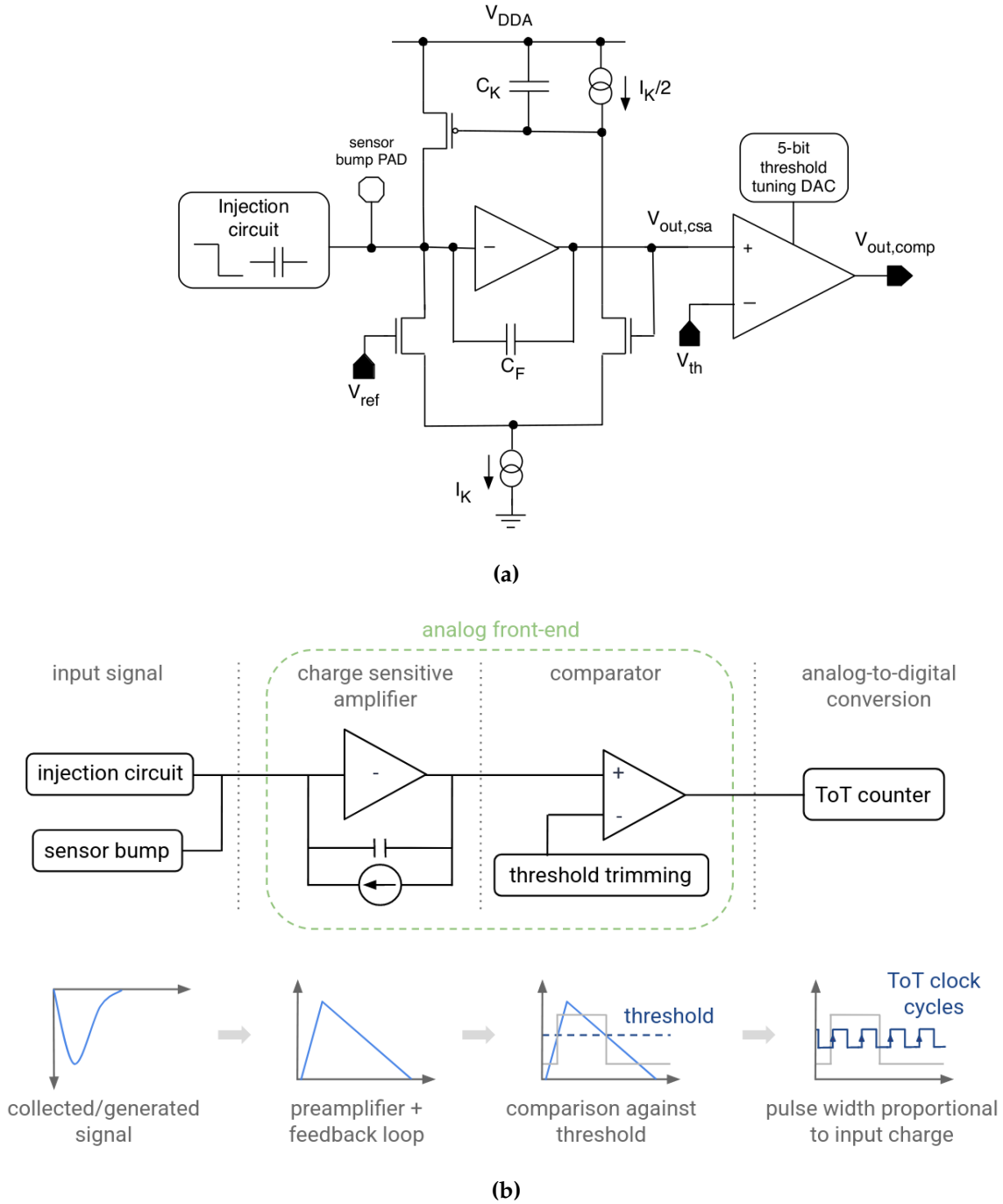


**Figure 3.2:** (a) Simplified schematic and (b) block diagram of the CROCv1 linear analog front-end, including also the input signal pathways and the interface with the digital domain. Top image from [97].

The threshold voltage applied to the comparator input for signal discrimination,  $V_{\text{Thr}}$ , is determined by the configuration of three Digital-to-Analog Converters (DACs)—GDAC, TDAC and LDAC—and is expressed as:

$$V_{\text{Thr}} = V_{\text{GDAC}} - TDAC \cdot V_{\text{LDAC}} \quad (3.1)$$

GDAC is a 10-bit DAC that sets the global threshold for the linear analog front-end. Due to local process variations in pixel circuitry, threshold dispersion can occur across the matrix. To compensate for this pixel-to-pixel variation, each channel includes a local threshold tuning circuit based on TDAC—a 5-bit current-mode, binary-weighted DAC. The resolution and dynamic range of the TDAC output are defined by LDAC—a 10-bit DAC that sets the least significant bit (LSB) size of the local threshold adjustment. Selecting an appropriate dynamic range is essential for effective in-pixel threshold tuning. If the range is too small, a significant fraction of pixels may remain untunable. On the other hand, if it is too wide, the resulting large LSB can reduce tuning precision and lead to increased threshold dispersion after calibration.

The CSA input is connected to the sensor bump-pad, allowing the collection of signals generated by ionizing particles. The pixel front-end also includes a charge injection circuit that delivers programmable signals to the CSA input for testing and calibration purposes. This functionality allows for precise evaluation of the threshold and noise performance of each pixel. The analog injection circuit generates a differential voltage step, referred to as  $\Delta V_{\text{Cal}}$ , using two voltages provided by a pair of 12-bit DACs. This step is applied across an injection capacitor with a nominal value of 8.02 fF. The charge injection circuit can operate in either high or low dynamic range mode, which differ by a factor of two in the step size. In the high dynamic range configuration, the 12-bit DAC voltage reference is the same as the internal ADC voltage reference, denoted as  $V_{\text{ref\_ADC}}$ . In the low dynamic range configuration, which is the default mode, it is set to half of  $V_{\text{ref\_ADC}}$ , resulting in finer resolution. The injected charge,  $Q$ , is converted from  $\Delta V_{\text{Cal}}$  units to number of electrons through the following relation:

$$Q_{\text{electrons}} = \begin{cases} \frac{C_{\text{inj}} V_{\text{ref\_ADC}}}{4096 q} Q_{\Delta V_{\text{Cal}}} + Q_{\text{off|electrons}} & , \text{ in high dynamic range} \\ \frac{C_{\text{inj}} V_{\text{ref\_ADC}}}{2 \cdot 4096 q} Q_{\Delta V_{\text{Cal}}} + Q_{\text{off|electrons}} & , \text{ in low dynamic range} \end{cases} \quad (3.2)$$

where  $q$  is the elementary charge,  $C_{\text{inj}}$  is the injection capacitor, and 4096 is the total range of the 12-bit voltage DACs.  $Q_{\text{off|electrons}}$  is typically on the order of 60 electrons and accounts for offset charge arising from mismatches in the baseline voltages of the two DACs. The accuracy of the conversion depends on precise knowledge of  $C_{\text{inj}}$  and  $V_{\text{ref\_ADC}}$ , which is typically around 0.8–0.9 V.

It is worth noting that the calibration circuit supports both analog and digital injections. The analog injection, described above, enables precise evaluation of the threshold and noise performance at the pixel level. In contrast, the digital injection bypasses the analog front-end and verifies the full digital functionality of the readout chain.

### Powering modes

The ASIC supports three different powering modes: direct, Low-DropOut (LDO) and Shunt Low-DropOut (SLDO). LDO powering is more convenient for bench testing of individual single-chip modules, while SLDO mode is the choice for serial powering in the final experiment, as will be discussed in Chapter 4. The SCCs on which the DUTs are mounted include jumper-configurable pins that allow selection among the three powering options.

In LDO mode, the internal voltage regulators are fed from a constant voltage provided by a power supply. This configuration enables separate monitoring of the current consumption in the analog and digital domains. In contrast, the internal regulators in SLDO mode are fed from a constant current provided by a power supply and a shunt element dissipates the excess current not required by the chip. These two modes are often preferred over direct powering, as the regulators provide protection against sudden variations in input voltage that could otherwise damage the chip.

The main reference current,  $I_{\text{ref}}$ , generates all other reference currents and voltages necessary for proper chip functioning. Therefore, the first step in the power trimming procedure—regardless of the powering mode—is to adjust  $I_{\text{ref}}$  to its nominal value. This is done by tuning the current until a voltage drop of approximately 0.5 V is measured across a designated resistor in the circuit. This voltage drop, known as  $V_{\text{ofs}}$ , is particularly important for serial powering operation and will be discussed in more detail in Chapter 4.

### DAQ system

The Data Acquisition (DAQ) system used to read out the CROCv1 chip was developed by the CMS Collaboration and is known as the Phase-2 Acquisition and Control Framework (Ph2-ACF) [98]. It comprises several hardware components, along with dedicated firmware and software layers.

The hardware setup is shown in Figure 3.3. At its core is a custom data acquisition and control board, called FC7, which hosts a Xilinx Kintex-7 FPGA. The FC7 is installed in a nano-crate developed by the Karlsruhe Institute of Technology and is connected to an interface card from Imperial College that supplies power to the FC7 and enables Ethernet-based communication with the DAQ PC via the IPbus protocol. The FC7 features two slots for FPGA Mezzanine Cards (FMCs), which allow for either electrical



or optical communication with the chip front-end. In the context of this thesis, only the so-called Kansas University (KSU) FMC for electrical communication is used. The DIO5 FMC is the baseline solution for providing external triggering and clocking functionalities; while it is not required for the front-end tuning, it is fundamental in test beam campaigns. Additionally, the FC7 includes a microSD card slot for storing firmware images that can be loaded onto the FPGA as needed.

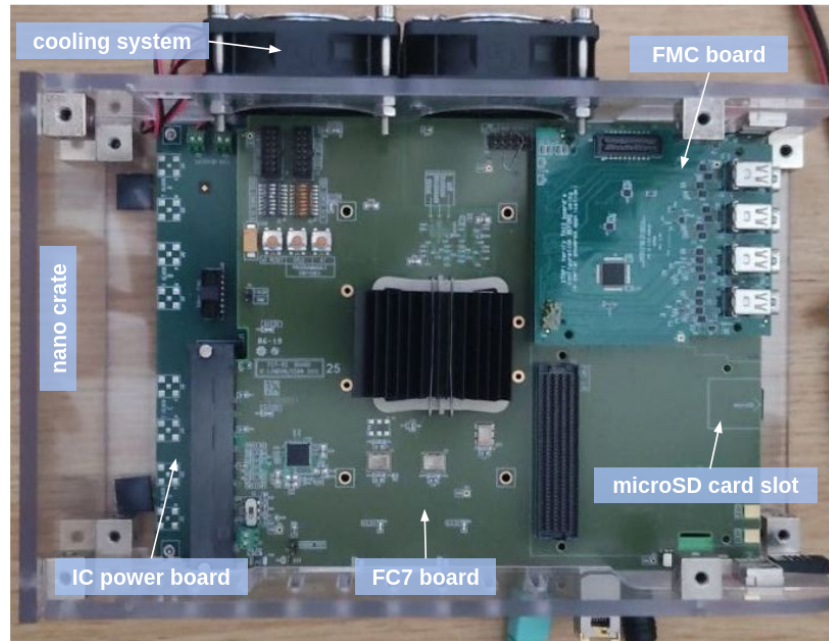


**Figure 3.3:** Ph2-ACF DAQ system for tuning and characterization of the CROCV1 front-end. The main hardware components are labeled.

The Ph2-ACF software [99] is written in C++ and uses the ROOT framework developed at CERN for data analysis. It enables configuration of the CROCV1 chip and provides a comprehensive suite of calibration procedures for tuning and characterization of the front-end, as described in Section 3.1.3. The software also manages the firmware images stored on the microSD card and loads them onto the FPGA. It runs on the DAQ PC and relies on a number of software dependencies and environment settings. To ensure portability and consistency across different computing environments, docker images were created as part of this thesis to run the Ph2-ACF software within a containerized setup. This approach allows users and developers to easily deploy the framework with all necessary dependencies pre-installed, providing a reliable and reproducible software environment for testing and development.



### 3.1.2. Description of the sensors

Two manufacturers participated in the R&D program on 3D pixel technology for the Phase-2 CMS tracker upgrade: Centro Nacional de Microelectrónica (CNM) [100] in Spain, and Fondazione Bruno Kessler (FBK) [101] in collaboration with Istituto Nazionale di Fisica Nucleare (INFN) in Italy. Although only FBK was selected for the final production—primarily due to its higher yield and lower fabrication cost—the performance of sensors from both manufacturers was evaluated in this thesis.

The sensors are fabricated on silicon-on-silicon  $p$ -type wafers, consisting of a high-resistivity active layer bonded to a low-resistivity support layer through the Direct Wafer Bonding (DWB) technique. The active layer has a nominal thickness of  $150\text{ }\mu\text{m}$  and a resistivity in the range of  $3\text{--}10\text{ k}\Omega\text{cm}$ , while the handle wafer has a resistivity in the range of  $0.1\text{--}1\text{ }\Omega\text{cm}$  and is thinned down to approximately  $100\text{ }\mu\text{m}$  after processing. This results in a total sensor thickness of  $250\text{ }\mu\text{m}$ . The sensor size has approximate dimensions of  $22.1\text{ mm}$  in width and  $17.3\text{ mm}$  in height.

All columnar implants are etched from the frontside using a single-sided Deep Reactive Ion Etching (DRIE) process and filled with polysilicon. CNM sensors feature a column diameter of  $8\text{ }\mu\text{m}$ , slightly larger than the  $5\text{ }\mu\text{m}$  column diameter in FBK sensors. The  $p^+$  ohmic columns extend beyond the active layer thickness and penetrate into the handle wafer, where a backside metal contact enables the application of bias voltage. In contrast, the  $n^+$  readout columns, which connect to the ASIC via bump-bonds, stop at a distance from the handle wafer of  $20\text{ }\mu\text{m}$  in CNM sensors and  $35\text{ }\mu\text{m}$  in FBK sensors.

Another difference between the two sensor designs lies in the approach to inter-pixel surface isolation. CNM employs the  $p$ -stop technique, involving localized  $p$ -type implants around each  $n^+$  column, whereas FBK uses the  $p$ -spray technique, applying a uniform  $p$ -type deposition across the sensor surface. Figures 3.4a and 3.4b show schematic front-view layouts of the CNM and FBK sensors, respectively.

Each pixel cell in these sensors features a single  $n^+$  readout column at the center, and four  $p^+$  ohmic columns located at the corners. The standard pixel cell size is  $25 \times 100\text{ }\mu\text{m}^2$ , and the pixel capacitance is below  $50\text{ fF}$  [102]. To ensure compatibility with the CROCv1 readout chip, the sensor matrix is designed with 864 pixels in the  $25\text{ }\mu\text{m}$  direction and 168 pixels in the  $100\text{ }\mu\text{m}$  direction. Moreover, a diagonal routing scheme is implemented for bump-bonding, enabling the alignment between the sensor and ROC matrices, as illustrated in Figure 3.5. The bump-pads are spaced  $50\text{ }\mu\text{m}$  apart, with an offset of  $25\text{ }\mu\text{m}$  in the long-pitch direction and  $12.5\text{ }\mu\text{m}$  in the short-pitch direction relative to the center of the pixel cell.

Since 3D pixel cells with a  $50\text{ }\mu\text{m}$  pitch were also considered during the initial R&D phase for the innermost TFPX rings, the performance of square pixel sensors is included for comparison. The pixel matrix of these sensors is naturally aligned with the ROC matrix, removing the need for diagonal routing.

Isolation of the active area from edge effects is achieved by fences of  $p^+$  ohmic columns surrounding the pixel matrix. These structures are visible in the peripheral regions of Figures 3.5a and 3.5b, which correspond to CNM and FBK sensors, respectively.

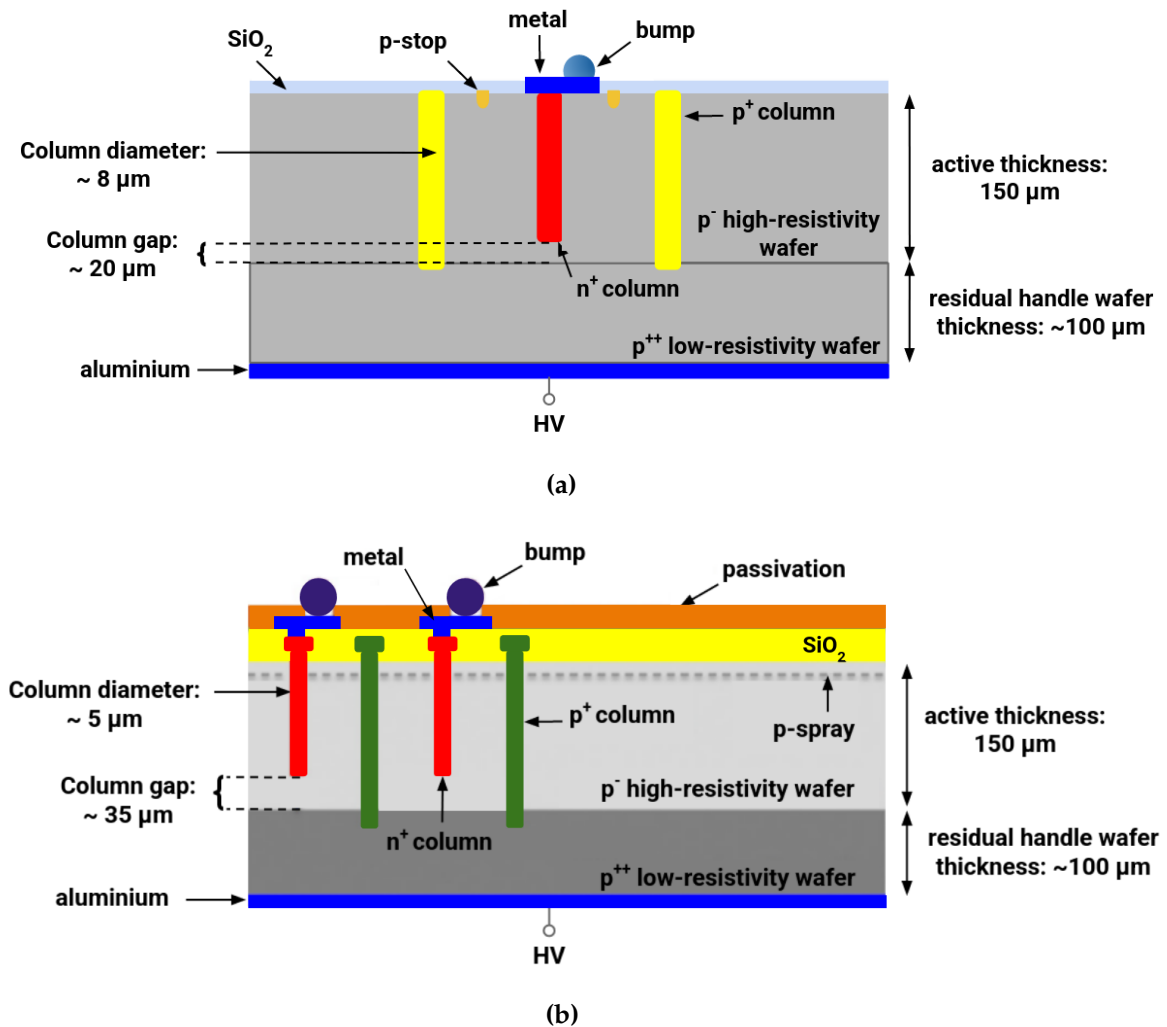


**Figure 3.4:** Schematic front-view layout of (a) a CNM and (b) an FBK 3D pixel sensor. The  $n^+$  columns are shown in red, while the  $p^+$  columns appear in yellow for CNM and green for FBK. Metal contacts under the bump-bonds and on the sensor backside are represented in blue. Key differences between the two designs are indicated, including column diameter,  $n^+$  column gap, and inter-pixel surface isolation technique. Images adapted from [103] and [104].

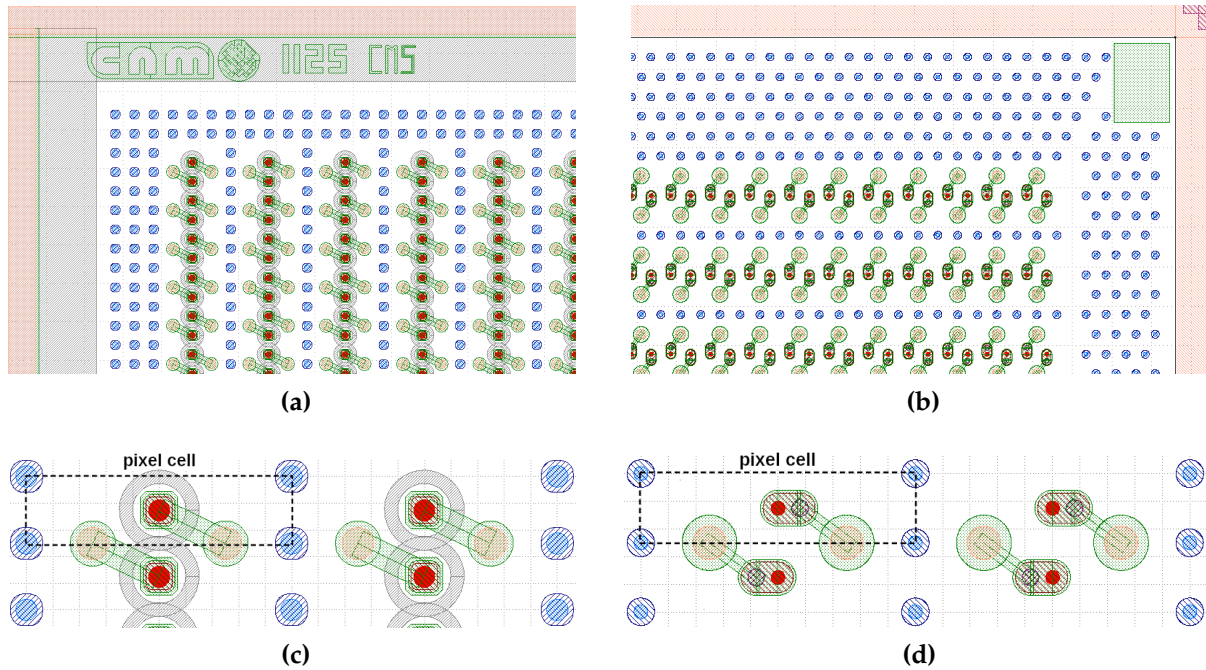


**Figure 3.5:** Top-view layout of (a) a CNM and (b) an FBK 3D pixel sensor. The sensor periphery includes ohmic column fences for edge isolation. Close-up views of four adjacent  $25 \times 100 \mu\text{m}^2$  pixel cells from CNM and FBK are shown in (c) and (d), respectively. One pixel cell is outlined with black dashed lines for reference. Light blue circles at the corners represent  $p^+$  columns, while the red circle at the center represents the  $n^+$  column. All columns are capped with polysilicon, indicated in dark blue and brown for the  $p^+$  and  $n^+$  electrodes, respectively. Orange circles represent the bump-pads, which connect to the  $n^+$  column through a metal routing shown in green. The  $p$ -stop implant used for  $n^+$  column isolation in CNM sensors is depicted by a gray ring. Images from [100] and [101].

### 3.1.3. Detector calibration procedure

Accurate calibration of the readout electronics is essential to ensure optimal detector performance and must be completed before exposure to a particle test beam. Among the key analog performance parameters, noise and threshold dispersion are particularly critical, as they determine the lowest operational threshold that can be reliably applied. These parameters directly impact the detector ability to distinguish true signals from electronic noise. Minimizing both is one of the main goals during design and operation, and requires thorough characterization of the front-end electronics.

The calibration procedure developed for modules equipped with CROCV1 and mounted on SCCs is presented below. The sequence is described using a non-irradiated bare chip or digital module, and the final tuning results are then compared to those obtained from hybrid pixel modules, where a 3D pixel sensor is bump-bonded to the CROCV1

chip. Table 3.2 summarizes the devices employed to explain the calibration procedure. It includes the main pixel geometry parameters and the measured value of  $V_{\text{ref\_ADC}}$ , which is necessary to convert injected charge from  $\Delta\text{VCal}$  units to electrons through equation 3.2.

**Table 3.2:** Summary of digital and hybrid pixel modules tested in the laboratory, including some geometric characteristics. The pixel size refers to the chip matrix for the digital module and to the sensor matrix for the single-chip 3D pixel modules.

Module name	Readout chip	Sensor	Column diameter [ $\mu\text{m}$ ]	Column gap [ $\mu\text{m}$ ]	Pixel size [ $\mu\text{m}^2$ ]	$V_{\text{ref\_ADC}}$ [mV]
bare-CROC	CROCv1	-	-	-	$50 \times 50$	790
CROC_FBK_A	CROCv1	FBK	5	35	$25 \times 100$	731
CROC_FBK_B	CROCv1	FBK	5	35	$25 \times 100$	780

All calibrations are performed using the Ph2-ACF DAQ system, described in Section 3.1.1. Since the pixel response exhibits some temperature dependence, the tuning must be performed under thermal conditions consistent with those expected during data acquisition. In test beam campaigns, this is typically achieved through active cooling, while in laboratory measurements, airflow from a standard fan is used to prevent the ASIC from overheating.

Before any calibration step, chip power trimming must be performed to ensure the proper functioning of all digital and analog front-end functionalities. This sets the CROCv1 front-end to its optimal working point. The preferred powering scheme for laboratory and beam tests is LDO mode. In this configuration, the power trimming is achieved partly by setting jumpers on the SCC and partly through software control registers. The low-voltage power supplies for the analog and digital domains are initially set to approximately 1.7 V, with a current compliance of 2 A each. The trimming process begins by adjusting  $I_{\text{ref}}$  as explained in Section 3.1.1. Then, the internal voltages for the digital and analog domains are fine-tuned to lie within 1.2 V and 1.3 V.

Once power trimming is complete, the threshold tuning procedure can be performed. The main objective is to calibrate all pixels to a common average threshold with minimal dispersion—typically targeting a threshold of 1000 electrons or the lowest value that keeps the fraction of masked pixels below 1%.

The first step is to tune the average hit detection threshold across the pixel matrix to a relatively high value, usually 2000 electrons for non-irradiated devices. This initial high threshold is necessary because the inherent pixel-to-pixel variations give rise to a threshold dispersion across the matrix and, without this precaution, pixels with

lower-than-average thresholds may appear noisy and be unnecessarily masked in later calibration stages. A binary search<sup>1</sup> is performed to find the GDAC setting that brings the average threshold as close as possible to the target. At each step of the search, a test charge corresponding to the target threshold is injected into all pixels a fixed number of times—typically 100. The GDAC value for which the average pixel occupancy across the matrix reaches 50% is selected as the global threshold. The pixel occupancy,  $Occ$ , is defined as:

$$Occ = \frac{n_{\text{Hits}}}{n_{\text{Events}}} \quad (3.3)$$

where  $n_{\text{Events}}$  is the number of pixel readouts and  $n_{\text{Hits}}$  is the number of times the pixel readout registered a signal above threshold.

In an ideal noise-free system, the threshold of a pixel is modeled by a Dirac delta distribution, and the pixel exhibits full occupancy for charge injections equal to or exceeding the threshold. However, in a real system, the electronic noise causes the threshold to be normally distributed. This makes the probability of registering a hit—equivalent to the probability that the pixel threshold lies below a given injected charge—to follow the Cumulative Distribution Function (CDF) of a Gaussian distribution, expressed as:

$$\Phi\left(\frac{Q - \mu}{\sigma}\right) = \frac{1}{2} \left[ 1 + \text{erf}\left(\frac{Q - \mu}{\sigma\sqrt{2}}\right) \right] \quad (3.4)$$

where  $\text{erf}$  is the error function and  $Q$  is the injected charge. The parameters  $\mu$  and  $\sigma$  are the mean and standard deviation of the Gaussian distribution, respectively. The mean  $\mu$  represents the most probable threshold value, while the width  $\sigma$  quantifies the pixel noise.

The behavior described by the pixel occupancy as a function of injected charge is known as the S-Curve, due to its characteristic sigmoid shape. Fitting the S-Curve to equation 3.4 provides the pixel threshold and noise. Figure 3.6a illustrates this concept, showing the Gaussian threshold distribution of a single pixel and the resulting S-Curve. A properly tuned system is expected to exhibit S-Curves with the inflection point, corresponding to 50% occupancy probability, near the target threshold.

Figure 3.6 presents the tuning status of the digital module after global threshold adjustment to an average of 2000 electrons. Figure 3.6b shows the superimposed S-Curves of all pixels. The threshold and noise for each pixel are extracted by fitting equation 3.4, and the resulting per-pixel values are then used to build the one-dimensional threshold and noise distributions shown in Figures 3.6c and 3.6d, respectively.

---

<sup>1</sup>A binary search is an algorithm for finding a target value in a sorted array by repeatedly dividing the search range in half. At each step, it compares the target to the middle element and narrows the search to the appropriate half.

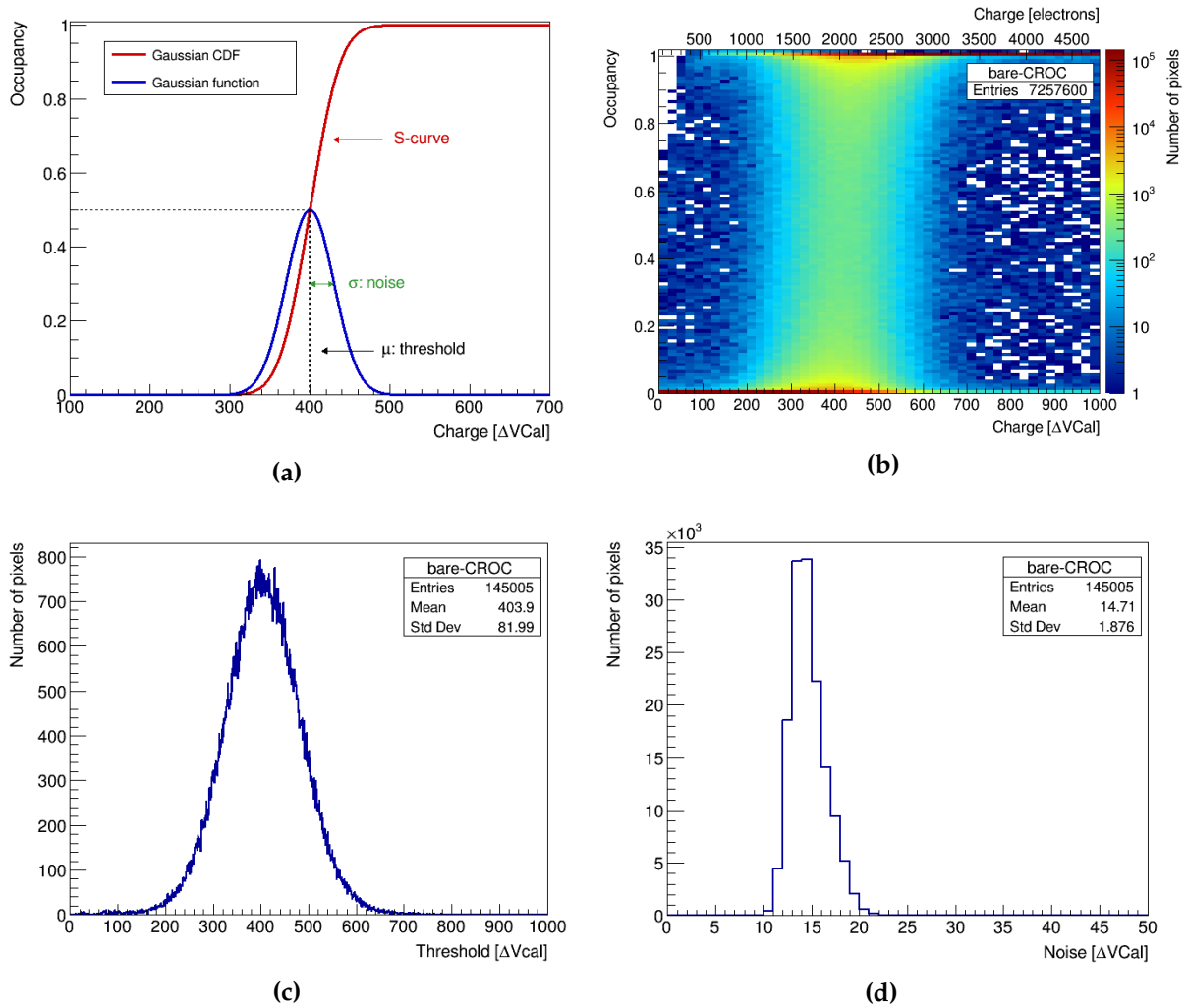


**Figure 3.6:** (a) Schematic representation of an S-Curve, illustrating the definition of threshold and noise for a single pixel. More details are given in the text. (b) Superimposed S-Curves of all pixels in the digital module tuned to a global target threshold of 2000 electrons. (c) and (d) show the corresponding one-dimensional threshold and noise distributions.

After the global threshold tuning, the pixel response across the matrix remains non-uniform, exhibiting a threshold spread of approximately 400 electrons, as indicated in Figure 3.6c. To reduce this dispersion and achieve a more homogeneous response, a threshold equalization step is performed using the local threshold tuning circuit. This procedure adjusts the TDAC value individually for each pixel, bringing its threshold as close as possible to the average value that was set as global threshold. TDAC was defined in Section 3.1.1 and modifies the pixel threshold as described by equation 3.1.

All pixels are initially set to the default value ( $TDAC = 16$ ), which corresponds to the midpoint of the TDAC range. A binary search is performed independently for



each pixel to find the TDAC setting that minimizes the deviation from the global threshold. At each step of the search, a charge equal to the target threshold is injected into the pixel a fixed number of times ( $n_{\text{Events}} = 100$ ), and the TDAC value for which the pixel occupancy is closest to 50% is selected. An effective equalization results in a one-dimensional TDAC distribution with a roughly Gaussian profile centered around the midpoint of the range, with minimal population at the edges (TDAC = 0 and 31). Pronounced asymmetry or edge saturation may indicate a suboptimal calibration. In such cases, adjusting the LDAC setting may improve the dynamic range of the local threshold trimming. Increasing the LDAC value broadens the TDAC output range but reduces its resolution.

Figure 3.7 shows the results after local threshold trimming. The one-dimensional TDAC distribution in Figure 3.7a exhibits the expected shape, indicating a successful equalization. The goodness of the local threshold trimming is further confirmed by the superimposed S-Curves and the narrower threshold distribution shown in Figures 3.7b and 3.7c, respectively. After equalization, the threshold spread is reduced to approximately 75 electrons, reflecting a significantly more uniform pixel response across the matrix. Although the threshold and noise distributions are presented in  $\Delta V_{\text{Cal}}$  units, the conversion to electrons is performed using equation 3.2, with the  $V_{\text{ref\_ADC}}$  value specified in Table 3.2.

The next step involves masking pixels that exhibit noisy behavior. A pixel is classified as noisy if it registers hits even in the absence of charge injections. Such behavior can arise from connection issues or from thresholds being set too low. Although, after equalization at a relatively high threshold, the latter is typically no longer a concern. Masking such problematic pixels is essential to prevent them from generating spurious hits during data acquisition.

To identify noisy pixels, the occupancy is evaluated by performing a fixed number of readouts without injecting any charge ( $n_{\text{Events}} = 10^7$ ). A pixel is considered noisy if it exhibits an occupancy greater than  $2 \times 10^{-5}$ , corresponding to more than 200 registered hits. This occupancy limit represents 1% of the expected hit rate in the innermost TBPX layer under the ultimate high-luminosity performance scenario, as reported in Figure 1.10.

Figure 3.8 shows the results after masking noisy pixels in the digital module tuned at an average threshold of 2000 electrons. The map in Figure 3.8a presents the spatial distribution of the 241 masked pixels. A significant number are clustered along two columns, suggesting a possible localized defect or physical damage affecting those columns. These pixels typically exhibit thresholds notably lower or higher than the average. Their removal results in a cleaner S-Curve plot and a further reduction in threshold dispersion, reaching approximately 50 electrons, as indicated in Figure 3.8c.



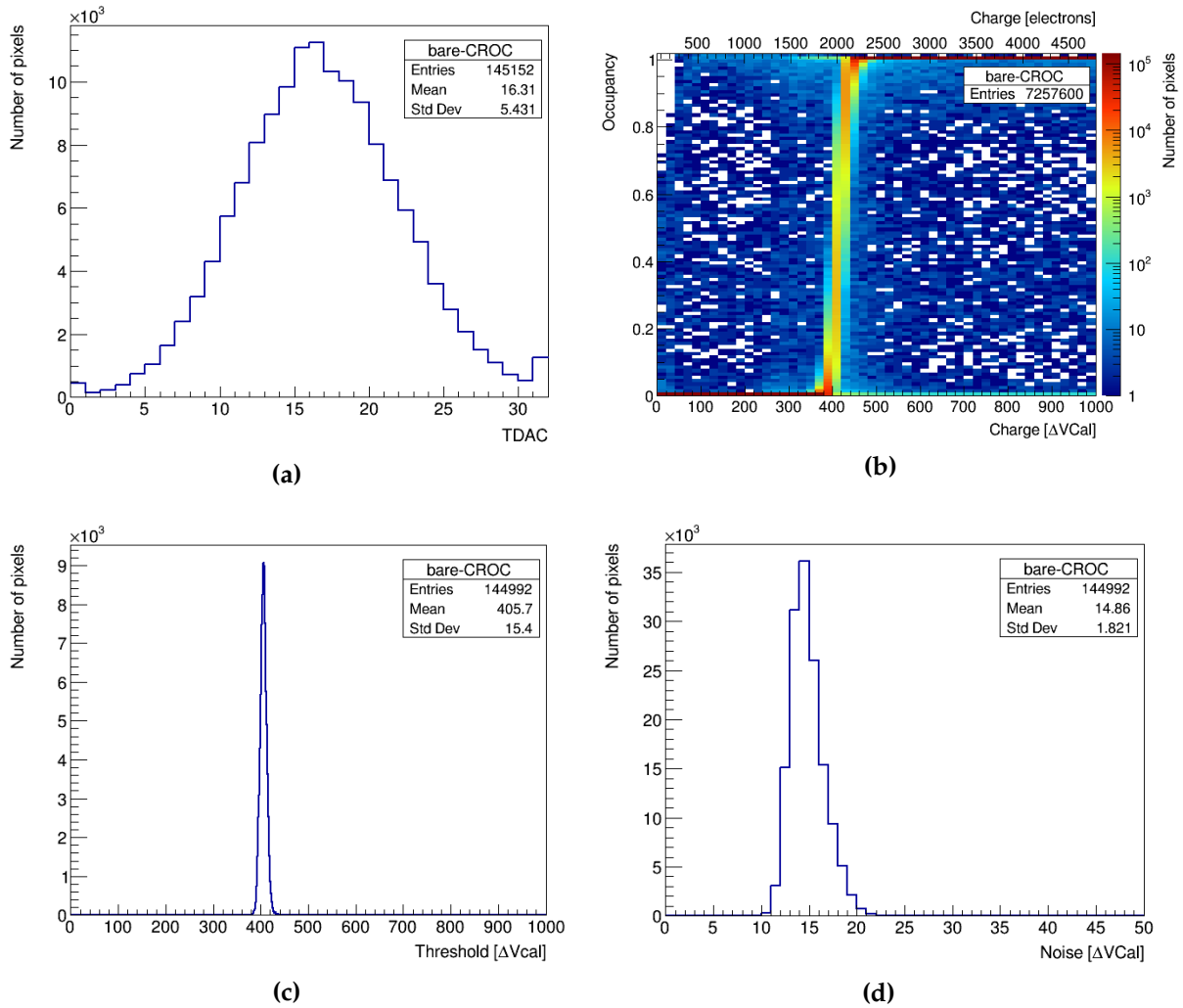


**Figure 3.7:** (a) One-dimensional TDAC distribution after threshold equalization. More details are given in the text. (b) Superimposed S-Curves of all pixels in the digital module tuned to a target threshold of 2000 electrons following equalization. (c) and (d) show the corresponding one-dimensional threshold and noise distributions.

Following the initial set of calibrations, the global threshold is progressively lowered, with noisy pixel masked on top of previously masked pixels at each step. For a final target tuning of 1000 electrons, at least one intermediate tuning iteration at 1200 electrons is recommended. If necessary, the local threshold trimming can also be repeated, allowing TDAC adjustments within  $\pm 1 \Delta$ VCal unit to speed up the process.

After tuning the pixel matrix to an average threshold of 1000 electrons, a final masking step is performed to exclude both noisy and stuck pixels. A pixel is classified as stuck if it fails to register hits under charge injections of sufficient magnitude—typically corresponding to the charge deposited by a MIP traversing  $150 \mu\text{m}$  of silicon. To identify them, the occupancy is evaluated by performing a fixed number of charge

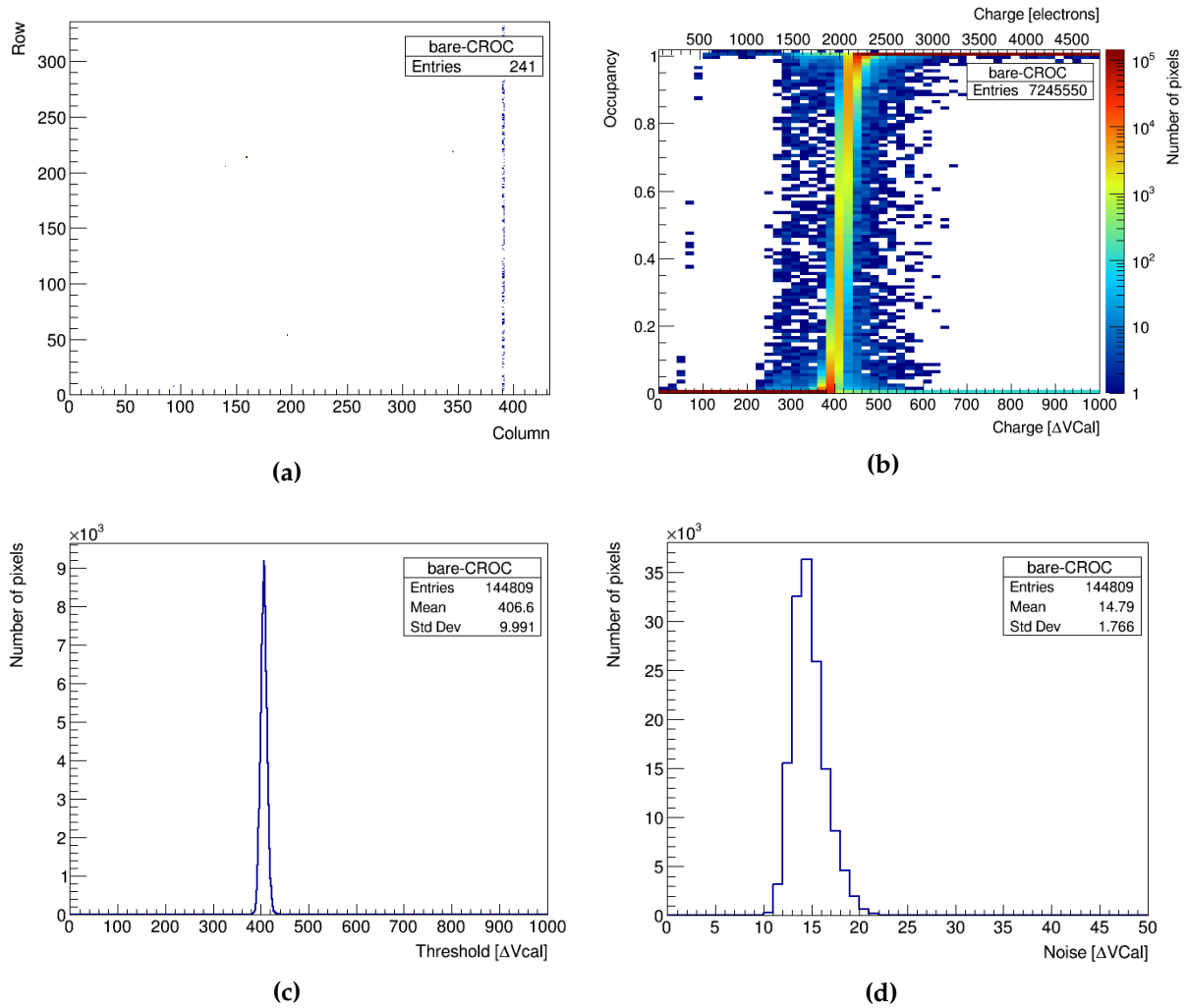


**Figure 3.8:** (a) Map of pixels masked due to noisy behavior. More details are given in the text. (b) Superimposed S-Curves of all pixels in the digital module tuned to a target threshold of 2000 electrons following equalization and noisy pixel masking. (c) and (d) show the corresponding one-dimensional threshold and noise distributions.

injections ( $n_{\text{Events}} = 100$ ). Pixels with occupancy below 0.9, corresponding to fewer than 90 registered hits, are considered stuck.

Figure 3.9 presents the results after masking noisy and stuck pixels in the digital module tuned to an average threshold of 1000 electrons. The cumulative mask map in Figure 3.9a shows 270 noisy pixels and 108 stuck pixels. The core of the threshold and noise distributions, extracted from the S-Curves in Figure 3.9b, are fitted to Gaussian functions. The mean threshold from the fit is close to the intended 1000 electrons, with a standard deviation of approximately 45 electrons. The noise distribution shows a mean equivalent noise charge of around 70 electrons with a spread of 6 electrons.

The final calibration step aims at characterizing the ToT response as a function of the

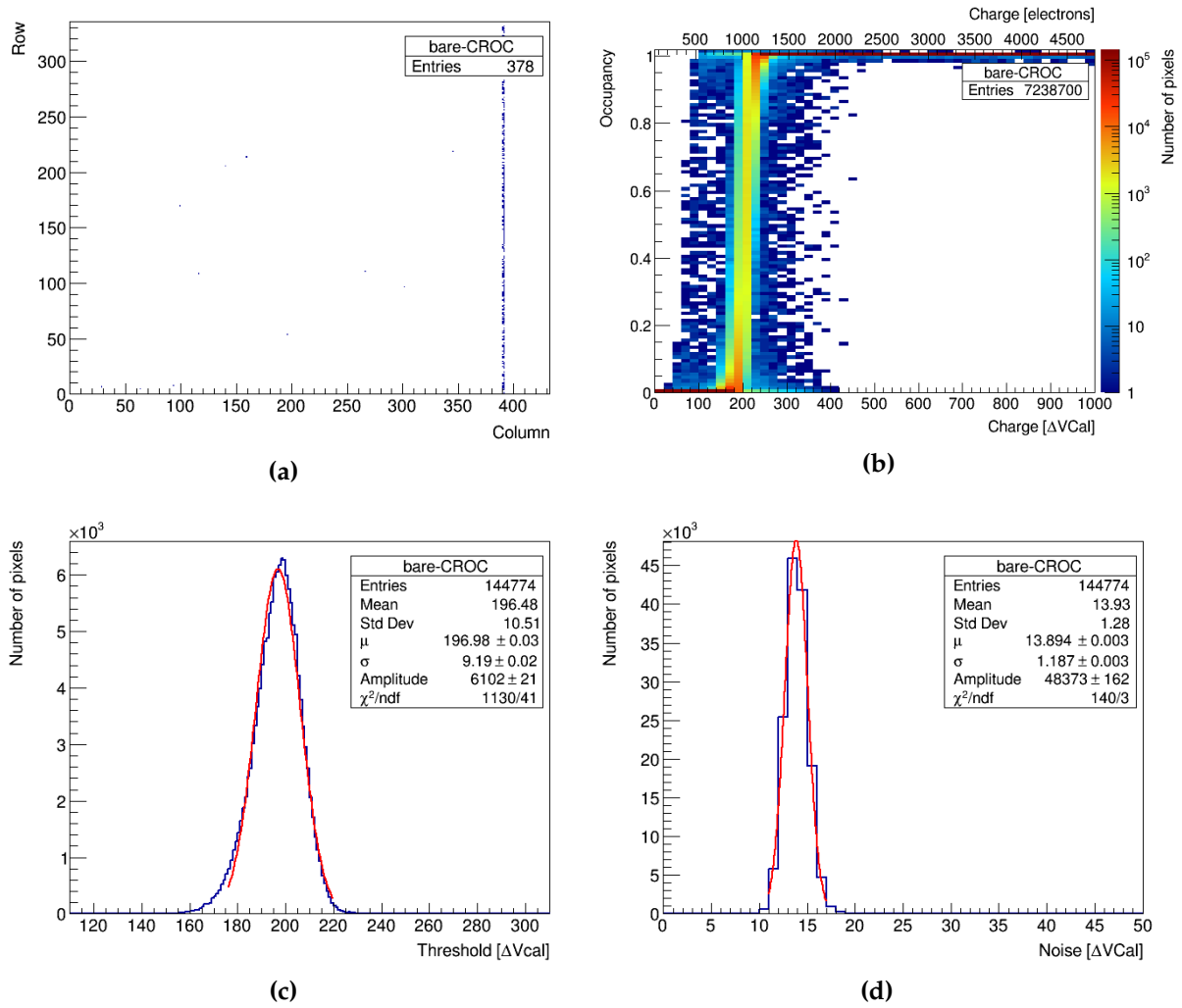


**Figure 3.9:** (a) Cumulative map of pixels masked due to noisy or stuck behavior. More details are given in the text. (b) Superimposed S-Curves of all pixels in the digital module tuned to a target threshold of 1000 electrons following the masking of noisy and stuck pixels. (c) and (d) show the corresponding one-dimensional threshold and noise distributions, each fitted to a Gaussian function with mean  $\mu$  and width  $\sigma$ .

injected charge in each pixel. The resulting gain curve is typically modeled as a linear function:

$$Q_{\text{ToT}} = a \cdot Q_{\Delta\text{VCal}} + b \quad (3.5)$$

where  $Q_{\Delta\text{VCal}}$  is the injected charge in  $\Delta\text{VCal}$  units, and  $Q_{\text{ToT}}$  is the corresponding output in ToT units, measured in 25 ns time intervals. The slope  $a$  and intercept  $b$  represent the gain characteristics. The slope depends directly on the Krummenacher current, which governs the discharge of the feedback capacitor in the preamplifier circuit. A higher current leads to a faster return to baseline, resulting in a reduced ToT. The intercept is also influenced by the Krummenacher current but is primarily

determined by the threshold level, which defines the  $\text{ToT} = 0$  point.

To evaluate the ToT response, a fixed number of charge injections ( $n_{\text{Events}} = 100$ ) is applied to each pixel for a given test charge, and the average ToT for each pixel is recorded. This process is repeated for increasing charge values to map the full ToT response. Once the measurements are completed, the gain curve of each pixel can be fitted to equation 3.5 to extract its individual slope and intercept. The ToT response can vary considerably across the pixel matrix. This variation arises from intrinsic differences in the analog front-end circuitry of each pixel and cannot be corrected through tuning, but it must be taken into account during data reconstruction and analysis.

Figure 3.10 shows the superimposed gain curves for all pixels in the digital module tuned to an average pixel threshold of 1000 electrons.

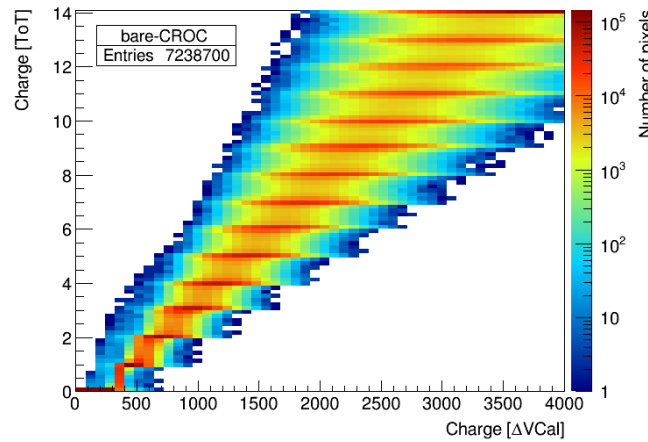


**Figure 3.10:** Superimposed gain curves of all pixels in the digital module tuned to a target threshold of 1000 electrons. Details are given in the text.

The tuning procedure for irradiated modules follows the same sequence of calibrations. However, due to increased noise after irradiation, the procedure needs to be slightly adapted to cope with the new conditions. The target threshold is 1000 electrons, or the lowest achievable value that keeps the fraction of masked pixels below 2%, as required by the CMS specifications shown in Table 3.1. The main difference in the procedure lies in the initial global threshold tuning, which is typically set to 3000 electrons before equalization. From there, the matrix is progressively tuned to lower thresholds through at least two intermediate iterations, commonly at 2000 electrons and 1200 electrons provided that the target threshold of 1000 electrons can be achieved. This gradual approach helps mitigate the increase in noisy pixels typically observed in irradiated modules and ensures that threshold trimming remains effective.

### Comparison between digital and hybrid pixel modules

The tuning procedure for a hybrid pixel module is identical to that of a digital module, with one important exception due to the presence of the sensor: the chip power trimming must be performed before applying the sensor bias voltage to avoid damaging the front-end electronics. Moreover, for accurate calibration, the sensor must be fully depleted, as this reflects the intended operating conditions. A partially depleted sensor exhibits different capacitance, which can alter the analog response of the pixel and compromise the validity of the tuning. In these measurements, a reverse-bias voltage of 30 V was applied to ensure full depletion.

After tuning the pixel matrix to an average threshold of 1000 electrons, noisy and stuck pixels were masked following the same criteria described for the digital module. Figures 3.11a and 3.11b show the resulting masks for the two hybrid modules under test: CROC\_FBK\_A and CROC\_FBK\_B. A total of 498 noisy pixels were masked in CROC\_FBK\_A, whereas CROC\_FBK\_B exhibited 27 noisy pixels and 2 stuck pixels.

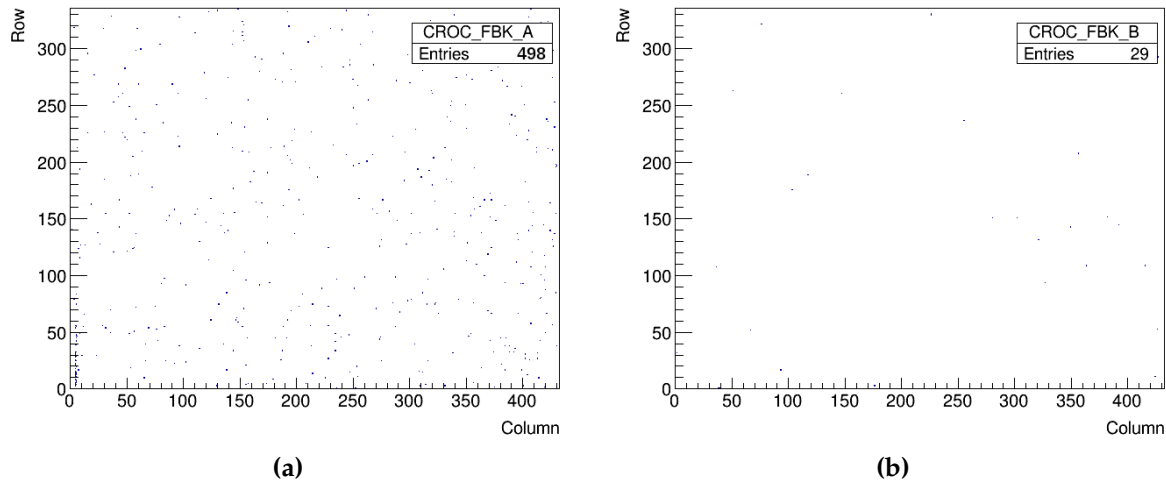


**Figure 3.11:** Cumulative map of pixels masked due to noisy or stuck behavior in modules (a) CROC\_FBK\_A and (b) CROC\_FBK\_B, both tuned to a threshold of 1000 electrons following a complete set of calibrations.

The final tuning status is shown in Figure 3.12. The S-Curves confirm the effective tuning to an average pixel threshold of 1000 electrons in both CROC\_FBK\_A and CROC\_FBK\_B. The corresponding one-dimensional threshold and noise distributions are fitted to Gaussian functions. Table 3.3 summarizes the results from the fits and includes a comparison with the digital module. As expected, the hybrid modules exhibit higher noise. This is primarily due to the added capacitance from the sensor, and potentially from parasitic effects introduced by the bump-bond connections.

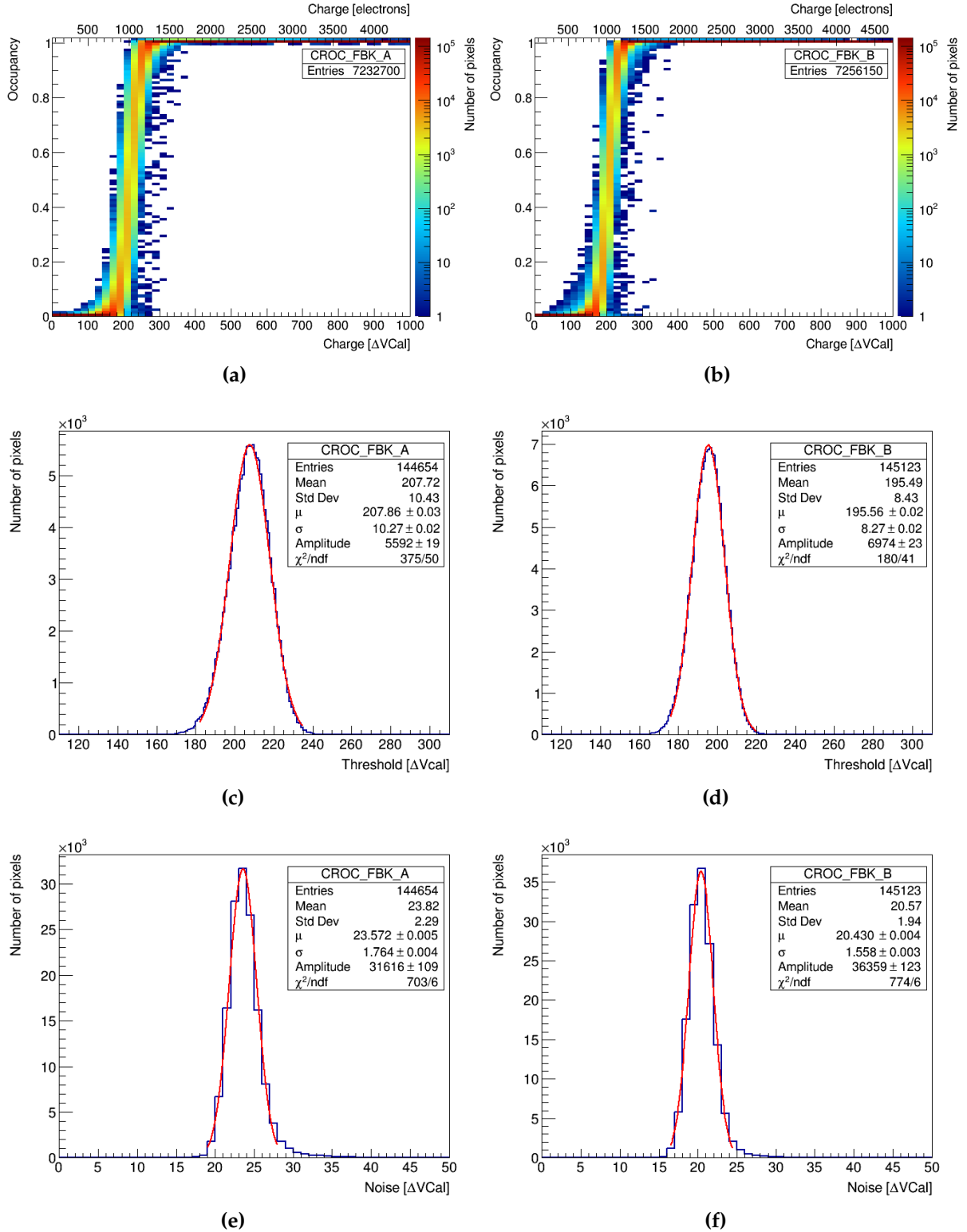


**Figure 3.12:** Superimposed S-Curves of all pixels in (a) CROC\_FBK\_A and (b) CROC\_FBK\_B, both tuned to a target threshold of 1000 electrons following a complete set of calibrations. (c) and (d) show the corresponding threshold distributions, while (e) and (f) show the corresponding noise distributions. All one-dimensional distributions are fitted to Gaussian functions with mean  $\mu$  and width  $\sigma$ .

**Table 3.3:** Comparison of results from the front-end tuning in single-chip digital and hybrid pixel modules. It includes key parameters from the threshold and noise distributions, obtained from Gaussian fits and converted to electrons using equation 3.2, as well as the percentage of masked pixels.

Module name	Threshold distribution		Noise distribution		Masked pixels [%]
	$\mu$ [electrons]	$\sigma$ [electrons]	$\mu$ [electrons]	$\sigma$ [electrons]	
bare-CROC	1011.0 $\pm$ 0.2	44.4 $\pm$ 0.1	67.08 $\pm$ 0.02	5.73 $\pm$ 0.02	0.26
CROC_FBK_A	988.6 $\pm$ 0.1	45.88 $\pm$ 0.09	105.30 $\pm$ 0.02	7.88 $\pm$ 0.02	0.34
CROC_FBK_B	992.2 $\pm$ 0.1	39.42 $\pm$ 0.09	97.38 $\pm$ 0.02	7.43 $\pm$ 0.01	0.02

## 3.2. Facilities and experimental setups

The performance of single-chip 3D pixel modules was evaluated both before and after irradiation through dedicated test beam campaigns. During these tests, the detectors are operated under conditions similar to those of the final experiment, allowing for precise characterization of their response to charged particle passage.

Irradiation campaigns simulate the long-term radiation damage expected during detector operation. By exposing the modules to high-intensity particle beams, the target fluence is reached under controlled conditions in a relatively short time. This allows for post-irradiation testing to assess the radiation tolerance of the devices and verify whether they continue to perform reliably within specifications.

Several irradiation and test beam campaigns were performed to achieve a thorough characterization of single-chip 3D pixel modules. The facilities and experimental setups used in these campaigns are described below.

### 3.2.1. Irradiation facilities and setups

Irradiation campaigns of CROCv1 3D pixel modules were conducted at the Karlsruhe Institute of Technology (KIT) [105] and the CERN PS IRRAD [106]. The proton beam energy used at each facility and its corresponding hardness factor are provided in Table 3.4. Since the TID depends on beam energy, a fluence of  $1 \times 10^{16} \text{ n}_{\text{eq}}\text{cm}^{-2}$  corresponds to approximately 15 MGy at KIT and 5 MGy at the CERN PS IRRAD. For comparison, the innermost TBPX layer is expected to accumulate 13.4 MGy and 17.8 MGy after integrated luminosities of  $3000 \text{ fb}^{-1}$  and  $4000 \text{ fb}^{-1}$ , respectively, as reported in Table 1.1. The radiation hardness of CROCv1 has been demonstrated up to a TID of approximately 10 MGy [107], which is considered sufficient given the foreseen replacement of this layer during the second half of HL-LHC operation.



**Table 3.4:** Particle beams used to irradiate CROCv1 3D pixel modules at the CERN PS and KIT irradiation facilities. The beam energy at the module position—slightly lower than the nominal energy in the beam line—and the corresponding  $\kappa$ -factor, as estimated in [108], are provided.

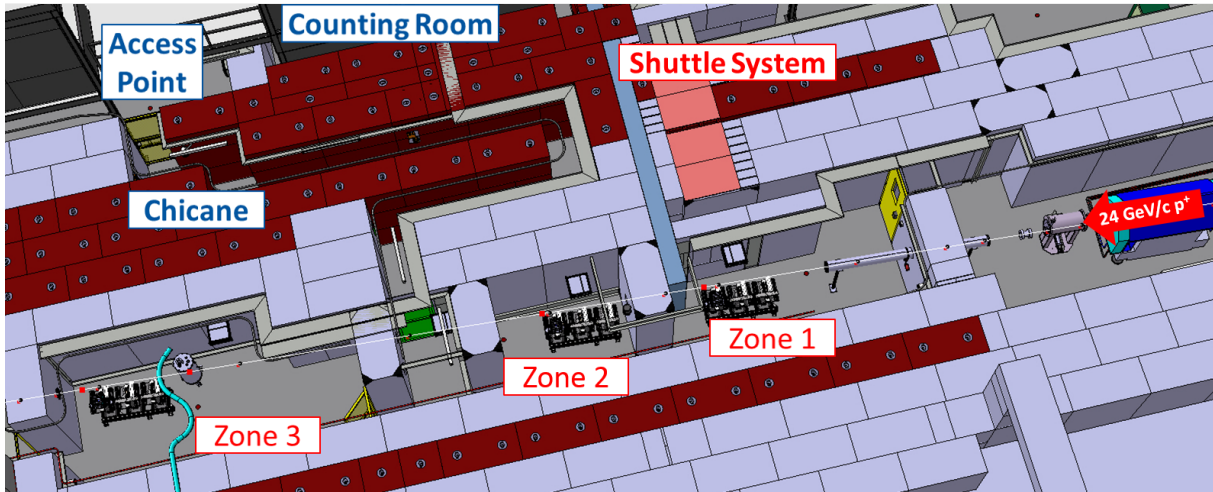
Irradiation facility	Beam type	Beam energy	$\kappa$ -factor
CERN PS IRRAD	Proton	23 GeV	0.62
KIT	Proton	23 MeV	2.20

Figure 3.13a shows the layout of the CERN PS IRRAD facility, which is divided into three zones according to the nature of the samples to be irradiated. The modules are mounted on remote-controlled stages that enable one-dimensional scanning along the horizontal axis in the plane transverse to the beam line. This scanning is essential to ensure full coverage of the target area, given the limited size of the beam spot. A similar setup is used at KIT, with the main difference being the ability to perform two-dimensional scanning along both horizontal and vertical axes.

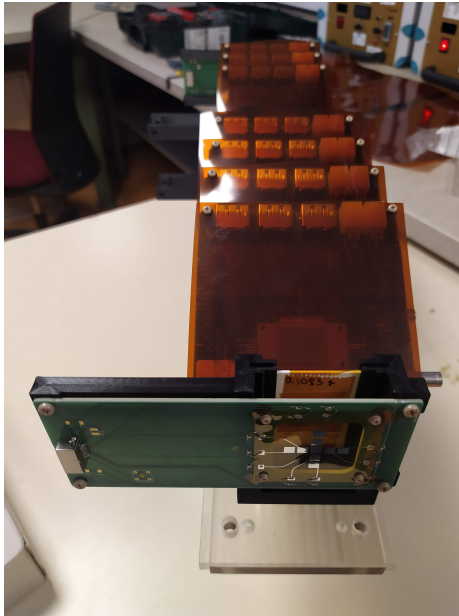
The beam used in the irradiation campaigns had an approximately Gaussian profile. At KIT, the Full Width at Half Maximum (FWHM) was about 7 mm in both directions. Combined with the possibility to perform a two-dimensional scanning, this enabled a uniform fluence profile across the DUT surface. In contrast, the lack of vertical scanning at the IRRAD facility results in a non-uniform fluence distribution. To mitigate this non-uniformity, a custom support—shown in Figures 3.13b and 3.13c—was designed to hold the modules tilted by  $30^\circ$  with respect to the horizontal plane, improving the irradiation uniformity along the vertical axis. The FWHM of the beam profile at the CERN PS was approximately 14.5 mm in the horizontal direction and 6.5 mm in the vertical direction.

Beam alignment with respect to the modules was verified using a laser system, as shown in Figure 3.13d. Prior to irradiation, the modules were coated with parylene to protect the wire bonds. Additionally, metallic foils were attached to some modules to monitor the dose profile—aluminum foils at the IRRAD facility and nickel foils at KIT. After irradiation, the foil activity was measured using HPGe spectroscopy. The foils used at IRRAD were segmented into small pieces to achieve a more precise measurement of the fluence across the DUT, as shown in Figure 3.13e. The estimated uncertainty in fluence measurements was approximately 7% at IRRAD and 15% at KIT.

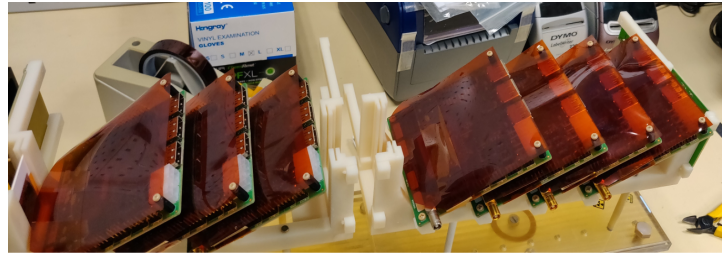
Although all modules were stored at low temperature to prevent annealing after the irradiation campaign, active cooling during irradiation was applied only at KIT. The devices remained unpowered during irradiation at both facilities.



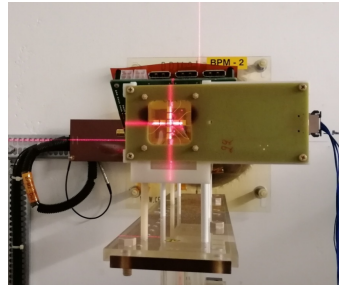
(a)



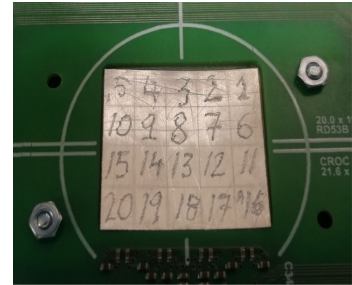
(b)



(c)



(d)



(e)

**Figure 3.13:** (a) Detailed layout of the CERN PS IRRAD facility. (b) and (c) show the module support used during the irradiation campaigns. The samples are tilted by  $30^\circ$ , as seen in the longitudinal view. (d) illustrates the beam alignment procedure using a laser. (e) shows the aluminum foil placed on the backside of a DUT. Top image from [106].

### 3.2.2. Test beam facilities and setups

Test beam measurements of CROCv1 3D pixel modules were carried out at the CERN SPS and Deutsches Elektronen-Synchrotron (DESY) [109], using the particle beams indicated in Table 3.5. These particle beams behave as MIPs, providing an operating environment similar to that expected in the final experiment. The corresponding test

beam setups are shown in Figures 3.14a and 3.14b. Both setups are equipped with an EUDET-type beam telescope [110] for high-precision tracking, with the AIDA telescope operated at the CERN SPS and the DATURA telescope operated at DESY.

**Table 3.5:** Particle beams used to evaluate the performance of the CROCv1 3D pixel modules at the CERN SPS and DESY test beam facilities.

Test beam facility	Beam type	Beam momentum [GeV/c]
CERN SPS	Pion	120
DESY	Electron	5-6

Figure 3.14c provides a schematic overview of a typical test beam setup with an EUDET-type telescope, highlighting the main hardware components and their interconnections. This telescope consists of six pixels planes based on MIMOSA26 monolithic detectors, usually arranged in two triplets positioned upstream and downstream of the DUTs along the beam direction. Each telescope plane is mounted within an aluminum jig, protected by lightproof kapton foils of  $25\mu\text{m}$  thickness on each side. The jigs are guided on a rail system, allowing adjustment of the telescope arms along the beam direction to ease the DUT installation. Active cooling for the jigs is provided via a water-based chiller system, keeping the telescope planes at a stable temperature of  $18^\circ\text{C}$ .

The MIMOSA26 detectors, introduced in Section 2.4.2, feature a  $50\mu\text{m}$  thickness and a pixel size of  $18.4 \times 18.4\mu\text{m}^2$ . Their pixel matrix is organized in 576 rows and 1152 columns, yielding an active area of about  $21.2 \times 10.6\text{mm}^2$ . Readout is performed in rolling-shutter mode, where all columns are read in parallel and rows are processed sequentially. Each row is read in 16 clock cycles at 80 MHz, resulting in a total integration time of  $115.2\mu\text{s}$  and a maximum readout rate of 8680 frames per second. Inside each pixel, amplification and correlated double sampling to suppress noise are applied. The resulting signals are then processed by offset-compensated discriminators, which perform the analog-to-digital conversion. The binary outputs of the discriminators are passed to a zero-suppression logic, which reduces the data volume to be stored in memory. The discriminator threshold is configurable and typically set between five and six times the pixel RMS noise, achieving a per-pixel noise occupancy of approximately  $6 \times 10^{-5}$ . Due to limited on-chip buffer size, the detector can support particle rates up to about  $1\text{MHzcm}^{-2}$ . For single-pixel clusters, the intrinsic spatial resolution of a MIMOSA26 detector is about  $5.3\mu\text{m}$ . The average telescope resolution depends not only on the configuration of the telescope planes but also on the particle type and energy used in the test beam facility.



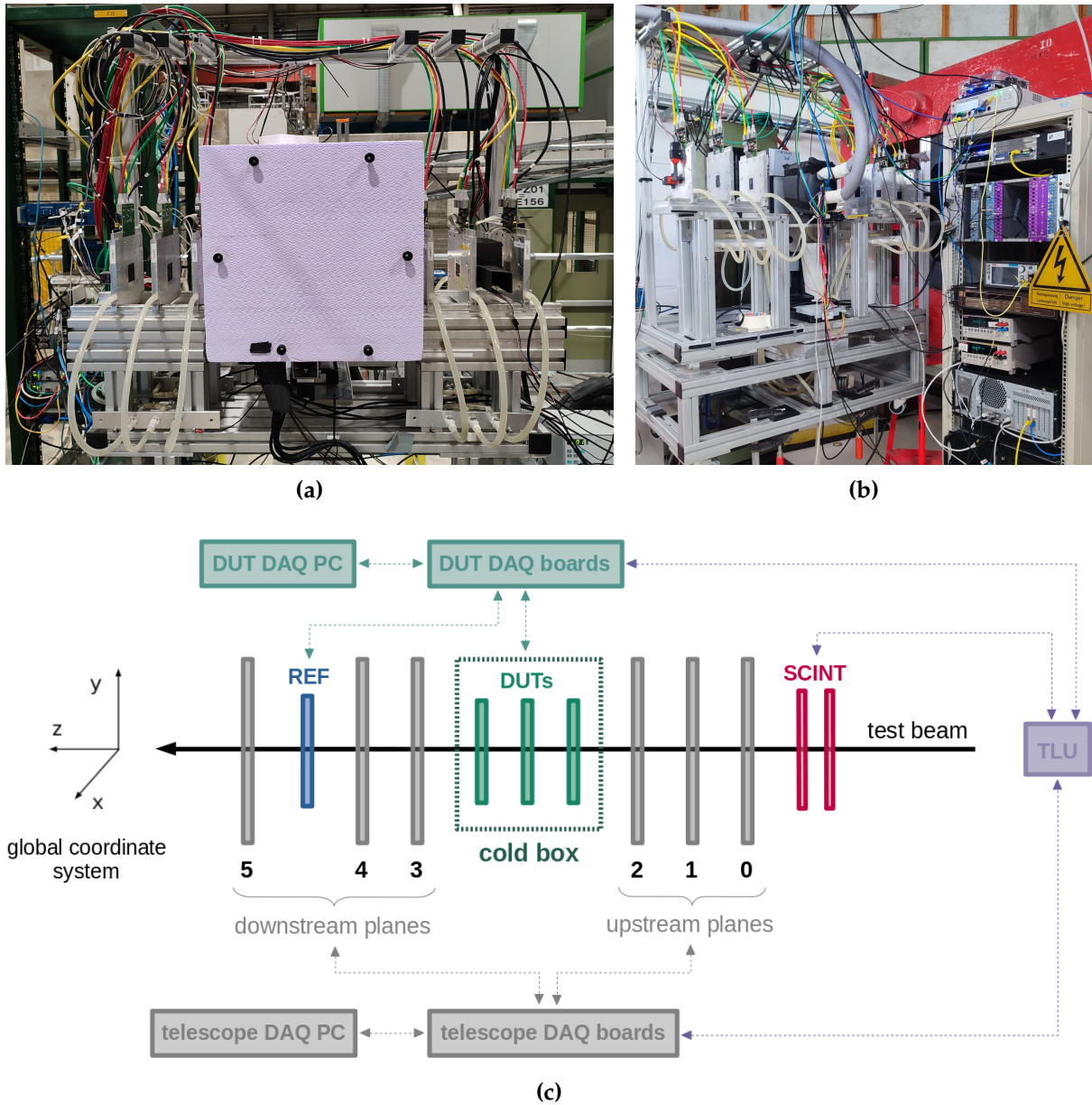


**Figure 3.14:** Images of the experimental setups at (a) the CERN SPS and (b) DESY test beam facilities. (c) A generic schematic of the test beam setup using the EUDET-type telescope. The telescope pixel planes are shown in gray. The timing-reference module is tagged as REF, the scintillators are marked as SCINT, and the devices under test are labeled as DUTs. The positions of REF and SCINT may vary between facilities. Connections to the TLU, DAQ boards and PCs are indicated by dashed arrows.

The long integration time of the MIMOSA26 detectors leads to a high track multiplicity per event, as additional particles may traverse the telescope and be detected after the trigger signal is issued. Since these detectors do not provide time information for individual hits, an external timing-reference plane (REF) with fast readout is required

to identify in-time tracks and reject out-of-time tracks, ensuring reliable measurements of the DUT performance, as further discussed in Section 3.3.1. In the test beam campaigns presented in this thesis, the REF was a single-chip module comprising an HPK planar pixel sensor interconnected with the CROCv1 chip, which features an integration time of only 25 ns. This fast timing capability allows suppression of track ambiguities in events that include a hit in every telescope plane, the DUT and the REF.

The telescope is complemented by a pair of plastic scintillators readout by PMTs, which detect charge particles traversing the setup and initiate data acquisition. Depending on the test beam facility, the scintillators are placed either upstream or downstream of the telescope planes. They are typically arranged in a crossed configuration, with the overlap region defining the spatial acceptance for triggering and particle detection. Triggering is managed by a custom Trigger Logic Unit (TLU) [111], which processes the PMT output signals using programmable logic and eventually issues a global trigger. This trigger is distributed to all DAQ systems in the setup, including the telescope planes, any DUT and the timing-reference module. To ensure synchronization across systems with different readout latencies, the TLU implements a handshake protocol: each DAQ system asserts its own busy signal during readout, and the TLU vetoes new triggers until all busy lines are cleared. For each accepted trigger or event, the TLU increments an internal trigger counter and records a timestamp, allowing for precise event alignment across all detector planes. A series of such events—typically between 250 000 and 500 000—acquired under consistent operating conditions constitutes a run.

In irradiated sensors, the leakage current shows a strong dependence on temperature, as discussed in Section 2.3. Maintaining the sensors at a stable, low temperature during operation helps mitigate radiation damage effects. For this purpose, the DUTs are placed inside a thermally insulated cold box flushed with dry air to prevent condensation. This cold box also shields the modules from ambient light and is mounted on a set of motorized stages that allow remote control of the position and orientation of the DUTs. Translation in the two directions orthogonal to the beam axis and rotation around the vertical axis are supported.

In the SPS test beam setup, the cold box is connected to a chiller that circulates coolant to maintain a stable internal temperature. The setup can host up to four DUTs simultaneously, with internal fans ensuring homogeneous airflow so that all devices experience uniform thermal conditions. This configuration is used for both irradiated and non-irradiated modules, with the operating temperature adjusted accordingly. In contrast, the DESY test beam setup is optimized for low-energy electrons, which are highly sensitive to multiple scattering. To reduce the material budget, this setup accommodates only a single DUT at a time, and only irradiated devices are placed inside a cold box. This box features a thin Kapton window at the beam entry point to reduce scattering. The DUT is coupled on its downstream face to a thin copper

plate using thermally conductive paste. This plate is cooled by Peltier elements, which are connected to an external ethanol-based chiller. Due to the additional material introduced by the downstream cooling assembly, only the upstream telescope arm is used for track reconstruction in this configuration.

### Data acquisition framework

The test beam data acquisition framework is responsible for recording data from all hardware components in the setup, including the telescope planes, TLU, DUT and REF. It merges the data streams from these subsystems into complete events and stores them on disk for offline analysis. The DAQ system provides the interface between the detector readout electronics and the user-controlled PCs. EUDAQ2 [112] is the global software for data taking used with EUDET-type beam telescopes. It is designed to be lightweight, modular and portable, enabling easy integration with dedicated DAQ systems for additional devices—such as Ph2-ACF for both the DUTs and the REF. The framework consists of fully independent modules or processes that communicate via TCP/IP, allowing for distributed data acquisition with modules running on separate machines.

The central coordination module in EUDAQ2 is the Run Control, which distributes commands to all other processes. Its graphical user interface allows users to configure and handle runs. Logging information from all modules is gathered by the Log Collector, displayed in a unified interface, and written to file for later reference. Data from each detector subsystem is handled by a dedicated Producer, which interfaces with the specific hardware to manage its initialization and configuration, based on instructions received from the Run Control. Producers read out the actual detector data and deliver it to the Data Collector, which performs event building by correlating the data streams from all subsystems and writes the resulting events to disk. To monitor data quality during acquisition, the Online Monitor module reads the events from disk, decodes them using dedicated Data Converter plugins, and generates basic histograms such as hit maps and correlation plots. This process ensures that all devices are properly synchronized in time and fall within the geometrical trigger acceptance.

Similarly to the Ph2-ACF software, docker images for EUDAQ2 were also developed as part of this thesis, providing a convenient and portable environment for offline inspection of event data files.

## 3.3. Test beam measurements

An overview of the test beam measurements and the performance evaluation of single-chip 3D pixel modules is presented below. The modules under test include four FBK sensors and two CNM sensors, all bump-bonded to the prototype CROCv1 readout

chip. A summary of these devices and their main geometric characteristics—including column diameter, gap beneath the  $n^+$  column, and pixel size—is provided in Table 3.6. Additional details about the sensors and the ROC can be found in Section 3.1.

Table 3.7 provides an overview of the test beam facilities used before and after irradiation, the irradiation site, and the particle fluence received by each module. In line with the planned replacement of the innermost TBPX layer for the second half of the HL-LHC operation period, two fluence scenarios are evaluated:  $1 \times 10^{16} \text{ n}_{\text{eq}}\text{cm}^{-2}$  and  $1.6 \times 10^{16} \text{ n}_{\text{eq}}\text{cm}^{-2}$ .

**Table 3.6:** Summary of single-chip 3D pixel modules tested in beam for the Phase-2 CMS tracker upgrade, including key geometric characteristics.

Module name	Readout chip	Sensor	Column diameter [ $\mu\text{m}$ ]	Column gap [ $\mu\text{m}$ ]	Pixel size [ $\mu\text{m}^2$ ]
CROC_CNM_1	CROCv1	CNM	8	20	$50 \times 50$
CROC_CNM_2	CROCv1	CNM	8	20	$25 \times 100$
CROC_FBK_1	CROCv1	FBK	5	35	$25 \times 100$
CROC_FBK_2	CROCv1	FBK	5	35	$25 \times 100$
CROC_FBK_3	CROCv1	FBK	5	35	$25 \times 100$
CROC_FBK_4	CROCv1	FBK	5	35	$25 \times 100$

**Table 3.7:** Overview of beam tests for the single-chip 3D pixel modules before and after irradiation, including irradiation facilities and equivalent 1 MeV neutron fluences.

Module name	Test beam facility before irradiation	Irradiation facility	Fluence [ $\text{n}_{\text{eq}}\text{cm}^{-2}$ ]	Test beam facility after irradiation
CROC_CNM_1	SPS	-	-	-
CROC_CNM_2	SPS	CERN PS	$1 \times 10^{16}$	SPS
CROC_FBK_1	SPS	-	-	-
CROC_FBK_2	SPS	CERN PS	$1 \times 10^{16}$	SPS
CROC_FBK_3	SPS	CERN PS	$1 \times 10^{16}$	SPS
CROC_FBK_4	-	KIT	$1.6 \times 10^{16}$	DESY

It is important to note that, prior to the test beam and irradiation campaigns, all modules underwent electrical characterization. As discussed in Section 2.1.7, the two primary measurements used for this purpose are the current-voltage (IV) and



capacitance-voltage (CV) characteristics. These measurements were essential to verify compliance with the electrical performance requirements listed in Table 3.1. They provide insight into key parameters such as power consumption and the operational voltage range, which is defined by the full depletion and breakdown voltages.

### 3.3.1. Data analysis procedure

The results presented in this thesis are based on test beam data analyzed using the Corryvreckan reconstruction framework [113, 114, 115]. Corryvreckan is a flexible, modular software written in C++. Each stage of the reconstruction chain is implemented as an independent module that can be dynamically loaded at runtime. The framework is designed to meet the requirements of offline event reconstruction in environments with heterogeneous detector readout architectures.

Corryvreckan employs a two-layer configuration system that enables customization of the analysis procedure. The main configuration file defines the structure of the reconstruction chain along with relevant global and module-specific parameters. The geometry configuration file describes the experimental setup, including the position and orientation of all detectors, as well as properties essential for the reconstruction, such as pixel pitch and matrix size.

The first stage of the reconstruction chain is event building, which involves decoding and processing the detector data stored by the DAQ system. Corryvreckan uses the dedicated converter plugins provided by EUDAQ2 to transform the data into structured pixel hit information, including the pixel charge and position. The complete data analysis workflow for DUT performance evaluation comprises multiple stages beyond event building. A schematic overview of the main steps is shown in Figure 3.15, with detailed explanations provided below.

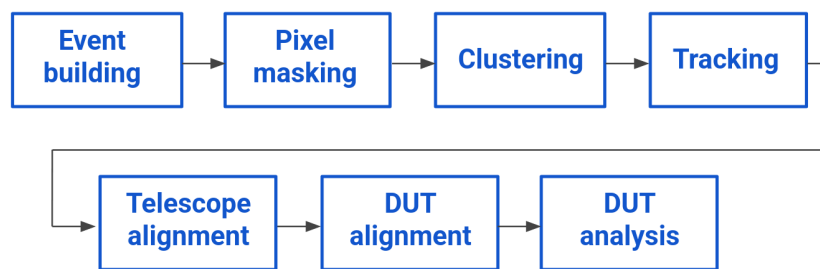


**Figure 3.15:** Block diagram of the data reconstruction and analysis chain.

To ensure a consistent and portable analysis environment, a docker image was developed as part of this work for Corryvreckan, incorporating custom code implementations necessary for the analysis.

## Pixel Masking

Masking noisy pixels is essential to prevent spurious hits that could bias the analysis and affect the DUT performance evaluation. Pixels can be masked offline either by providing a predefined mask file in the configuration or by using one of the masking algorithms available in Corryvreckan.

For the telescope planes, an algorithm based on the pixel firing frequency is used to mask noisy pixels. It estimates the local average hit rate and identifies outliers that are a certain number of standard deviations away from this estimate.

For the DUTs and the timing-reference plane, noisy and stuck pixels were masked during the tuning procedure with the criteria described in Section 3.1.3. Additional masking was applied only to pixels that did not register any hits, likely because they were located outside the trigger acceptance region.

## Clustering

The hit clustering algorithm identifies groups of neighboring pixels that fired within the same event, using only spatial information to associate them. These groups, referred to as clusters, represent localized energy deposits—typically caused by a single particle traversing the detector—and are treated as single entities in subsequent steps of the reconstruction and analysis chain. The method used to determine the cluster position differs between the telescope planes and the DUTs.

Since the telescope planes feature a binary readout, no charge information is available. Therefore, the cluster position is determined using a simple arithmetic mean of the pixel coordinates:

$$x_{\text{hit}} = \frac{\sum_{i=1}^N x_i}{N} \quad \text{and} \quad y_{\text{hit}} = \frac{\sum_{i=1}^N y_i}{N} \quad (3.6)$$

where  $(x_{\text{hit}}, y_{\text{hit}})$  denote the coordinates of the cluster center,  $(x_i, y_i)$  are the coordinates of the individual pixel centers, and  $N$  is the total number of pixels in the cluster.

In contrast, for the DUTs, a charge-weighted center-of-gravity (CoG) algorithm is used to determine the cluster position:

$$x_{\text{hit}} = \frac{\sum_{i=1}^N Q_i x_i}{\sum_{i=1}^N Q_i} \quad \text{and} \quad y_{\text{hit}} = \frac{\sum_{i=1}^N Q_i y_i}{\sum_{i=1}^N Q_i} \quad (3.7)$$

where  $Q_i$  is the charge measured in each pixel of the cluster. This method provides a more accurate estimate of the particle impact position and significantly improves the spatial resolution.<sup>2</sup>

---

<sup>2</sup>Alternative methods for estimating the particle impact position—such as  $\eta$ -algorithm [116] or template-based reconstruction [117]—can offer higher precision but are more computationally demanding. Given their limited improvement in this work, they were not employed.

### Track reconstruction

From the collection of clusters across the telescope planes, particle trajectories can be reconstructed, and their impact points on the DUT extrapolated. These reconstructed trajectories are referred to as tracks, and their reconstruction involves two main steps: track finding and track fitting.

Track finding begins by connecting all combinations of clusters in the first and last telescope planes with straight lines, forming initial track candidates. Clusters in the intermediate telescope planes are subsequently added to a track if they lie within a specific spatial region centered around the projected track intercept. This region is elliptical in shape, with configurable semi-major and semi-minor axes that determine the acceptance window for cluster association. As clusters are added, the track candidate is iteratively updated to refine its trajectory. Only candidates that include a cluster on every telescope plane are retained for track fitting.

Track fitting is performed using one of two models, depending on the test beam facility where the data were acquired. For SPS test beam data, where multiple scattering is negligible, a simple straight-line fit is applied. This model assumes a constant particle direction throughout the telescope. The quality of the fit is evaluated using the  $\chi^2$  statistic, which compares the predicted track intercepts on each plane— $(x_{\text{track}}, y_{\text{track}})$ —with the measured cluster positions— $(x_{\text{hit}}, y_{\text{hit}})$ . It is defined as:

$$\chi^2 = \sum_{i=1}^N \left( \frac{(\Delta x_i)^2}{\sigma_x^2} + \frac{(\Delta y_i)^2}{\sigma_y^2} \right) \quad (3.8)$$

where  $\Delta x = x_{\text{track}} - x_{\text{hit}}$  and  $\Delta y = y_{\text{track}} - y_{\text{hit}}$  are the residuals in the  $x$  and  $y$  coordinates, respectively. The parameters  $\sigma_x$  and  $\sigma_y$  denote the spatial uncertainties of the cluster position in each coordinate, given by the digital spatial resolution.  $N$  is the number of clusters, which matches the number of telescope planes used in the fit.

In contrast, particles in the DESY test beam are more subject to multiple scattering due to the beam properties. Thus, a different treatment of the data is required during the analysis. The General Broken Line (GBL) model accounts for the stochastic deflections of the particle as it traverses different materials. While the mean deflection is zero, the variance of the angular deviations depends on the traversed material and the particle energy. The GBL algorithm includes uncertainties from both position measurement and multiple scattering simultaneously and reconstructs the trajectory as a sequence of linear segments with kinks at the telescope planes. A detailed description of the GBL formalism and the expression for  $\chi^2$  in this case can be found in [118, 119].

Figure 3.16 illustrates the passage of a particle through a detector, resulting in a cluster composed of two neighboring pixels. The estimated cluster position and the projected track intercept are indicated. The residuals in the  $x$  and  $y$  directions are also shown.

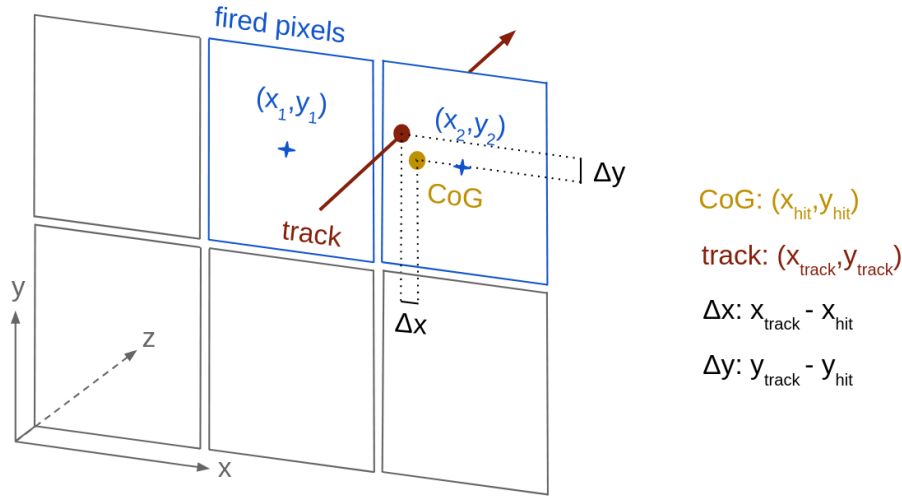


**Figure 3.16:** Schematic representation of a cluster consisting of two adjacent pixels. These pixels are indicated in blue, with crosses marking their geometrical centers, which serve as their individual reference positions. The cluster position, estimated using a charge-weighted center-of-gravity (CoG) algorithm, is shown in yellow. The intercept of the reconstructed track and the residuals are indicated in red and black, respectively.

### Telescope alignment

Alignment of the telescope planes is fundamental to accurately determine their positions and orientations relative to one designated as the alignment-reference plane. While the position of the planes along the beam line ( $z$  coordinate) must be measured manually during the test beam and provided to the analysis through the configuration files, the positions in the  $x$  and  $y$  coordinates cannot be precisely measured by hand. Even small shifts or rotations can cause significant errors in track reconstruction, directly affecting the evaluation of the DUT performance. Therefore, without proper alignment, the entire analysis can be compromised.

A successful alignment should result in residual distributions that are well centered around zero and as narrow as possible. The width of these distributions depends on the tracking telescope resolution and is influenced by factors such as beam energy, material budget, and spacing between the detector planes. Additionally, the distribution of  $\chi^2$  per degree of freedom from the track fits should peak near one, indicating a good match between track predictions and cluster position measurements.

In the first step, a prealignment of the telescope planes is performed by calculating correlations between each detector and the alignment-reference plane. These correlations are obtained by comparing the cluster positions in each detector with those in the

reference plane. The relative shifts are estimated from the position of the maximum in the one-dimensional correlation distributions, and corresponding corrections are applied to each plane in the  $x$  and  $y$  directions. With this initial prealignment and relatively loose cluster-track association criteria, track reconstruction becomes feasible. Approximately 50 000 events are sufficient to achieve a successful prealignment.

The reconstructed tracks are used in the second alignment step for both translational and rotational corrections in each plane relative to the alignment-reference detector. Multiple iterations are usually required until the residuals are well centered and narrow. Around 80 000 tracks per iteration are generally adequate. During each iteration, the alignment algorithm adjusts the position of each telescope plane (excluding the reference detector), refits all tracks individually, and minimizes the sum of the resulting  $\chi^2$  values using Minuit2 [120]. To improve stability and convergence, the first iteration is often performed allowing only translational shifts, with rotational corrections introduced in subsequent iterations. The acceptance window for cluster-track association is gradually reduced at each iteration—down to the pixel pitch—as the alignment improves and the tracks get closer to the clusters. Similarly, the cut on the maximum track  $\chi^2$  becomes more stringent at each iteration. This approach allows to retain only high-quality tracks for the alignment.

A final step to further refine the alignment uses the Millepede-II algorithm [121], which performs a global minimization of all the alignment parameters simultaneously using all telescope planes and fitting all available tracks. The algorithm iteratively updates the alignment parameters and stops when the convergence criterion, defined as the absolute sum of all residuals divided by the total number of free parameters, falls below  $10^{-5}$ .

The residual distributions in both  $x$  and  $y$  coordinates for one of the MIMOSA26 telescope planes after the final alignment are shown in Figures 3.17a and 3.17b, respectively. These distributions, combined with the track  $\chi^2$  per degree of freedom distribution shown in Figure 3.17c, confirm the quality of the telescope alignment.

### DUT alignment

Alignment of the DUT is also essential to accurately determine its position and orientation for a precise data analysis. The alignment strategy follows a similar approach to that used for the telescope and also involves several iterations.

In the first step, the DUT is prealigned using the correlation distributions relative to the alignment-reference plane, as described above for the telescope. For the alignment step, around 300 000 tracks are typically reconstructed using the same tight selection criteria applied in the final iteration of the telescope alignment. However, slightly looser criteria may also be used once the telescope is well aligned in order to increase

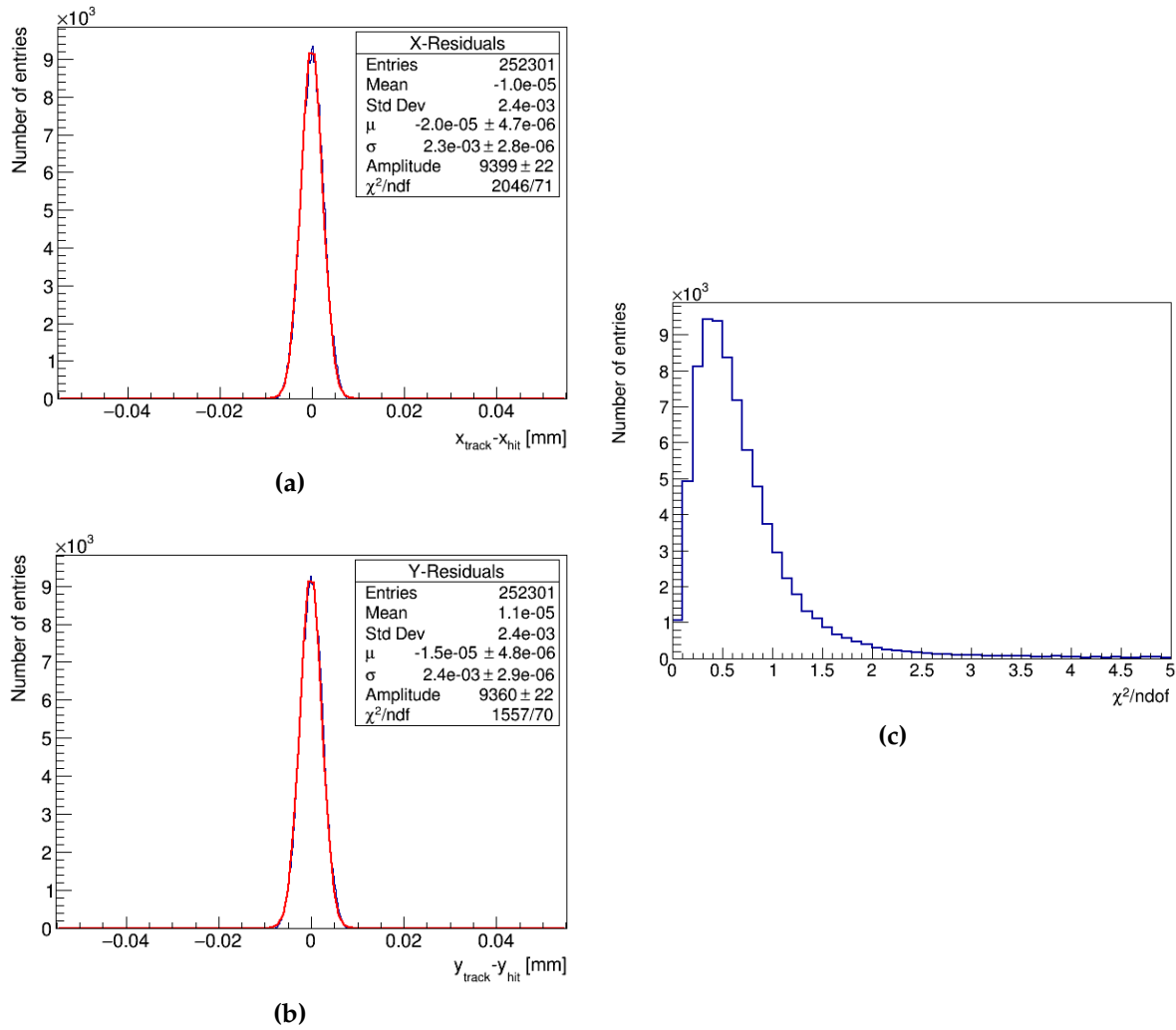


**Figure 3.17:** Distribution of residuals in the (a)  $x$  and (b)  $y$  coordinates for one of the MIMOSA26 telescope planes after the final alignment. They are fitted to Gaussian functions, with mean  $\mu$  and standard deviation  $\sigma$ . (c) Distribution of track  $\chi^2$  over the degrees of freedom. The data corresponding to these distributions were recorded using a 120 GeV pion beam at the CERN SPS.

statistics if the dataset is limited. As an additional selection, only tracks with a  $\chi^2$  per degree of freedom below 10 are used for the DUT alignment.

In the second step, the algorithm performs translational and rotational corrections of the DUT relative to the alignment-reference plane. In each iteration, the DUT position is adjusted to minimize the residuals between the cluster positions and the projected track intercepts on the DUT. The acceptance window for cluster-track association is defined in the same way as for the telescope planes and is progressively reduced—down to the pixel pitch—at each iteration as the alignment improves. This alignment procedure is applied individually to each DUT in the system, including the timing-reference plane.

Figure 3.18 shows the one-dimensional residual distributions along the  $x$  and  $y$  coordinates for two DUTs: one with a pixel size of  $25 \times 100 \mu\text{m}^2$  and another with  $50 \times 50 \mu\text{m}^2$ .

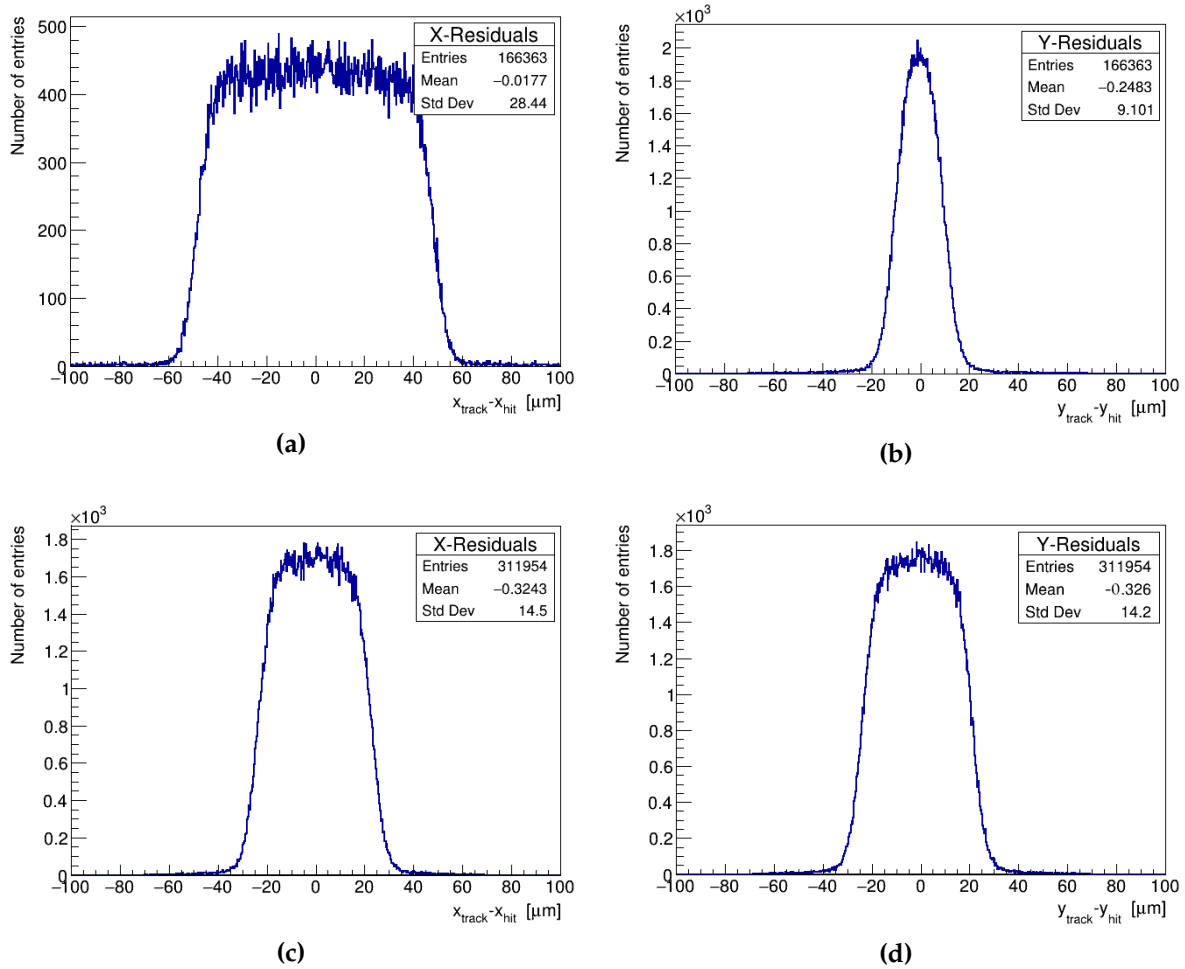


**Figure 3.18:** Distribution of residuals along both coordinates for two fully depleted, non-irradiated DUTs after the final alignment. (a) and (b) show the residuals in the  $x$  and  $y$  directions, respectively, for the DUT with  $25 \times 100 \mu\text{m}^2$  pixel size. (c) and (d) show the corresponding residuals for the DUT with  $50 \times 50 \mu\text{m}^2$  pixel size. These residuals correspond to measurements at normal beam incidence.

### DUT performance analysis

After completing the alignment of all detectors in the setup, the performance of the DUT can be evaluated. All events in the dataset are used for this analysis, with the only requirement imposed on the bunch crossing identifier of the timing-reference plane. Since the latency between a hit and its readout is expected to remain constant, valid events should fall within a single bunch crossing. To exclude out-of-time or



spurious hits that may populate other bunch crossings, a selection is applied based on the bunch crossing distribution of the timing-reference plane. Figure 3.19a shows an example of a typical distribution, with the selected region indicated. Only events within  $\pm 1$  bunch crossing around the peak are used in the analysis.

The acceptance region for cluster-track association in the final track reconstruction is defined by an ellipse with semi-axes equal to three times the digital spatial resolution of the telescope planes. Only tracks with a  $\chi^2$  per degree of freedom below 5 are considered for the computation of the observables that quantify the DUT performance. In addition, track isolation is required on the timing-reference module to suppress cases where closely spaced tracks could interfere with the reconstruction of each other. This is particularly important in test beam conditions where the track multiplicity per event often exceeds one. Figure 3.19b shows a typical distribution of distances between track intercepts on the timing-reference plane. The isolation cut is applied at the inflection point of the distribution, typically in the range from 30  $\mu\text{m}$  to 40  $\mu\text{m}$ .

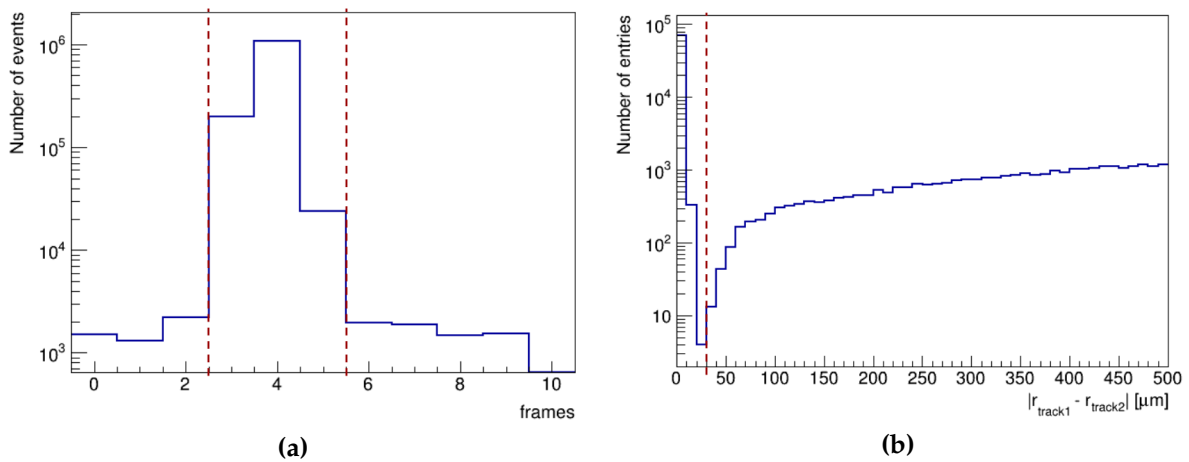


**Figure 3.19:** (a) Bunch crossing distribution and (b) distribution of distances between track intercepts on the timing-reference plane. The selected region in (a) is delimited by vertical dashed lines, while in (b), the dashed line indicates the lower edge of the accepted region.

For cluster-track association on the DUT and the timing-reference plane, a more relaxed acceptance region is used: an ellipse with semi-axes equal to five times the digital spatial resolution of the respective detector in each direction. Following this association, the DUT performance can be evaluated. The precise definitions and calculation methods for the main observables are provided in Section 3.3.2.

### 3.3.2. Definition of observables

The main observables used to quantify the DUT performance in this thesis are hit detection efficiency, cluster charge, cluster size, and spatial resolution. These are studied both at normal beam incidence and under rotated configurations. The rotation of the DUT refers to a rotation around an axis that is parallel to the long edge of the pixel, provided the pixel cell is rectangular, and perpendicular to the beam, as illustrated in Figure 3.20. Normal beam incidence corresponds to a  $0^\circ$  rotation angle.

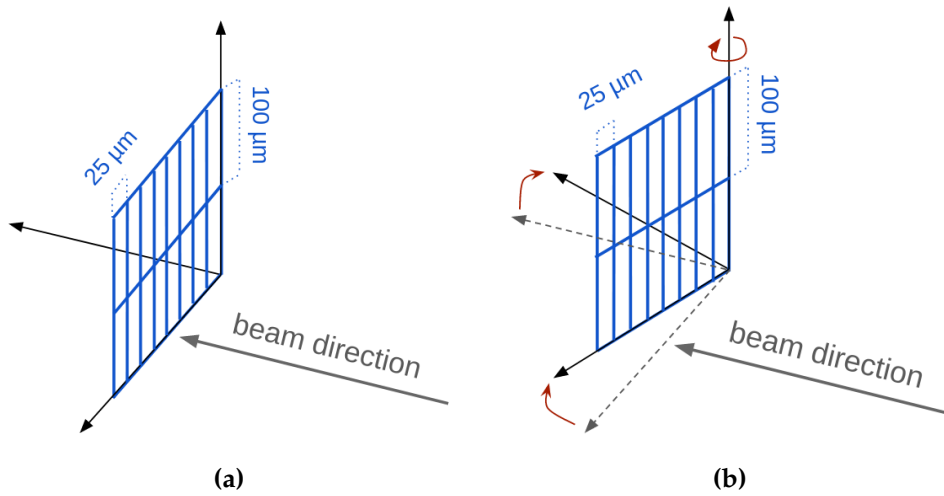


**Figure 3.20:** Schematic representation of a DUT with a sensor pixel size of  $25 \times 100 \mu\text{m}^2$ , tested (a) at normal beam incidence and (b) under a rotation angle around an axis parallel to the long edge of the pixel and perpendicular to the beam line.

The primary measurements are performed as a function of bias voltage, rotation angle, and average pixel threshold. When observables are plotted within the pixel cell, the map represents the average value across all pixel cells in the matrix that registered a hit—not the response of an individual pixel. In the following, single-pixel cell maps are shown to illustrate the main features of the detector response. For additional insight, selected observables are also visualized across a  $2 \times 2$  pixel grid in Appendix 6. In rectangular pixel cells, the coordinate axes are defined as follows: the  $x$ -direction corresponds to the  $100 \mu\text{m}$  pitch, and the  $y$ -direction corresponds to the  $25 \mu\text{m}$  pitch.

#### Hit detection efficiency

To calculate the hit detection efficiency, additional selection criteria are applied to the final set of reconstructed tracks. First, each track must be associated with a cluster on the timing-reference plane to reject out-of-time tracks, which arise from the long integration time of the telescope planes, as discussed in Section 3.2.2.

In addition, the projected track intercept on the DUT must lie at least one pixel away

from any masked pixel. This requirement excludes tracks near masked regions, where partial charge loss can degrade cluster reconstruction and hinder correct cluster-track association, artificially lowering the measured efficiency. Tracks that meet both of these conditions are referred to as in-time tracks in the following.

The hit detection efficiency quantifies the probability that a particle passing through the active area of the module produces a detectable hit. It serves as a measure of the DUT performance in detecting incident particles. The efficiency,  $\epsilon$ , and its statistical uncertainty,  $\sigma_\epsilon$ , are defined as:

$$\epsilon = \frac{N_{\text{in-time tracks}}^{\text{hit}}}{N_{\text{in-time tracks}}} \quad \text{and} \quad \sigma_\epsilon = \left[ \frac{(1 - \epsilon) \epsilon}{N_{\text{in-time tracks}}} \right]^{1/2} \quad (3.9)$$

where  $N_{\text{in-time tracks}}$  is the total number of in-time tracks, and  $N_{\text{in-time tracks}}^{\text{hit}}$  is the number of those tracks that are associated with a cluster on the DUT.

To account for the presence of masked pixels, the measured hit detection efficiency can be multiplied by an acceptance factor,  $\alpha$ , defined as:

$$\alpha = 1 - \frac{N_{\text{masked}}}{N_{\text{total}}} \quad (3.10)$$

where  $N_{\text{masked}}$  is the number of masked pixels, and  $N_{\text{total}}$  is the total number of pixels in the detector matrix.

### Cluster charge and size

The clusters on the DUT, whose positions are estimated using equation 3.7, are characterized by two important observables: cluster charge and cluster size. The cluster size refers to the number of pixels that make up the cluster, while the cluster charge corresponds to the sum of the charge collected by the individual pixels. These observables are sensitive to sensor characteristics such as the depletion depth and charge sharing among adjacent pixels. For this reason, they are commonly used to assess the DUT response under varying conditions.

The one-dimensional distribution of the cluster charge is best described by a Landau distribution convoluted with a Gaussian. The Landau component models the stochastic ionization energy loss of charged particles traversing the sensor, which is affected by fluctuations in both the number of interactions with orbital electrons and the energy transferred in each interaction, as discussed in Section 2.2.1. The Gaussian component should account for electronic noise and pixel-to-pixel gain variations. The most probable value (MPV) extracted from the Landau-Gaussian fit is used as an estimator of the typical collected charge in the DUT, as it is less sensitive to the high-energy tail of the distribution.

### Hit spatial resolution

The spatial resolution of a detector quantifies its precision in determining the position of a single particle. It depends on both the granularity of the sensor and the method used to reconstruct the cluster position. When particles deposit charge in only one pixel or when charge sharing with a neighboring pixel is not enough to surpass its pixel threshold, the position of the single-pixel cluster is estimated to lie at the center of the pixel cell, which is defined as  $(x_{\text{hit}}, y_{\text{hit}}) = (0, 0)$  in the following. Under these conditions and assuming a uniform distribution of track intercepts across the pixel cell, the so-called digital spatial resolution is defined as the standard deviation of the residuals and its expression becomes:

$$\sigma_{\text{digital}}^2 = \frac{\int_{-p/2}^{p/2} (x_{\text{track}} - x_{\text{hit}})^2 D(x_{\text{track}}) dx_{\text{track}}}{\int_{-p/2}^{p/2} D(x_{\text{track}}) dx_{\text{track}}} \Rightarrow \sigma_{\text{digital}} = \frac{p}{\sqrt{12}} \quad (3.11)$$

where  $p$  is the pixel pitch and  $D(x_{\text{track}}) = 1$  represents a uniform distribution of track intercepts within the pixel cell.

However, in practice, charge sharing between adjacent pixels—caused by either diffusion or inclined particle incidence—frequently results in multi-pixel clusters. This enables a more accurate reconstruction of the cluster position using the charge-weighted CoG method with the analog charge information of individual pixels. This approach typically leads to smaller residuals, improving the spatial resolution beyond the digital limit.

During beam tests, the residuals measured at the DUT are influenced by the resolution of the telescope used to reconstruct the tracks. To extract the intrinsic DUT spatial resolution, the telescope resolution must be accurately known. Assuming uncorrelated Gaussian errors, the standard deviation of the residual distribution is the sum in quadrature of the DUT and telescope contributions, leading to the following expression:

$$\sigma_{\text{DUT}} = \left[ \sigma_{\text{residuals}}^2 - \sigma_{\text{telescope}}^2 \right]^{1/2} \quad (3.12)$$

where  $\sigma_{\text{residuals}}$  is the standard deviation of the residual distribution. The telescope and DUT spatial resolutions are denoted by  $\sigma_{\text{telescope}}$  and  $\sigma_{\text{DUT}}$ , respectively. The telescope resolution at the DUT position depends on several factors, including the particle beam energy, the number and configuration of the telescope planes, and the relative position of the DUT within the setup. Consequently, the telescope resolution must be evaluated separately for each DUT and each test beam facility, as the configuration and alignment may vary from one setup to another.

In this thesis, the spatial resolution is studied for DUTs with a  $25 \times 100 \mu\text{m}^2$  pixel size, with particular focus on the coordinate corresponding to the short pixel pitch. To

estimate the telescope resolution, a data-driven method was developed. This approach requires precise DUT alignment and assumes no rotation around the axis parallel to the short pixel edge and perpendicular to the beam direction.

As discussed above, the residuals are influenced by both charge sharing and telescope resolution, but the impact of each depends on the pixel pitch. To isolate these effects and understand the underlying concept behind the data-driven method, a toy Monte-Carlo simulation was performed. Figures 3.21a and 3.21b show the DUT residual distributions along the long and short pixel pitches, assuming no charge sharing and perfect telescope resolution (using Monte Carlo truth). The standard deviations of these distributions represent the digital spatial resolution in each direction.

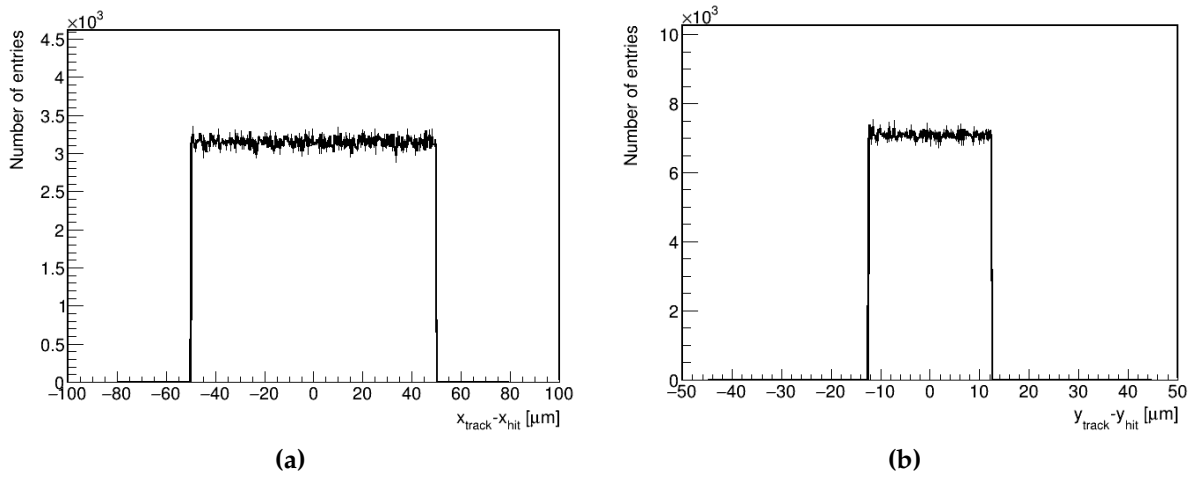


**Figure 3.21:** Residual distributions from a toy Monte Carlo simulation for a module with  $25 \times 100 \mu\text{m}^2$  pixel size at normal beam incidence: (a) along the long pixel pitch and (b) along the short pixel pitch. The simulation assumes no charge sharing and perfect telescope resolution..

The influence of charge sharing is studied by modeling a region near the pixel boundaries where charge is assumed to spread into adjacent pixels. Specifically, all particles crossing the pixel cell within a certain distance from the edge are treated as producing multi-pixel clusters. In this simplified scenario, the cluster position is approximated by the particle intercept with an added Gaussian smearing, which reflects the improved but still finite precision of the charge-weighted CoG method. Figures 3.22a and 3.22b show the resulting residual distributions along the long and short pixel pitches, respectively, for two different assumptions about the size of the charge-sharing region. As expected, charge sharing leads to smaller residuals, which accumulate around zero, and improves the spatial resolution relative to the digital limit. Nevertheless, it is important to note that this simulation is an idealized representation, since not all particles near the edge necessarily produce multi-pixel clusters. Moreover, the

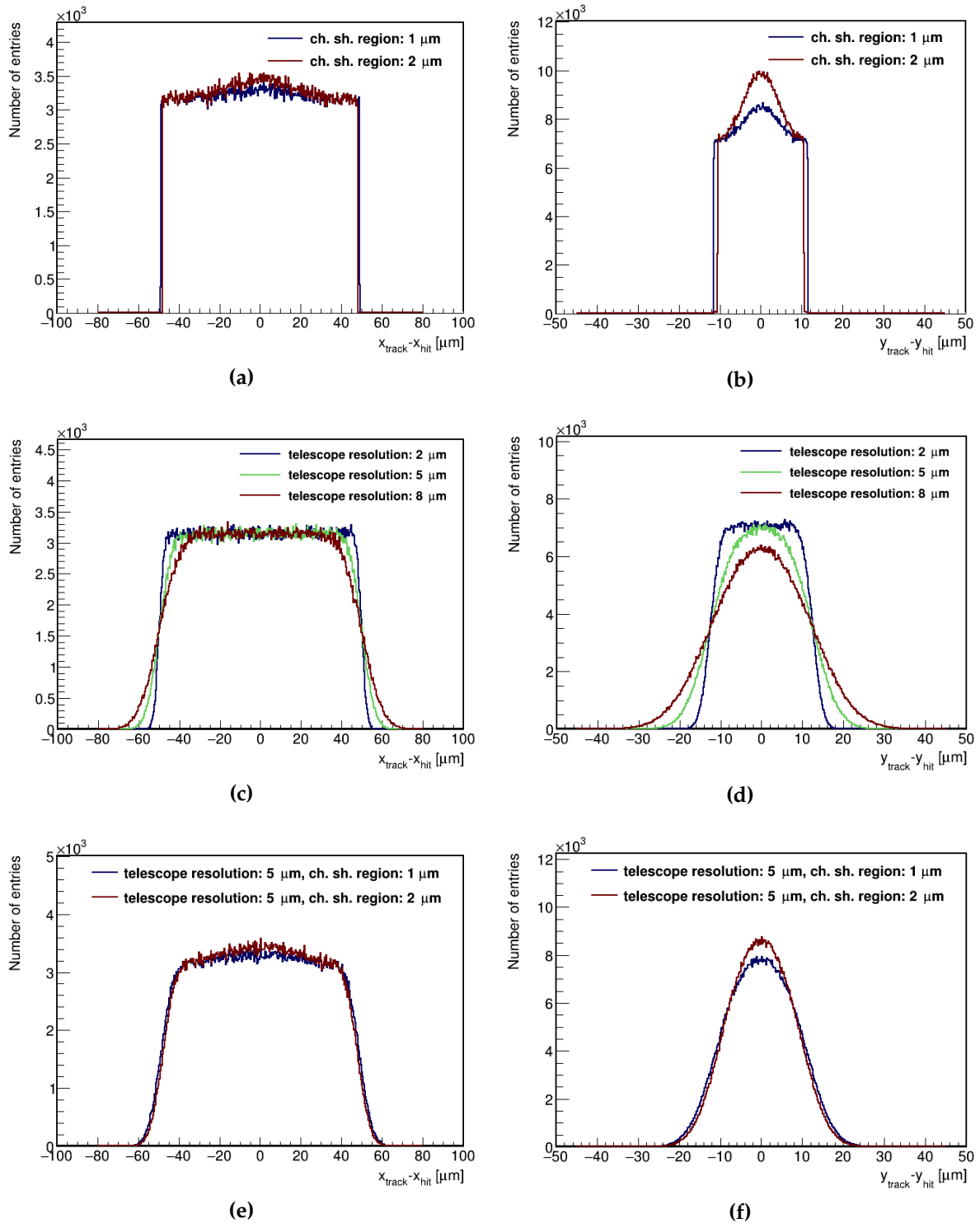
applied smearing serves as a rough approximation, since a precise understanding of how charge sharing improves the residuals would require detailed modeling of charge transport and detector response.

The impact of finite telescope resolution is evaluated by applying a Gaussian smearing to the true particle intercept. This mimics the uncertainty introduced by imperfect track reconstruction. Figures 3.22c and 3.22d show the resulting residual distributions for the long and short pixel pitches, with different assumptions for the telescope resolution. The previously sharp distribution edges, characteristic of the digital case and modeled by a step function, become smoothed and broadened. The resulting edge profile can be modeled by a Gaussian CDF, with the telescope resolution as standard deviation. For a given telescope resolution, the residual distribution along the short pixel pitch is more significantly altered, while in the long-pitch direction, the core of the distribution remains largely unchanged and still resembles the digital case.

When both charge sharing and telescope resolution are included, the residual distributions reflect a combination of these effects, as illustrated in Figures 3.22e and 3.22f for the long and short pixel pitches, respectively. Along the 100  $\mu\text{m}$  pitch, the effects of charge sharing and telescope resolution are disentangled due to limited charge sharing across the short pixel boundary. This separation, which is not observed in the residuals along the 25  $\mu\text{m}$  pitch, enables the estimation of the telescope resolution by fitting the edge of the distribution with a Gaussian CDF. The full residual distribution is modeled using the difference of two Gaussian CDFs, expressed as:

$$\begin{aligned}
 f(\Delta x) &= \Phi\left(\frac{\Delta x + \mu}{\sigma_{\text{telescope}}}\right) - \Phi\left(\frac{\Delta x - \mu}{\sigma_{\text{telescope}}}\right) = \\
 &= \frac{1}{2} \left[ 1 + \operatorname{erf}\left(\frac{\Delta x + \mu}{\sigma_{\text{telescope}} \sqrt{2}}\right) \right] - \frac{1}{2} \left[ 1 + \operatorname{erf}\left(\frac{\Delta x - \mu}{\sigma_{\text{telescope}} \sqrt{2}}\right) \right] \quad (3.13)
 \end{aligned}$$

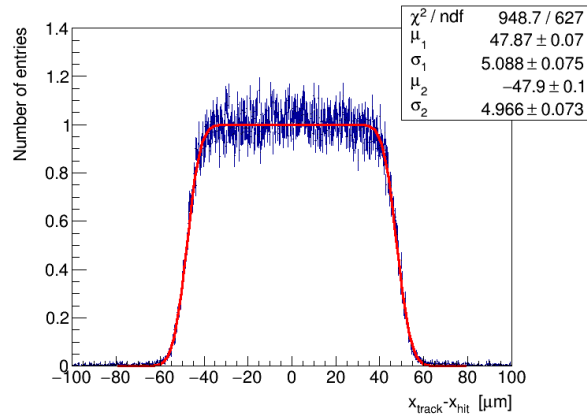
where  $\Delta x$  denotes the residuals,  $\mu = p/2$  is the mean of the Gaussian, corresponding to half the pixel pitch, and  $\sigma_{\text{telescope}}$  is the standard deviation, representing the telescope resolution at the DUT position. When the DUT is rotated, with the definition given in Figure 3.20, the extracted telescope resolution must be projected onto the DUT plane along the short-pitch direction. This is achieved by dividing the resolution by the cosine of the rotation angle.



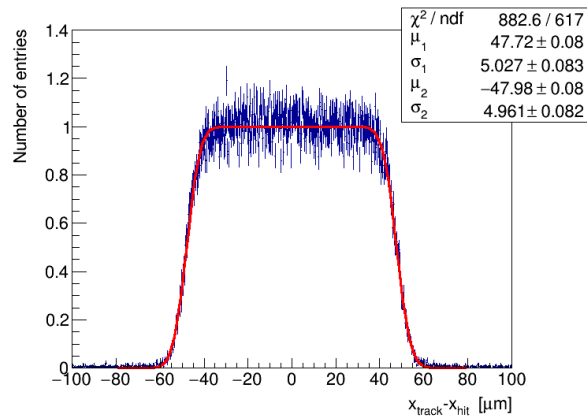
**Figure 3.22:** Residual distributions from a toy Monte Carlo simulation for a module with  $25 \times 100 \mu\text{m}^2$  pixel size at normal beam incidence, illustrating the individual effects of charge sharing and telescope resolution, as well as their combination. The distributions along the long pixel pitch are shown in (a), (c) and (e), while the corresponding distributions along the short pixel pitch are shown in (b), (d) and (f).



Figure 3.23 shows the residual distributions along the long pixel pitch for a non-irradiated sensor biased at 50 V. The measurements were taken at normal incidence and with a rotation angle of  $10^\circ$ . As expected, both distributions appear very similar. This is because the rotation angle—defined in Figure 3.20—does not induce additional charge sharing across the short pixel boundary. Consequently, the residual distribution along the long-pitch direction remains largely unchanged.



(a)



(b)

**Figure 3.23:** Residual distributions along the long pixel pitch for a non-irradiated DUT with  $25 \times 100 \mu\text{m}^2$  pixel size: (a) at normal incidence and (b) rotated by  $10^\circ$ . In both cases, the sensor is biased at 50 V. The distributions are normalized to the mean number of entries in the central region and fitted with the difference of two Gaussian CDFs. The parameters  $\sigma_1$  and  $\sigma_2$  represent independent estimates of the telescope resolution ( $\sigma_{\text{telescope}}$ ).

To account for possible instability during data-taking—such as mechanical stress on the cables when the modules rotate, which could eventually move the DUTs—the dataset is divided into smaller subsets of events. For each subset, a residual distribution along the short pixel pitch is constructed. This approach mitigates potential biases in the extracted standard deviation due to small shifts in the DUT position. The standard deviation is calculated independently for each subset, and their average is taken as the representative residual width for the full dataset.

The residual distributions along the short pixel pitch exhibit non-Gaussian tails, mainly due to cluster-track misassociations. To reliably extract the width of the distribution core, two fitting models are used. The first is a sum of two Gaussian functions:

$$f(\Delta y) = N(\mu, \sigma_{\text{residuals}}^2) + N(\mu, \sigma_{\text{bg}}^2) \quad (3.14)$$

where  $N(\mu, \sigma_{\text{residuals}}^2)$  describes the core of the distribution and  $N(\mu, \sigma_{\text{bg}}^2)$  captures the broader tails. The second model combines a Gaussian and a constant term:

$$f(\Delta y) = N(\mu, \sigma_{\text{residuals}}^2) + c \quad (3.15)$$

where  $N(\mu, \sigma_{\text{residuals}}^2)$  describes the core of the distribution and the constant  $c$  accounts for a uniform background contribution. The final residual width used to compute the DUT spatial resolution is the average of the  $\sigma_{\text{residuals}}$  values extracted from both models, over all event subsets. The difference between the widths obtained from the two models is assigned as a systematic uncertainty to the measurement.

Figure 3.24 shows the residual distributions for the first subsets of events fitted with the Gaussian-plus-constant model at normal beam incidence and at  $10^\circ$  rotation, along with the standard deviations extracted from all subsets and their average. Figure 3.25 reports similar results using the double-Gaussian fitting model.

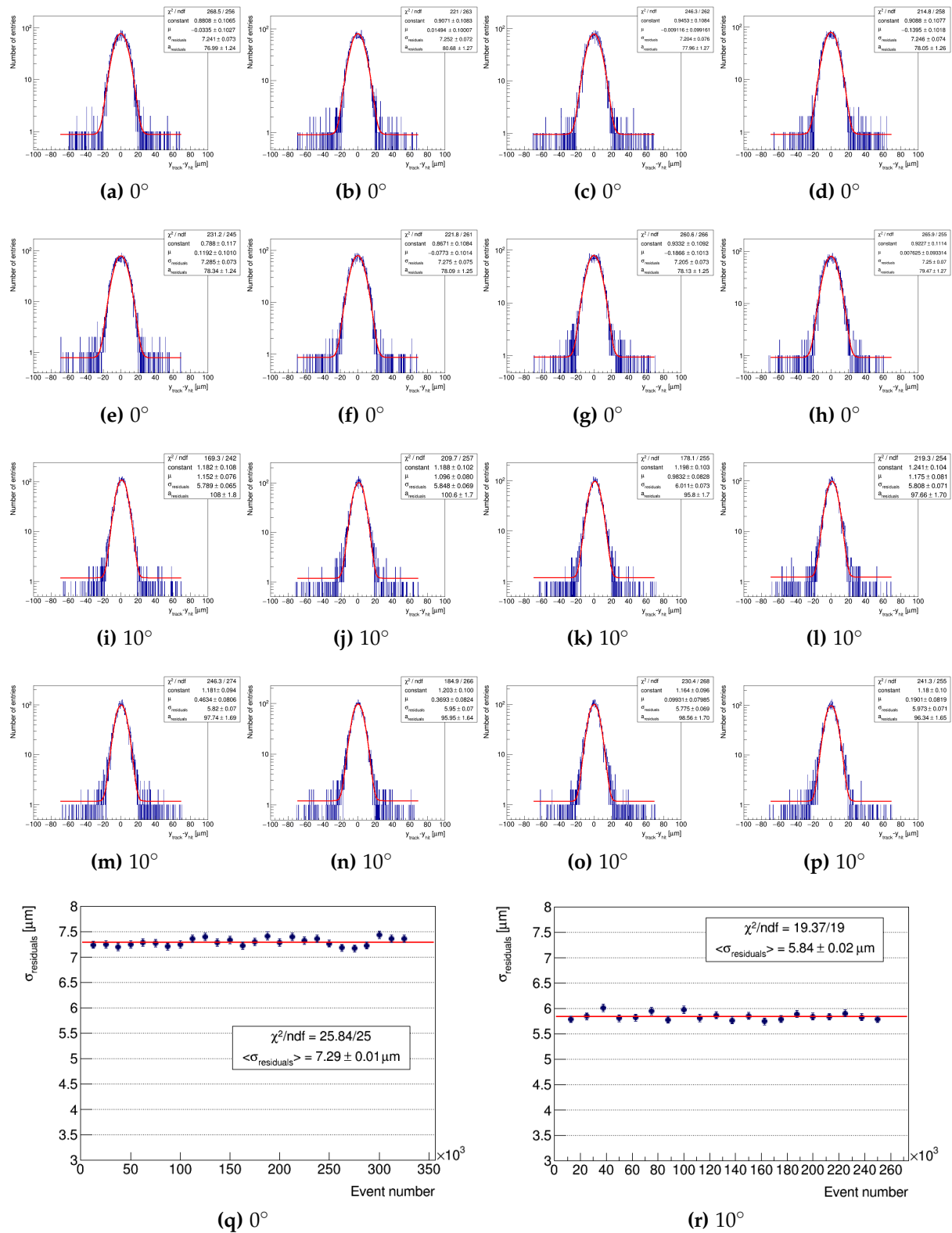


**Figure 3.24:** Residual distributions along the short pixel pitch for a non-irradiated DUT with  $25 \times 100 \mu\text{m}^2$  pixels, divided into event subsets and fitted with a Gaussian plus a constant term. Note the logarithmic scale on the  $y$ -axis. (a)-(h) and (i)-(p) show data at normal incidence and at a  $10^\circ$  rotation angle, respectively. The standard deviations from all subsets are shown in (q) and (p), with a red line indicating the average.

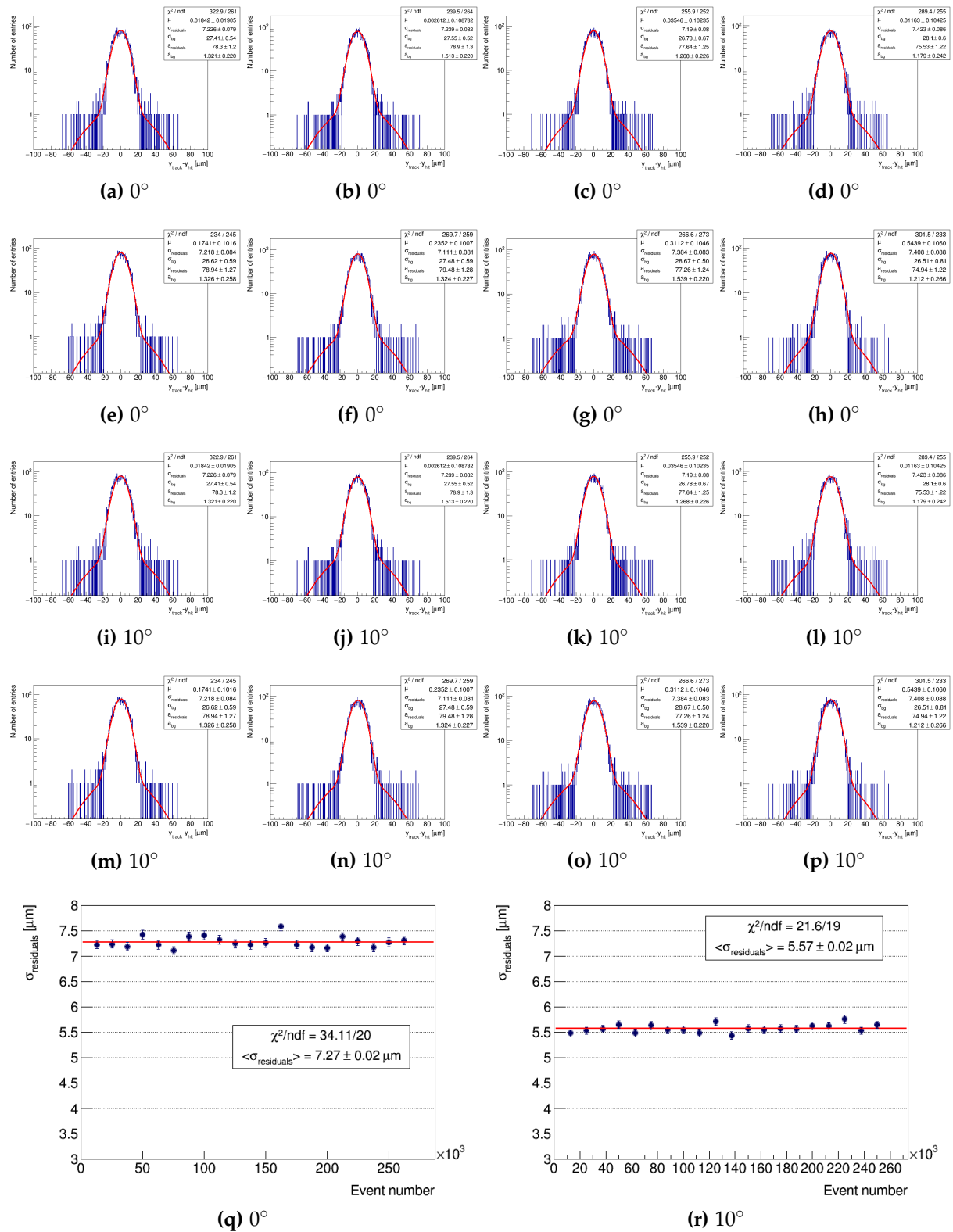


**Figure 3.25:** Residual distributions along the short pixel pitch for a non-irradiated DUT with  $25 \times 100 \mu\text{m}^2$  pixels, divided into event subsets and fitted with the sum of two Gaussian functions. The  $y$ -axis uses a logarithmic scale. (a)-(h) and (i)-(p) show data at normal incidence and at a  $10^\circ$  rotation angle, respectively. The standard deviations from all subsets are shown in (q) and (r), with a red line indicating the average.

### 3.3.3. Performance of non-irradiated devices

Several non-irradiated CROCv1 modules were characterized at the SPS test beam area, and their performance is presented below. Four modules feature 3D pixel sensors from either FBK or CNM with a pixel size of  $25 \times 100 \mu\text{m}^2$ . The nomenclature used to identify the modules indicates the sensor manufacturer. In addition, results from a CNM 3D pixel sensor with a  $50 \mu\text{m}$  pitch are provided for comparison. Table 3.6 provides more details on these devices, such as column diameter and  $n^+$  column gap.

The modules were tuned to an average pixel threshold ranging from 1000 to 1200 electrons and operated at a temperature of  $-10^\circ\text{C}$ . In all devices, the percentage of masked pixels—including both noisy and stuck pixels—is below 1%.

#### Hit detection efficiency

The hit detection efficiency was measured at normal incidence as a function of the bias voltage, up to a maximum of 80 V, with full depletion occurring below 10 V in all devices. As shown in Figure 3.26, the efficiency exceeds 97% once full depletion is reached. Although CMS defines efficiency requirements only for irradiated devices—96% at normal incidence and 97% at inclined incidence—the stricter 97% criterion is used consistently throughout this analysis to enable direct comparison across all measurements.

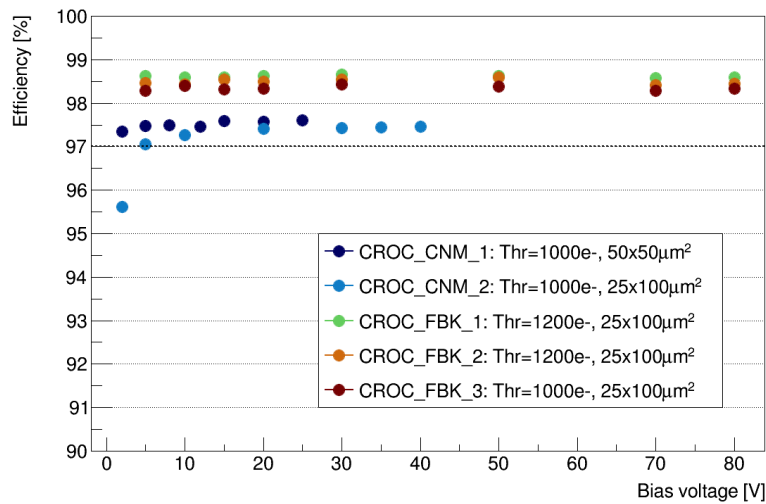


**Figure 3.26:** Hit detection efficiency at normal incidence as a function of bias voltage for several non-irradiated modules. There are three sensors from FBK and one from CNM with a pixel size of  $25 \times 100 \mu\text{m}^2$ , as well as one CNM sensor with a  $50 \mu\text{m}$  pitch. The horizontal dashed line indicates the 97% efficiency criterion.

Comparison between the CNM sensors with  $25 \times 100 \mu\text{m}^2$  and  $50 \times 50 \mu\text{m}^2$  pixels shows that both cell designs asymptotically achieve the same performance. The

discrepancy in efficiency between FBK and CNM modules arises from differences in the 3D pixel sensor design. The columnar electrodes, made of passive material, represent an inherent source of inefficiency. FBK sensors achieve higher efficiency than CNM sensors because their electrodes have a smaller diameter and, therefore, a smaller insensitive volume.

Efficiency cell maps for the CNM sample with a  $25 \times 100 \mu\text{m}^2$  pixel size are shown in Figures 3.27a-3.27c for three bias voltages: below full depletion (2 V), at the onset of the efficiency plateau (5 V), and well above full depletion (30 V). The variations in efficiency across the pixel cell arise from the progressive depletion of the active volume, which starts from the central  $n^+$  column and extends toward the  $p^+$  columns located at the pixel corners. The inefficiency associated with the columnar electrodes—clearly visible in these maps—is significantly reduced at the central electrode as the bias increases. This is because its shorter depth allows sufficient charge to be generated in the active material beneath the column.

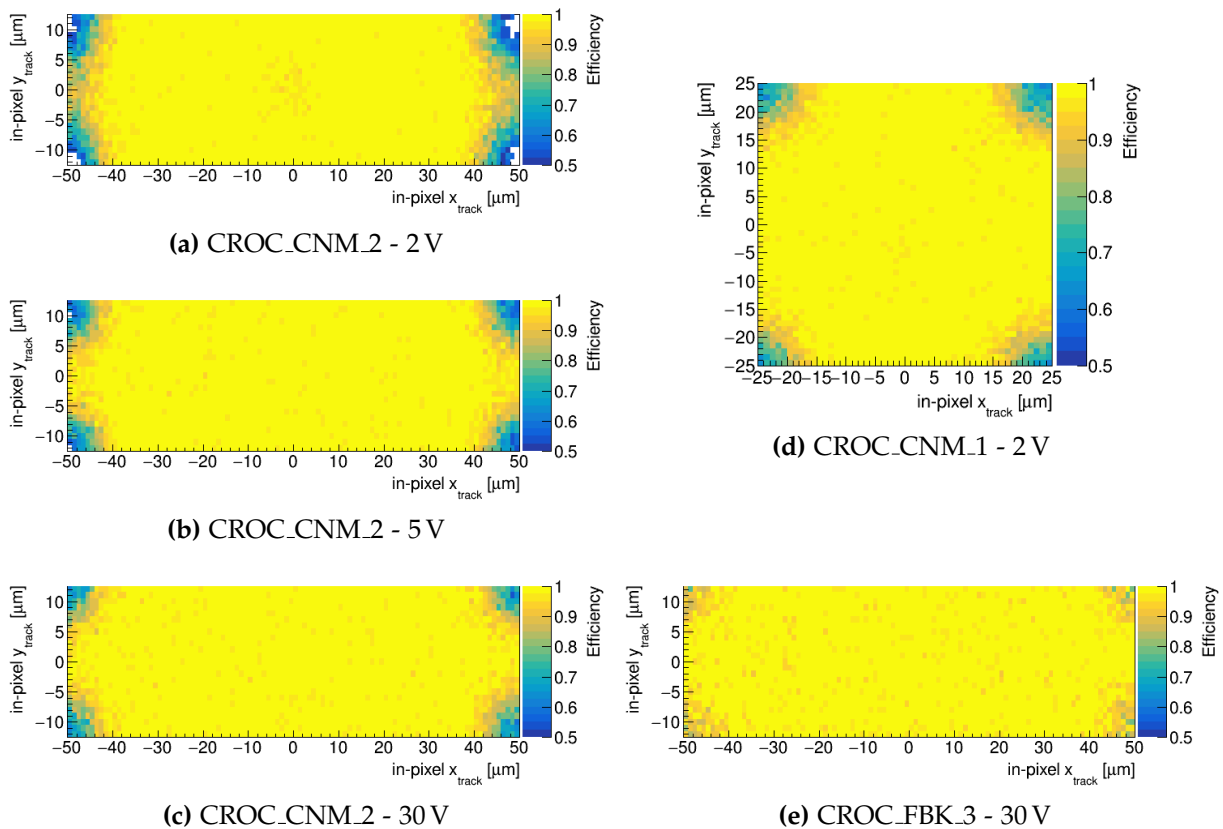


**Figure 3.27:** Hit detection efficiency cell maps at normal incidence for several non-irradiated modules: the CNM sensor with  $25 \times 100 \mu\text{m}^2$  pixel size biased at (a) 2 V, (b) 5 V and (c) 30 V; (d) the CNM sensor with  $50 \mu\text{m}$  pitch biased at 2 V; and (e) one of the FBK sensors biased at 30 V. White regions indicate an efficiency below 0.5.

For comparison, the efficiency cell maps for the CNM sample with a  $50\text{ }\mu\text{m}$  pitch biased at 2 V and the FBK sample biased at 30 V are shown in Figures 3.27d and 3.27e, respectively. To facilitate the evaluation across different bias voltages and sensor manufacturers, Figure 3.28 presents the efficiency profiles along the long edge of the rectangular pixel cells. These profiles highlight the improved efficiency near the pixel corners in the FBK sensor, attributed to the smaller radius of its columnar electrodes compared to those of the CNM sensor.

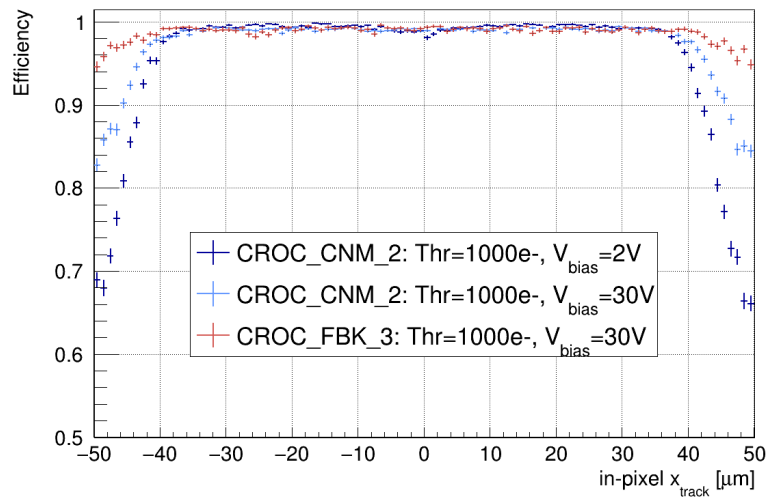


**Figure 3.28:** Hit detection efficiency profiles along the long edge of the  $25 \times 100\text{ }\mu\text{m}^2$  pixel cells for non-irradiated CNM and FBK modules at various bias voltages and normal incidence.

Detector simulations have shown that, for a track angular distribution similar to that in minimum bias proton-proton collision events, the column inefficiency becomes negligible due to the naturally tilted trajectories of the particles. At inclined incidence, particles passing through the columnar volume deposit more energy in the surrounding active material, producing a signal above threshold that enables hit reconstruction.

To reproduce this effect under controlled conditions, the modules were rotated relative to the beam direction—as illustrated in Figure 3.20. Efficiency cell maps for a fully depleted FBK sensor at normal incidence and rotated by  $5^\circ$  are shown in Figure 3.29. Even at this relatively small rotation angle, the efficiency at the  $p^+$  column positions is recovered, confirming the behavior predicted by simulations. In particular, the overall hit detection efficiency increases from approximately 98.5% at normal beam incidence to 99.5% at a  $5^\circ$  rotation angle.



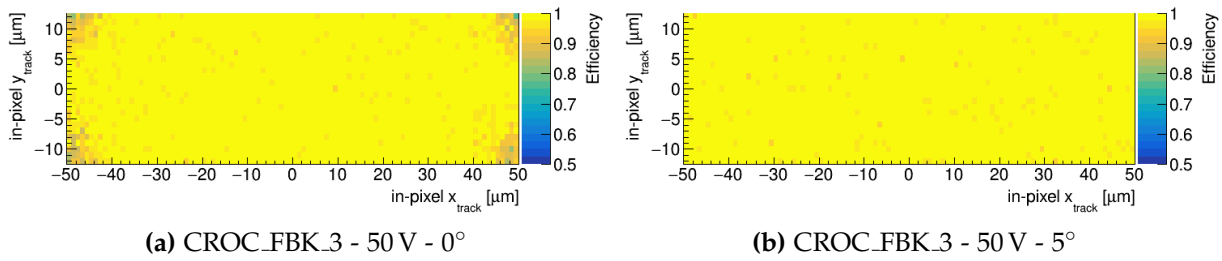


**Figure 3.29:** Hit detection efficiency cell map for a non-irradiated FBK module (a) at normal incidence and (b) rotated by 5°. The sensor is biased at 50 V in both cases.

### Cluster charge

The cluster charge distributions measured for all FBK modules at normal incidence are shown in Figures 3.30 for two bias voltages above full depletion: 5 V and 30 V. CNM devices are not included, as no calibration was performed for them. The distributions are very similar across modules and show only minor variation with bias voltage, as expected, since the collected charge tends to saturate after full depletion.

The observed variation corresponds to a modest 2% increase in MPV between 5 V and 30 V. This increase is attributed to the stronger electric field at higher bias voltage, which reduces charge sharing caused by diffusion. As a result, charge carriers that would otherwise diffuse into pixels outside the cluster are instead collected by the hit pixel, slightly increasing the measured cluster charge.

The cluster charge MPV, extracted from a fit to the central region of the distribution using a Landau convoluted with a Gaussian, is approximately 10 500 electrons at 30 V. This is consistent with theoretical expectations for a 150 μm thick sensor, assuming the generation of around 70 electron-hole pairs per micron in silicon.

The distributions also exhibit small bumps at low cluster charge values. The one centered around 2500 electrons is attributed to particles traversing the  $n^+$  column, which can generate signal in the 35 μm gap beneath the electrode. Structures at even lower charges are mainly artifacts from the ToT calibration—described in Section 3.1.3—particularly related to the ToT = 0 point. A minor contribution may also arise from a small angular spread in the track distribution: although tracks are nominally perpendicular, slight deviations from normal incidence occur. In these cases, a particle passing through an ohmic column near its edge may enter the active volume along its path, producing just enough charge to exceed the threshold.

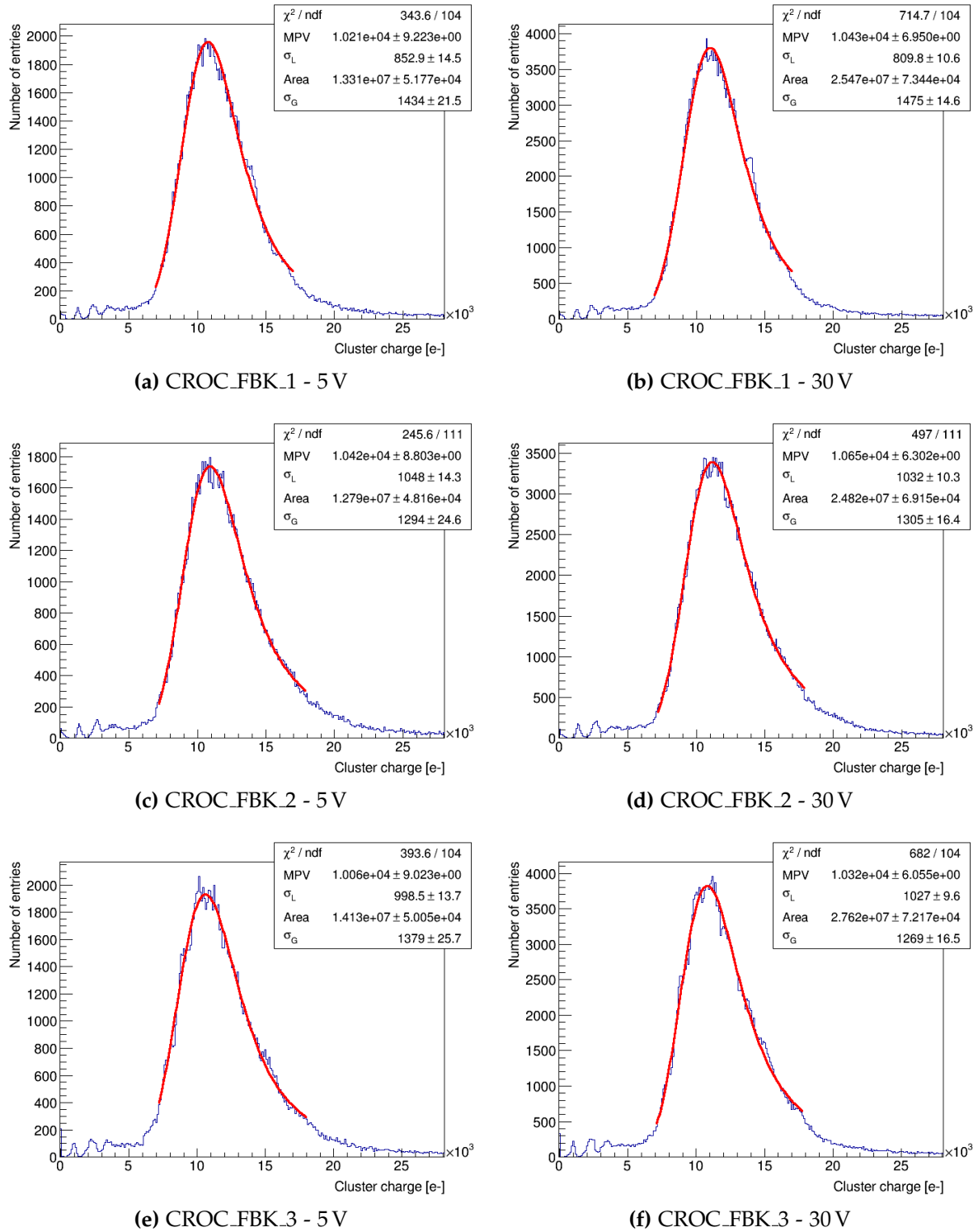


**Figure 3.30:** Cluster charge distributions for all non-irradiated FBK modules biased at 5 V and 30 V, under normal incidence of a 120 GeV/c pion beam. They are fitted to a Landau distribution with most probable value MPV and width  $\sigma_L$ , convoluted with a Gaussian distribution with width  $\sigma_G$ .

Figure 3.31 shows the cluster charge MPV across the pixel cell for module CROC\_FBK\_3 at three different bias voltages: 5 V, 30 V and 80 V. The maps appear very similar, confirming that the cluster charge MPV remains largely uniform above full depletion. As expected, lower values are observed at the electrode positions, particularly around the  $p^+$  columns, where no charge is generated at normal incidence due to their extension through the full sensor thickness.

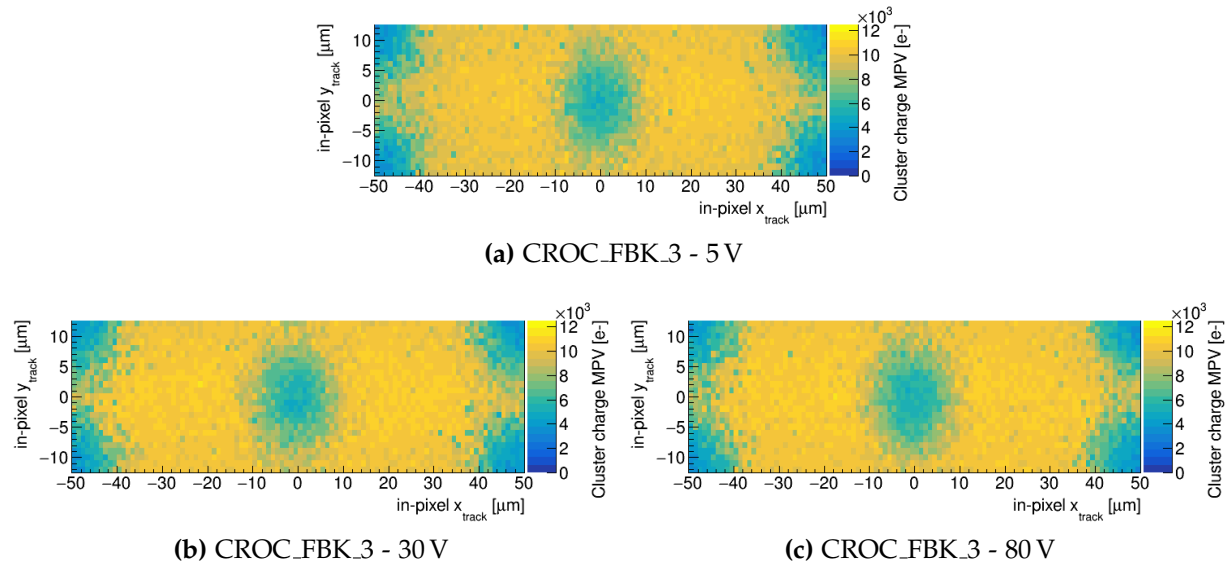


**Figure 3.31:** Cluster charge MPV cell maps for a non-irradiated FBK sensor biased at (a) 5 V, (b) 30 V and (c) 80 V. All measurements were taken at normal beam incidence.

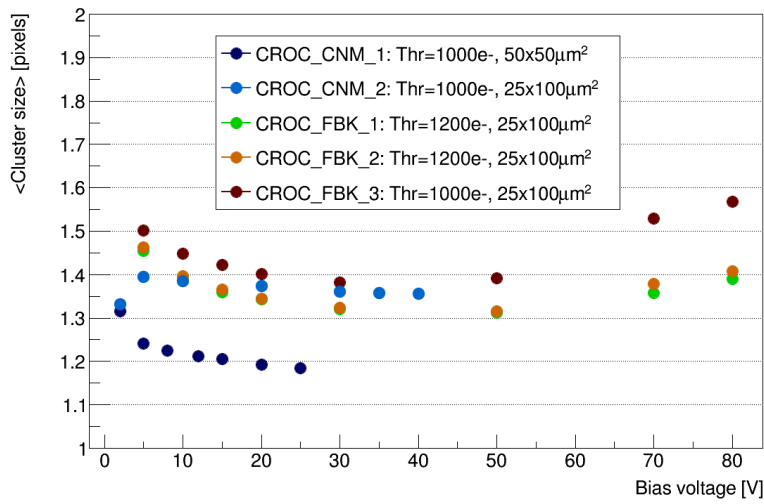
### Cluster size

The dependence of average cluster size on bias voltage for non-irradiated modules at normal incidence is shown in Figure 3.32. This observable is strongly influenced by the configuration and strength of the electric field, which evolves with increasing bias. At low voltages, charge sharing is mainly caused by diffusion at the pixel periphery, where the electric field lines run parallel to the pixel edges [72]. As the sensor approaches full depletion, this leads to an increase in cluster size. However, since these devices reach full depletion at very low voltages, this behavior is only visible in the CNM module with  $25 \times 100 \mu\text{m}^2$  pixels, for which measurements below full depletion (2 V) are available.

Once the sensor is fully depleted, the electric field becomes strong enough to considerably reduce the charge sharing driven by diffusion, causing a decrease in cluster size. However, at bias voltages well above full depletion, the cluster size gradually increases again. This effect may be attributed to localized charge multiplication (microavalanches) in high-field regions of neighboring pixels, which can artificially enlarge

the observed cluster size. To ensure optimal performance and avoid such artificial increases, 3D pixel sensors should be operated above full depletion and below the voltage range where microavalanches occur.

All sensors with  $25 \times 100 \mu\text{m}^2$  pixels exhibit similar cluster sizes, regardless of the manufacturer. In contrast, the sample with square pixels consistently shows smaller clusters, primarily because its reduced pixel pitch limits the region near the cell edges where diffusion can cause charge sharing.



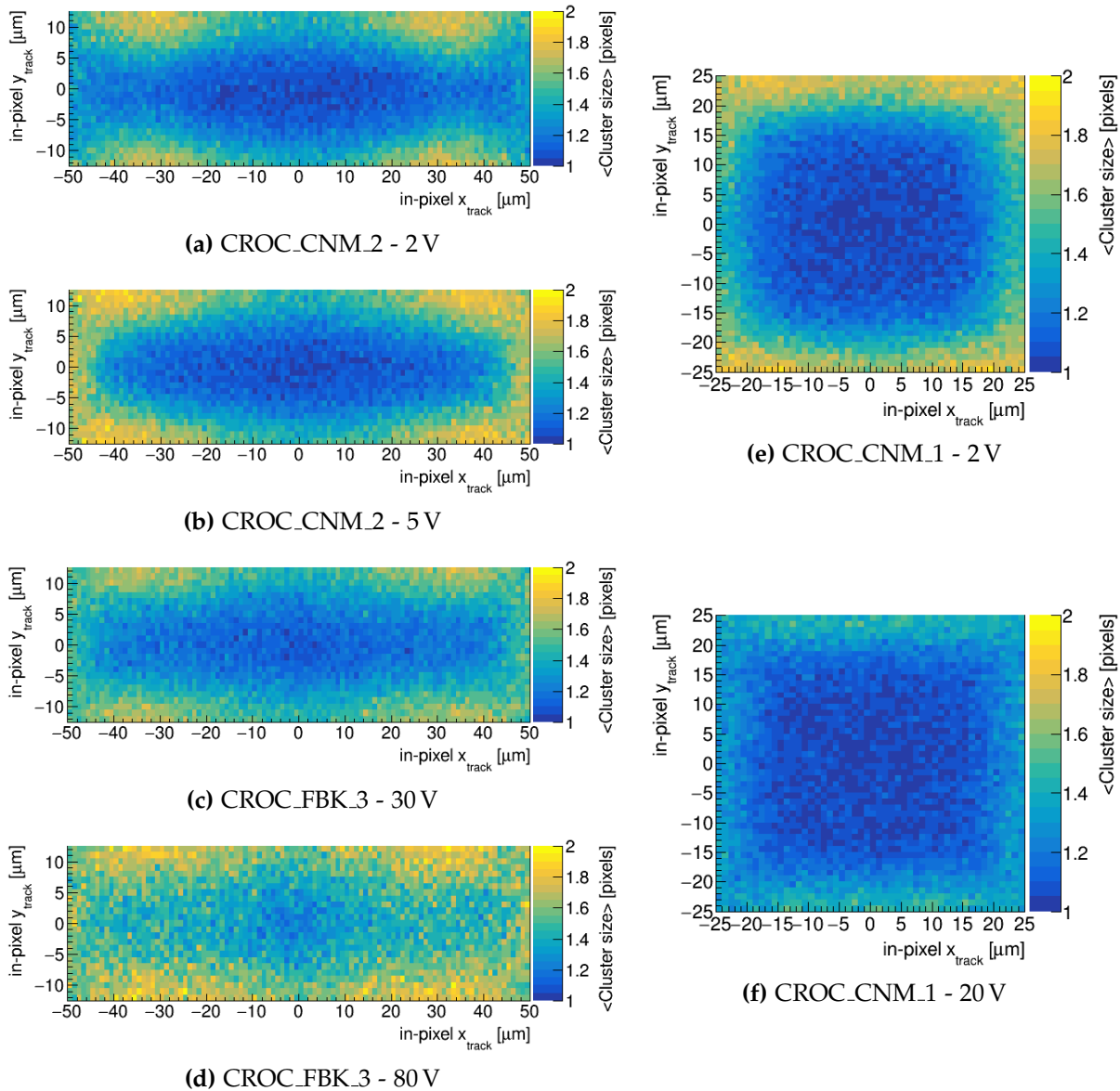
**Figure 3.32:** Average cluster size as a function of bias voltage for several non-irradiated modules at normal incidence. There are three sensors from FBK and one from CNM with a pixel size of  $25 \times 100 \mu\text{m}^2$ , as well as one CNM sensor with a  $50 \mu\text{m}$  pitch.

Figure 3.33 shows cluster size cell maps at normal incidence for several sensors biased at different voltages. The rectangular maps for 2 V and 5 V belong to module CROC\_CNM\_2, while those for 30 V and 80 V belong to module CROC\_FBK\_3. Similar maps for the CNM sensor with square pixels at 2 V and 20 V are also included.

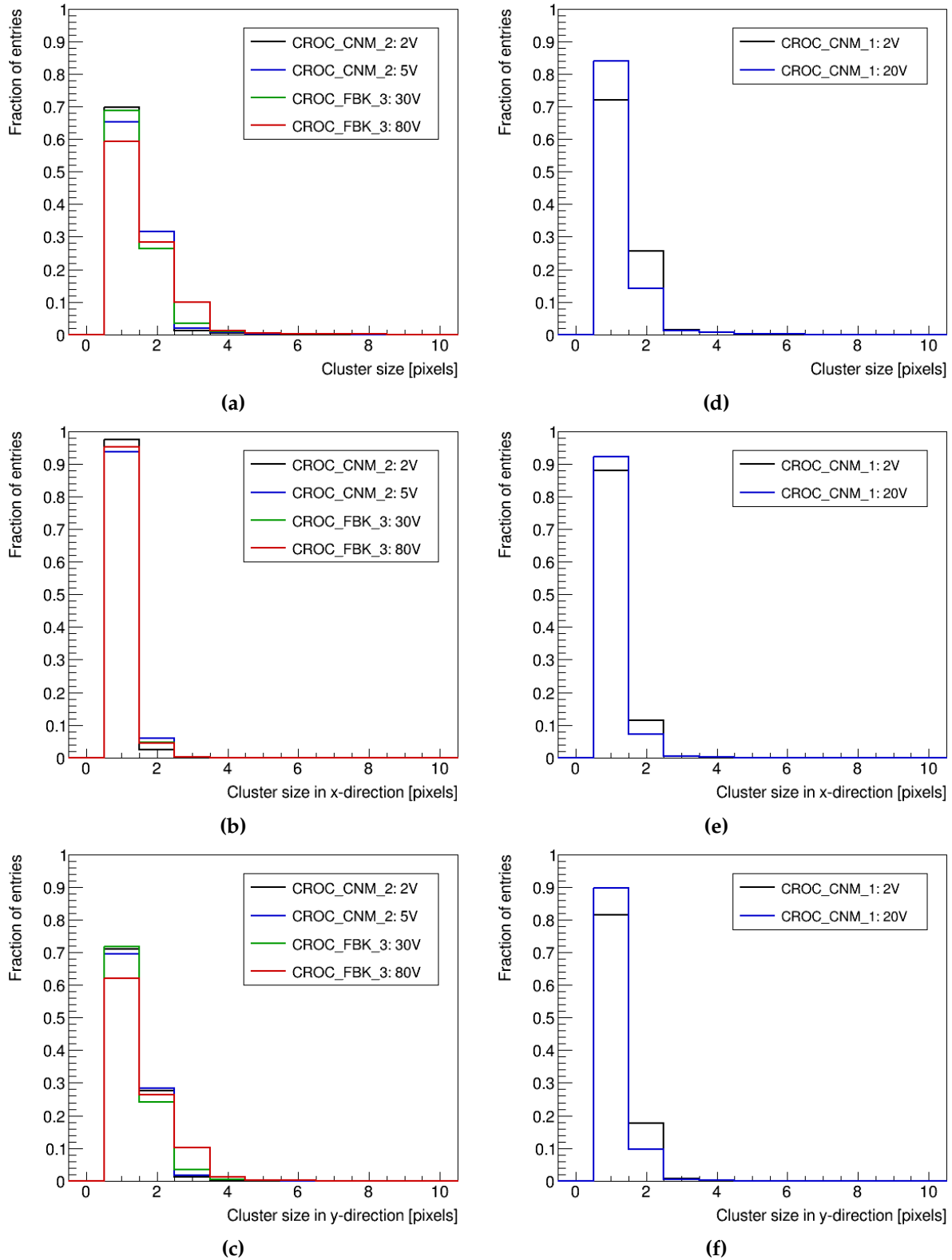
As expected, the cluster size increases with distance from the central electrode, reaching a maximum near the pixel edges. Once full depletion is achieved, charge sharing due to diffusion occurs across both cell boundaries, as seen in the map corresponding to 5 V. This charge sharing decreases throughout the cell periphery with increasing bias voltage, as observed at 30 V. For voltages well above full depletion, such as 80 V, the cluster size grows uniformly across the pixel cell rather than being confined to the edges, consistent with charge multiplication effects in high-field regions.

Figure 3.34 presents the one-dimensional cluster size distributions along the  $x$ -direction (long pitch for rectangular pixels),  $y$ -direction (short pitch for rectangular pixels), and their combination (total cluster size) for the same modules and bias voltages shown in

the cell maps. These distributions support the earlier discussion regarding the evolution of cluster size with increasing bias voltage. For the modules with  $25 \times 100 \mu\text{m}^2$  pixels, the dominant contribution to the total cluster size comes from the short-pitch direction, where most charge sharing occurs. In contrast, for the sensor with  $50 \mu\text{m}$  pitch, the contributions from both directions are comparable, as expected from the symmetric geometry.



**Figure 3.33:** Cluster size cell maps at normal incidence for several non-irradiated modules: the CNM sensor with  $25 \times 100 \mu\text{m}^2$  pixel size biased at (a) 2 V and (b) 5 V; one of the FBK sensors biased at (c) 30 V and (d) 80 V; and the CNM sensor with  $50 \mu\text{m}$  pitch biased at (e) 2 V and (f) 20 V.



**Figure 3.34:** One-dimensional cluster size distributions for several non-irradiated modules at normal incidence, showing the total cluster size as well as the cluster size in the  $x$  (long pitch) and  $y$  (short pitch) directions separately. (a)-(c) correspond to modules with  $25 \times 100 \mu\text{m}^2$  pixel size, and (d)-(f) to the sensor with  $50 \mu\text{m}$  pitch.

The evolution of the average cluster size as a function of rotation angle is shown in Figure 3.35. Measurements were performed for FBK sensors biased at 50 V. As expected, the cluster size increases with angle because particles are more likely to traverse multiple pixels, depositing enough charge in each to exceed the threshold. The average cluster size roughly doubles when the module is rotated by  $20^\circ$ .

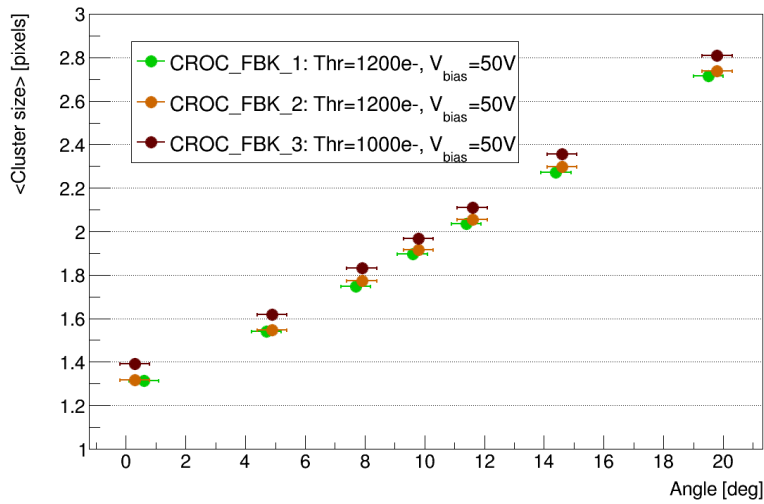
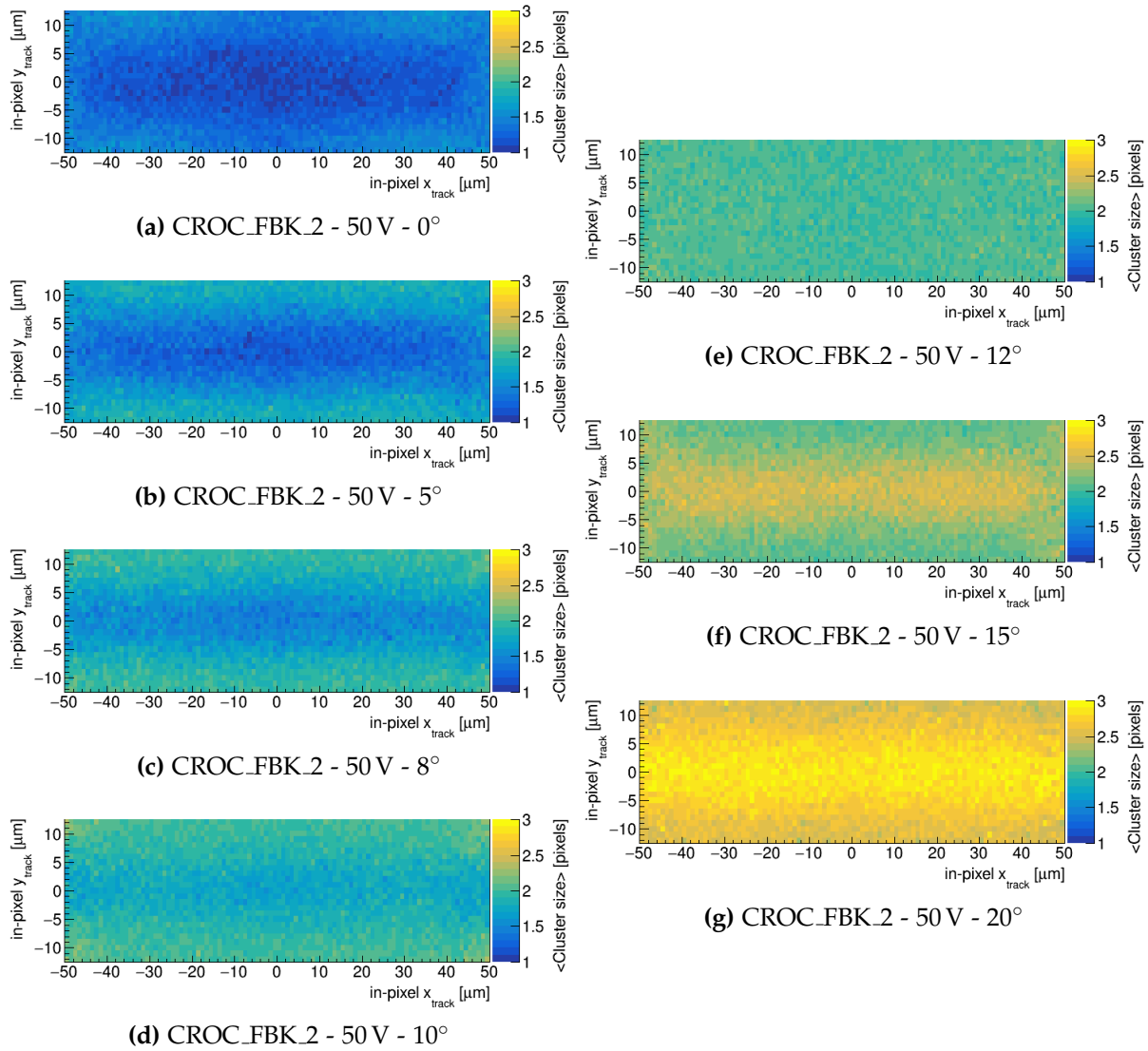


**Figure 3.35:** Average cluster size as a function of the rotation angle for all non-irradiated FBK modules biased at 50 V.

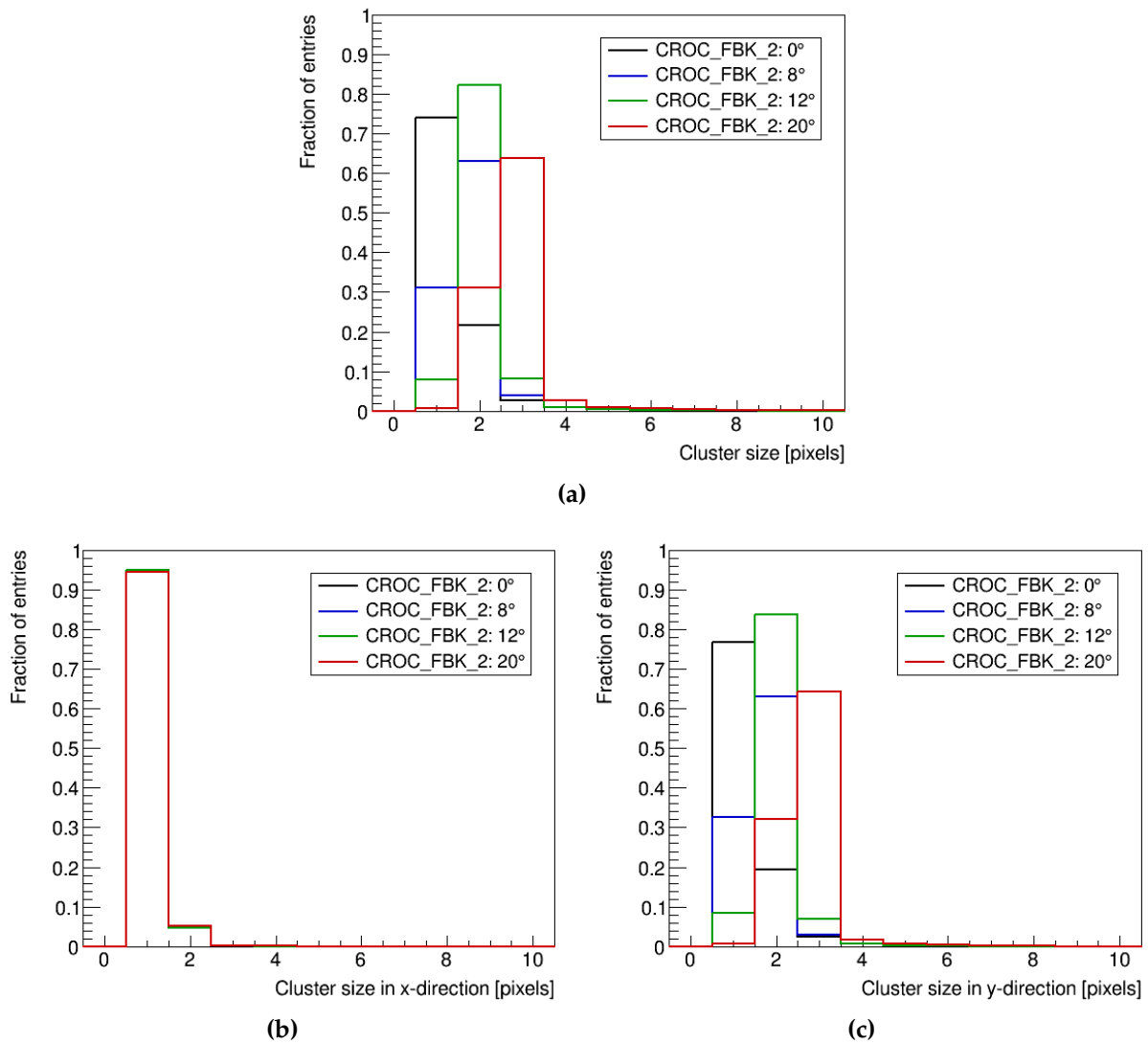
The corresponding cluster size cell maps for one of the modules are shown in Figure 3.36, illustrating how the regions associated with larger cluster size vary with the rotation angle. In these maps, the cluster size at each position represents the average value for all tracks whose midpoints fall within that area of the pixel cell. At small angles, larger cluster sizes are observed along the cell periphery near the long pixel edges. As the angle increases, the distribution becomes more uniform across the cell, with cluster sizes approaching 2 at  $12^\circ$ . At higher angles, the central region begins to show larger clusters, due to tracks whose midpoints lie near the center of the cell and deposit enough charge to generate signals above threshold in three adjacent pixels.

Figure 3.37 shows the corresponding one-dimensional cluster size distributions for four different rotation angles along the  $x$ -direction (long pixel pitch),  $y$ -direction (short pixel pitch), and their combination. As expected, the distribution along the long-pitch direction remains largely unchanged, while that along the short-pitch direction shifts significantly with increasing angle.





**Figure 3.36:** Cluster size cell maps for a non-irradiated FBK sensor biased at 50 V and rotated by: (a)  $0^\circ$ , (b)  $5^\circ$ , (c)  $8^\circ$ , (d)  $10^\circ$ , (e)  $12^\circ$ , (f)  $15^\circ$ , and (g)  $20^\circ$ .



**Figure 3.37:** One-dimensional cluster size distribution for a non-irradiated FBK sensor biased at 50 V and rotated by different angles. The distributions show (a) the total cluster size, (b) the cluster size in the  $x$ -direction (long pitch) separately, and (c) the cluster size in the  $y$ -direction (short pitch) separately at different rotation angles.

### Spatial resolution

The spatial resolution of the FBK sensors along the short pixel pitch was estimated using the methodology described in Section 3.3.2. The telescope resolution was found to be approximately  $5\text{ }\mu\text{m}$  for all devices, with small variations depending on the DUT position within the telescope setup and its rotation angle.

The spatial resolution along the  $25\text{ }\mu\text{m}$  pitch, shown in Figure 3.38 as a function of the rotation angle, remains well below the digital limit of  $7.2\text{ }\mu\text{m}$ , as given by equation 3.11. Since the resolution depends strongly on charge sharing between neighboring pixels, it is closely related to the cluster size shown in Figure 3.35. The best resolution—around

2.5  $\mu\text{m}$ —is achieved at rotation angles where the average cluster size approaches 2, which corresponds to optimal charge sharing conditions for the charge-weighted CoG method used in cluster reconstruction.

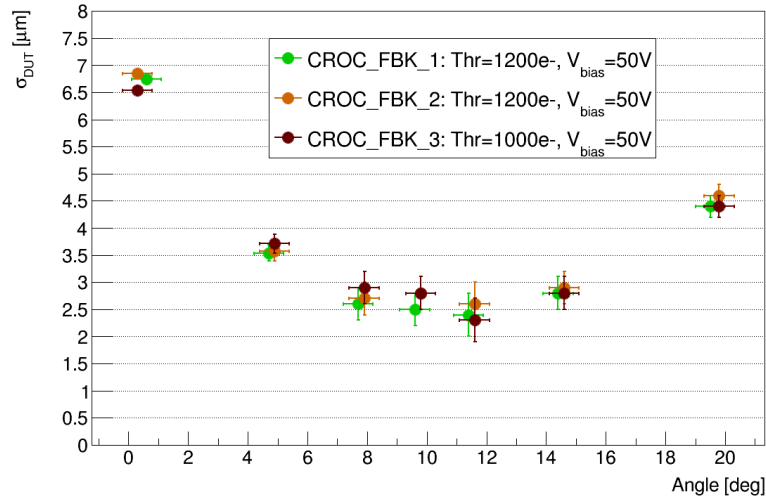


**Figure 3.38:** DUT spatial resolution along the short pixel pitch,  $\sigma_{\text{DUT}}$ , as a function of the rotation angle for all non-irradiated FBK modules biased at 50 V.

### 3.3.4. Performance of irradiated devices

Post-irradiation performance was evaluated only for modules with rectangular pixels. In particular, three of the modules tested before irradiation—CROC\_FBK\_2, CROC\_FBK\_3 and CROC\_CNM\_2—were irradiated to a fluence of  $1 \times 10^{16} \text{ n}_{\text{eq}}\text{cm}^{-2}$  at the CERN PS and subsequently retested in beam at the SPS. An additional module with the same geometric characteristics, CROC\_FBK\_4, was irradiated to a higher fluence of  $1.6 \times 10^{16} \text{ n}_{\text{eq}}\text{cm}^{-2}$  at KIT and characterized in a test beam for the first time at DESY. Details on these devices are provided in Tables 3.6 and 3.7.

The modules irradiated to the low fluence were operated at a temperature of  $-30^\circ\text{C}$  and tuned to an average pixel threshold of 1000 electrons, unless otherwise specified. The module irradiated to the high fluence was operated under different conditions: a temperature of  $-22^\circ\text{C}$  and an average pixel threshold of 1200 electrons.

Figure 3.39 shows the percentage of masked pixels—including both noisy and stuck pixels—as a function of bias voltage for all irradiated devices. For the FBK modules irradiated to the low fluence, the number of masked channels remains stable below 2% up to 150 V. In contrast, the CNM module exhibits a steep increase at 130 V. Raising its threshold to 1200 electrons reduces the percentage of masked pixels from 9% to 3%. Therefore, from this point onward, only results obtained with a threshold of 1200 electrons will be shown for the CNM module at that bias voltage. For the module

exposed to the high fluence, the percentage of masked pixels remains below 3% up to 130 V, but rises sharply to 10% at 140 V.

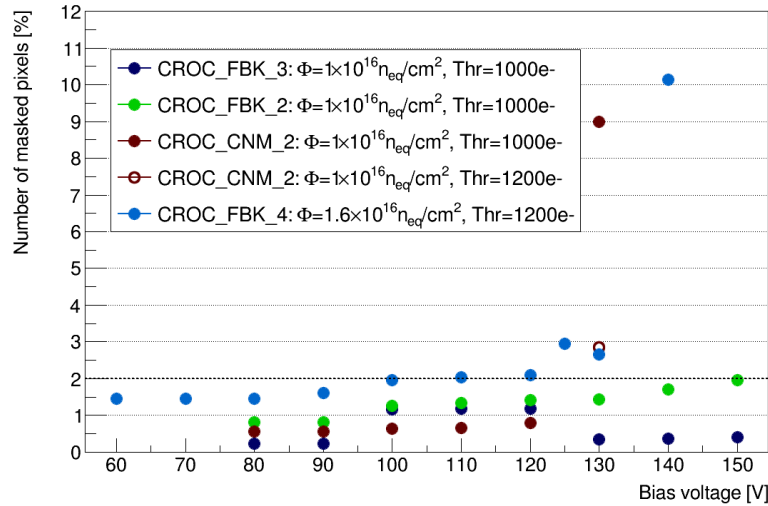


**Figure 3.39:** Percentage of masked pixels, including both noisy and stuck pixels, as a function of bias voltage for modules irradiated to  $1 \times 10^{16} \text{ n}_{\text{eq}}\text{cm}^{-2}$  and  $1.6 \times 10^{16} \text{ n}_{\text{eq}}\text{cm}^{-2}$ . All sensors feature a pixel size of  $25 \times 100 \mu\text{m}^2$ . The horizontal dashed line indicates the CMS requirement of a maximum of 2% masked pixels at a fluence of  $1 \times 10^{16} \text{ n}_{\text{eq}}\text{cm}^{-2}$ .

### Hit detection efficiency

All modules achieve a hit detection efficiency above 97% at normal incidence after irradiation, as shown in Figure 3.40. For a fluence of  $1 \times 10^{16} \text{ n}_{\text{eq}}\text{cm}^{-2}$ , the efficiency plateau is reached at bias voltages around 80–90 V, while the module irradiated to  $1.6 \times 10^{16} \text{ n}_{\text{eq}}\text{cm}^{-2}$  requires a higher voltage of approximately 100 V. This defines an operational range of 30–60 V, in which the modules maintain excellent performance and a low fraction of masked pixels, meeting the CMS requirements listed in Table 3.1.

The acceptance, as defined in equation 3.10, is used to evaluate the impact of masked pixels on efficiency. Figures 3.40b and 3.40c show the acceptance-corrected efficiency for modules irradiated to the low and high fluences, respectively.

Efficiency cell maps at normal incidence are presented in Figure 3.41, illustrating the progressive depletion of the active volume with increasing bias voltage after irradiation. Figures 3.41a–3.41d correspond to one of the FBK modules irradiated to  $1 \times 10^{16} \text{ n}_{\text{eq}}\text{cm}^{-2}$  and biased at voltages ranging from 40 V to 120 V. Similarly, Figures 3.41e–3.41h show the maps for the module irradiated to  $1.6 \times 10^{16} \text{ n}_{\text{eq}}\text{cm}^{-2}$ , biased at voltages between 60 V and 120 V.

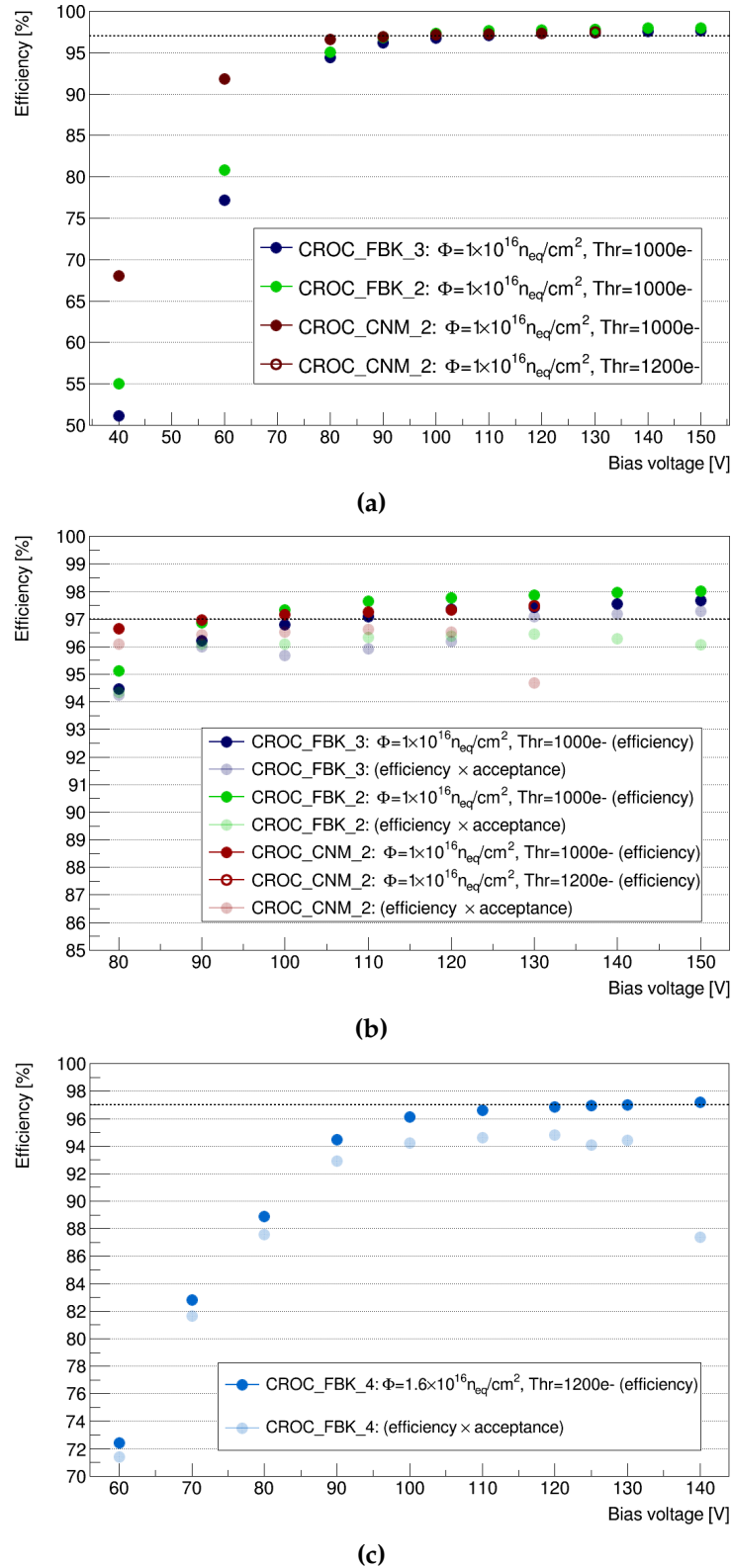


**Figure 3.40:** (a) Hit detection efficiency at normal incidence as a function of bias voltage for modules irradiated to  $1 \times 10^{16} \text{ n}_{\text{eq}}/\text{cm}^2$ . (b) Zoom of the efficiency plateau region in (a), comparing results with and without acceptance correction. (c) Efficiency with and without acceptance correction for the module irradiated to  $1.6 \times 10^{16} \text{ n}_{\text{eq}}/\text{cm}^2$ . Solid colors represent efficiency, while lighter colors show acceptance-corrected efficiency. The horizontal dashed line indicates the 97% efficiency criterion.

In both fluence scenarios, the inefficiency at the  $n^+$  column position persists until the bias voltage is sufficient to fully deplete the region beneath the column, enabling enough charge collection to exceed the threshold despite charge carrier trapping.

As expected, the more heavily irradiated module requires a higher bias voltage to reach full efficiency across the pixel cell. In addition, the maps for this module appear less sharply defined—especially noticeable around the columnar electrode positions, where regions of intrinsic inefficiency are more spread out. This effect is attributed to the reduced telescope resolution in the DESY test beam setup, where only the upstream triplet is used for track reconstruction, as discussed in Section 3.2.1. In particular, the telescope resolution was approximately  $7\text{ }\mu\text{m}$  at SPS and  $11\text{ }\mu\text{m}$  at DESY—estimated using the methodology described in Section 3.3.2.

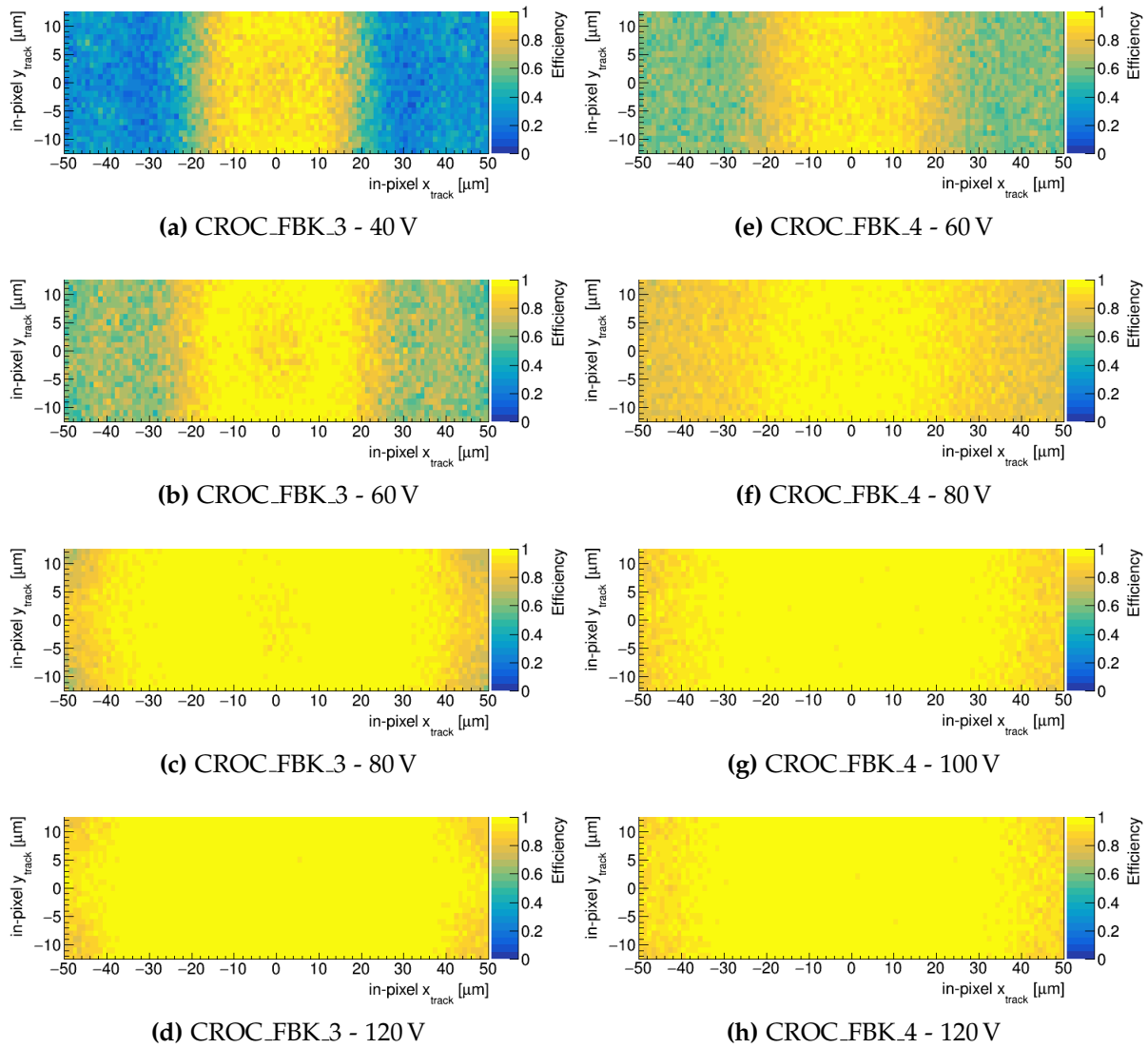


**Figure 3.41:** Hit detection efficiency cell maps at normal incidence of an FBK module irradiated to  $1 \times 10^{16} \text{ n}_{\text{eq}}\text{cm}^{-2}$ , biased at (a) 40 V, (b) 60 V, (c) 80 V, and (d) 120 V. Similar maps from the module irradiated to  $1.6 \times 10^{16} \text{ n}_{\text{eq}}\text{cm}^{-2}$  are shown for a bias voltage of (e) 60 V, (f) 80 V, (g) 100 V and (h) 120 V.

Hit detection efficiency was also evaluated as a function of the rotation angle—defined in Figure 3.20. These measurements were conducted at 120 V for modules irradiated to  $1 \times 10^{16} \text{ n}_{\text{eq}}\text{cm}^{-2}$ , without masking noisy or stuck pixels. The FBK and CNM devices were tuned to thresholds of 1000 and 1200 electrons, respectively.

Figure 3.42 shows the increase in efficiency with rotation angle for all modules, exceeding 99% from approximately  $6\text{--}8^\circ$  onward. The mitigation of columnar inefficiency with increasing angle—previously discussed for non-irradiated modules—is visualized in Figure 3.43, which compares efficiency cell maps at normal incidence and at rotations of  $4^\circ$  and  $10^\circ$  for one of the FBK modules.

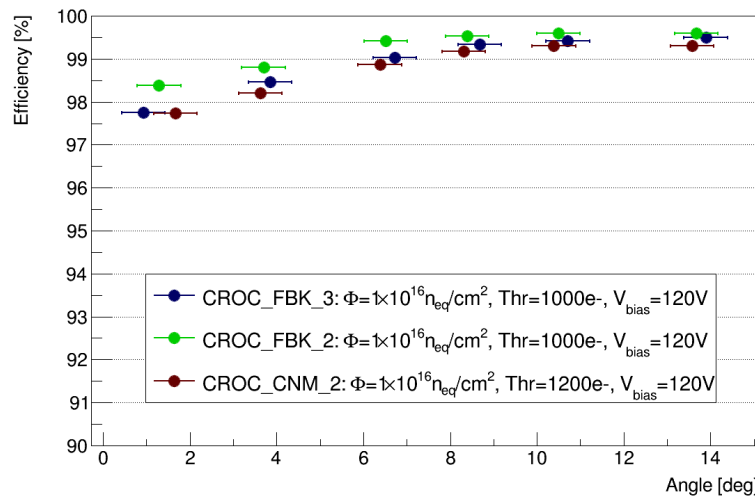


**Figure 3.42:** Hit detection efficiency as a function of the rotation angle for all modules irradiated to  $1 \times 10^{16} \text{ n}_{\text{eq}}\text{cm}^{-2}$  and biased at 120 V.

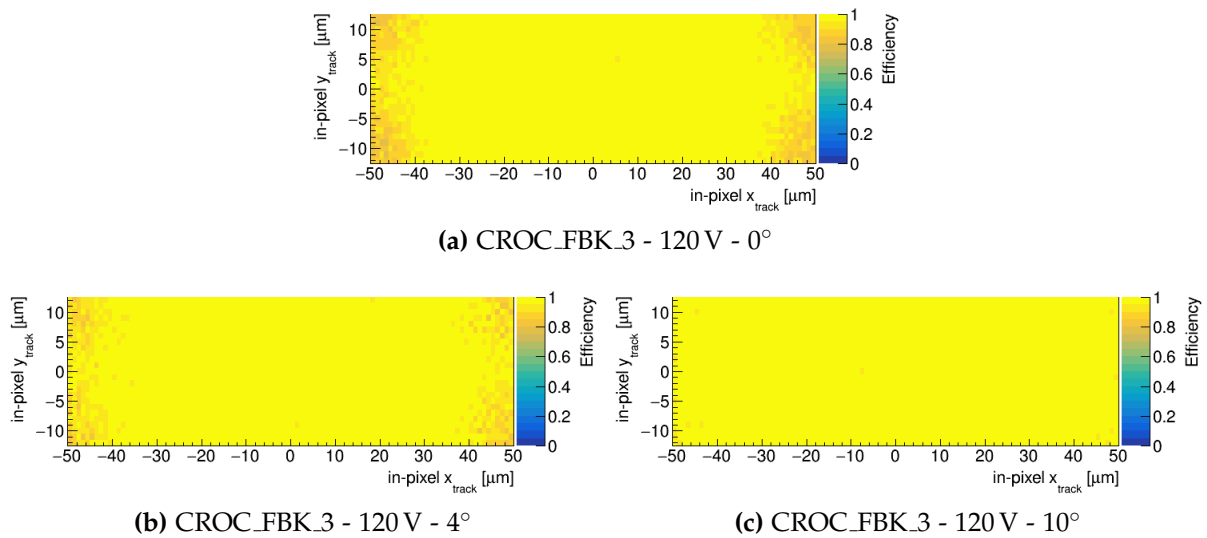


**Figure 3.43:** Hit detection efficiency cell maps for an FBK module irradiated to  $1 \times 10^{16} \text{ n}_{\text{eq}}\text{cm}^{-2}$  (a) at normal beam incidence, (b) rotated by  $4^\circ$ , and (c) rotated by  $10^\circ$ . The sensor is biased at 120 V in all cases.



The variation of efficiency within the pixel cell as a function of both bias voltage and rotation angle can also be examined through the corresponding profiles. Figure 3.44 shows the profiles along the long pixel pitch for module CROC.FBK\_3, which was irradiated to  $1 \times 10^{16} \text{ n}_{\text{eq}}\text{cm}^{-2}$ . These profiles complement the cell maps shown in Figures 3.41 and 3.43 by comparing efficiency at normal incidence for various bias voltages with the case of a  $10^\circ$  rotation. They highlight the improved efficiency at the  $n^+$  column position with increasing bias voltage, as well as the recovery of efficiency at the  $p^+$  columns when the module is rotated.

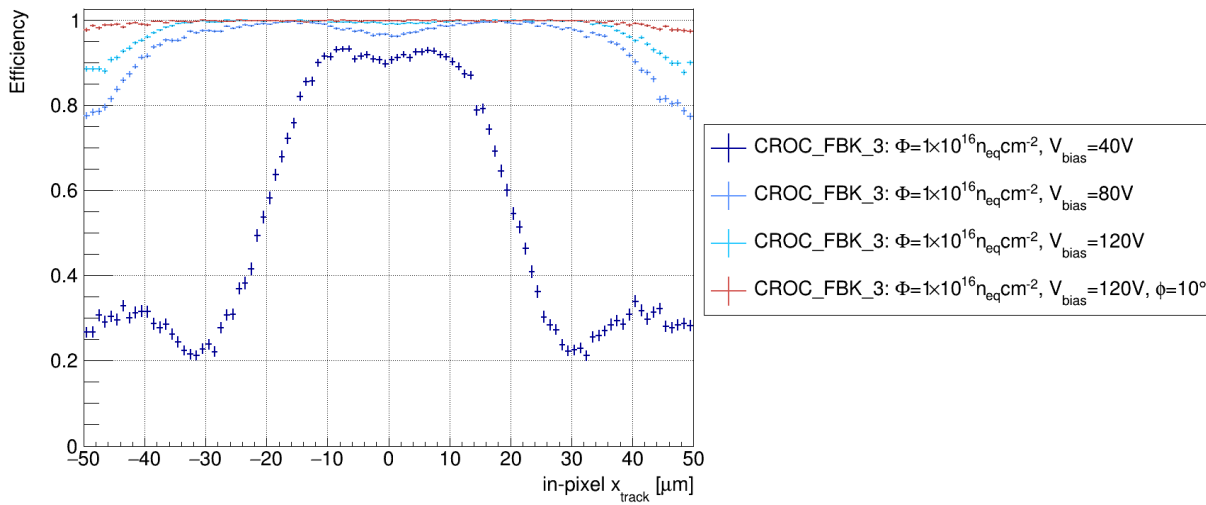
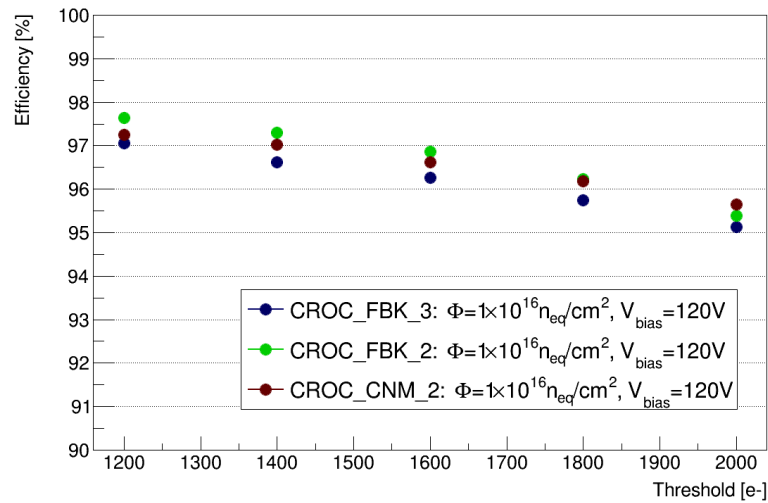


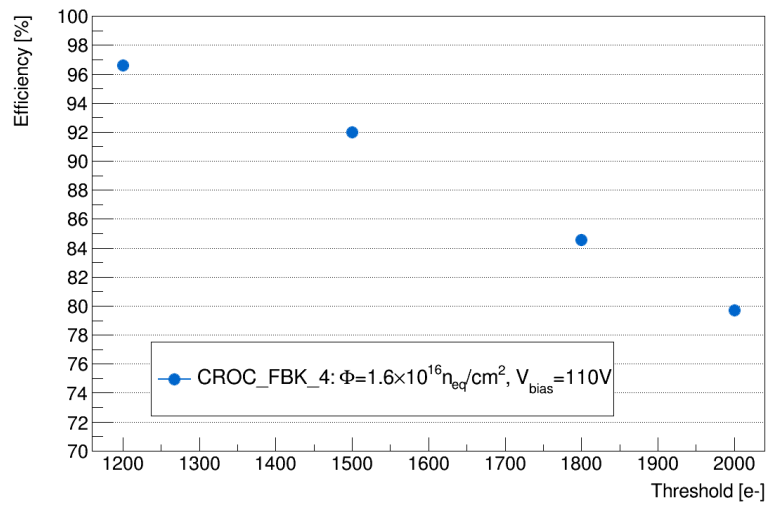
**Figure 3.44:** Hit detection efficiency profiles along the long pixel pitch for an FBK module irradiated to  $1 \times 10^{16} \text{ n}_{\text{eq}}\text{cm}^{-2}$ . The plot compares measurements at normal incidence for different bias voltages with those at a rotation angle of  $10^\circ$ .

The hit detection efficiency also depends on the average pixel threshold to which the modules are tuned. Figure 3.45 presents the results of this study, conducted at normal incidence for modules irradiated to  $1 \times 10^{16} \text{ n}_{\text{eq}}\text{cm}^{-2}$  and  $1.6 \times 10^{16} \text{ n}_{\text{eq}}\text{cm}^{-2}$ . These measurements were performed without masking noisy or stuck pixels, with the sensors biased at 120 V and 110 V, respectively.

An efficiency loss of approximately 2% is observed when the threshold is doubled in the less irradiated devices. This reduction becomes more pronounced with increasing fluence, reaching about 16% in the more heavily irradiated module. These results highlight the importance of tuning the modules to the lowest possible threshold.



(a)



(b)

**Figure 3.45:** Hit detection efficiency at normal incidence as a function of the average pixel threshold for modules irradiated to (a)  $1 \times 10^{16} \text{ n}_{\text{eq}}\text{cm}^{-2}$  and (b)  $1.6 \times 10^{16} \text{ n}_{\text{eq}}\text{cm}^{-2}$ . The sensors were biased at 120 V and 110 V, respectively.

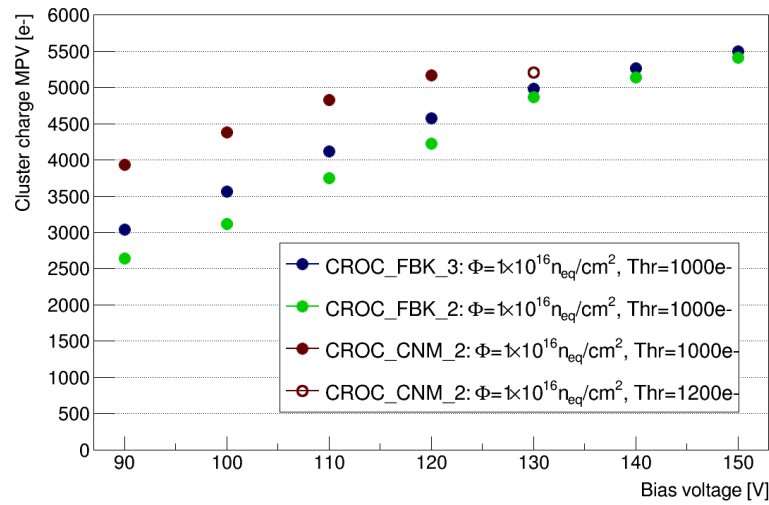
### Cluster charge

The evolution of the cluster charge MPV with bias voltage at normal incidence is shown in Figure 3.46 for modules irradiated to  $1 \times 10^{16} \text{ n}_{\text{eq}}\text{cm}^{-2}$  and  $1.6 \times 10^{16} \text{ n}_{\text{eq}}\text{cm}^{-2}$ . The MPVs are extracted from fits to the core of the cluster charge distributions using a Landau convoluted with a Gaussian, as illustrated in Figure 3.47 for FBK modules biased at 140 V.

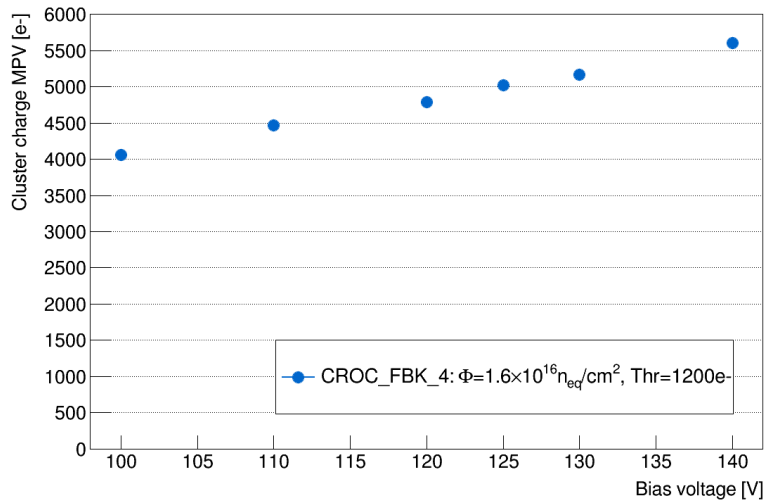
It is important to note that the modules were irradiated with proton beams of different energies: 23 GeV for the low fluence and 23 MeV for the high fluence. Since the radiation damage profile depends on the energy of the incident particles, comparisons

of charge collection between the two fluence levels should be interpreted with caution. In particular, low-energy protons lead to a significantly higher TID, which can enhance surface damage and, consequently, alter the measured cluster charge.

The MPV increases with bias voltage for both irradiation levels, reflecting improved charge collection as the depleted volume expands and the electric field strengthens. A mild saturation is observed at high voltages in the less irradiated devices. In both cases, the MPV reaches approximately 5500 electrons at the highest bias voltage, corresponding to about half the cluster charge measured before irradiation.



(a)



(b)

**Figure 3.46:** Most probable value (MPV) of the cluster charge as a function of bias voltage for modules irradiated to (a)  $1 \times 10^{16} \text{ n}_{\text{eq}}\text{cm}^{-2}$  with a 23 GeV proton beam and (b)  $1.6 \times 10^{16} \text{ n}_{\text{eq}}\text{cm}^{-2}$  with a 23 MeV proton beam. The measurements were performed under normal incidence of a 120 GeV/c pion beam for (a) and a 5.2 GeV/c electron beam for (b).

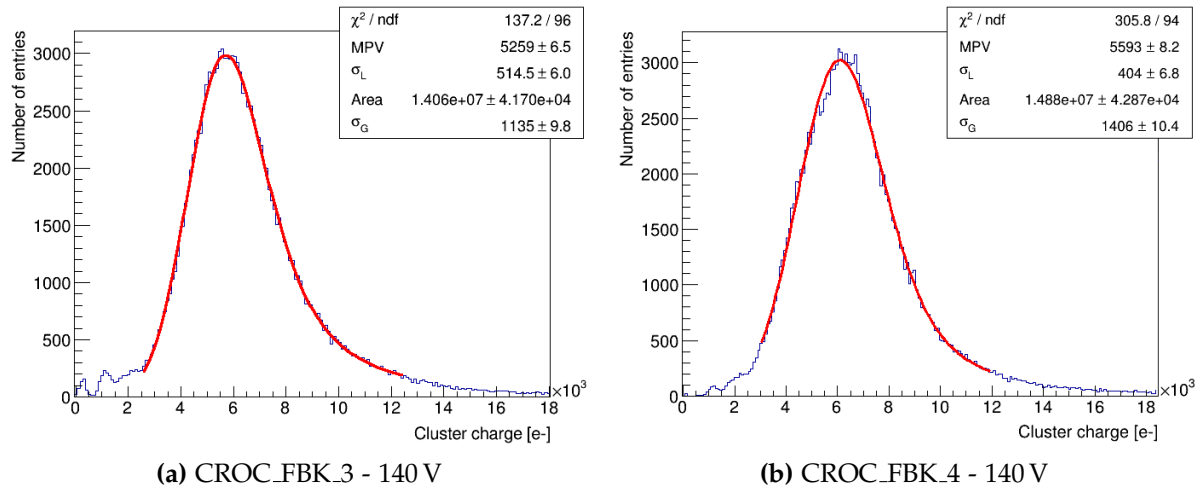


**Figure 3.47:** Cluster charge distributions at 140 V for FBK modules irradiated to (a)  $1 \times 10^{16} \text{ n}_{\text{eq}}\text{cm}^{-2}$  and (b)  $1.6 \times 10^{16} \text{ n}_{\text{eq}}\text{cm}^{-2}$ . The measurements were performed under normal incidence of a 120 GeV/c pion beam and a 5.2 GeV/c electron beam, respectively. The fits use a Landau distribution with most probable value MPV and width  $\sigma_L$ , convoluted with a Gaussian distribution with width  $\sigma_G$ .

The maps in Figure 3.48 show the evolution of the cluster charge MPV across the pixel cell for modules CROC\_FBK\_3 and CROC\_CNM\_2 at different bias voltages. Under normal beam incidence, the MPV increases progressively from the  $p^+$  columns toward the central region, reflecting the increasing impact of charge trapping with distance from the collecting electrode. This effect becomes less pronounced at higher bias voltages, as the stronger electric field reduces the probability of charge trapping. As expected, the cluster charge at the  $n^+$  column position is lower, since only  $35 \mu\text{m}$  of active material are available for charge generation, as previously discussed for non-irradiated modules.

Overall, the CNM module exhibits higher cluster charge MPV than the FBK module at the same bias voltage. This may be attributed to the shorter inter-electrode distance in CNM sensors, which leads to a more intense electric field for a given bias.

Figure 3.49 shows similar plots for the FBK module irradiated to  $1.6 \times 10^{16} \text{ n}_{\text{eq}}\text{cm}^{-2}$ . As expected from the trends observed in Figure 3.46, the spatial distribution of the cluster charge MPV remains largely unchanged between the two fluence scenarios. The main difference appears at the  $n^+$  column position, which is less well defined due to the reduced telescope resolution in the DESY test beam setup—approximately  $11 \mu\text{m}$  compared to  $7 \mu\text{m}$  at SPS. These values were estimated using the methodology described in Section 3.3.2.

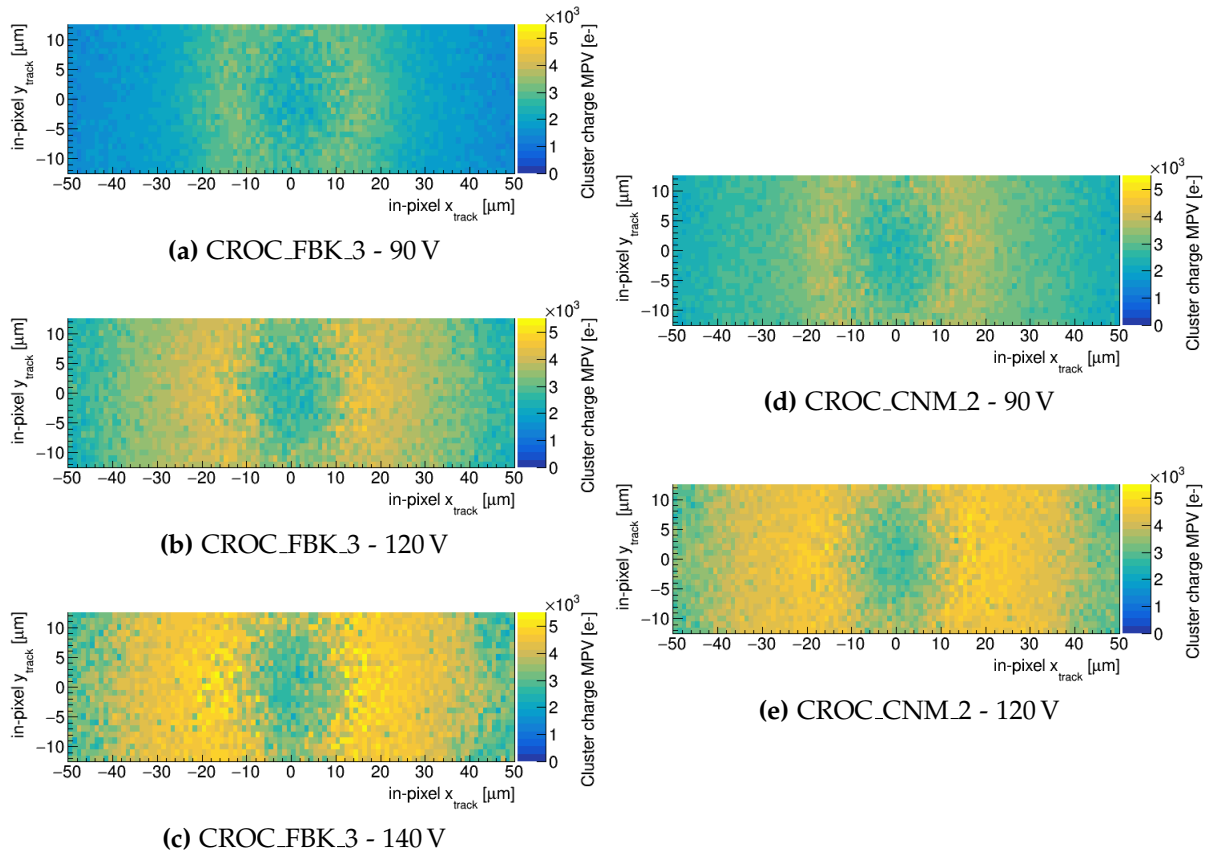


**Figure 3.48:** Cluster charge MPV cell maps at normal incidence for two modules irradiated to  $1 \times 10^{16} \text{ n}_{\text{eq}}\text{cm}^{-2}$ . The FBK sensor is biased at (a) 90 V, (b) 120 V and (c) 140 V, while the CNM sensor is biased at (d) 90 V and (e) 120 V.

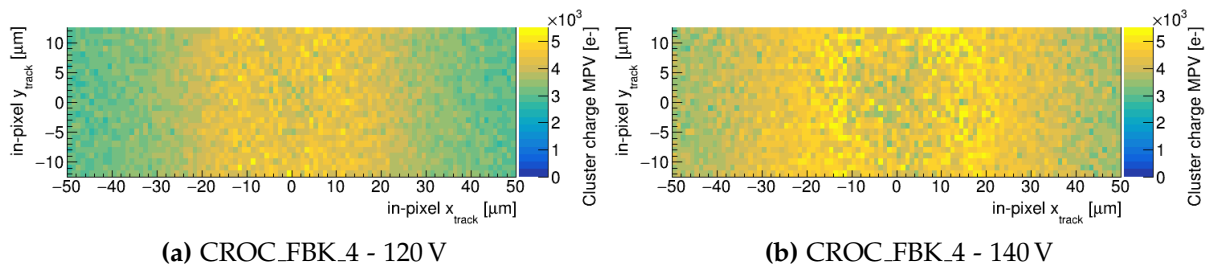
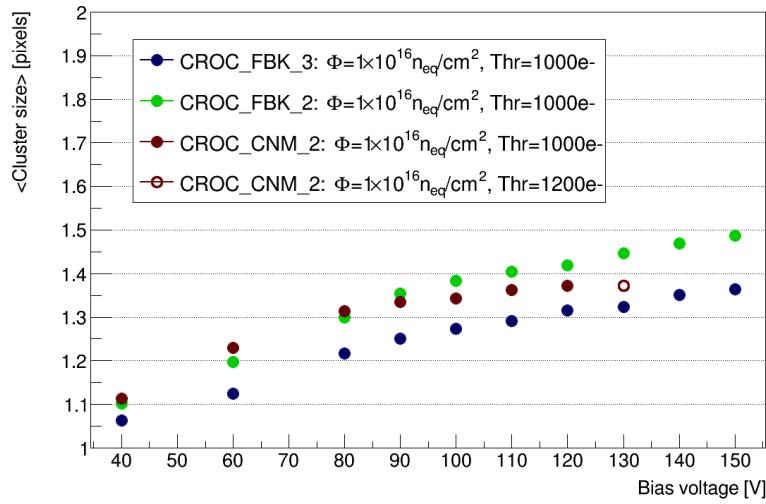


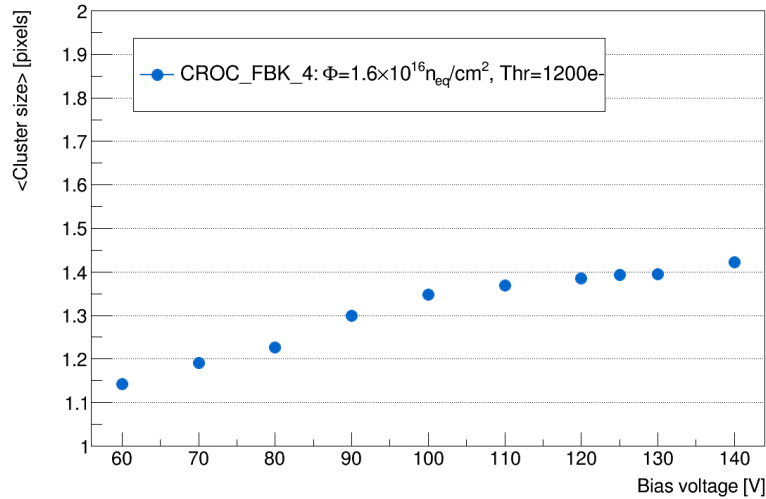
**Figure 3.49:** Cluster charge MPV cell maps at normal incidence for an FBK module irradiated to  $1.6 \times 10^{16} \text{ n}_{\text{eq}}\text{cm}^{-2}$ . The sensor is biased at (a) 120 V and (b) 140 V.

### Cluster size

The average cluster size as a function of bias voltage at normal incidence is shown in Figures 3.50a and 3.50b for modules irradiated to  $1 \times 10^{16} \text{ n}_{\text{eq}}\text{cm}^{-2}$  and  $1.6 \times 10^{16} \text{ n}_{\text{eq}}\text{cm}^{-2}$ , respectively. In both cases, the cluster size increases with bias voltage and begins to saturate at higher values. As previously discussed for non-irradiated modules, this trend results from charge sharing due to diffusion at the pixel periphery, which becomes enhanced as the sensor depletes.



(a)



(b)

**Figure 3.50:** Average cluster size as a function of bias voltage for modules irradiated to (a)  $1 \times 10^{16} \text{ n}_{\text{eq}}\text{cm}^{-2}$  and (b)  $1.6 \times 10^{16} \text{ n}_{\text{eq}}\text{cm}^{-2}$ . Measurements were performed at normal incidence.

The dependence of cluster size on rotation angle was also investigated for irradiated modules, given its strong influence on spatial resolution. Figure 3.51 illustrates the evolution of the average cluster size as a function of angle for modules irradiated to  $1 \times 10^{16} \text{ n}_{\text{eq}}/\text{cm}^2$  at a bias voltage of 120 V. Compared to measurements before irradiation, the angular dependence is less pronounced, primarily due to radiation-induced effects such as charge trapping. Nonetheless, the average cluster size still grows by approximately 30% at a rotation angle of  $14^\circ$ .

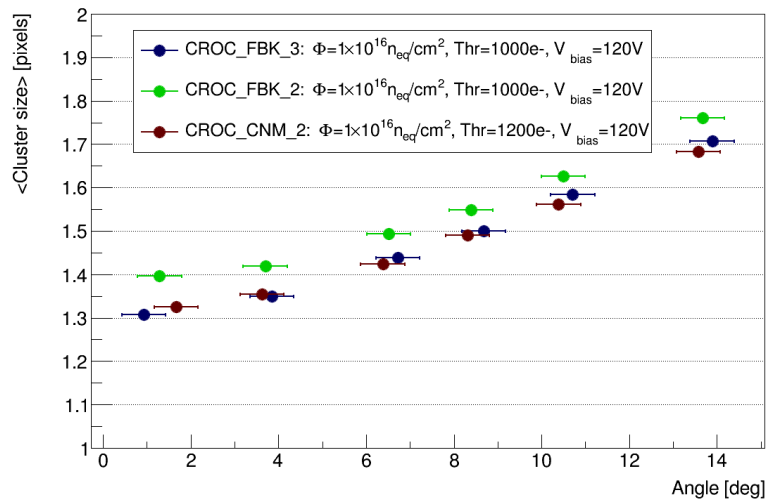


**Figure 3.51:** Average cluster size as a function of the rotation angle for modules irradiated to  $1 \times 10^{16} \text{ n}_{\text{eq}}\text{cm}^{-2}$ . All measurements were performed at a bias voltage of 120 V.

Cluster size cell maps for one of the FBK modules irradiated to  $1 \times 10^{16} \text{ n}_{\text{eq}}/\text{cm}^2$  are shown in Figure 3.52, at normal incidence and at four different rotation angles. As observed before irradiation, the cluster size at normal incidence increases with distance from the central electrode and reaches a maximum near the pixel edges, where charge sharing due to diffusion is most significant.

However, at non-zero rotation angles, the cluster size distribution evolves differently than in non-irradiated modules. As the rotation angle increases, the cluster size grows more uniformly across the pixel cell, with the central region consistently showing the smallest cluster size. This is primarily attributed to charge trapping, whose impact becomes more severe when particles crossing the central region generate charge in areas of very low electric field strength—where it is more likely to be trapped before collection.



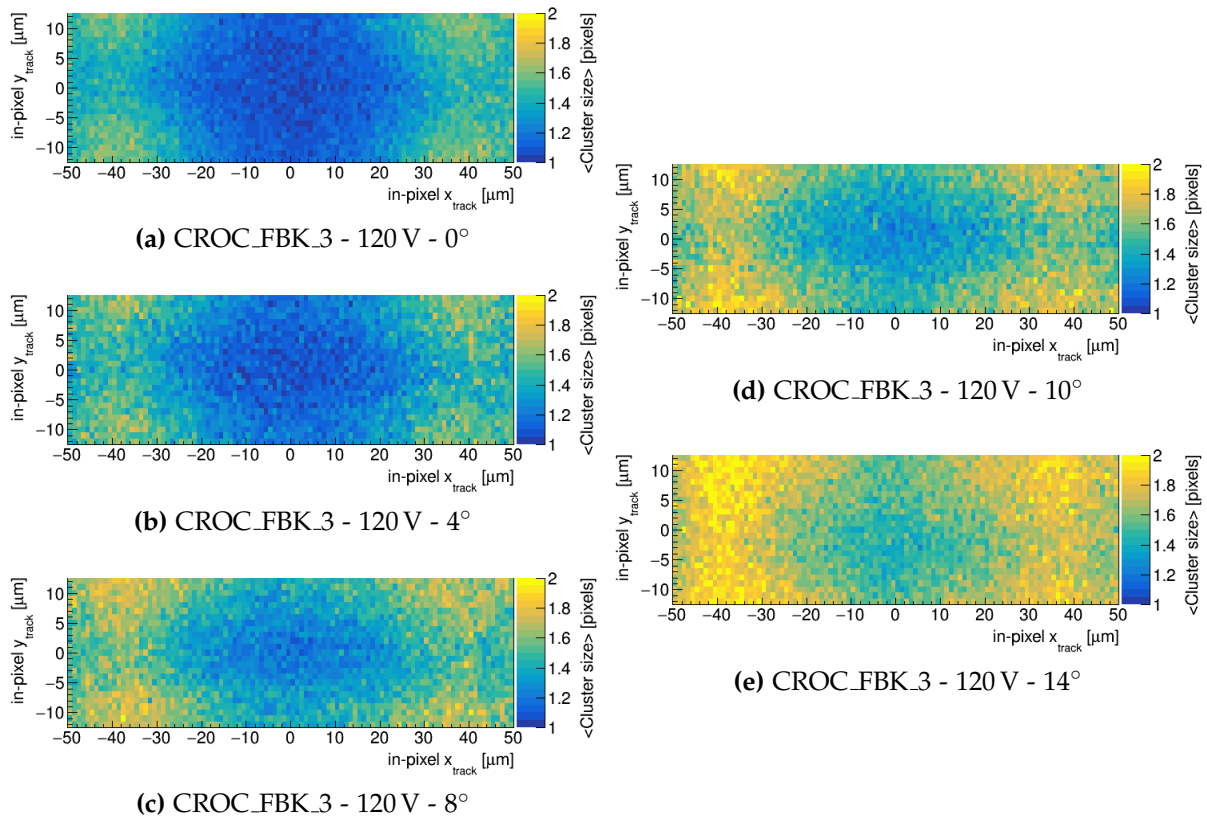


**Figure 3.52:** Cluster size cell maps for an FBK module irradiated to  $1 \times 10^{16} \text{ n}_{\text{eq}}/\text{cm}^2$ . The maps correspond to rotation angles of (a)  $0^\circ$ , (b)  $4^\circ$ , (c)  $8^\circ$ , (d)  $10^\circ$ , and (e)  $14^\circ$ . All measurements were performed at a bias voltage of 120 V.

The importance of tuning the modules to the lowest achievable threshold is evident not only from the hit detection efficiency but also from the cluster size. Figure 3.53 shows the average cluster size as a function of the average pixel threshold for modules irradiated to  $1 \times 10^{16} \text{ n}_{\text{eq}}/\text{cm}^2$  and  $1.6 \times 10^{16} \text{ n}_{\text{eq}}/\text{cm}^2$ . These measurements were performed at normal incidence, with the sensors biased at 120 V and 110 V, respectively. Noisy and stuck pixels were not masked during the data taking.

The cluster size decreases by approximately 15% at both fluences when the threshold is doubled. This reduction occurs because the charge shared with neighboring pixels due to diffusion increasingly falls below the detection threshold.

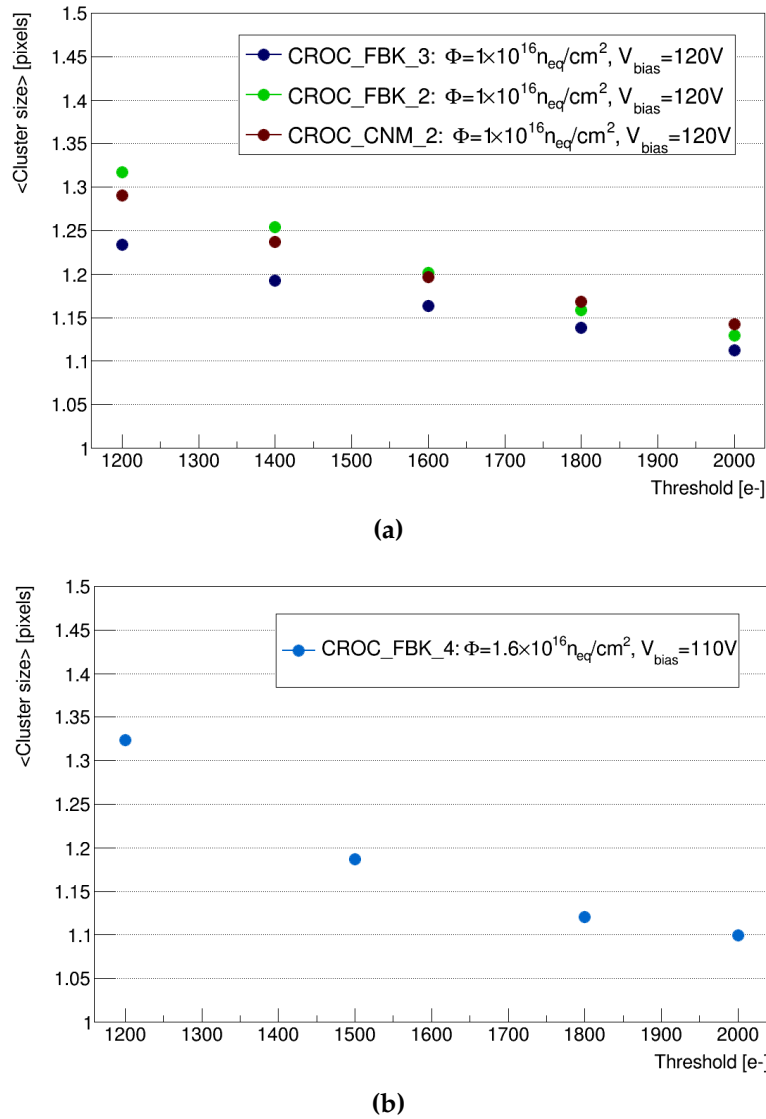


**Figure 3.53:** Average cluster size as a function of the average pixel threshold for modules irradiated to (a)  $1 \times 10^{16} \text{ n}_{\text{eq}}\text{cm}^{-2}$  and (b)  $1.6 \times 10^{16} \text{ n}_{\text{eq}}\text{cm}^{-2}$ . The sensors were biased at 120 V and 110 V, respectively.

### Spatial resolution

The spatial resolution of modules irradiated to  $1 \times 10^{16} \text{ n}_{\text{eq}}\text{cm}^{-2}$  was estimated using the methodology described in Section 3.3.2. The telescope resolution at SPS was determined to be approximately  $7 \mu\text{m}$  for all devices, with small variations depending on the DUT position within the telescope setup and its rotation angle. This resolution is worse than that obtained for non-irradiated devices, likely due to a different configuration of the telescope planes, which appears to reduce its tracking performance.

Figure 3.54 shows the spatial resolution along the  $25\text{ }\mu\text{m}$  pixel pitch as a function of the rotation angle. As expected, the resolution degrades after irradiation but remains well below the digital limit of  $7.2\text{ }\mu\text{m}$ . The best resolution—around  $3.5\text{ }\mu\text{m}$ —is achieved at a rotation angle similar to the one that yielded the optimal resolution before irradiation.

It is worth noting that the average cluster size at this angle is lower than 2 after irradiation, as shown in Figure 3.50. This discrepancy compared to the pre-irradiation case is explained by charge trapping, which can reduce the collected charge in one of the pixels, preventing it from surpassing the threshold—even if sufficient charge was initially generated by the traversing particle. As a result, clusters that would have consisted of two pixels may sometimes be reconstructed as single-pixel clusters, lowering the average cluster size. Increasing the angle beyond this point leads to more two-pixel clusters, but some of these originate from events that initially involved three pixels, with one of them failing to register a hit due to trapping. Since charge trapping degrades the cluster position reconstruction in both scenarios, the best spatial resolution is achieved at the angle where its impact is minimized.

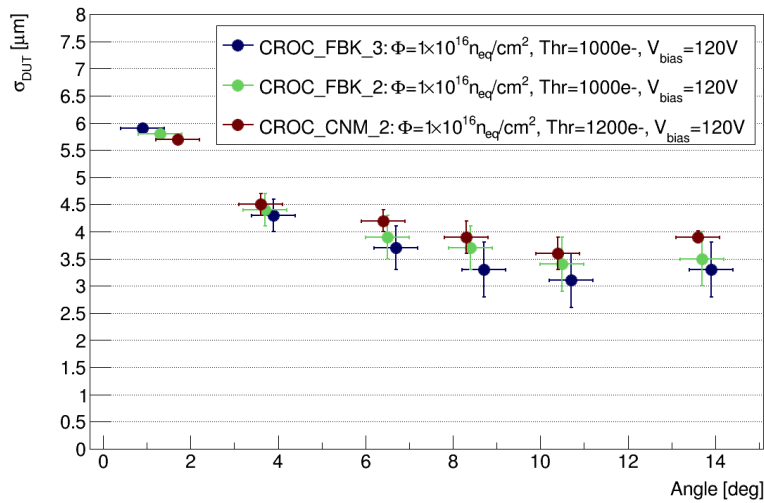


**Figure 3.54:** DUT spatial resolution along the short pixel pitch,  $\sigma_{DUT}$ , as a function of the rotation angle for modules irradiated to  $1 \times 10^{16}\text{ n}_{eq}\text{cm}^{-2}$  and biased at 120 V.

### 3.4. Comparison between test beam measurements and simulation

Digitization represents a crucial step in the CMSSW processing chain, as introduced in Section 1.3. It models the detector response to ionizing particles, converting simulated energy deposits into electronic signals. For 3D pixel detectors, the current digitization

algorithm relies on a simplified approach that introduces several approximations to reduce computational complexity [122].

In this model, the electric field is assumed to have only a radial component, neglecting the regions of very low or even null field that are present in the actual sensor geometry. The motion of charge carriers toward the electrodes is emulated as a sequence of discrete drift steps, each accompanied by Gaussian diffusion. Charge sharing is attributed solely to diffusion and is dynamically evaluated based on the proximity of charge carriers to the pixel boundaries. The signal induced in a pixel corresponds to the number of carriers that reach its collecting electrode. Furthermore, the model does not account for radiation-induced effects such as charge trapping, which become increasingly relevant after irradiation.

Despite these simplifications, the model provides a reasonable description of the detector response for non-irradiated devices, successfully reproducing key features observed in test beam data. As a result, it has been used in large-scale simulation studies to compare the performance of 3D and planar pixel technologies, contributing to the optimization of the Phase-2 tracker layout. However, a more sophisticated simulation is required to overcome the above-mentioned limitations and accurately describe the response after irradiation.

To this end, efforts are ongoing within the CMS Collaboration to develop a more complete simulation based on the PixelAV framework [123, 124]. PixelAV offers a realistic description of semiconductor physics, with a refined charge transport model, electric field maps derived from TCAD simulations, and signal induction based on the Shockley-Ramo theorem. Moreover, it aims to incorporate a charge trapping model to simulate radiation damage effects in irradiated 3D pixel sensors.

The simulation data were provided by Morris Swartz and Tamás Álmós Vámi through internal communication. The simulation uses the geometrical parameters of an FBK 3D pixel cell, as described in Section 3.1.2. In addition, it includes typical dopant concentrations as specified by the manufacturers:  $10^{12} \text{ cm}^{-3}$  for the sensor bulk,  $10^{19} \text{ cm}^{-3}$  for the  $p^+$  columnar electrodes, and  $10^{20} \text{ cm}^{-3}$  for the  $n^+$  columnar electrodes.

As part of this thesis, simulation results were compared against test beam measurements to validate the model and provide feedback for further improvement of the simulation. To ensure a fair comparison, a Gaussian smearing was applied to simulate the uncertainty in track position that arises from the finite telescope resolution in test beam measurements. Two smearing values were considered for the standard deviation of the Gaussian distribution— $2.5 \mu\text{m}$  and  $5 \mu\text{m}$ . An electronic noise contribution was also included in the simulated results, and the pixel threshold was matched to that used in the test beam data.

The comparisons presented below focus on non-irradiated FBK modules, as the agree-

ment after irradiation was limited. Figure 3.55 shows hit detection efficiency cell maps at normal incidence and a bias voltage of 50 V, including simulation results with both telescope resolution assumptions. The corresponding efficiency profiles along both pixel pitches are also shown. Similar comparisons for the average cluster size at a rotation angle of  $8^\circ$  and the same bias voltage are presented in Figure 3.56. Good agreement is observed in both cases, especially when using a telescope resolution of  $5\text{ }\mu\text{m}$ , which matches the value extracted from the test beam data analysis.

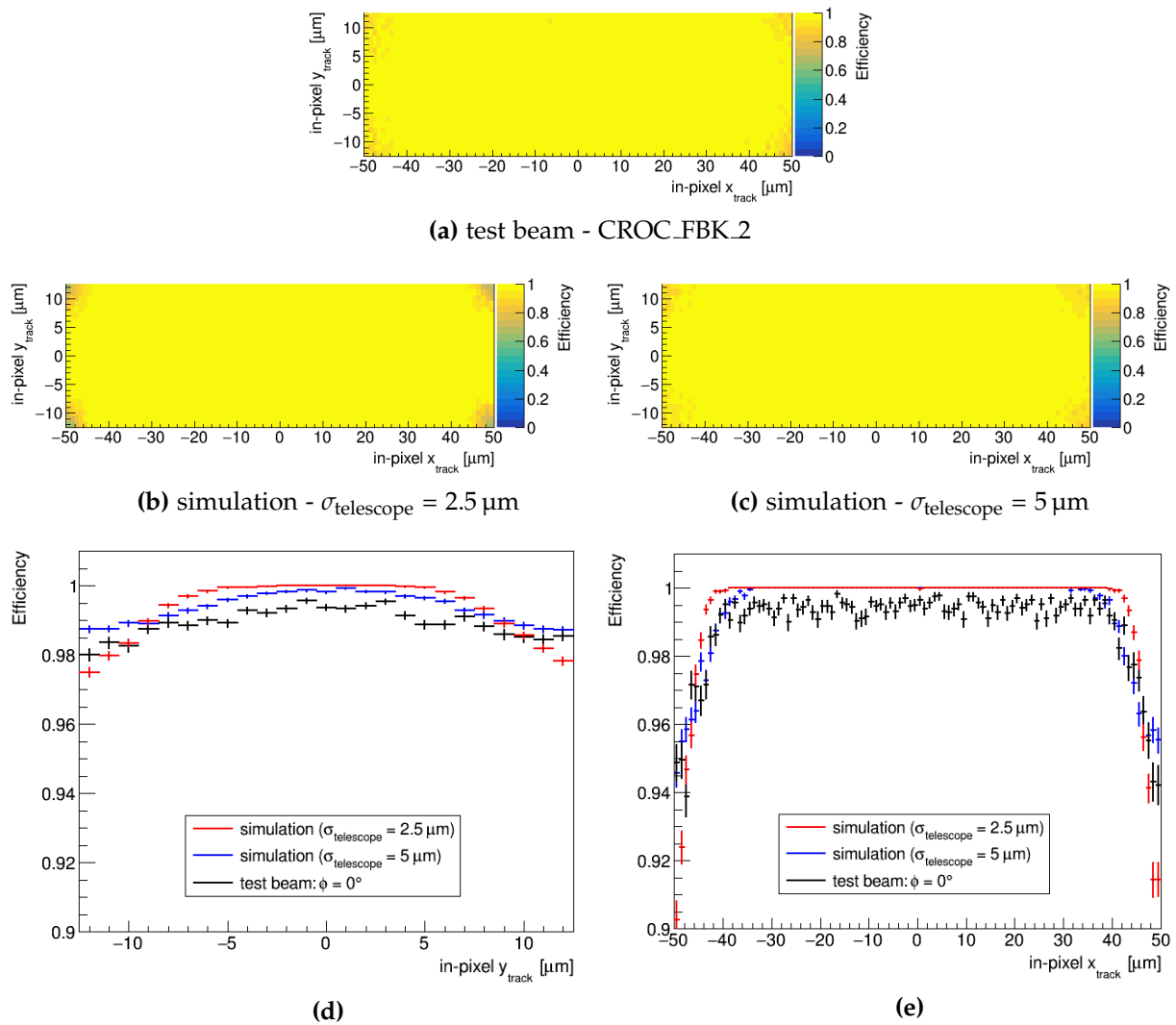


**Figure 3.55:** Comparison of test beam data and simulation for a non-irradiated FBK sensor biased at 50 V under normal incidence. Telescope resolution effects are simulated with track position uncertainties of  $2.5\text{ }\mu\text{m}$  and  $5\text{ }\mu\text{m}$ . Subfigures (a)-(c) show hit detection efficiency cell maps, while (d) and (e) display the corresponding profiles along the short and long pixel pitches, respectively.

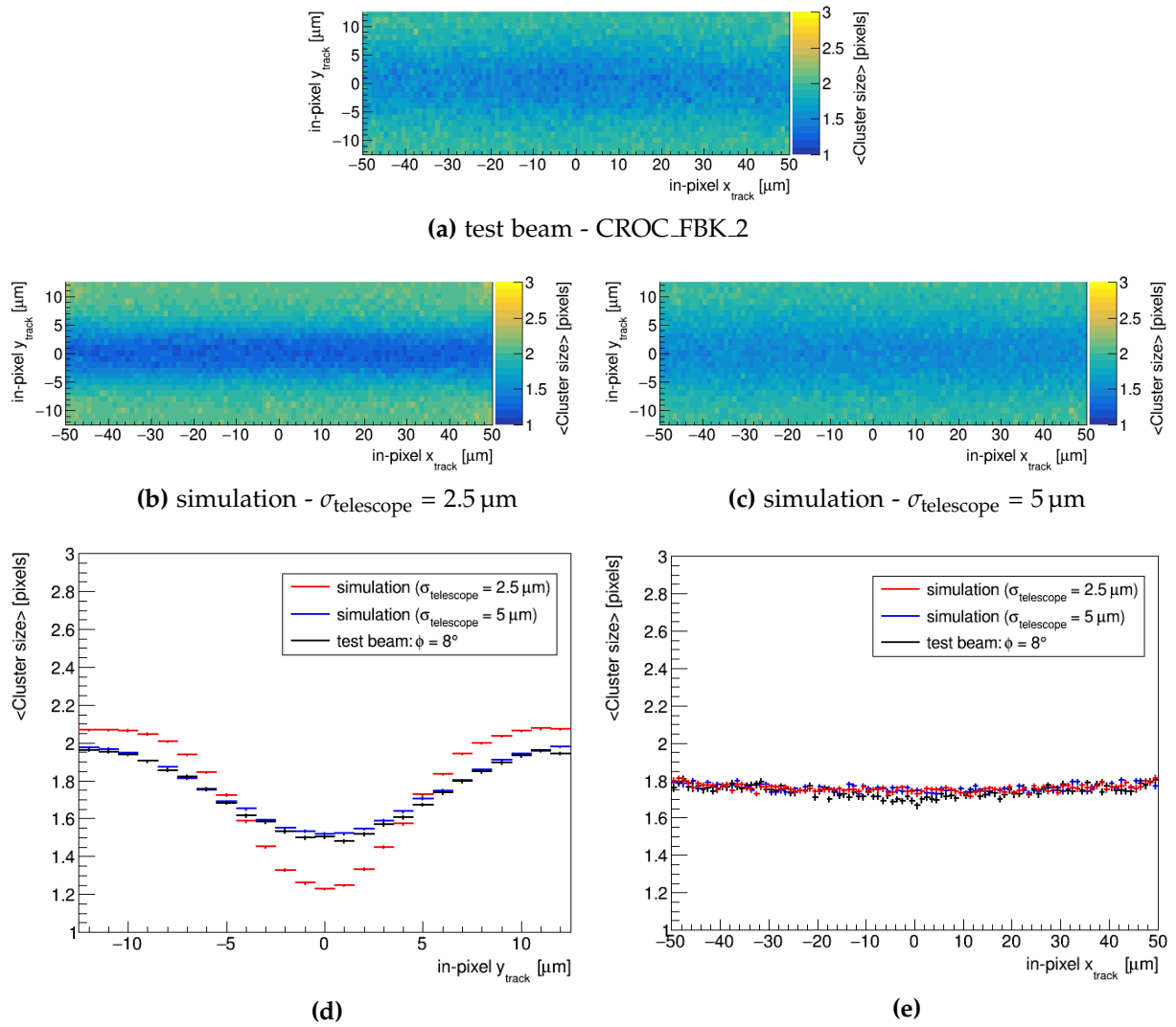


**Figure 3.56:** Comparison of test beam data and simulation for a non-irradiated FBK sensor biased at 50 V and rotated by  $8^\circ$ . Telescope resolution effects are simulated with track position uncertainties of  $2.5 \mu\text{m}$  and  $5 \mu\text{m}$ . Subfigures (a)-(c) show average cluster size cell maps, while (d) and (e) show the corresponding profiles along the short and long pixel pitches, respectively.

These comparisons serve to validate not only the simulation itself but also the data-driven method described in Section 3.3.2, which is used to determine both the telescope resolution and the DUT spatial resolution along the short pixel pitch. Figure 3.57 shows the residual distributions for a non-irradiated module biased at 50 V and rotated by  $8^\circ$ , using only the simulation with a telescope resolution of  $5 \mu\text{m}$ .

Given the good agreement with test beam data, the same fitting models are applied to simulation results. The residual distribution along the short pixel pitch is fitted with a sum of two Gaussian functions (equation 3.14), while the distribution along the long pixel pitch is fitted using the difference of two Gaussian CDFs (equation 3.13). The

telescope resolution extracted from the fit is consistent with the expected  $5\text{ }\mu\text{m}$ , and the DUT spatial resolution along the short pixel pitch is derived using equation 3.12. A comparison of the DUT spatial resolution obtained from simulation and test beam data is presented in Figure 3.58 as a function of the rotation angle, showing agreement with differences below  $1\text{ }\mu\text{m}$  across the full angular range.

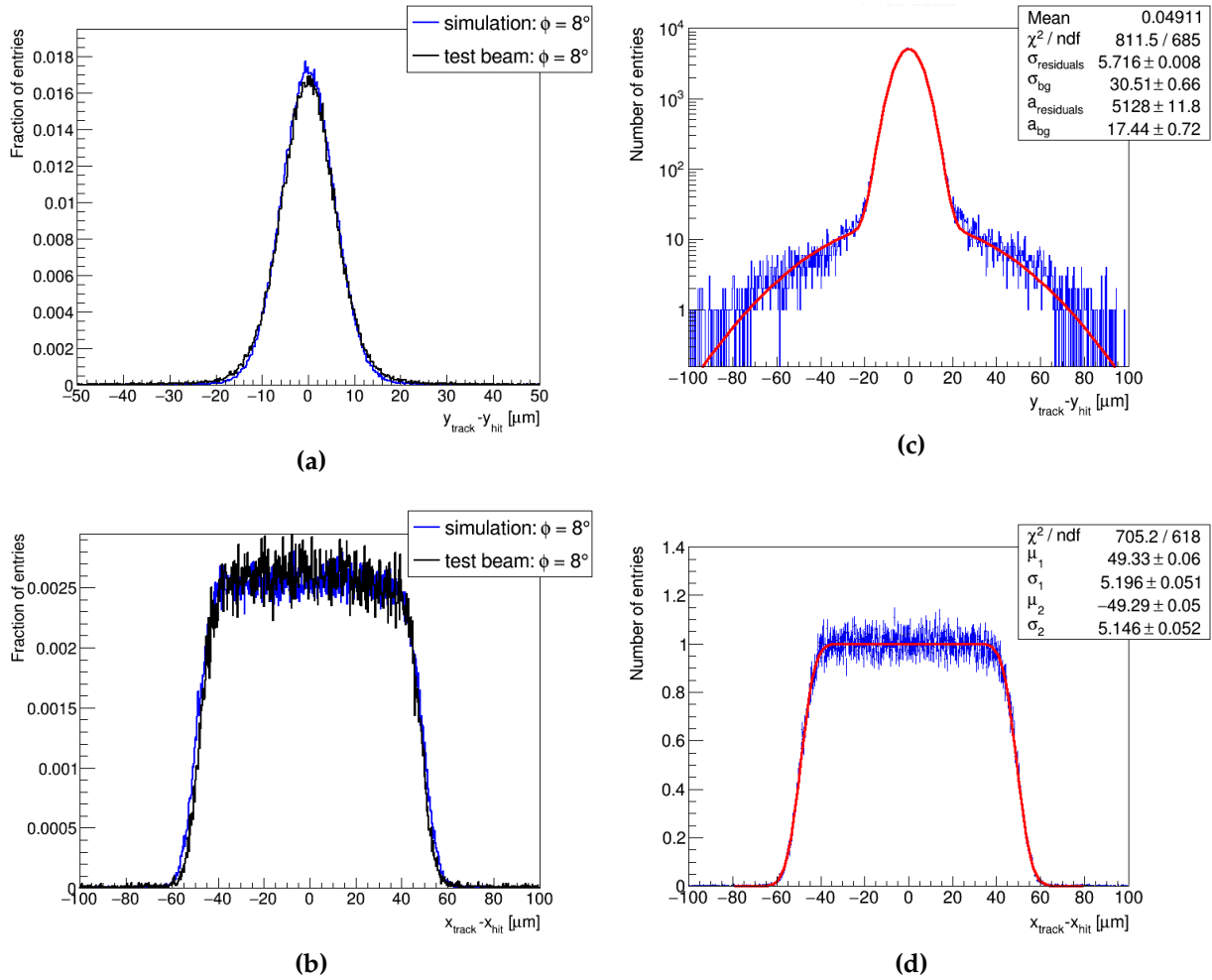


**Figure 3.57:** Comparison of test beam data and simulation for a non-irradiated FBK sensor biased at 50 V and rotated by  $8^\circ$ . Telescope resolution effects are simulated with a track position uncertainty of  $5\text{ }\mu\text{m}$ . One-dimensional residual distributions along (a) the short pixel pitch and (b) the long pixel pitch, normalized to the number of entries. The distributions from simulation are fitted with a sum of two Gaussian functions in (c) for the short pitch, and with the difference of two Gaussian CDFs in (d) for the long pitch. The distribution in (d) is normalized to the mean number of entries in the central region, and the fit parameters  $\sigma_1$  and  $\sigma_2$  represent independent estimates of the telescope resolution.



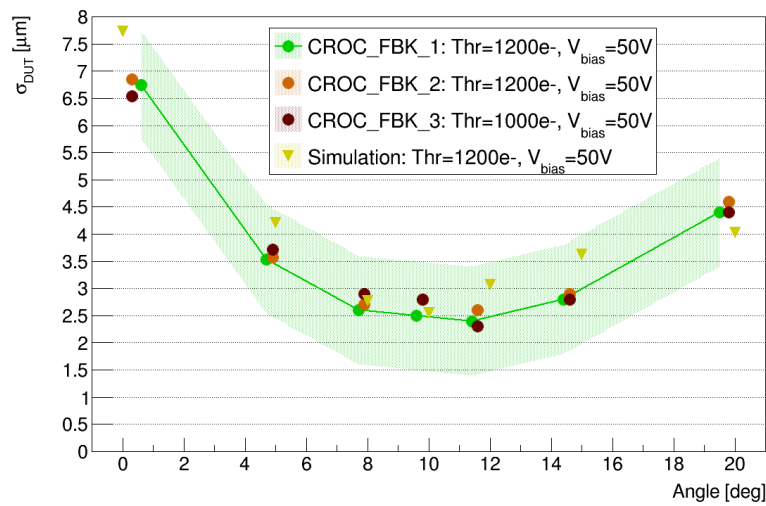


**Figure 3.58:** Comparison of test beam data and simulation for a non-irradiated FBK sensor biased at 50 V. Telescope resolution effects are simulated with a track position uncertainty of  $5\text{ }\mu\text{m}$ . The DUT spatial resolution along the short pixel pitch,  $\sigma_{\text{DUT}}$ , is shown as a function of the rotation angle. A shaded band of  $1\text{ }\mu\text{m}$  width is included to illustrate the level of agreement between simulation and test beam data.

### 3.5. Summary

The results presented in this chapter are part of a comprehensive R&D program aimed at the qualification of 3D pixel sensors for use in the innermost layer of the CMS Inner Tracker. Two manufacturers participated in this program: Fondazione Bruno Kessler (FBK) and Centro Nacional de Microelectrónica (CNM). Sensors from both fabrication centers were bump-bonded to the full-scale readout chip prototype, known as CROCv1, and characterized in beam tests before and after irradiation.

Non-irradiated modules exhibit excellent performance, reaching full depletion at bias voltages below 10 V, hit detection efficiency above 97%, and spatial resolution as low as  $2.5\text{ }\mu\text{m}$ . CNM sensors show slightly lower efficiency at normal incidence compared to FBK sensors, owing to their larger column diameter. The efficiency loss due to the presence of columnar electrodes is completely recovered under a small rotation of the devices relative to the beam. Therefore, this inefficiency is not expected to impact the overall detector performance once installed in the CMS experiment, where particles will cross the sensors with a wide range of incidence angles.

Following irradiation to a fluence of  $1 \times 10^{16}\text{ n}_{\text{eq}}/\text{cm}^2$ , the modules maintain a hit detection efficiency above 97% at normal incidence for bias voltages between 90 V and 150 V, with fewer than 2% masked pixels. The spatial resolution is measured to be as low as  $3.5\text{ }\mu\text{m}$ , representing an acceptable degradation compared to the non-irradiated case. At this irradiation level, CNM and FBK sensors exhibit similar performance. Even

at the highest tested fluence of  $1.6 \times 10^{16} \text{ n}_{\text{eq}}/\text{cm}^2$ , the operational margin remains sufficiently broad, with hit detection efficiency above 96% at normal incidence and a low fraction of masked pixels across bias voltages from 100 V to 130 V.

To accurately determine the telescope and hit spatial resolutions, a data-driven method was developed as part of this thesis. The results obtained from test beam measurements with this approach are consistent with simulations, providing strong validation of the methodology.

Some of the most relevant results have been published in [125], which also includes test beam measurements performed on 3D pixel sensors bump-bonded to the half-scale readout chip prototype, known as RD53A. In summary, the overall performance of 3D pixel detectors before and after irradiation fulfills the CMS requirements for installation in the innermost layer of the Inner Tracker. The production of the final sensors is currently underway at FBK, with system integration and commissioning scheduled to begin at the end of 2026.

## Chapter 4

# System-level testing and integration quality control

This chapter focuses on bump-bond quality control and system-level testing with hybrid pixel modules developed for the CMS IT. The first part covers the commissioning and validation of the setups and procedures established to assess the connectivity between the sensor and the readout electronics—an essential step before deployment in the final experiment. The second part presents some tests conducted to evaluate the performance of the modules and specific functionalities of the readout electronics when operated within the power distribution scheme foreseen for the CMS IT.

### 4.1. Bump-bond quality control

Since poor connections ultimately degrade the detector performance, bump-bond quality control in hybrid pixel modules is essential to ensure the integrity of the electrical and mechanical connections between the sensor and the readout electronics. Two different procedures are presented below, intended for use during double and quad module production to verify the status of each module before installation in the CMS IT. To qualify for installation, a module must have fewer than 600 pixels with connectivity issues per chip.

Initial tests were performed with single-chip modules, and the results presented here represent the starting point of the module production phase at IFCA, which is ongoing at the time of writing. The devices under test, CROC\_FBK\_A and CROC\_FBK\_B, are 3D pixel single-chip modules. Table 3.2 summarizes their characteristics, including the measured values of  $V_{\text{ref\_ADC}}$  required for converting  $\Delta V_{\text{Cal}}$  units to electrons via equation 3.2.

#### 4.1.1. Evaluation with an X-ray method

This method aims to identify bump-bonds that are fully or partially disconnected using an X-ray source. The experimental setup employs a PHYWE XR 4.0 X-ray machine, shown in Figure 4.1a. It features an X-ray tube with a tungsten target, whose typical emission spectrum is presented in Figure 4.1b. This spectrum includes characteristic  $L_\alpha$ ,  $L_\beta$ , and  $L_\gamma$  peaks superimposed on a bremsstrahlung background. The tube voltage and current—adjustable via the machine’s control panel—determine the maximum energy and intensity of the emitted X-rays. For the quality control tests, the tube is operated at 35 kV and 1 mA.

To achieve uniform illumination, the module is positioned approximately 12 cm from the X-ray tube outlet, and no collimator is used. It is connected to the Ph2-ACF DAQ system described in Section 3.1.1. To prevent overheating and ensure stable operation, a fan is installed inside the machine.

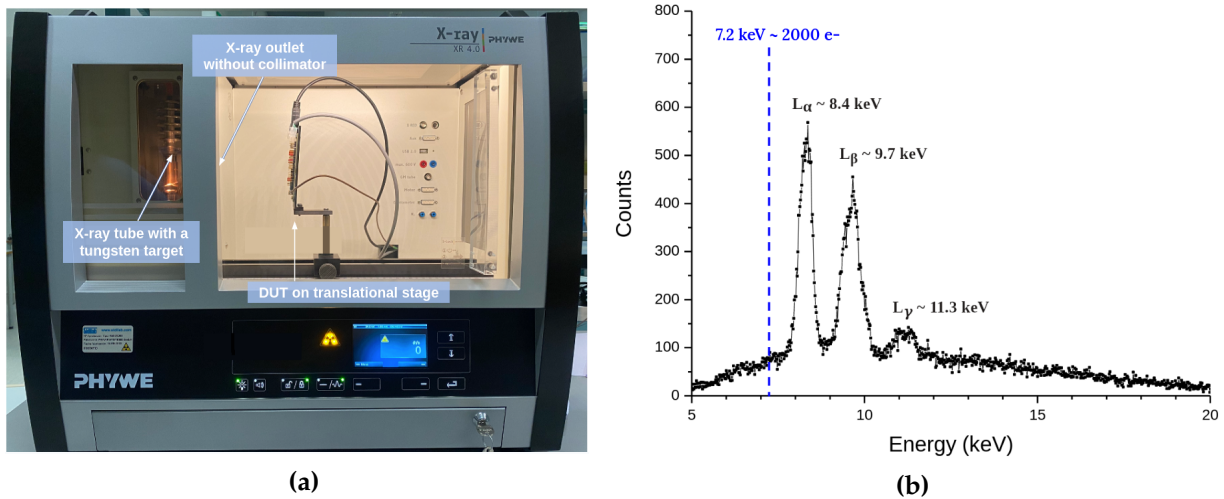


**Figure 4.1:** (a) X-ray setup used for bump-bond quality control. The module under test is positioned approximately 12 cm from the X-ray tube outlet. A fan for active cooling (not visible in the image) is installed inside the machine. (b) Typical X-ray emission spectrum from a tungsten target, showing characteristic  $L_\alpha$ ,  $L_\beta$ , and  $L_\gamma$  peaks. Right image adapted from [126].

Since this method relies on detecting real hits produced by X-rays, a uniform response across the pixel matrix is required for reliable quality control. To ensure this, the modules are fine-tuned to an average pixel threshold of 2000 electrons, following the chip power trimming and the calibration procedure described in Section 3.1.3.

This relatively high threshold is chosen to remain well above the noise level, minimizing spurious hits, while still ensuring sufficient X-ray statistics for testing purposes. Assuming a mean energy of 3.6 eV to generate an electron-hole pair in silicon, a threshold of 2000 electrons corresponds to a deposited energy of 7.2 keV, which lies just below the tungsten  $L_\alpha$  peak at 8.4 keV.

For these tests, the chips are operated in LDO mode and the sensors are biased at 30 V to ensure full depletion. After global threshold adjustment and threshold equalization, noisy and stuck pixels are masked. Figures 4.2a and 4.2b show the resulting masks for modules CROC\_FBK\_A and CROC\_FBK\_B, respectively. Only 6 noisy pixels were masked in CROC\_FBK\_A, and 2 stuck pixels in CROC\_FBK\_B.

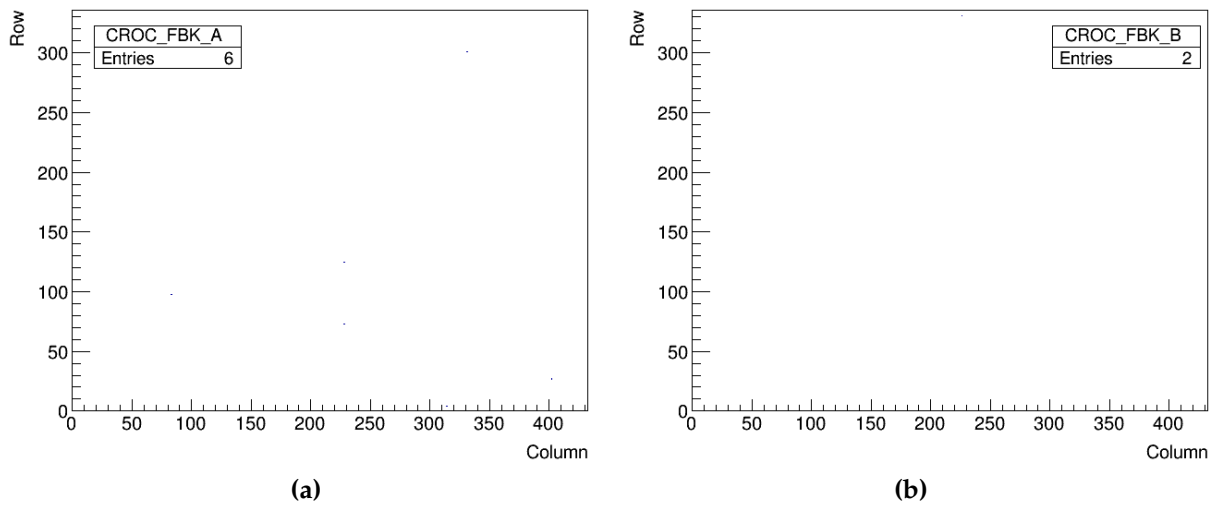


**Figure 4.2:** Map of pixels masked due to noisy or stuck behavior in modules (a) CROC\_FBK\_A and (b) CROC\_FBK\_B, both tuned to a threshold of 2000 electrons. Measurements were performed following threshold equalization.

The final tuning status for both modules is presented in Figure 4.3, which includes the superimposed S-Curves of all pixels, along with the corresponding one-dimensional threshold and noise distributions. The results confirm successful fine-tuning to the target threshold.

Once tuning is completed, each module is exposed to X-rays for approximately five minutes—the time required to evaluate occupancy across the entire pixel matrix using the Ph2-ACF software. Since this software provides direct occupancy measurements, and each pixel is read out a fixed number of times ( $n_{\text{Events}} = 10^7$ ), the number of registered hits per pixel can be reconstructed by inverting equation 3.3.

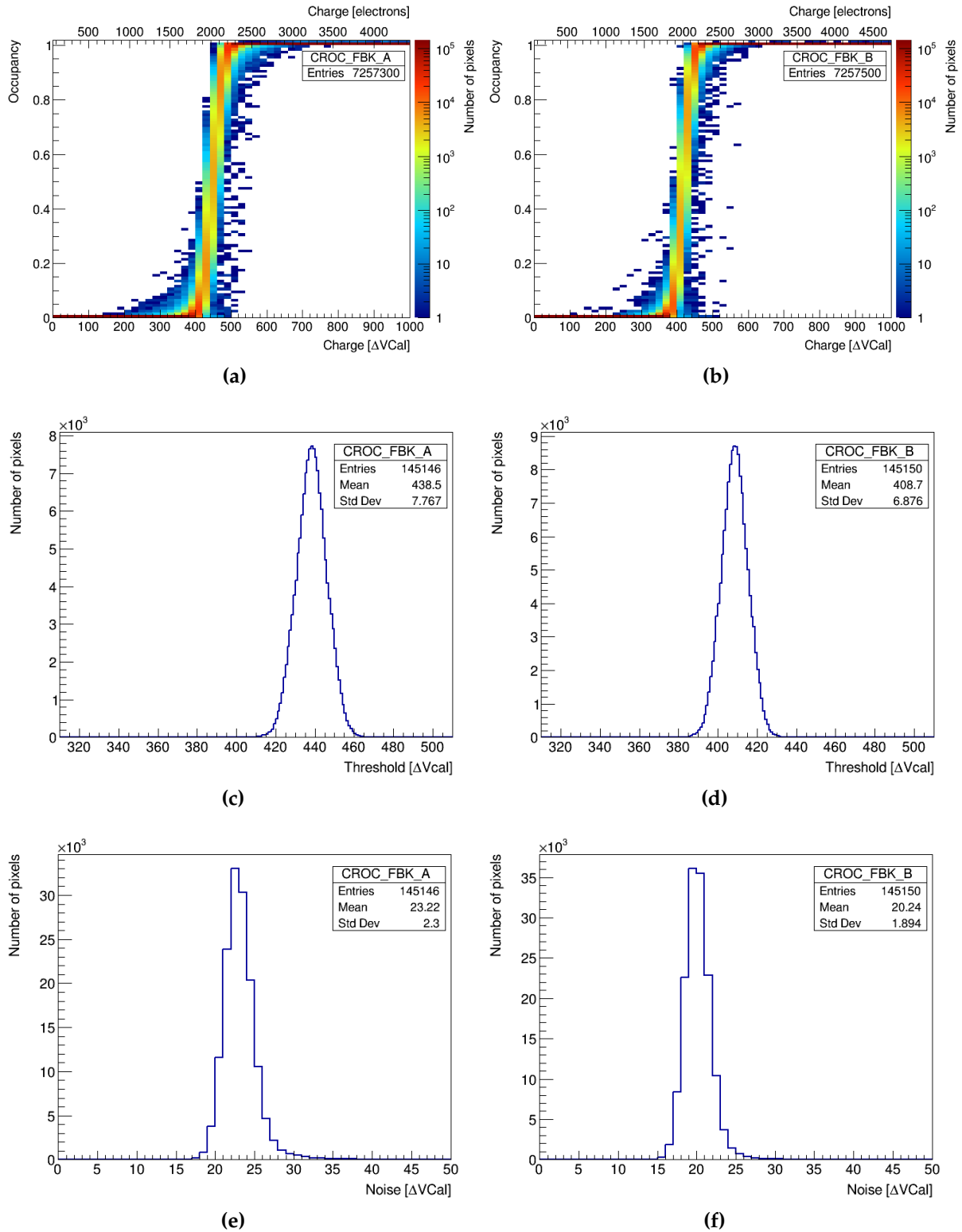


**Figure 4.3:** Superimposed S-Curves of all pixels in (a) CROC\_FBK\_A and (b) CROC\_FBK\_B, both tuned to a target threshold of 2000 electrons. (c) and (d) show the corresponding threshold distributions, while (e) and (f) show the corresponding noise distributions. Measurements were performed after masking noisy and stuck pixels.

Figures 4.4a and 4.4b show the hit maps for modules CROC\_FBK\_A and CROC\_FBK\_B, respectively. Both maps exhibit an overall uniform response, consistent with uniform X-ray illumination and proper bump-bond connectivity. However, some pixels register zero or very few hits, indicating defective bump-bonds. This is particularly evident in CROC\_FBK\_B, where a localized cluster of disconnected bumps is clearly visible in the lower-left corner of the map.

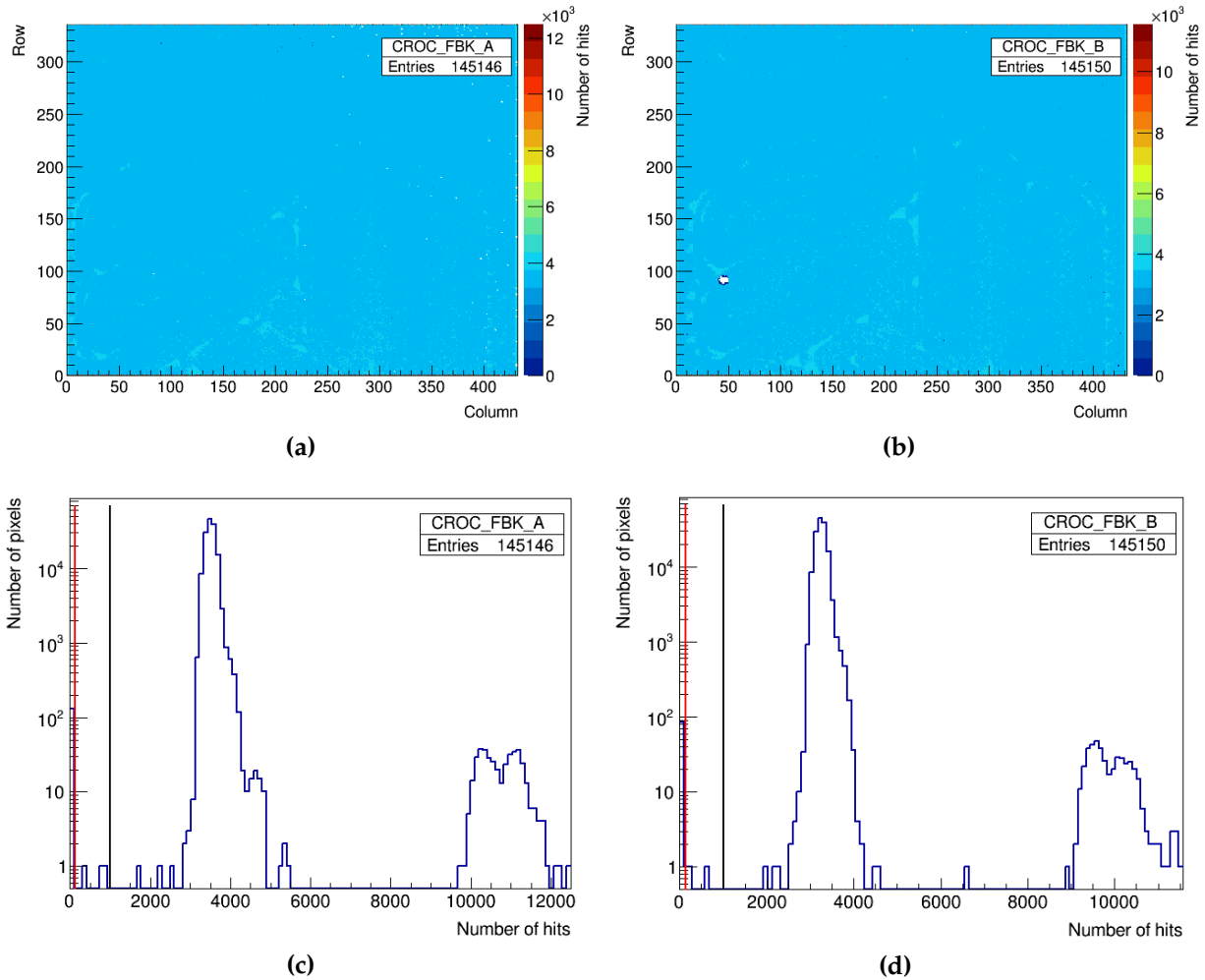


**Figure 4.4:** Map of hits per pixel in (a) CROC\_FBK\_A and (b) CROC\_FBK\_B. (c) and (d) show the corresponding one-dimensional distributions. The red and black vertical lines indicate the limits of 100 hits and 1000 hits used for the identification of missing and problematic bump-bonds, respectively. More details are given in the text.

The corresponding one-dimensional hit distributions are shown in Figures 4.4c and 4.4d. These histograms reveal three different pixel populations: a group with zero hits, a main peak centered around 3500 hits, and a smaller group of pixels centered between 10 000 and 10 500 hits—approximately three times the main peak value. While the first group represents disconnected bumps, the latter corresponds to edge pixels located



in the first and last matrix rows. As shown in the sensor layout in Figure 3.5b, the edges have a different design from the rest of the matrix, which may give rise to inhomogeneous electric fields and an extended depletion region beyond the nominal pixel boundaries. This leads to charge collection from outside the intended pixel area, resulting in an artificially increased occupancy for these edge pixels.

Defective bump-bonds are classified into two categories based on the number of registered hits. Pixels with fewer than 100 hits are categorized as missing bump-bonds, indicating a near-complete disconnection. Those recording between 100 and 1000 hits are labeled as problematic bump-bonds, reflecting partial but insufficient connectivity. These classification thresholds are indicated by vertical red and black lines in the one-dimensional hit distributions.

Figures 4.5a and 4.5b show the spatial distribution of defective bump-bonds in modules CROC\_FBK\_A and CROC\_FBK\_B, respectively. As anticipated from the hit maps, most defective bumps in CROC\_FBK\_B are clustered in the lower-left corner, whereas those in CROC\_FBK\_A are more dispersed, mainly toward the right side of the matrix. The results are summarized in Table 4.1, which reports 133 and 89 defective bump-bonds in CROC\_FBK\_A and CROC\_FBK\_B, respectively, with the majority identified as missing.

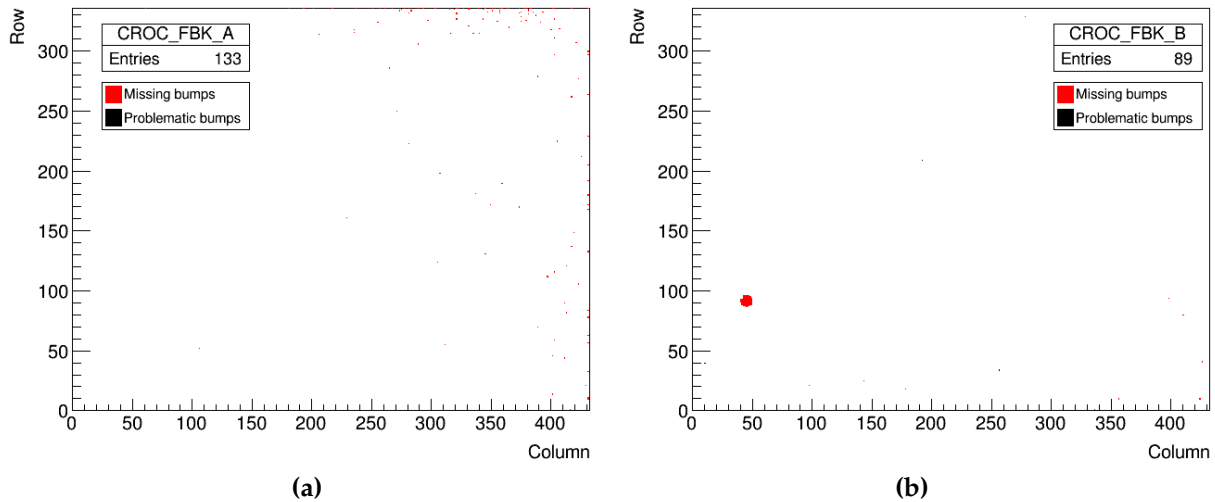


**Figure 4.5:** Map of defective bump-bonds in (a) CROC\_FBK\_A and (b) CROC\_FBK\_B, identified using the X-ray quality control method. Missing and problematic bump-bonds are shown in red and black, respectively. More details are given in the text.

**Table 4.1:** Classification of defective bump-bonds in the hybrid pixel modules under test, using the X-ray quality control method. Bump-bonds are categorized as either missing or problematic based on the number of hits. More details are given in the text.

Module name	Missing bumps	Problematic bumps	Total number of defective bumps
CROC_FBK_A	130	3	133
CROC_FBK_B	86	3	89

#### 4.1.2. Evaluation with an electrical method

This method aims to identify bump-bonds that are fully or partially disconnected without the need for an external radiation source, using only the Ph2-ACF DAQ system described in Section 3.1.1. A fan provides active cooling during module operation.

The principle of this approach is to evaluate and compare pixel performance under two sensor biasing regimes: reverse bias, to fully deplete the sensor, and a small forward bias. In pixels with proper bump-bond connectivity, the transition between these regimes is expected to produce a shift in the measured threshold and noise due to the change in sensor capacitance between the depleted and undepleted states. In contrast, for pixels with disconnected bump-bonds, no significant change is expected between the two biasing regimes, as the sensor capacitance is not seen by the front-end.

For these tests, the modules do not require fine-tuning, so threshold equalization is not performed. Instead, the modules are only tuned to a high average pixel threshold that enhances the expected performance shifts, facilitating the identification of defective bump-bonds. Since no threshold equalization is needed, this approach is faster than the X-ray method. To further reduce testing time, noisy and stuck pixels were not masked. As a result, stuck pixels are misidentified as having defective bump-bonds, as the method cannot inherently distinguish between the two cases. However, this simplification is acceptable, as prior knowledge of stuck pixels from the X-ray method allows for a proper interpretation of the results.

The chips are operated in LDO mode, and the sensors are initially biased with a reverse voltage of 30 V to ensure full depletion. After chip power trimming, a global threshold adjustment to 6000 electrons is applied, following the procedure described in Section 3.1.3. The tuning status for modules CROC\_FBK\_A and CROC\_FBK\_B is shown in Figures 4.6a – 4.6c and 4.7a – 4.7c, respectively. These include the superimposed S-Curves of all pixels and the one-dimensional threshold and noise distributions.

The sensor is then operated under forward bias. The applied voltage corresponds to the highest value for which the current remains negative—this is possible because the low-voltage return line is not exactly at 0 V. Although forward voltages up to 1 V could

be applied, this configuration is preferred, as it already induces the desired change in sensor capacitance while minimizing the risk of damaging the device. For both modules, the selected voltage was 0.35 V.

In the forward-bias configuration, the status of the previous tuning is reevaluated. The results are shown in Figures 4.6d – 4.6f and 4.7d – 4.7f for modules CROC\_FBK\_A and CROC\_FBK\_B, respectively. Compared to the results from the reverse-bias configuration, the S-Curves of most pixels exhibit a clear shift toward higher injected charges. Only a small subset remains centered around 6000 electrons with little to no change in shape, potentially indicating defective bump-bonds.

The threshold and noise distributions also shift to higher values, but they contain significantly fewer entries than those obtained under reverse bias. This reduction occurs because the S-Curves of approximately 40% of the pixels move beyond the scanned range and cannot be fitted. However, this does not affect the effectiveness of the method, as these large shifts are consistent with proper bump-bond connectivity.

Figures 4.8a – 4.8b and 4.8d – 4.8e show the one-dimensional distributions of threshold and noise shifts for modules CROC\_FBK\_A and CROC\_FBK\_B, respectively. These distributions are obtained by subtracting the forward-bias measurement from the reverse-bias measurement of each pixel.

Three pixel populations are observed in the threshold shift distributions. Pixels with shifts centered around zero are potentially associated with defective bump-bonds, since they show little to no change between biasing conditions. Instead, the other two populations correspond to well-connected bumps. The main difference between these two groups is that, for pixels centered around 6000 electrons—approximately 1330  $\Delta V_{Cal}$  in CROC\_FBK\_A and 1250  $\Delta V_{Cal}$  in CROC\_FBK\_B—the S-Curves under forward bias extended beyond the scanned range and could not be fitted. As a result, no threshold measurement was available in forward bias for those pixels, and a default value of zero was used in the shift calculation. This led to a shift equal to the value measured under reverse bias. The same artifact appears in the noise shift distributions as a sharp peak around 20–25  $\Delta V_{Cal}$ .

Pixels with negligible changes in both threshold and noise are identified as having defective bump-bonds, which are classified into two categories. Pixels with an absolute threshold shift below 40  $\Delta V_{Cal}$  and an absolute noise shift below 15  $\Delta V_{Cal}$  are categorized as missing bumps. Among the remaining pixels, those with an absolute threshold shift below 75  $\Delta V_{Cal}$  and an absolute noise shift below 25  $\Delta V_{Cal}$  are labeled as problematic bumps. These criteria are indicated in the one-dimensional distributions with vertical red and black lines, respectively. To better visualize the defective pixels, the noise shift is plotted against the threshold shift in Figures 4.8c and 4.8f, where red and black rectangles enclose pixels with missing and problematic bumps, respectively.

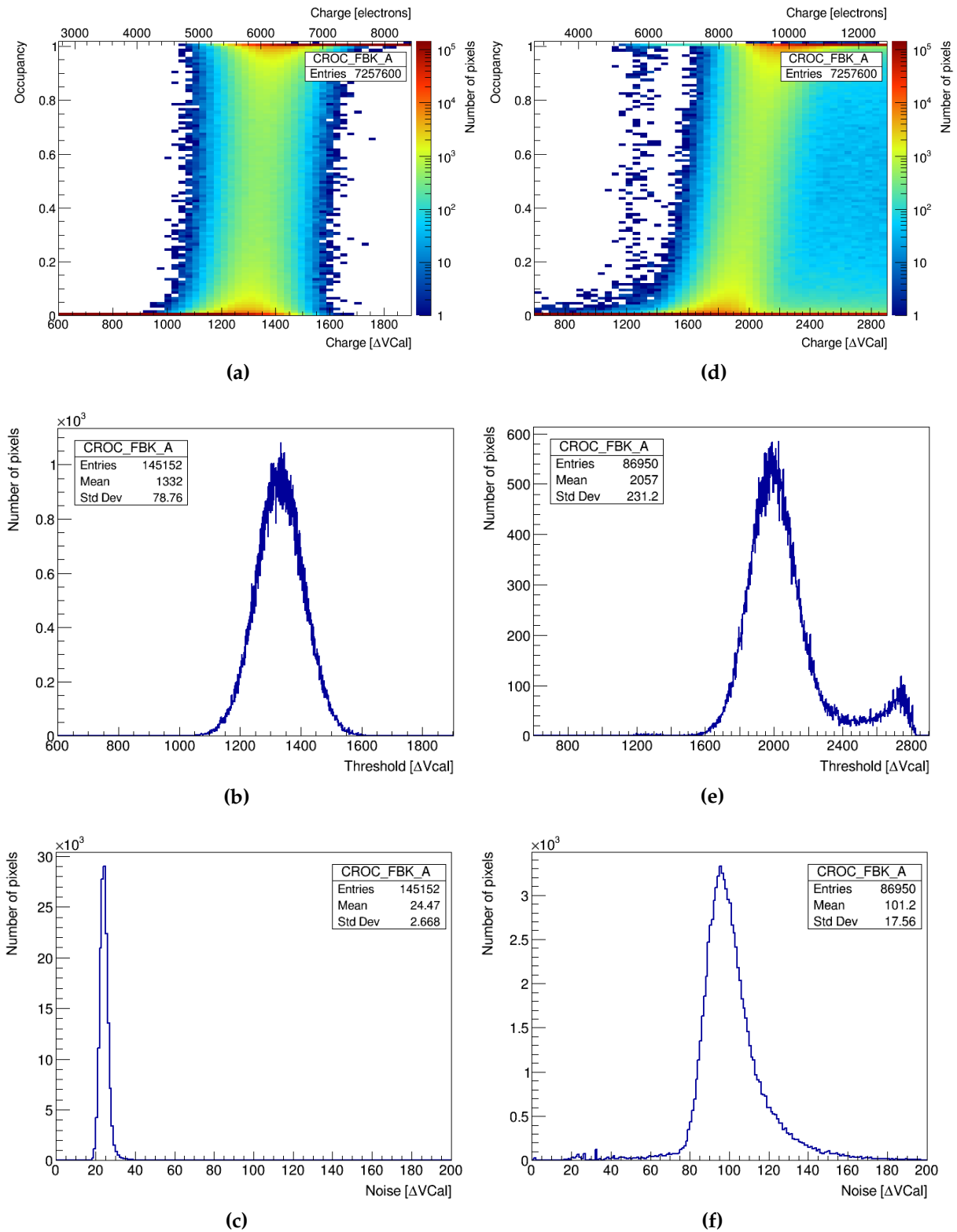


**Figure 4.6:** Superimposed S-Curves of all pixels in CROC\_FBK\_A tuned to a target threshold of 6000 electrons, under (a) reverse bias and (d) forward bias. (b) and (e) show the corresponding threshold distributions, while (c) and (f) show the corresponding noise distributions. Note the different axis ranges between reverse and forward bias.

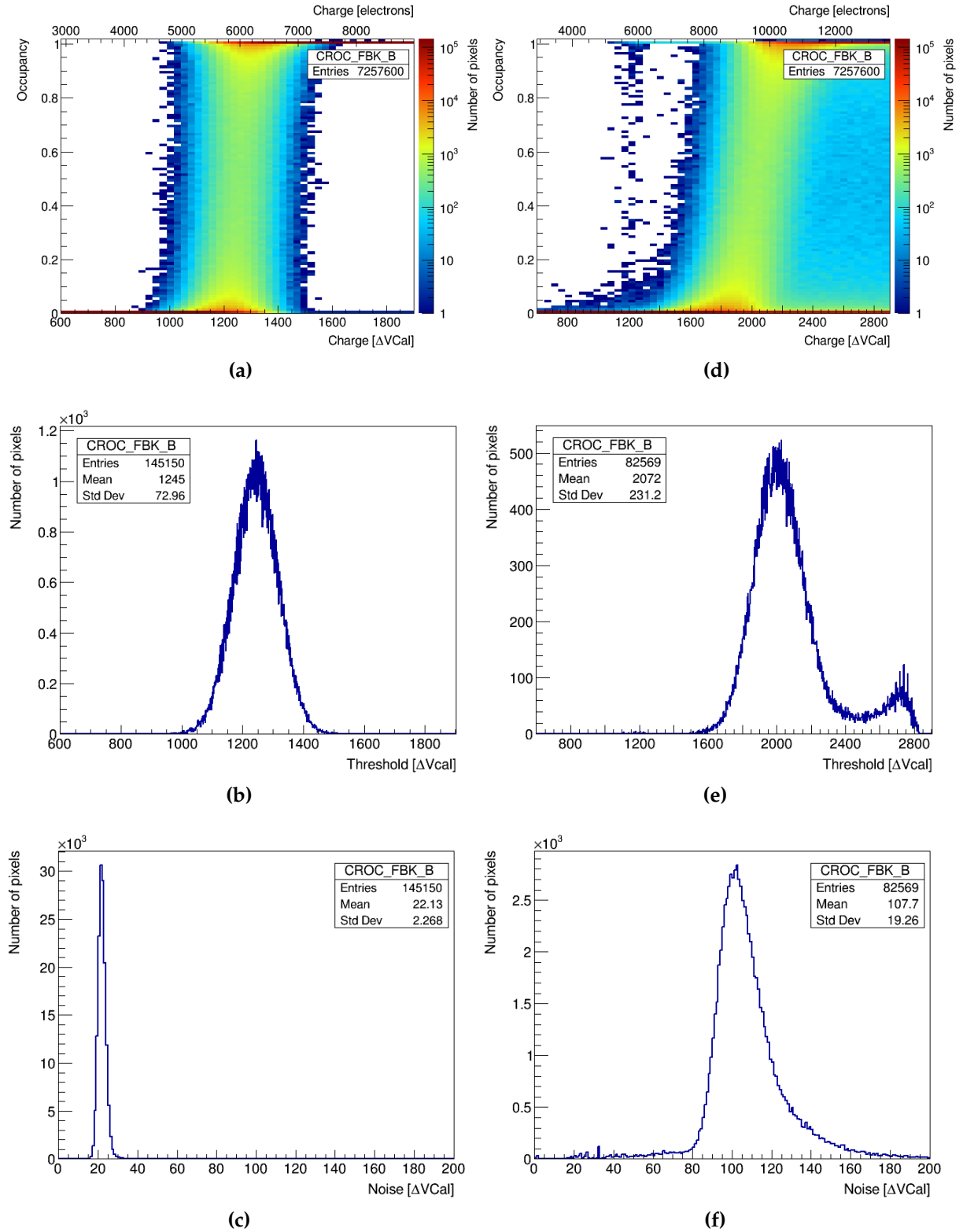


**Figure 4.7:** Superimposed S-Curves of all pixels in CROC\_FBK\_B tuned to a target threshold of 6000 electrons, under (a) reverse bias and (d) forward bias. (b) and (e) show the corresponding threshold distributions, while (c) and (f) show the corresponding noise distributions. Note the different axis ranges between reverse and forward bias.

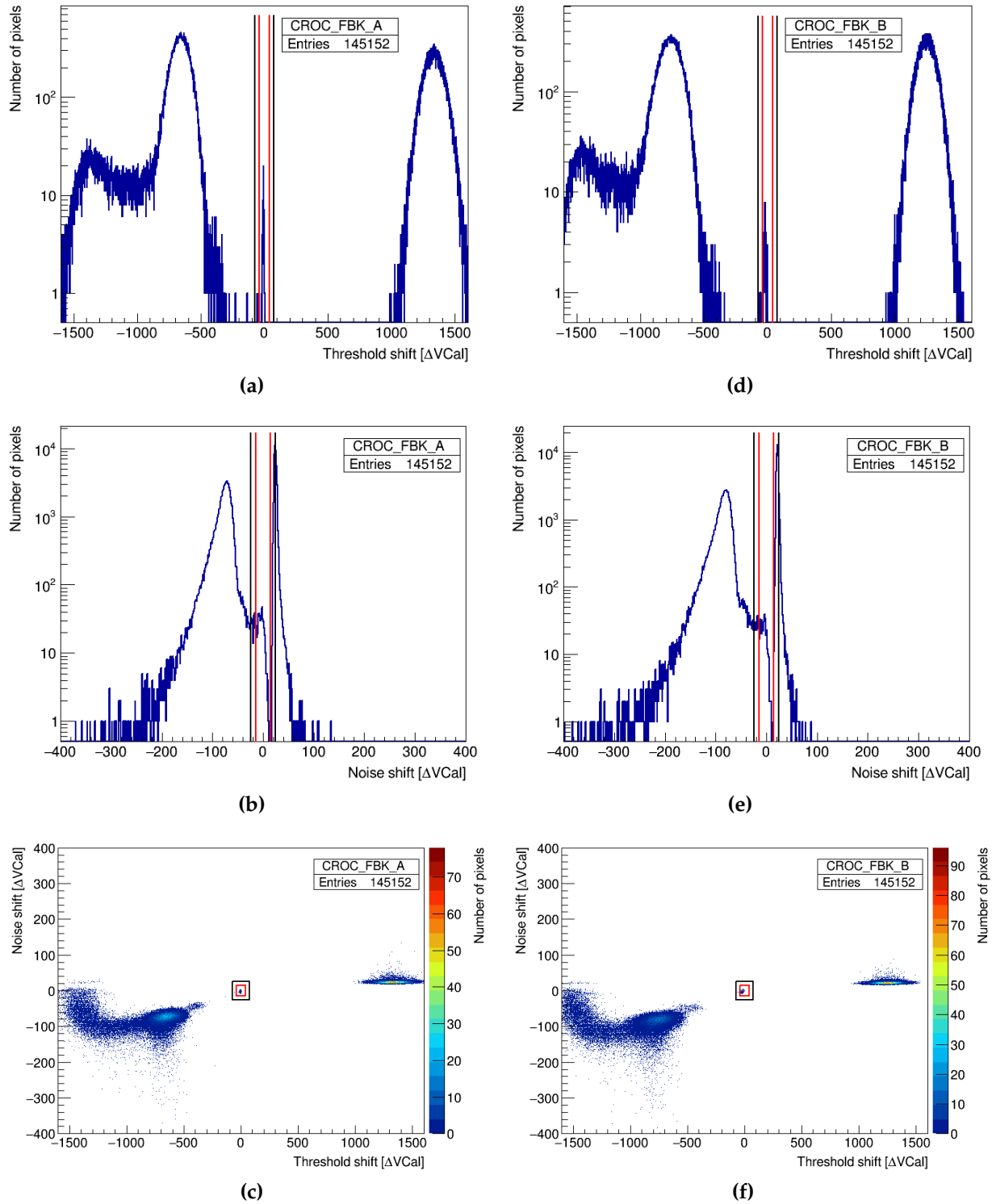


**Figure 4.8:** (a) Threshold shift distribution and (b) noise shift distribution for module CROC\_FBK\_A. The red and black vertical lines indicate the selection limits for the identification of missing and problematic bump-bonds, respectively. (c) shows the noise shift versus threshold shift for CROC\_FBK\_A, with red and black rectangles enclosing missing and problematic bump-bonds. Similar distributions are shown for module CROC\_FBK\_B in (d)–(f). More details are given in the text.

Figure 4.9 shows the spatial distribution of defective bump-bonds in each module. In CROC\_FBK\_A, they are predominantly located on the right side of the matrix, while in CROC\_FBK\_B, most are concentrated within a localized cluster in the lower-left corner. The results are summarized in Table 4.2, which reports 133 defective bumps in CROC\_FBK\_A and 91 in CROC\_FBK\_B, with the majority identified as missing.

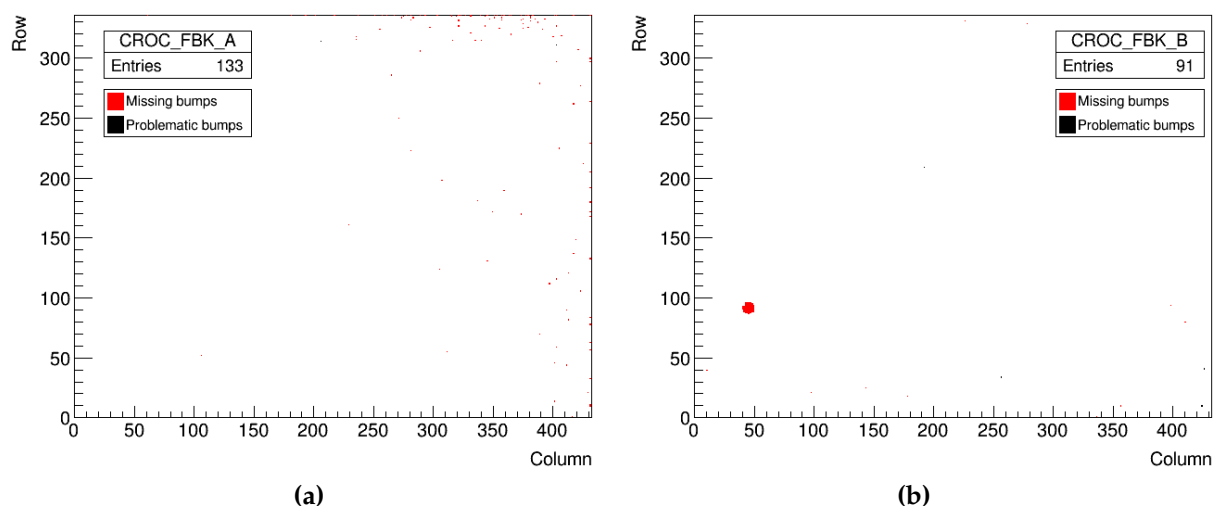


**Figure 4.9:** Map of defective bump-bonds in (a) CROC\_FBK\_A and (b) CROC\_FBK\_B, identified using the electrical quality control method. Missing and problematic bump-bonds are shown in red and black, respectively. More details are given in the text.

**Table 4.2:** Classification of defective bump-bonds in the hybrid pixel modules under test, using the electrical quality control method. Bump-bonds are categorized as either missing or problematic based on the threshold and noise shifts between reverse and forward bias. More details are given in the text.

Module name	Missing bumps	Problematic bumps	Total number of defective bumps
CROC_FBK_A	131	2	133
CROC_FBK_B	87	4	91

### 4.1.3. Comparison between methods

Table 4.3 summarizes the number of defective bump-bonds identified in each module using both the X-ray and electrical methods. For completeness, it also includes the noisy and stuck pixels that were masked during module tuning in the X-ray procedure.

In the case of module CROC\_FBK\_A, both methods identified 133 defective bump-bonds, with a 100% match. For module CROC\_FBK\_B, the electrical method detected



91 defective bumps, while the X-ray method found only 89. However, all these 89 bumps were classified as defective by both methods. The two additional bumps flagged by the electrical method correspond to the pixels masked as stuck during the X-ray analysis, confirming consistency between the procedures. This excellent agreement underscores the effectiveness of both methods in detecting bump-bonds with poor or no connectivity.

In both modules, the number of defective bump-bonds remains well below the acceptance threshold of 600 per chip, demonstrating compliance with the CMS IT requirements for installation in the final experiment.

**Table 4.3:** Comparison of defective bump-bonds identified in the modules under test using the X-ray and electrical quality control methods. Pixels identified as noisy or stuck during the tuning performed in the X-ray method are also included.

	CROC.FBK.A		CROC.FBK.B	
	X-ray method	Electrical method	X-ray method	Electrical method
Noisy pixels	6	-	0	-
Stuck pixels	0	-	2	-
Defective bumps	133	133	89	91

The electrical method was initially selected as the standard procedure for bump-bond quality control during the module production phase, while the X-ray method was reserved for further investigation of modules exhibiting anomalous behavior. This decision was driven by several advantages of the electrical approach: it does not require additional expensive equipment—which is often unavailable at assembly centers—avoids the use of external radiation sources and their associated safety protocols, and enables parallel testing of multiple modules.

Since these tests were conducted, an alternative electrical method based on crosstalk measurements between neighboring pixels has been developed [127]. This newer passive approach also shows strong agreement with the methods discussed in this thesis. Like the reverse-forward biasing method, it relies on the Ph2-ACF DAQ system and requires no additional setup. Its main advantage lies in its ease of automation, which has led to its adoption as the preferred procedure for bump-bond quality control. It is worth noting that automating the reverse-forward biasing method is more challenging, as inadequate control during forward-bias operation could potentially damage the modules.

## 4.2. System-level tests

System-level tests were conducted at the INFN-Florence laboratory to evaluate the performance of 3D pixel modules and specific functionalities of the readout electronics when operated within a serial-power chain. Before presenting the results of these tests, an overview of the power distribution scheme foreseen for the CMS IT is provided, with special focus on the serial-powering architecture.

### 4.2.1. Power distribution scheme

The Phase-2 CMS tracker will feature increased area and granularity compared to the current tracker, resulting in a significantly higher power demand. Around 50 kW and 100 kW will be required to power all modules in the IT and OT systems, respectively.

Providing low-voltage power to the readout electronics through direct powering is not feasible, as the required thick cables would significantly increase the material budget, compromising tracker performance. The approach adopted for the Phase-1 CMS tracker, based on local DC/DC converters, remains suitable only for the OT, where radiation levels are lower and space is less constrained. For the IT, the only viable solution is a serial powering scheme, which relies on integrated on-chip regulators—the SLDO introduced in Section 3.1.1. These are both lightweight and sufficiently radiation hard to withstand the extreme conditions expected during HL-LHC operation. This innovative powering system represents a significant technological challenge, since it has never been implemented at this scale in high-energy physics [128].

Figure 4.10 shows a schematic representation of the IT power distribution system. In the serial powering scheme, a chain of modules connected in series is supplied with a constant current, which passes from one module to the next. Within each module, the CROC chips are connected in parallel and share the incoming current. Each CROC contains two independent SLDO regulators that generate the required voltages for the analog and digital domains. This separation ensures that current fluctuations in the relatively noisier digital circuitry do not interfere with the sensitive analog front-end.

The bias voltage needed to deplete the sensors is provided via direct powering and distributed in parallel to all modules within a serial-power chain. This may involve one or two high-voltage lines, depending on the location inside the IT. The high-voltage return line is shared with that of the low voltage, as shown in Figure 4.10. Since each module has a local reference set by its readout electronics, the modules operate at different ground potentials depending on their position within the serial-power chain. Consequently, the effective bias voltage applied to the sensor varies from module to module. For this reason, one of the CMS qualification requirements for 3D pixel sensors—listed in Table 3.1—was to ensure a wide operational margin before breakdown with excellent performance.

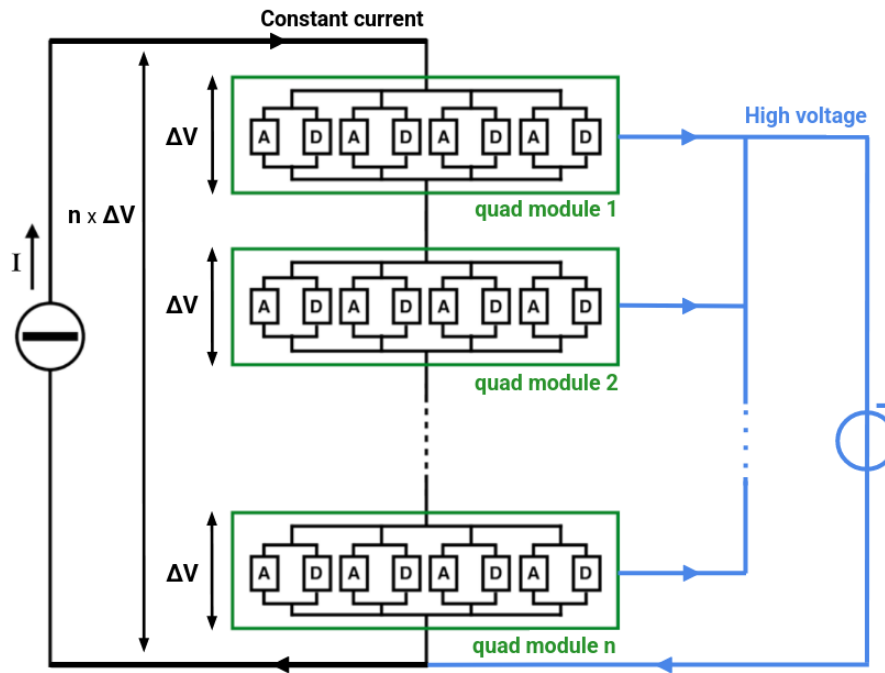


**Figure 4.10:** Schematic representation of the power distribution system in a serial-power chain consisting of  $n$  quad modules. The analog and digital domains of each chip are labeled A and D, respectively. A constant current  $I$  flows through the chain, with each module exhibiting a voltage drop  $\Delta V$ . The high voltage for sensor biasing is distributed in parallel, as indicated in blue. Image adapted from [129].

Each SLDO combines the functionalities of an LDO regulator and a shunt circuit [130]. A simplified SLDO power scheme is shown in Figure 4.11a. The LDO component is responsible for voltage regulation, ensuring that the chip core receives a stable voltage of 1.2–1.3 V for optimal performance of both analog and digital domains. The shunt component manages any excess current not consumed by the chip, effectively decoupling its varying current needs from the constant current flowing through the chain. This architecture enables the chain to behave as a steady load from the perspective of the power supply.

The SLDO circuit can be modeled electrically as a resistor in series with an offset voltage. This resistive input behavior is essential to ensure efficient and consistent current sharing among chips and regulators connected in parallel. During startup, the chip passes through a transient region at low current where it is not yet operational. Once sufficient current is supplied, internal voltage and current references are established, the output voltage stabilizes, and the input voltage begins to exhibit ohmic behavior. The ideal VI curve of the SLDO in either the analog or digital domain is illustrated in Figure 4.11b.

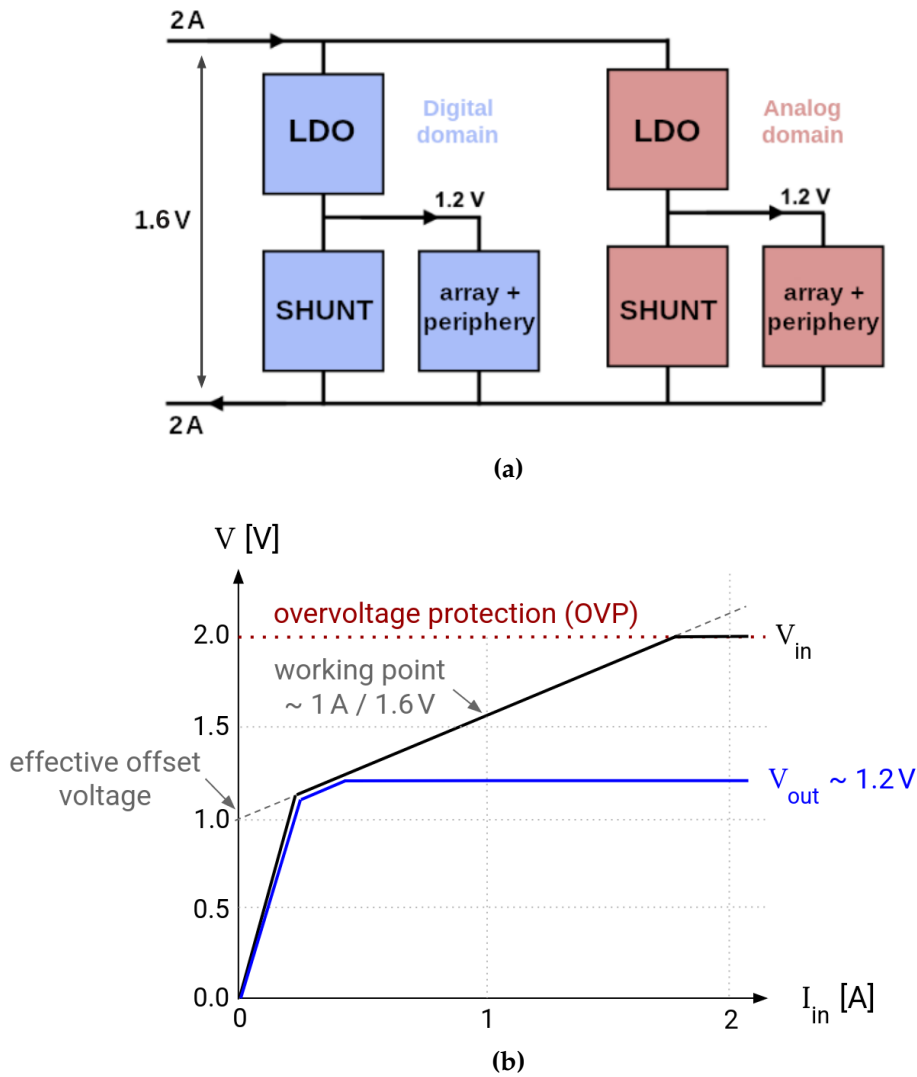


**Figure 4.11:** (a) Simplified SLDO power scheme of the CROCv1 chip. The analog and digital domains are shown in red and blue, respectively. (b) Ideal VI characteristic of the SLDO in either domain. The unregulated input voltage,  $V_{in}$ , and the regulated output voltage,  $V_{out}$ , are plotted as a function of the input current per domain,  $I_{in}$ . Top image adapted from [128].

The main parameters governing SLDO operation—input impedance and offset voltage—are configurable through external resistors and, along with the input current, define the working point. This point must be carefully chosen to minimize power dissipation while delivering sufficient current for reliable chip operation. To accommodate rapid fluctuations in the circuitry and maintain stability, the input current must include a headroom of approximately 15–20% above the nominal consumption. Taking this into account, each chip is typically supplied with around 2 A, corresponding to 4 A and 8 A for serial-power chains with double and quad modules, respectively.

Minimizing power losses requires a tradeoff between the offset voltage and input impedance. A low offset combined with a high resistance can result in large increases in input voltage—and hence power dissipation—for small changes in current. Simulations have shown that an effective offset voltage of 1 V, paired with an input resistance of 500–600 m $\Omega$ , provides a good compromise. This configuration yields a solid working point of 1.5–1.6 V at an input current of 1 A per domain, ensuring sufficient margin above the output voltage for stable regulation [131].

Although careful tuning of the SLDO working point minimizes power losses during normal operation, the system must also be robust against potential failure scenarios. Each regulator is designed to handle input currents up to 2 A and input voltages up to 2 V. To prevent damaging the regulator circuit in an over-voltage event, a current clamp is implemented in parallel with the SLDO. This protection system activates when the input voltage approaches the upper limit, diverting excess current and keeping the voltage within safe levels.

To avoid current imbalance within a module, the offset voltage must be well-matched across all chips connected in parallel. While a target offset can be set by trimming the main reference current, as discussed in Section 3.1.1, small chip-to-chip variations may still exist, leading to uneven current sharing. To mitigate these mismatches, the offset voltages of all chips in a module are tied together through a resistor network, which is described in [97]. This offset-sharing scheme should also provide robustness against individual chip failures.

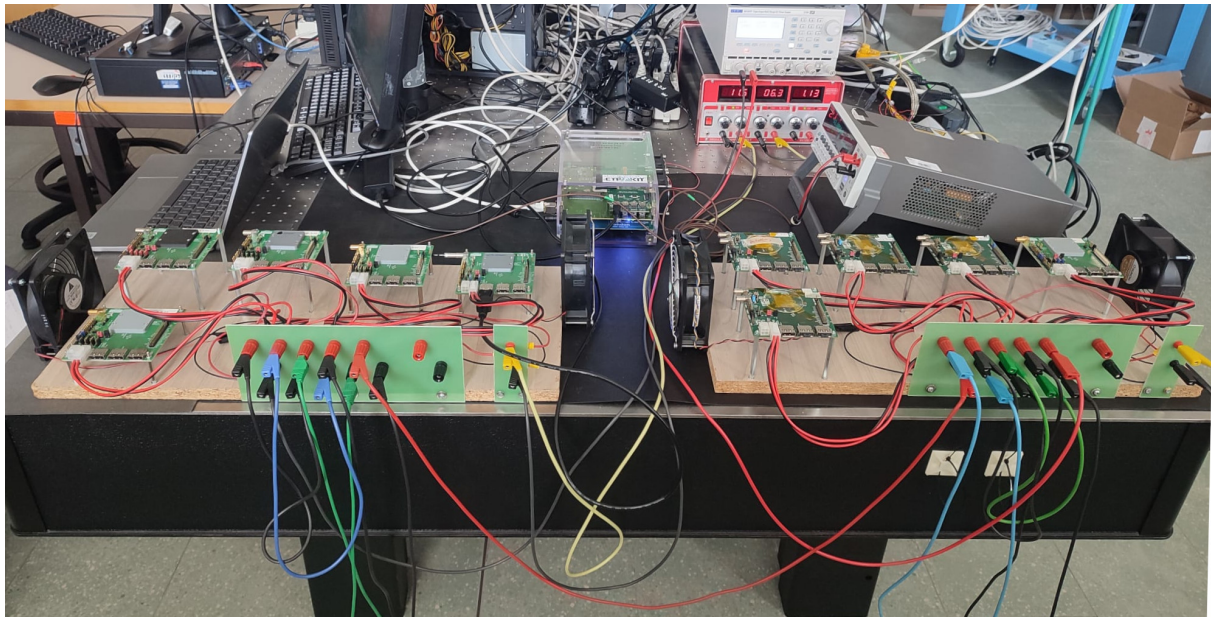
If one of the chips enters an open-circuit state, it stops drawing current and no longer contributes to the shared offset voltage. As a result, the remaining working chips must shunt the additional current, and the drop in the common offset increases the current required to reach a given input voltage. Thanks to the serial-power chain design, only the chips connected in parallel are affected by such a failure, while the remaining modules in the chain continue to operate normally.

#### 4.2.2. Performance in a serial-power chain

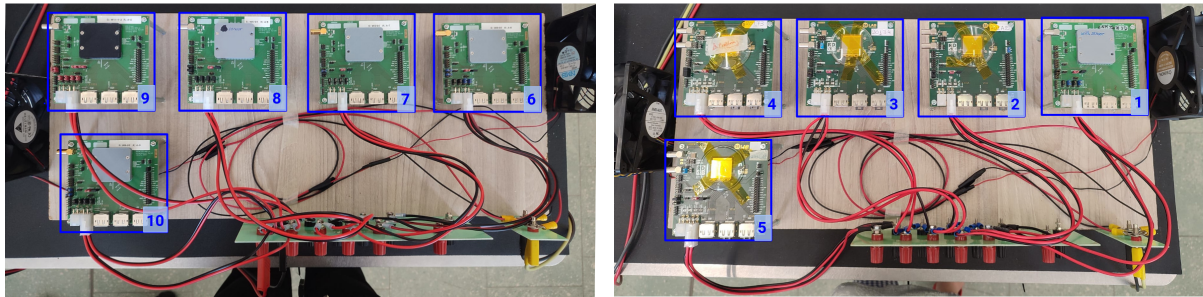
Modules in a serial-power chain operate at different local ground potentials and, therefore, the sensor bias voltage varies along the chain, as discussed in Section 4.2.1. Chains in the IT comprise between eight and twelve modules, with the longest chain in the TBPX consisting of ten modules. Assuming a voltage drop of 2.5 V per module—including contributions from both the module itself and the inter-module connections—the maximum bias voltage difference in a ten-module chain can reach 22.5 V when using a single high-voltage line or 10 V when using two. This variation could eventually impact the performance of sensors with a low depletion voltage, such as 3D pixel sensors, and should therefore be investigated.



To evaluate the performance of a non-irradiated 3D pixel module as a function of its position in a serial-power chain, a setup with ten CROCv1 SCCs connected in series was assembled. The chain included four digital modules, four modules with planar pixel sensors and two modules with 3D pixel sensors. Figure 4.12 shows a picture of the entire setup, with the module numbering indicating the order of current flow through the chain. Four fans were placed near the modules to provide active cooling during operation.



(a)



(b)

**Figure 4.12:** Experimental setup of a serial-power chain with ten single-chip modules. (a) Full view of the setup, including DAQ system, power supplies and fans for system cooling. (b) Close-up view of the modules, with the numbering indicating the order of current flow through the chain.

Details of the 3D pixel module under test are provided in Table 4.4. The module was mounted on an SCC equipped with 510 m $\Omega$  resistors on both the analog and digital SLDO inputs. As described in Section 3.1.3, chip power trimming is essential

to reach the optimal working point and ensure proper operation of both digital and analog domains. In SLDO mode, this is achieved partly by configuring jumpers on the SCC and partly through software control registers. The trimming process begins by adjusting the main reference current so that  $V_{\text{ofs}}$  is as close as possible to 0.5 V. The output voltages of the digital and analog regulators are then fine-tuned to fall within the target range of 1.2–1.3 V.

**Table 4.4:** Details of the 3D pixel module under test in a serial-power chain, including some geometric characteristics and the measured value of  $V_{\text{ref\_ADC}}$  for charge conversion from  $\Delta V_{\text{Cal}}$  units to electrons through equation 3.2.

Module name	Readout chip	Sensor	Column diameter [ $\mu\text{m}$ ]	Column gap [ $\mu\text{m}$ ]	Pixel size [ $\mu\text{m}^2$ ]	$V_{\text{ref\_ADC}}$ [mV]
CROC_CNM.A	CROCv1	CNM	8	20	$50 \times 50$	775

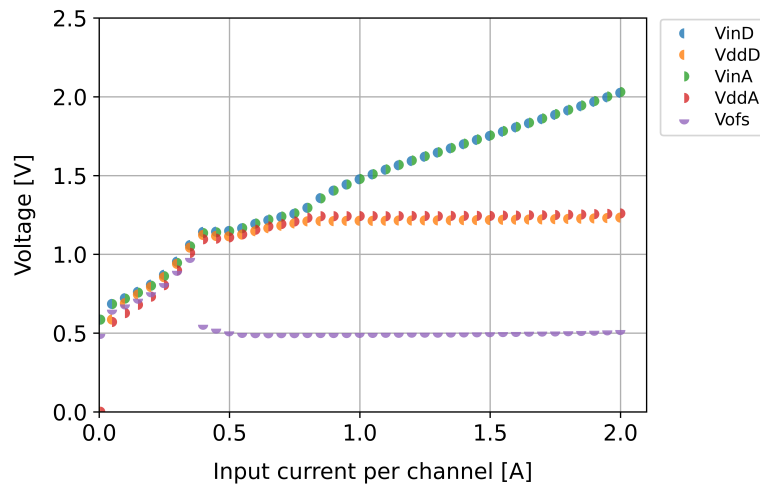
The module was tested both in standalone mode and within the serial-power chain. In standalone mode, a total current of 2 A was supplied—corresponding to 1 A per domain—with a generously high compliance voltage of 2.5 V. In the serial-power chain, the same current was delivered, but the compliance voltage was increased to 25 V to accommodate the cumulative voltage drop across all ten modules.

Figure 4.13 shows the VI characteristics of the module, measured while ramping the total input current from 0 A to 4 A, after trimming the main reference current. The measurements were made using a multimeter and a scanner card connected to the SCC monitoring pins. The input current is reported per domain, assuming equal sharing between the analog and digital circuits.

Following startup, the input voltage increases linearly with current, while the output voltage remains stable—consistent with the ideal SLDO behavior illustrated in Figure 4.11b. At the nominal working point of 1 A per domain, an input voltage of approximately 1.5 V is reached, as expected given the input impedance of 510 m $\Omega$ . Comparable VI curves were obtained when the module was operated both in standalone mode and within the serial-power chain.

As seen in Figure 4.13, the value of  $V_{\text{ofs}}$ , which is common to both the analog and digital SLDOs, was correctly set during the trimming process. It is important to note that the effective offset voltage is twice the reference  $V_{\text{ofs}}$ , as it may need to exceed the preregulator output voltage and therefore cannot be directly generated [97].





**Figure 4.13:** VI characteristics of the CROCv1 chip connected to the CNM 3D pixel sensor under test. The analog and digital domains are labeled as *A* and *D*, respectively. The unregulated input voltage,  $V_{in}$ , the regulated output voltage,  $V_{dd}$ , and the reference offset voltage,  $V_{ofs}$ , are shown. Comparable measurements were obtained in both standalone and serial-power configurations.

The performance of the 3D pixel module under test was first evaluated in a standalone configuration. The chip was powered in SLDO mode, and the sensor was biased at 30 V—well above its full depletion voltage. Following the procedure described in Section 3.1.3, the module was tuned to an average pixel threshold of 1000 electrons, with 150 pixels masked for being either noisy or stuck.

Using this tuning as a reference, the module performance was then reassessed at three positions in the serial-power chain: the first, sixth, and tenth, corresponding to the order of current flow indicated in Figure 4.12b. The total voltage required to power the chain was approximately 17 V. Assuming an equal voltage drop across each module, the sensor was effectively biased at 45.3 V, 36.8 V, and 30 V when placed in the first, sixth, and tenth positions, respectively.

Figure 4.14 compares the one-dimensional threshold and noise distributions obtained in standalone mode and at the three selected positions along the serial-power chain. Table 4.5 summarizes the main parameters of these distributions, converted from  $\Delta V_{Cal}$  units to electrons using equation 3.2.

The results indicate that the performance of a 3D pixel module is not significantly affected by its position in the chain. The small variation observed in the threshold mean is likely due to non-uniform cooling and is negligible from the performance perspective. This confirms the robustness of the serial-powering scheme and its suitability for the CMS IT.

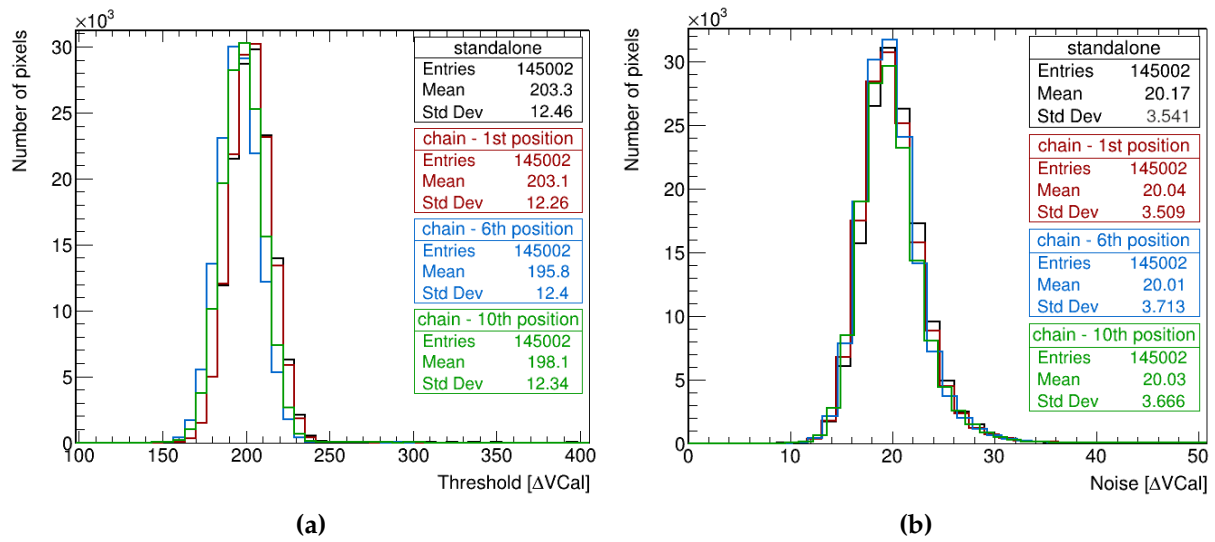


**Figure 4.14:** (a) Threshold and (b) noise distributions for a 3D pixel module tested at three different positions of a serial-power chain. The performance in standalone mode at a bias voltage of 30 V is shown in black. Measurements at the first, sixth and tenth positions in the chain are depicted in red, blue and green, respectively.

**Table 4.5:** Summary of the front-end tuning results for a single-chip 3D pixel module tested in standalone mode and at three positions along a serial-power chain. It includes the mean,  $\mu$ , and standard deviation,  $\sigma$ , of the threshold and noise distributions. The conversion from  $\Delta V_{\text{Cal}}$  units to electrons is given by equation 3.2.

Measurement position	Threshold distribution		Noise distribution	
	$\mu$ [electrons]	$\sigma$ [electrons]	$\mu$ [electrons]	$\sigma$ [electrons]
standalone	1024	59	96	17
1 <sup>st</sup> in chain	1023	58	95	17
6 <sup>th</sup> in chain	989	59	95	18
10 <sup>th</sup> in chain	999	59	95	17

### 4.2.3. Performance under system failure

The offset voltages of all chips in a double or quad module are tied together to suppress small chip-to-chip variations that could lead to uneven current sharing, as discussed in Section 4.2.1. To test this offset-sharing functionality, a setup was assembled with four digital CROCV1 SCCs connected in parallel, emulating a quad module. Each SCC was equipped with 604 mΩ input resistors on both analog and digital SLDOs. Unlike an actual quad or double module, this SCC-based configuration allows for deliberate

offset mismatches, enabling tests under extreme conditions. Figure 4.15 shows the setup with all four chips sharing their offset voltages.

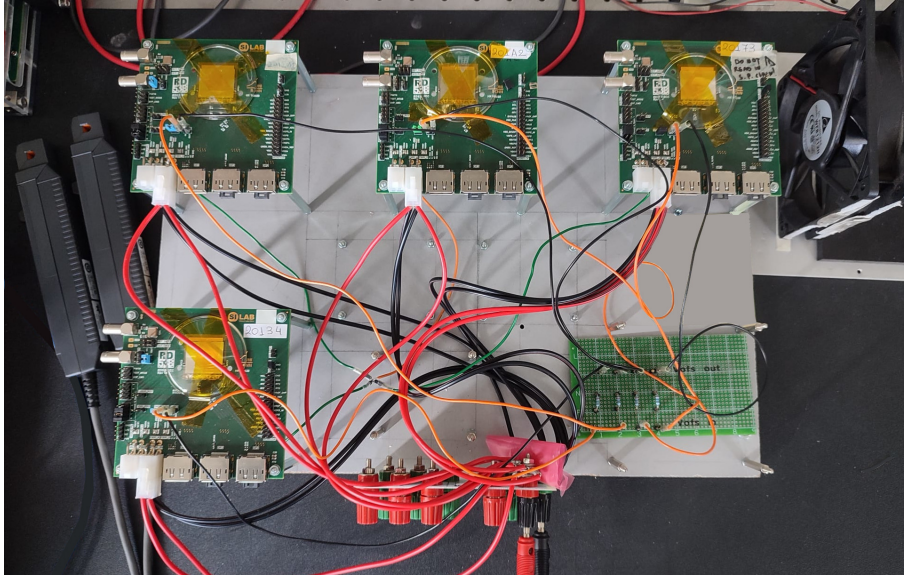


**Figure 4.15:** Experimental setup with four digital CROCV1 SCCs connected in parallel to emulate a quad module. Connections for offset voltage sharing are visible. A fan was included for cooling, and current probes were used to monitor current sharing.

To perform this test, the chips were powered in SLDO mode. The main reference current was first trimmed in standalone configuration, setting  $V_{ofs}$  to approximately 0.45 V for two chips and 0.55 V for the other two. The offset voltages of all four chips were then connected to enable sharing. Figure 4.16a shows the unregulated input voltage for each chip as a function of the total input current, measured while ramping from 0 A to 16 A. As expected, all chips exhibit similar ohmic behavior. At the nominal working point of 8 A—corresponding to 2 A per chip or 1 A per domain—the input voltage reaches approximately 1.6 V, consistent with the 604 m $\Omega$  input impedance.

Figures 4.16b – 4.16e show the individual VI characteristics of each chip. These curves report the input current per domain, assuming equal sharing between the analog and digital circuits. Following startup, the overall behavior matches the expected SLDO response shown in Figure 4.11b. Despite the initial offset mismatches, all chips converged to a common value of 0.5 V, demonstrating that the offset-sharing network effectively equalizes these reference voltages. Furthermore, current distribution across the four chips was found to be uniform during startup at 8 A, confirming successful current balance during operation.

The robustness of the offset-sharing configuration was further evaluated under a failure scenario in which one of the chips enters an open-circuit state. This condition was emulated by not powering one of the SCCs. As discussed in Section 4.2.1, this reduces

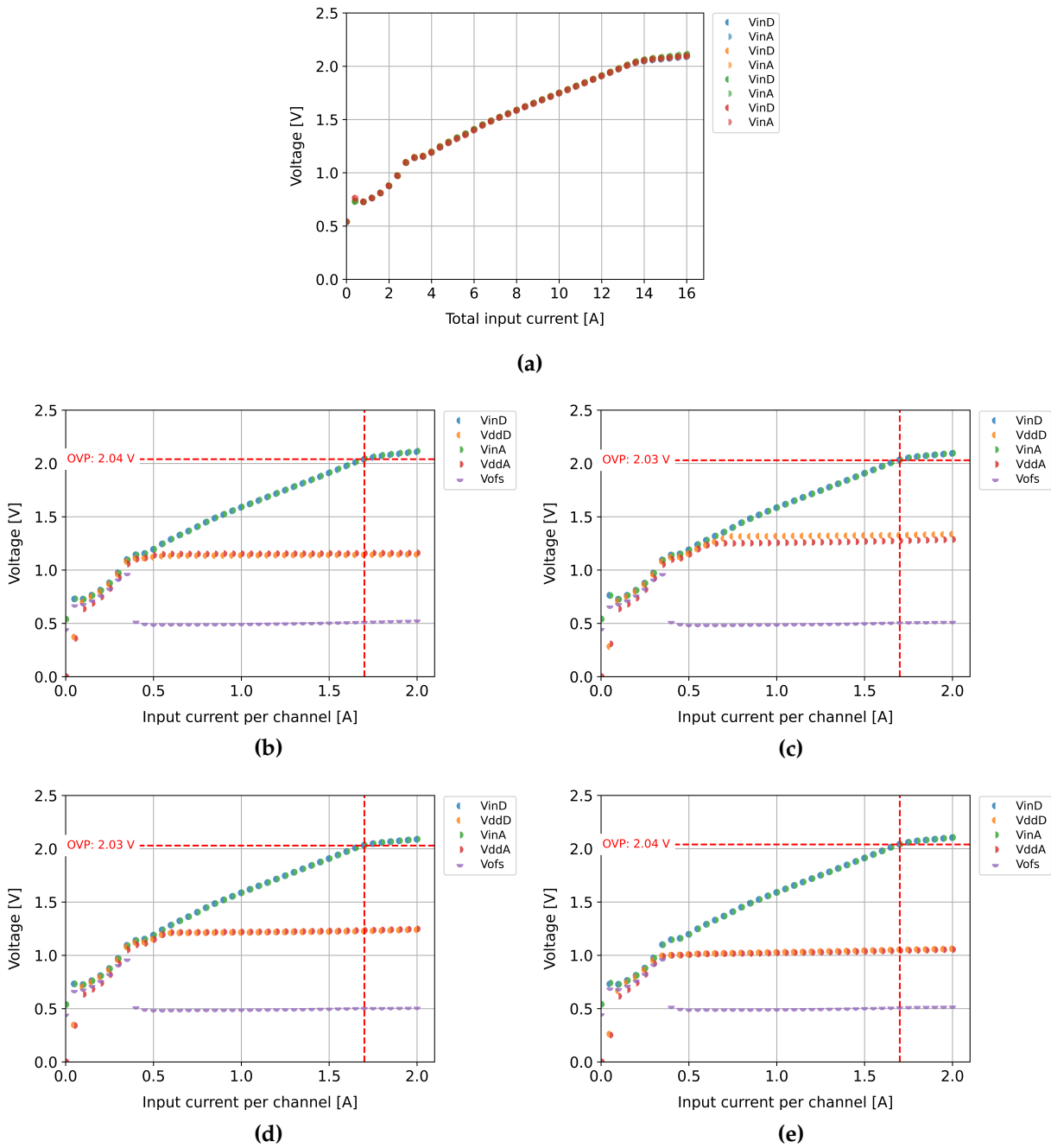


**Figure 4.16:** (a) Combined VI characteristics of four CROCv1 chips connected in parallel to emulate a quad module. The unregulated input voltage is reported as a function of the total input current. Each color corresponds to a different chip, with analog and digital domains labeled as *A* and *D*, respectively. (b)-(e) VI characteristics of each chip, showing the input voltage,  $V_{in}$ , the regulated output voltage,  $V_{dd}$ , and the reference offset voltage,  $V_{ofs}$ , as a function of input current per domain. A horizontal red dashed line indicates the over-voltage protection (OVP) limit.

the effective offset voltage seen by the remaining chips, requiring a higher input current for them to reach the operational regime. The goal of this test was to assess whether the working point of 8 A, established for a quad module, remains sufficient under a single-chip failure scenario.

The main reference currents of all chips were first trimmed in standalone configuration to set their respective  $V_{\text{ofs}}$  values as close as possible to 0.5 V. Offset sharing was then enabled among the four chips, with one left unpowered. Figures 4.17a – 4.17c show the VI characteristics of the three functioning chips, measured while ramping the total input current from 0 A to 12 A. These curves report the input current per domain, assuming equal sharing between the analog and digital circuits.

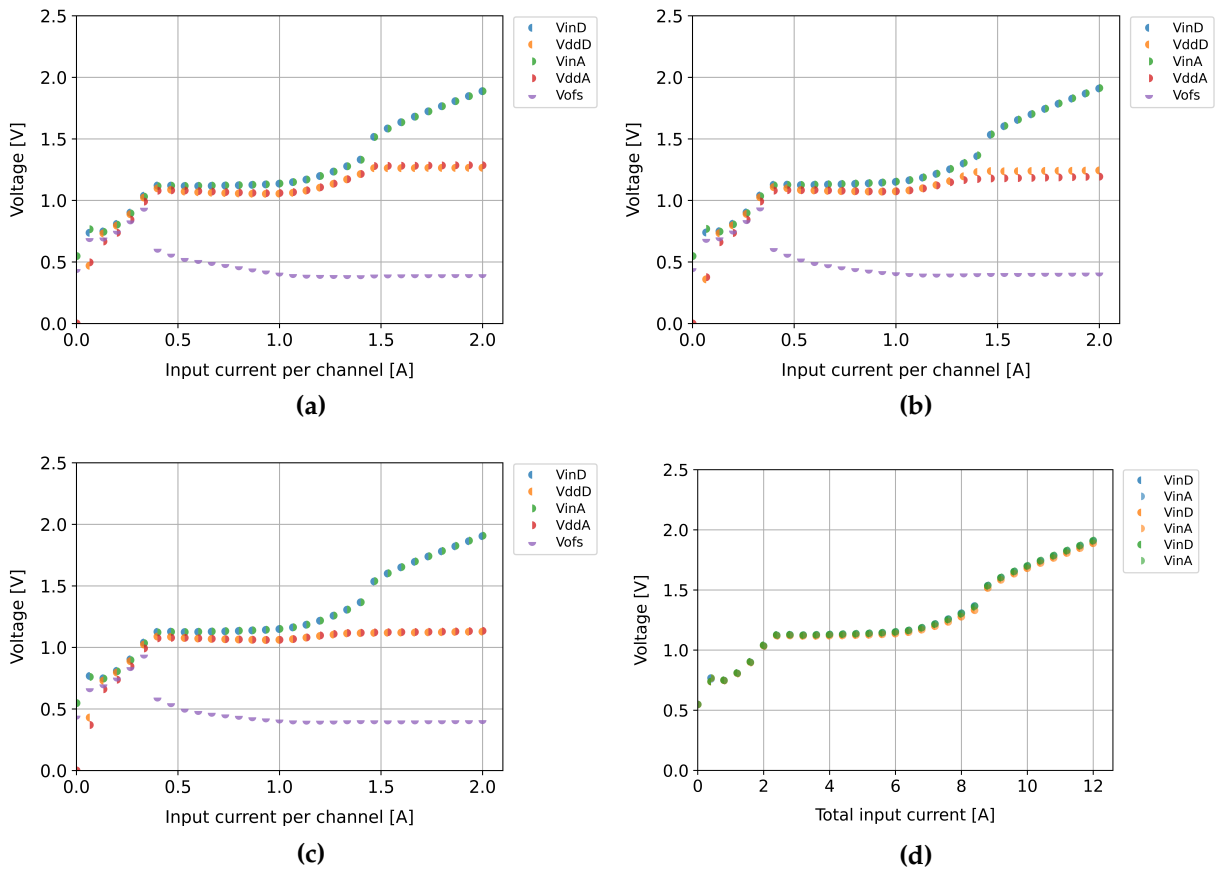


**Figure 4.17:** (a)-(c) VI characteristics of the three functioning CROCv1 chips in an emulated quad module under a failure scenario, where the fourth chip is left unpowered. The unregulated input voltage,  $V_{\text{in}}$ , the regulated output voltage,  $V_{\text{dd}}$ , and the reference offset voltage,  $V_{\text{ofs}}$ , are shown as a function of the input current per domain. The analog and digital domains are labeled as *A* and *D*, respectively. (d) Combined VI characteristics showing the input voltage as a function of the total input current. Each color corresponds to a different chip.

As expected, the shared  $V_{ofs}$  drops to approximately 0.365 V, around 25% below the nominal value. This shift delays the onset of the SLDO ohmic behavior to higher input currents. As shown in Figure 4.17d, the regulation region does not begin until approximately 9 A, indicating that the system is not fully operational at the working point. This was further confirmed by monitoring the current distribution among chips during startup, which became uniform only from 9 A onward.

However, the input resistors on the tested SCCs did not match those specified for an actual quad module. While 604 m $\Omega$  resistors were used for both domains on the SCCs, a quad module employs 604 m $\Omega$  and 698 m $\Omega$  for the analog and digital domains, respectively. Since the analog circuit is responsible for generating the voltage and current references, increasing the resistance on the digital circuit should shift more current to the analog domain, thus helping with the startup.

The test was repeated after replacing the digital input resistors on all SCCs with 680 m $\Omega$  resistors—the closest available to the target value. With this modification, the system entered the regulation region at the nominal working point of 8 A, as shown in Figure 4.18. Moreover, the current sharing was observed to be balanced across the three functioning chips during startup. These results confirm that a quad module can sustain a single-chip failure scenario without requiring an increase in total input current.

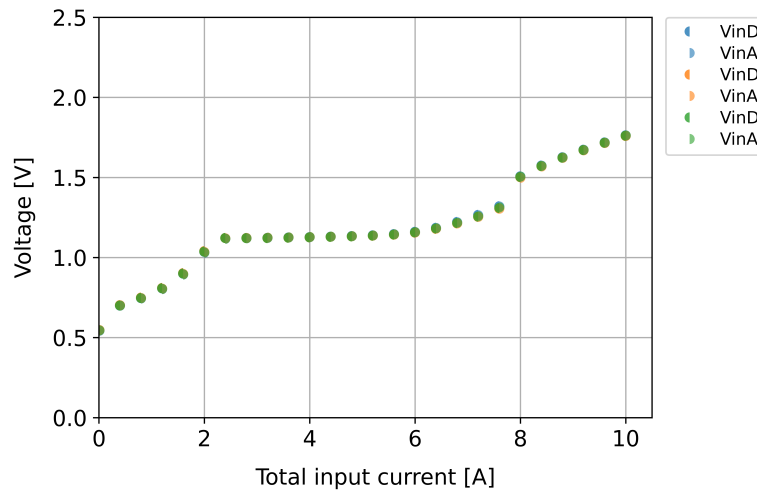


**Figure 4.18:** VI characteristic for the three working CROCv1 chips in an emulated quad module under a failure scenario, using different input resistors for the analog and digital SLDO circuits. The unregulated input voltage is reported as a function of total input current. Each color corresponds to a different chip, with analog and digital domains labeled as *A* and *D*, respectively.

## 4.3. Summary

The results presented in this chapter are part of a broad effort aimed at the integration and validation of the hybrid pixel modules developed for the CMS Inner Tracker, with a focus on bump-bond quality control and system-level testing.

The first part covers the commissioning of the setups and the application of procedures established to assess the connectivity between the sensor and the readout electronics—an essential step during module assembly to prevent performance degradation from defective bump-bonds. The tests presented in this thesis were carried out on single-chip modules and marked the beginning of the module production phase at IFCA, one of the designated assembly centers. Several methods were developed for this purpose. Two of them—an electrical technique and an X-ray approach—were employed in the context of this thesis and demonstrated excellent effectiveness and mutual agreement. The same procedures are currently being applied to double and quad modules to assess their suitability for installation in the CMS Inner Tracker.

The second part presents two system-level tests conducted to validate the robustness of the modules within the powering scheme foreseen for the CMS Inner Tracker. The first test confirmed that module performance remains stable across different positions in a serial-power chain, despite variations in the effective sensor bias voltage. The second test evaluated specific functionalities of the readout electronics, demonstrating that the system can tolerate a failure scenario in which one of the readout chips enters an open-circuit state, without compromising the operation of the remaining chips or requiring additional current.



## Chapter 5

# Performance evaluation of 3D pixel sensors via laser characterization

3D pixel sensors exhibit high radiation hardness and fast signal formation due to the decoupling of the inter-electrode distance from the sensor thickness, which leads to a shorter charge collection distance, as discussed in Section 2.4. These characteristics make 3D pixel technology an ideal candidate for implementing the 4D-tracking paradigm in next-generation experiments. As such, they are being actively investigated for timing applications in the proposed FCC experiments and potential upgrades of vertex detectors for the HL-LHC, where extreme radiation environments are foreseen [78, 132, 133, 134]. Detectors in these future experiments require precise timing capabilities, with resolutions reaching down to tens or even units of picoseconds to reliably associate particle hits with their corresponding production vertices.

A major challenge for 3D pixel sensors in timing applications—especially when compared to avalanche and planar sensor technologies—is the non-uniformity of their electric and weighting fields. This spatial inhomogeneity causes a position-dependent variation in the signal detection time relative to the charge carrier generation time. Figure 5.1 shows electric field maps from TCAD simulations for two different 3D pixel cell geometries. Accurately characterizing these variations is essential, as they directly affect the overall time resolution of the sensor.

In this thesis, the impact of pixel cell geometry on the timing performance of 3D pixel sensors was investigated. A detailed description of the sensors under test, the experimental methodology for timing characterization, and the evaluation of their timing performance are presented below.

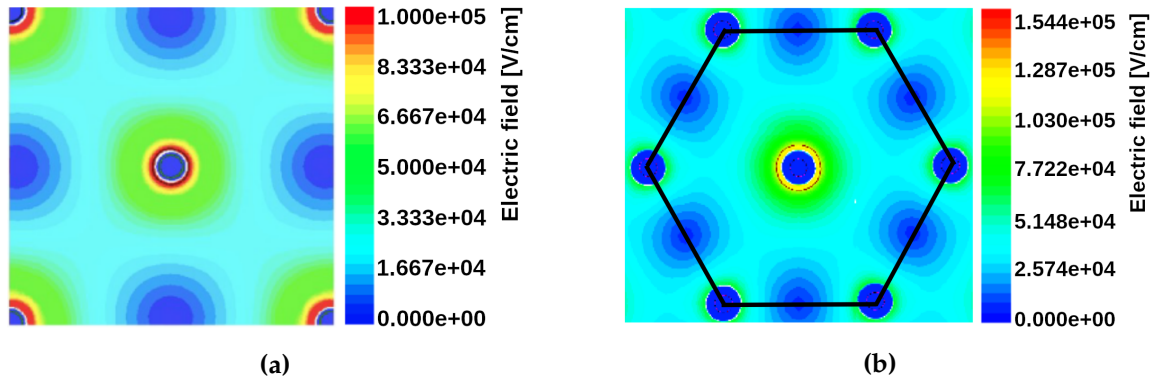


**Figure 5.1:** Electric field maps from TCAD simulations for (a) a square 3D pixel cell with a  $55\text{ }\mu\text{m}$  pitch biased at 150 V, and (b) a hexagonal 3D pixel cell with a  $25\text{ }\mu\text{m}$  radius biased at 100 V. The hexagonal cell outline is shown in black. Images adapted from [135, 136].

## 5.1. 3D pixel sensors under test

The samples under test, manufactured by IMB-CNM, contain 25 electrically isolated structures, each designed for individual characterization. These structures are non-irradiated 3D columnar-electrode sensors with a backside aluminum layer and either square or hexagonal pixel cell geometries. Figure 5.2 shows the schematic layout of a single structure for each geometry, including both top and side views. Each structure consists of a central pixel cell surrounded by eight or six neighbors, depending on whether the layout is square or hexagonal. The neighboring cells are connected together to a single readout pad, while the central cell is read out independently.

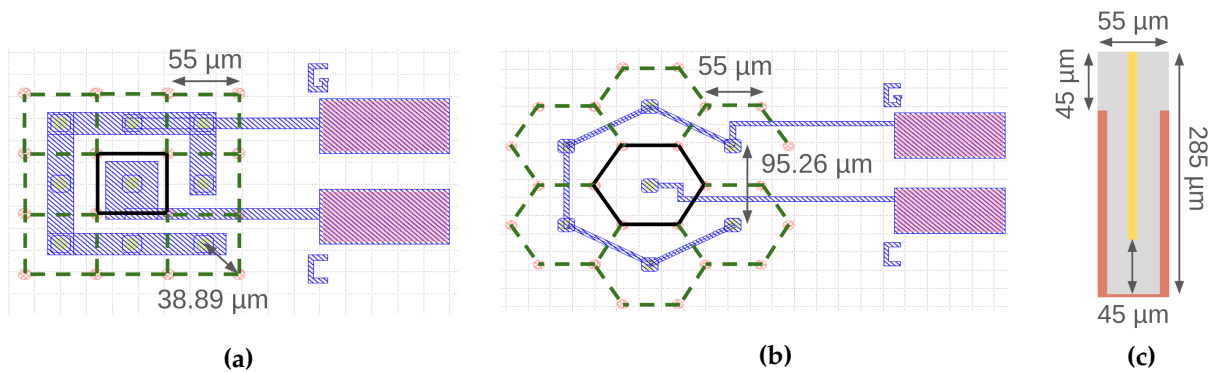


**Figure 5.2:** Layout of the 3D pixel sensors under test. Schematic top view of (a) square and (b) hexagonal cell geometries. The readout cell is outlined in black, while neighboring cells are outlined in green. Metal pads are shown in blue and pink. Images adapted from [100]. (c) Schematic side view of a pixel cell, showing  $p^+$  and  $n^+$  electrodes in red and yellow, respectively. All relevant dimensions are indicated with arrows.

The sensors are double-sided  $n$ -in- $p$  devices with a thickness of 285  $\mu\text{m}$ . Both  $p^+$  and  $n^+$  electrodes, each with a 10  $\mu\text{m}$  diameter, extend vertically through the substrate, stopping 45  $\mu\text{m}$  short of the frontside or backside, respectively. The square layout has a pixel pitch of 55  $\mu\text{m}$ , while the hexagonal layout features a radius of 55  $\mu\text{m}$ .

Based on the results of the electrical characterization presented in Section 5.2, the best-performing structure from each sample was selected as the sensor under test for the timing performance evaluation.

## 5.2. Electrical measurements

Electrical characterization is an essential step in assessing the functionality and performance of silicon sensors. As discussed in Section 2.1.7, the two primary measurements used for this purpose are the current-voltage (IV) and capacitance-voltage (CV) characteristics. These provide key insights into parameters such as the power consumption and the operational voltage range, which is defined by the full depletion and breakdown voltages.

IV measurements were conducted on all 25 structures of each sample to identify the best-performing sensor for subsequent timing studies. However, CV measurements could not be reliably performed due to limitations in the available instrumentation, which lacked the precision needed to resolve the expected capacitance values of the sensors under test—on the order of a few tens of femtofarads.

The IV characterization was carried out using a probe station located in a cleanroom environment at room temperature. The station, shown in Figure 5.3a, is enclosed in a Faraday cage that shields the system from external electromagnetic interference. Samples were mounted via vacuum suction onto a conductive copper chuck, which also served as the ground contact for the sensor backside. The bias voltage was applied from the frontside using two probing needles in contact with the metal pads of the central and shorted neighboring cells, both biased at the same potential. The leakage current was measured through the same probes that delivered the bias voltage. This configuration enabled independent measurements in the central and neighboring cells.

The probe station is also equipped with a microscope for precise needle positioning, which is connected to a video camera for real-time visualization on a computer screen. Figure 5.3b shows an example microscope image for the sensor with hexagonal cell layout.

The measurements were performed by ramping the reverse-bias voltage from 0 V to 150 V in 1 V steps. The sensor selection criterion required the leakage current to remain below 100 nA at a bias voltage of 20 V, with no indication of breakdown within the scanned range. This threshold is intended to minimize the contribution of

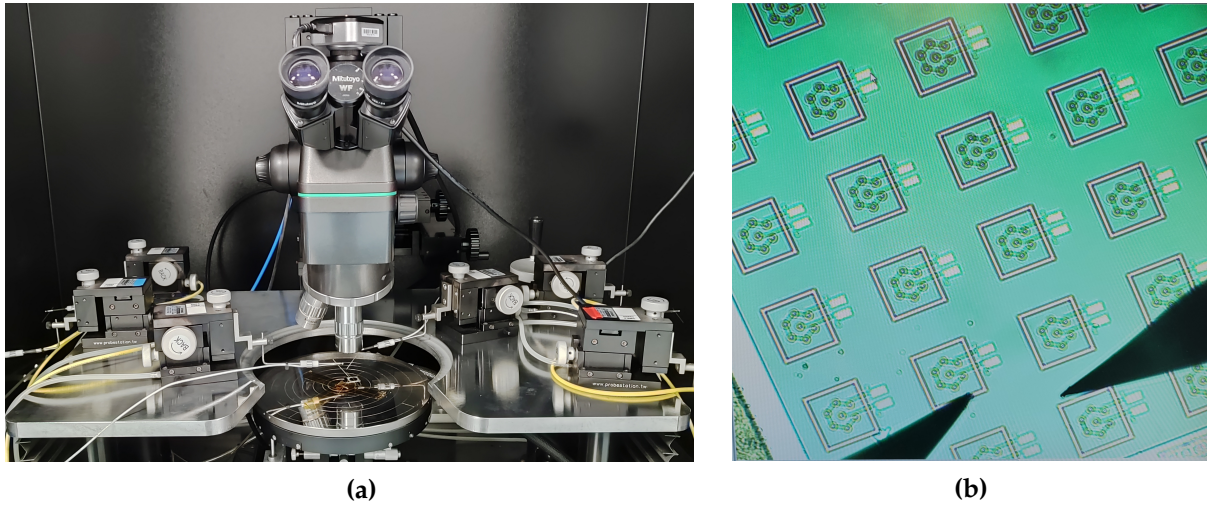


**Figure 5.3:** (a) Probe station used for the electrical characterization of the samples under test. The samples are fixed by vacuum to a conductive copper chuck. The high voltage is applied using probing needles, while the ground connection is provided through the chuck. Two needles are used to contact the pads of the central and neighboring cells separately. (b) Microscope image of the 3D pixel sensor with hexagonal cell geometry, with the probing needles shown in black.

leakage current to system noise, which is essential for maintaining a high SNR and, consequently, optimal sensor performance.

Figure 5.4 presents the resulting IV curves for the best-performing sensors in each sample, with the current shown in absolute value. For the central cell, a drop is observed at bias voltages below 20 V, which is attributed to a measurement artifact. A small potential mismatch between the two probing needles likely induce a surface current that partially cancels the true leakage current, resulting in a small net negative value. As the applied voltage increases, the actual leakage current becomes dominant, and the measured current increases monotonically.

### 5.3. Laser-based measurements

The timing characteristics of the sensors under test were evaluated using the Two-Photon Absorption Transient Current Technique (TPA-TCT) [137]. This method builds upon the standard Single-Photon Absorption Transient Current Technique (SPA-TCT) [138, 139], which relies on the generation of charge carriers through single-photon absorption and the measurement of the induced current according to Ramo's theorem—described in Section 2.2.2. The resulting current profile can provide insight not only into the amount of charge generated by external ionizing radiation, but also

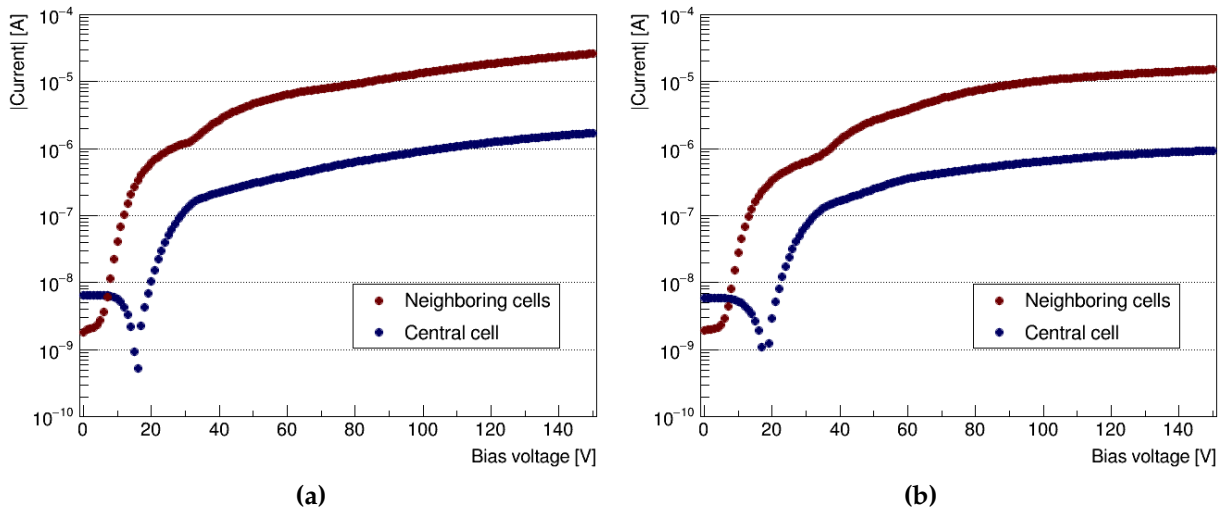


**Figure 5.4:** IV characteristics of the 3D pixel sensor under test with (a) square cell geometry and (b) hexagonal cell geometry. Blue and red curves correspond to the central and shorted neighboring cells, respectively. Note that the current is shown in absolute value. More details are given in the text.

into the local conditions experienced by the carriers—such as the electric and weighting fields—which influence the sensor timing performance.

SPA-TCT employs picosecond laser pulses with photon energies above the silicon band gap to generate charge carriers. Lasers in the visible to near-infrared range produce electron-hole pairs along their path through the sensor, with a linear relationship between charge carrier density and laser irradiance. Red lasers with typical wavelengths around 660 nm penetrate only a few micrometers, providing good spatial resolution near the sensor surface. In contrast, the longer absorption length of infrared lasers with typical wavelengths around 1060 nm result in no spatial resolution along the beam direction for sensor thicknesses of a few hundred micrometers. As discussed in Section 2.2.1 and shown in Figure 2.12, the single-photon absorption probability becomes negligible for wavelengths above approximately 1100 nm.

TPA-TCT instead relies on the generation of charge carriers through the simultaneous absorption of two photons with energies below the silicon band gap [140]. This non-linear process is achieved using tightly focused femtosecond laser pulses, with the charge carrier density depending quadratically on the laser irradiance. Infrared lasers with typical wavelengths around 1550 nm produce electron-hole pairs only within a small ellipsoidal voxel centered at the beam focus. This highly localized carrier generation provides excellent spatial resolution, enabling detailed three-dimensional mapping of the sensor properties.



### 5.3.1. Experimental setup

The experimental setup used for the TPA-TCT measurements is located at the CERN SSD laser facility [141, 142]. Figure 5.5 shows a schematic of the setup, which is partially enclosed in a Faraday cage to shield it from external electromagnetic interference. The setup includes a fiber laser module (FYLA LFC1500X) that generates femtosecond pulses with a central wavelength of 1550 nm. The laser beam is guided onto the sensor using a combination of mirrors and focusing optics. The objective used in this work has a numerical aperture of 0.5, ensuring a tightly focused beam for localized charge generation. The pulse energy is attenuated with a neutral density filter, while the repetition rate is controlled through an acousto-optic modulator. The readout system consists of a current-sensitive amplifier (CIVIDEC C2-TCT, 2 GHz, 46 dB) and a fast oscilloscope (Agilent DSO9254A, 2.5 GHz, 20 GSa/s) for signal acquisition.

Since the infrared laser beam is invisible to the human eye, a red laser is used for initial coarse alignment. Fine alignment is then performed using an infrared microscope that combines a camera and a lamp, both operating at a wavelength of 1550 nm. This microscope allows accurate localization of regions of interest on the sensor surface, which is particularly useful for the sensors under test in this thesis. The beam paths for the infrared laser, the red laser, and the microscope lamp are also indicated in Figure 5.5. The sensor is placed on a high-precision stage, the hexapod, which allows translational and rotational shifts for accurate alignment of the sample with the laser focus.

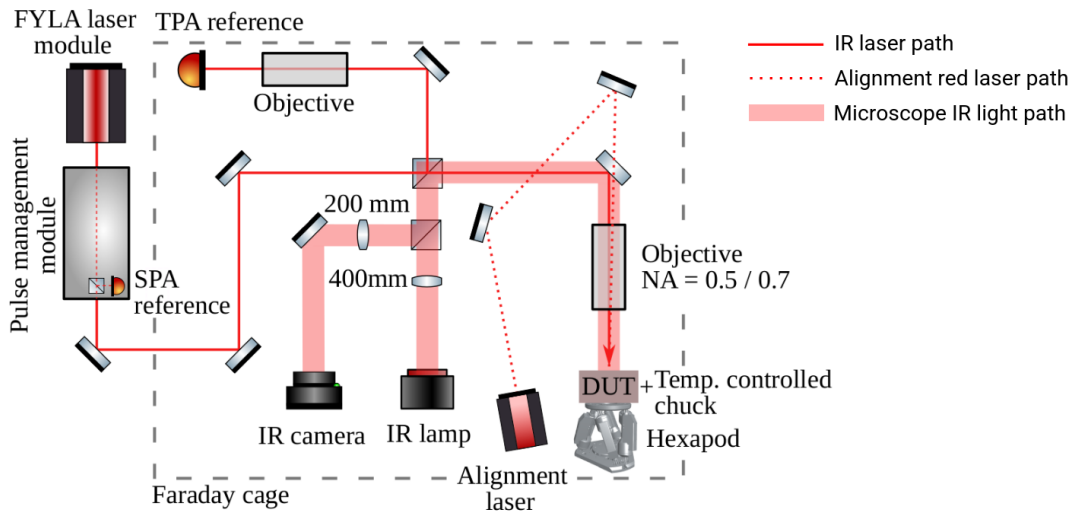


**Figure 5.5:** Schematic of the TPA-TCT setup at the CERN SSD laser facility, with the main components labeled. The beam paths for the infrared laser, the red laser, and the infrared microscope lamp are indicated according to the legend. More details are given in the text. Image adapted from [142].

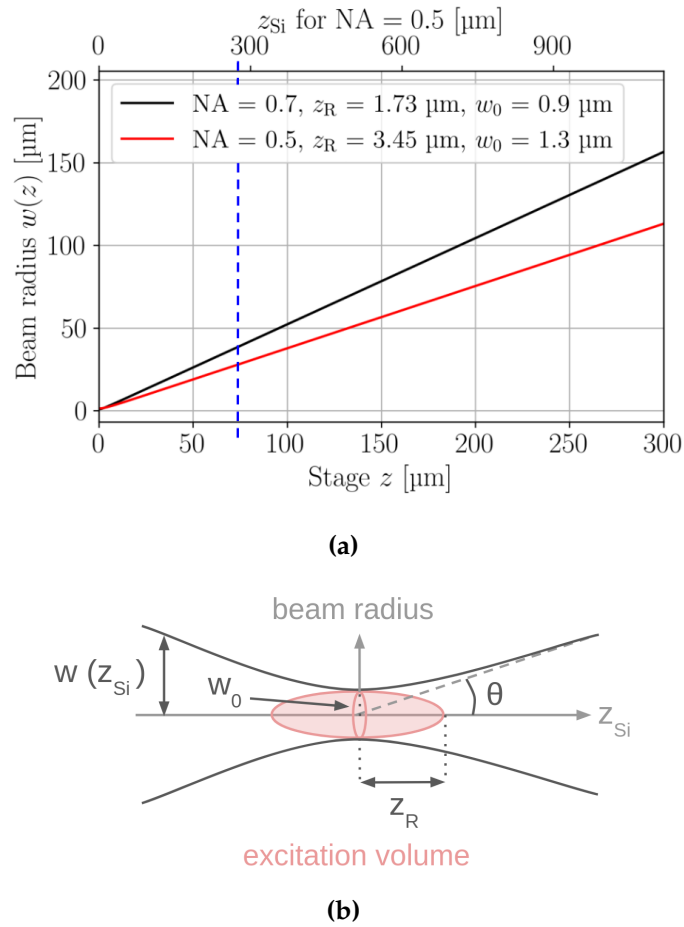
Owing to the large beam divergence required for tight focusing and high spatial resolution in TPA-TCT, beam clipping at the sensor surface—mainly due to metal pads—can become a limiting factor. As the focal point is moved deeper into the sensor, the beam cross-section at the illuminated surface increases, raising the likelihood of clipping. This effect can distort the excitation volume and reduce the laser intensity at the focus, ultimately degrading the signal and complicating the analysis.

Figure 5.6a shows the beam radius at the illuminated surface as a function of the focal depth for two objectives with different numerical apertures. The beam parameters affected by the numerical aperture are illustrated in Figure 5.6b, which presents a schematic of the beam profile and the resulting ellipsoidal excitation volume. For a numerical aperture of 0.5, the excitation voxel has a transverse radius of approximately  $1.3\text{ }\mu\text{m}$  and a longitudinal extent of about  $6.9\text{ }\mu\text{m}$  [142].

According to Figure 5.6a, focusing the beam at a depth of  $285\text{ }\mu\text{m}$ —the maximum depth explored in this work—requires a metal-free region on the surface with a radius of at least  $30\text{ }\mu\text{m}$  to avoid beam clipping. For the sample with hexagonal cell geometry, beam illumination from the frontside was feasible. However, in the sample with square pixels, nearly the entire surface of the readout cell is covered by metal, as shown in Figure 5.2a, making frontside illumination prone to significant beam clipping. To mitigate this, the square sample was illuminated from the backside, following the removal of the aluminum layer.

The samples were mounted on generic PCBs compatible with the experimental setup, using conductive glue to ensure both mechanical stability and electrical contact. Each PCB features a central hole at the sample position to enable backside illumination. The sensors under test were wire-bonded to the PCBs: the pad corresponding to the central pixel cell was connected to the readout terminal, and the pad for the neighboring cells was grounded via a  $50\text{ }\Omega$  resistor. The terminal connected to the backside of the sensor was used to apply a reverse-bias voltage with a power supply. Figure 5.7 shows one of the samples mounted and wire-bonded to the PCB.





**Figure 5.6:** (a) Beam radius  $w$  at the illuminated surface as a function of the focal point depth inside the sensor. This depth is labeled as  $z$  in the lab's coordinate system and  $z_{\text{Si}}$  in the silicon sensor's coordinate system, which differ due to refractive index change at the air-silicon interface [143]. Results are shown for two objectives with different numerical apertures, NA. The vertical blue line corresponds to the thickness of the sensors under test:  $285 \mu\text{m}$ . (b) Schematic profile of a Gaussian beam, showing the excitation volume in red. It is defined by the beam waist,  $w_0$ , and the Rayleigh length,  $z_R$ . The beam divergence angle is denoted by  $\theta$ . Top image adapted from [142].

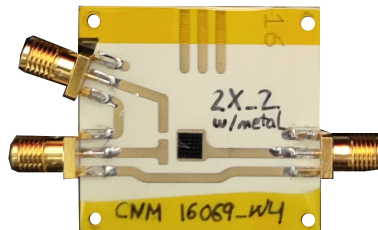


**Figure 5.7:** Image of one of the samples mounted and wire-bonded to a PCB compatible with the TPA-TCT setup.

### 5.3.2. Definition of observables

Due to the presence of both surface metal and columnar electrodes, beam clipping can occur and affect the amplitude of the measured signals. Therefore, all observables sensitive to signal amplitude—and thus to beam intensity variations—must be interpreted carefully for accurate characterization of sensor performance. To ensure a robust evaluation of the sensor's timing capabilities, the observables and analysis methodology were deliberately chosen to be insensitive to beam clipping effects. The primary observables used to quantify timing performance in this thesis are the time-of-arrival and the sensor time jitter. These are defined and discussed in detail below, along with the methodology employed to extract them.

To properly interpret the measurements, it is important to establish the coordinate system used throughout this work. The origin is defined at the illuminated surface of the sensor: the frontside for the hexagonal sample, and the backside for the square one. The sensor surface is assigned to the depth at which half of the ellipsoidal excitation volume lies within the sensor.

#### Time-of-arrival

The time-of-arrival (ToA) is defined as the time at which the sensor detects the particle interaction, estimated from the recorded current transient. This observable was measured across the entire pixel cell, as a function of both depth and applied bias voltage. To reduce systematic effects from variations in signal amplitude—such as those caused by beam clipping—the ToA was extracted using the principle of the constant-fraction discrimination (CFD) technique [53]. In particular, a threshold corresponding to 50% of the signal amplitude was applied, as illustrated in Figure 5.8.

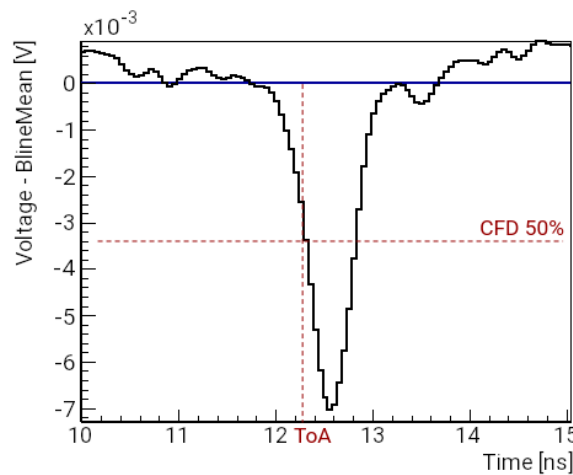


**Figure 5.8:** ToA extraction from a current transient using the principle of the constant-fraction discrimination (CFD) technique. The ToA, indicated by a vertical dashed line, corresponds to the point where the signal reaches 50% of its maximum amplitude.

It should be noted that the absolute ToA values include an arbitrary time offset. This offset is primarily determined by the fixed delay between the laser trigger and the signal detection, which is dominated by the signal propagation time through the readout cables.

For the ToA evaluation, the repetition rate was set to 1 kHz, and each measurement represents the average of either 128 or 256 individual current transients. This averaging significantly improves the SNR and reduces time jitter contributions from both the sensor and the laser trigger.

### Sensor time jitter

Time resolution quantifies the smallest time difference a detector system can reliably resolve, and it arises from various sources of timing uncertainty. For the samples studied in this thesis, the most relevant contributions are time walk and sensor time jitter. Time walk refers to variations in the measured ToA caused by differences in signal amplitude when using a fixed-threshold discriminator, as represented in Figure 5.9a. Since this effect can be effectively corrected using the CFD technique, the time resolution is ultimately limited by sensor time jitter.

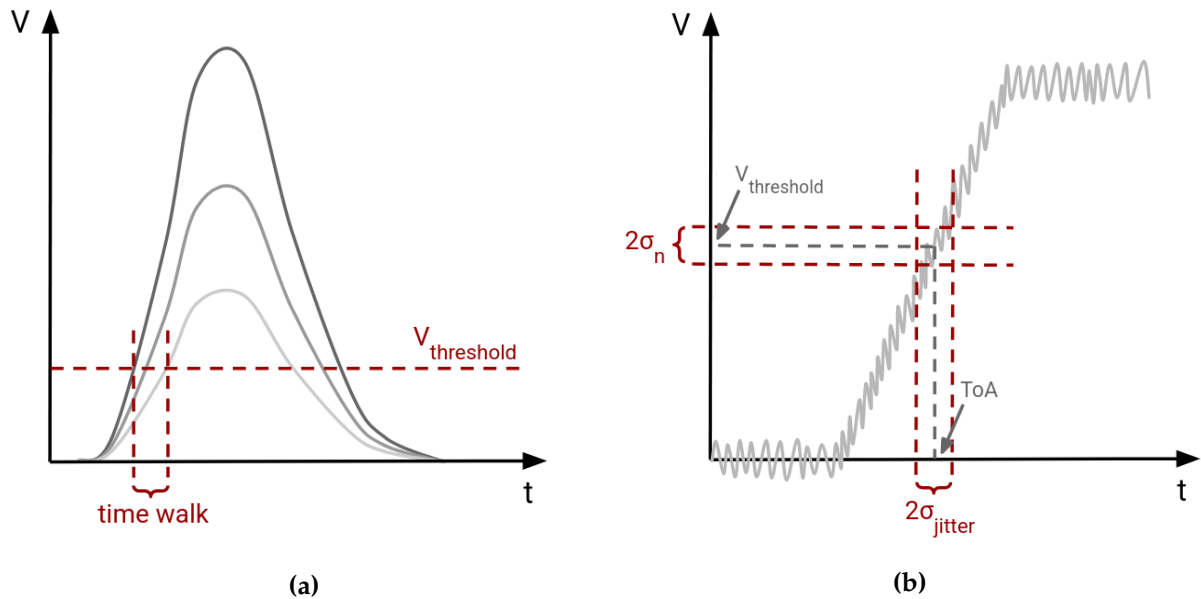


**Figure 5.9:** (a) Schematic representation of time walk using three pulses of different amplitude and a fixed-threshold discriminator,  $V_{\text{threshold}}$ . (b) Schematic representation of sensor time jitter, showing noise fluctuations on the rising edge of a pulse. The noise level and resulting time jitter are denoted as  $\sigma_n$  and  $\sigma_{\text{jitter}}$ , respectively. The discriminating threshold and ToA are also indicated.

Sensor time jitter also refers to variations in the measured ToA, but in this case, they are caused by random noise fluctuations in the signal, as illustrated in Figure 5.9b. It depends on the noise level,  $\sigma_n$ , and the rate at which the signal changes with time, as expressed in equation 5.1. Assuming the leading edge of the signal can be approximated as a constant slope, the jitter can also be estimated through the rise time (RT) and the signal-to-noise ratio (SNR).

$$\sigma_{\text{jitter}} = \frac{\sigma_n}{dV/dt} \approx \frac{\text{RT}}{\text{SNR}} \quad (5.1)$$

To evaluate sensor time jitter, the time difference between two laser pulses is measured repeatedly. In each measurement, the ToA of both pulses is extracted using the same CFD to eliminate time walk effects. A histogram is then built from the differences between the two ToA values, and its standard deviation,  $\sigma$ , is extracted through a Gaussian fit. Assuming the two pulses are statistically identical and uncorrelated, the sensor time jitter is calculated as:

$$\sigma_{\text{jitter}} = \frac{\sigma}{\sqrt{2}} \quad (5.2)$$

The TPA-TCT pulse train was employed for the first time to generate the required two-pulse waveforms and evaluate sensor time jitter with three-dimensional spatial resolution, extending the capabilities of the SPA-TCT-based method introduced in [78]. This advancement enables localized characterization of sensor time jitter across the detector volume, offering deeper insight into the spatial dependence of timing performance.

Measurements were performed at the maximum laser repetition rate of 8.2 MHz, allowing two pulses to be captured per waveform. Both pulses were recorded on the same oscilloscope channel, minimizing jitter contributions from the readout system. Additionally, laser jitter between consecutive pulses in the TPA-TCT pulse train is negligible, due to the high stability of the resonant cavity formed within the femtosecond laser's optical fiber. This setup therefore enables a direct measurement of the sensor time jitter, independent of contributions from the laser and readout system.

### 5.3.3. Timing performance of square 3D pixel sensors

The ToA across the square pixel cell was measured at two different depths under a bias voltage of 20 V, ensuring full depletion of the sensor. Measurements were performed at  $z_{\text{Si}} \simeq 100 \mu\text{m}$ , where the  $p^+$  and  $n^+$  electrodes overlap, and at  $z_{\text{Si}} \simeq 23 \mu\text{m}$ , a depth located beneath the  $n^+$  electrode roughly halfway between the column tip and the sensor backside. Figure 5.10 shows the corresponding ToA maps. As expected, signals within the inner radius of the  $n^+$  column are observed only at  $z_{\text{Si}} \simeq 23 \mu\text{m}$ .

Comparing the measured ToA maps with the simulated electric field map in Figure 5.1a, the expected inverse relationship between ToA and electric field strength is observed. The highest ToA values appear near the pixel edges between the  $p^+$  columns, where the electric field is low or even null, while lower ToA values are observed toward the pixel center, where the electric field is stronger. Overall, the central region at  $z_{Si} \approx 100 \mu\text{m}$  exhibits slightly lower ToA values, consistent with the higher electric field expected at depths where the  $p^+$  and  $n^+$  columns overlap [144].

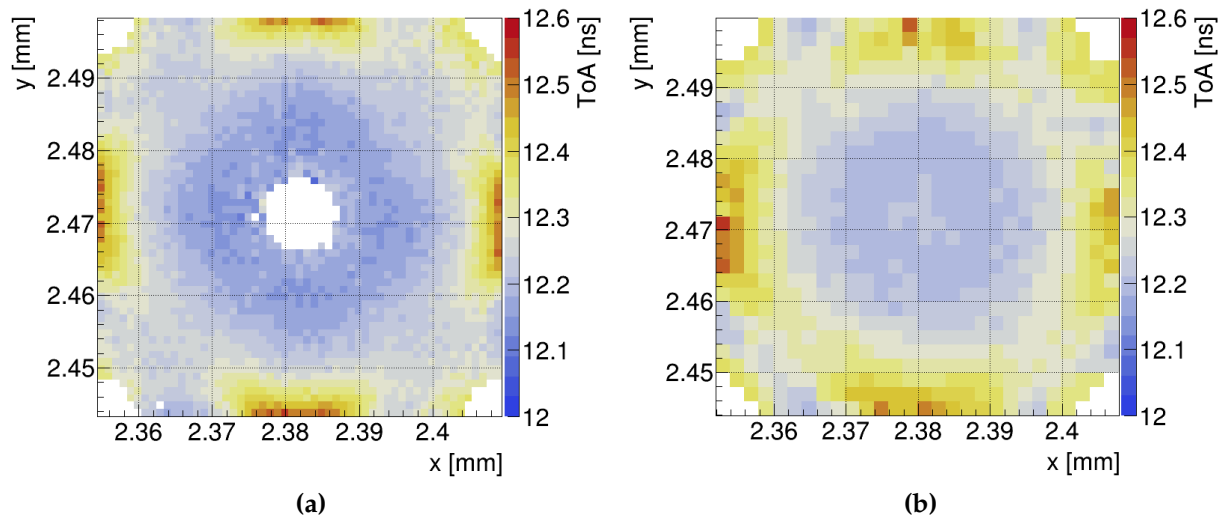


**Figure 5.10:** ToA distribution across the square pixel cell at two depths: (a)  $z_{Si} \approx 100 \mu\text{m}$ , and (b)  $z_{Si} \approx 23 \mu\text{m}$ . Measurements were performed at a bias voltage of 20 V. Note the difference in granularity by a factor of 2. More details are given in the text.

ToA was also evaluated at several bias voltages to study its evolution with increasing electric field intensity. Measurements were conducted at  $z_{Si} \approx 100 \mu\text{m}$  for bias voltages ranging from 2 V to 20 V. The Median Absolute Deviation (MAD) provides a more robust estimate of the ToA spread across the pixel cell compared to the Root Mean Square Deviation (RMS), as it is less sensitive to outliers. Figure 5.11 shows the MAD of the ToA distribution as a function of bias voltage. A MAD of 47 ps is observed across the square pixel cell at 20 V.

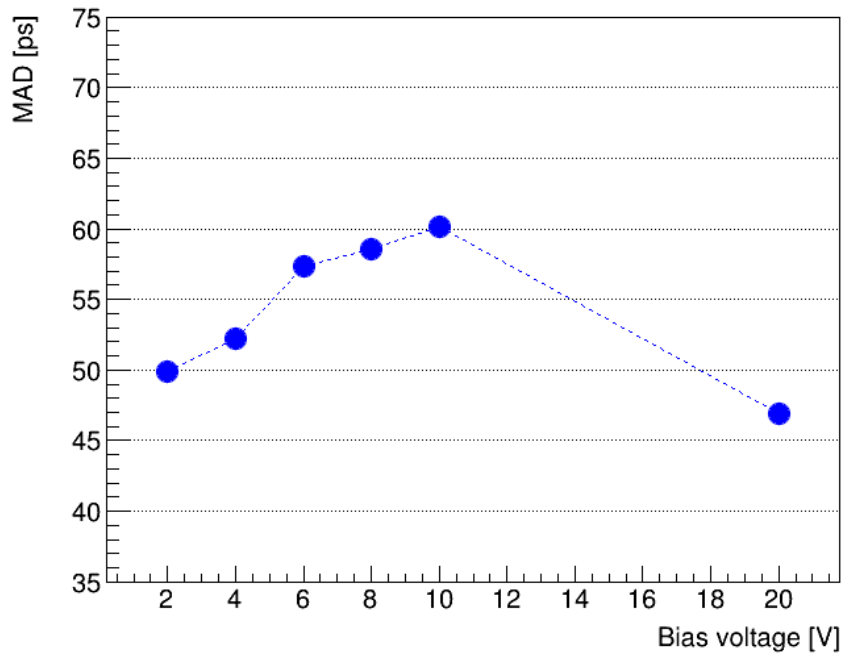


**Figure 5.11:** MAD of the ToA distribution across the square pixel cell as a function of bias voltage. Measurements were performed at  $z_{Si} \simeq 100 \mu\text{m}$ .

The ToA spread is influenced by distinct transient behaviors in the inner and outer regions of the pixel cell, which respond differently to changes in bias voltage. The boundary between these regions is indicated by a black dashed line in Figures 5.12a – 5.12c, which show the ToA maps at  $z_{Si} \simeq 100 \mu\text{m}$  for bias voltages of 6 V, 10 V, and 20 V. The inner region is characterized by very fast ToA values even at low bias voltages, while the outer region exhibits a slower, more dispersed response.

Figures 5.12d – 5.12f present the one-dimensional ToA distributions of these maps, while Figures 5.12g – 5.12i and 5.12j – 5.12l show similar distributions for the inner and outer regions separately. As the bias voltage increases, the inner and outer distributions tend to converge due to a more uniform electric field across the pixel cell. This causes an artifact in the MAD as a function of bias voltage, showing an initial increase followed by a decrease once the field becomes strong enough for the two distributions to significantly overlap.

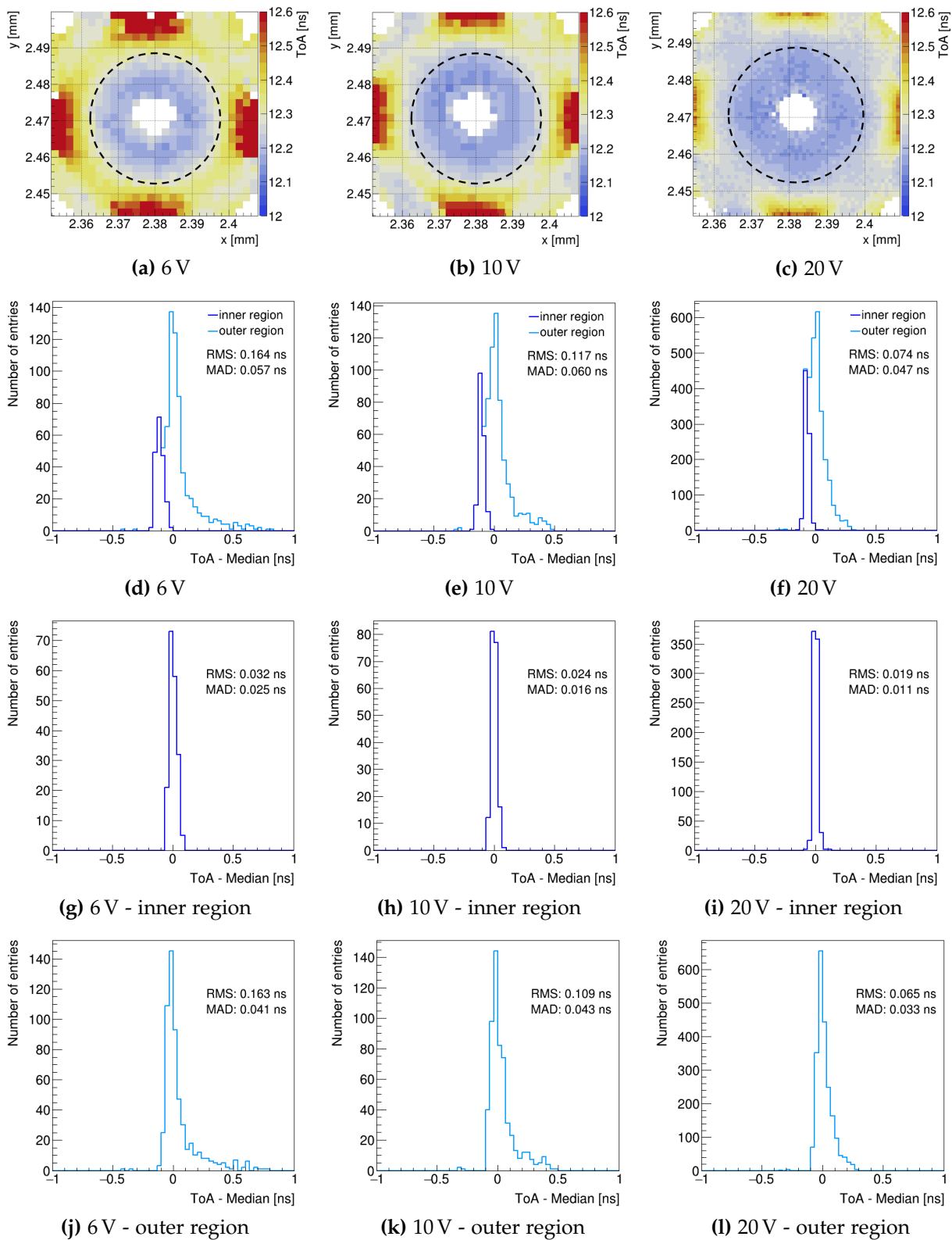


**Figure 5.12:** ToA across the square pixel cell at  $z_{Si} \simeq 100 \mu m$ , for bias voltages of (a) 6 V, (b) 10 V, and (c) 20 V. The black dashed line marks the boundary between the inner and outer regions of the pixel cell. The corresponding one-dimensional ToA distributions are shown in (d)–(f), with histograms for each region stacked on top of one another. Separate distributions for the inner and outer regions are shown in (g)–(i) and (j)–(l), respectively. Each distribution is corrected by its respective median value.



Figures 5.13a and 5.13b show the inverse ToA profiles for several bias voltages, extracted from the maps at  $z_{Si} \simeq 100 \mu\text{m}$  along the horizontal and diagonal axes, respectively. To reduce statistical fluctuations, each profile was averaged over three adjacent bins centered on the respective axis. The inverse ToA serves as a qualitative indicator of the electric field strength. In the horizontal profile, it increases from the lowest-field regions toward the central  $n^+$  column, where the electric field is strongest. Along the diagonal, the inverse ToA rises toward both the  $n^+$  and  $p^+$  columns, reaching a minimum between them. The increase is slightly more pronounced near the  $n^+$  column, due to the stronger weighting field in its vicinity [72].

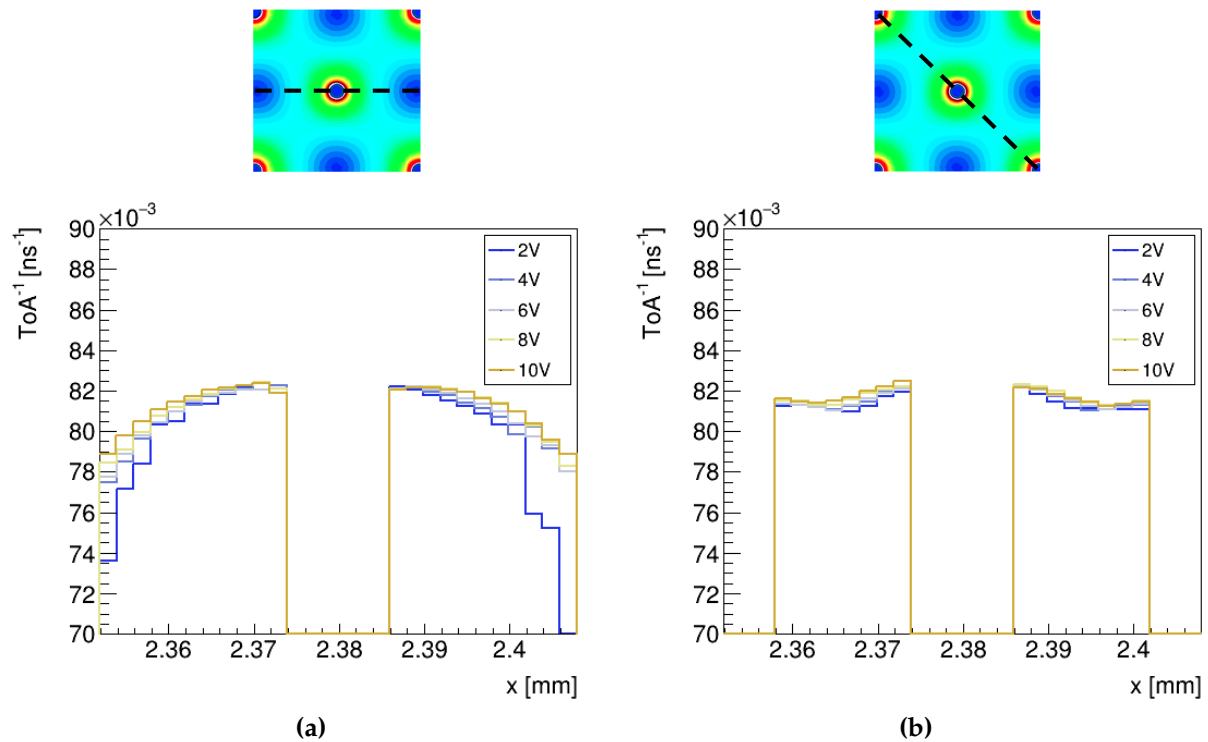


**Figure 5.13:** Inverse ToA profiles along (a) the horizontal and (b) the diagonal axes of the square pixel cell at  $z_{Si} \simeq 100 \mu\text{m}$  under a bias voltage of 20 V. These axes are indicated by black dashed lines in the electric field maps shown for reference.

Since the electrodes do not extend throughout the entire sensor thickness, the electric field also varies as a function of depth. To investigate the dependence of ToA on depth, measurements were performed at two different positions within the pixel cell at a bias voltage of 20 V. Figure 5.14a shows results from a position approximately midway between the  $n^+$  column and one of the  $p^+$  electrodes. An increase in ToA is observed near both the frontside and backside of the sensor, where there is no overlap between different types of electrodes. Figure 5.14b presents the measurements performed directly at the  $n^+$  electrode position, where meaningful signals are only found along the column gap. In this region, the ToA decreases with depth as the focal

point approaches the electrode tip, where the electric field reaches its maximum.

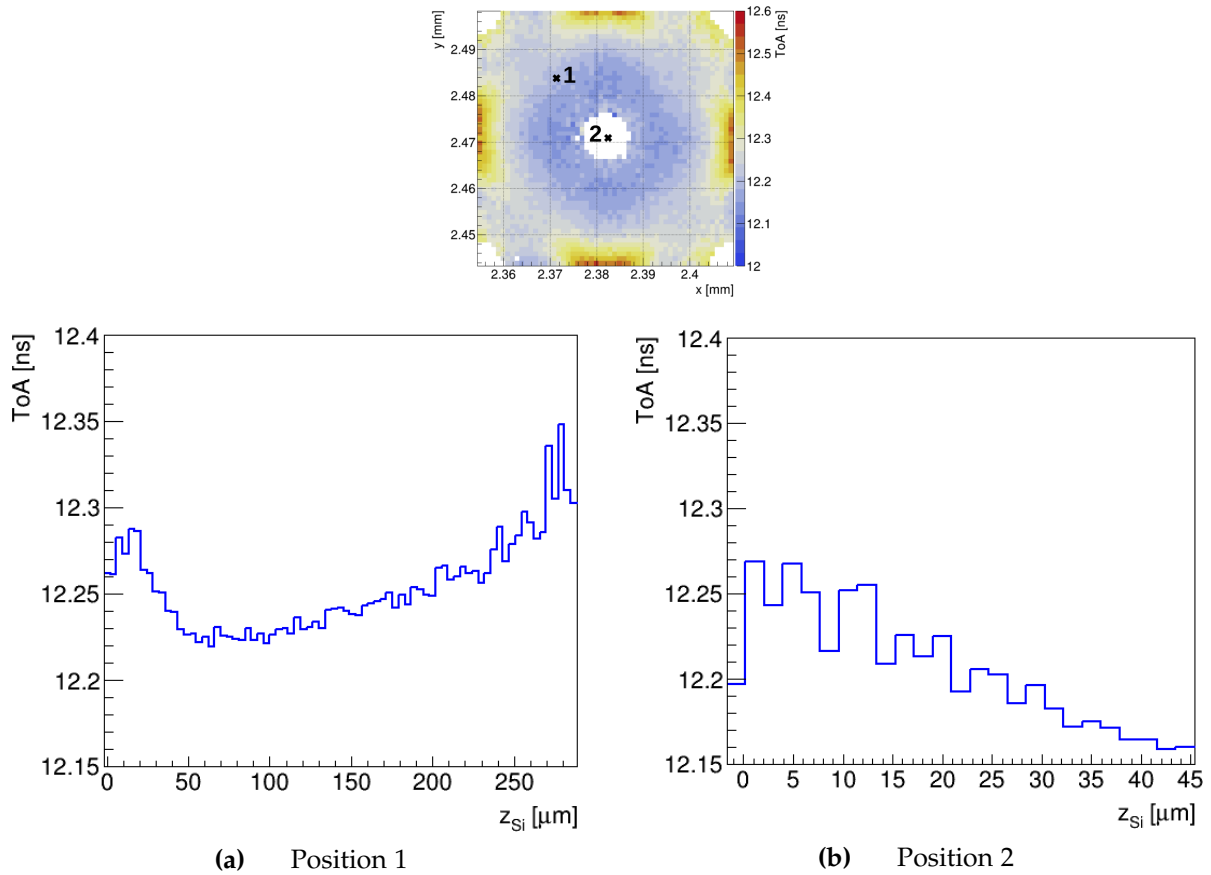


**Figure 5.14:** (a) and (b) show the ToA as a function of depth at two different positions within the square pixel cell. These positions are indicated in the ToA map shown for reference. Measurements were performed at a bias voltage of 20 V.

#### 5.3.4. Timing performance of hexagonal 3D pixel sensors

Similar studies were conducted on the sample with hexagonal cell layout. The ToA across the pixel cell was evaluated at a bias voltage of 20 V at two different depths, as shown in Figure 5.15. Measurements were taken at  $z_{Si} \simeq 100 \mu m$ , where the  $p^+$  and  $n^+$  electrodes overlap, and at the sensor surface  $z_{Si} \simeq 0 \mu m$ , where a small region of the map is obscured due to the presence of the readout metal track. As observed with the square sample, the lowest ToA values cluster around the central  $n^+$  column, while the highest values appear near the pixel edges between the  $p^+$  electrodes.

Figures 5.16a and 5.16b show the inverse ToA profiles at a bias voltage of 20 V, extracted from the map at  $z_{Si} \simeq 100 \mu m$  along the horizontal and vertical axes, respectively. As with the square sample, each profile was averaged over three adjacent bins centered on the respective axis to improve statistical precision. The inverse ToA increases toward

the central  $n^+$  column, where both the electric and weighting fields are stronger. This increase is more pronounced along the vertical axis, which connects two low-field regions.

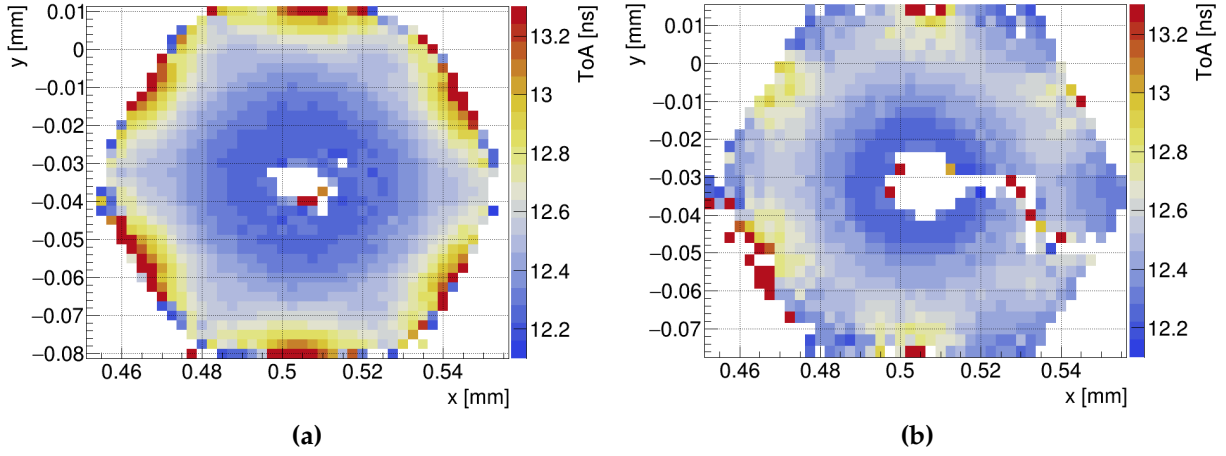


**Figure 5.15:** ToA distribution across the hexagonal pixel cell at two depths: (a)  $z_{Si} \approx 100 \mu m$ , and (b)  $z_{Si} \approx 0 \mu m$ . Measurements were performed at a bias voltage of 20 V. More details are given in the text.

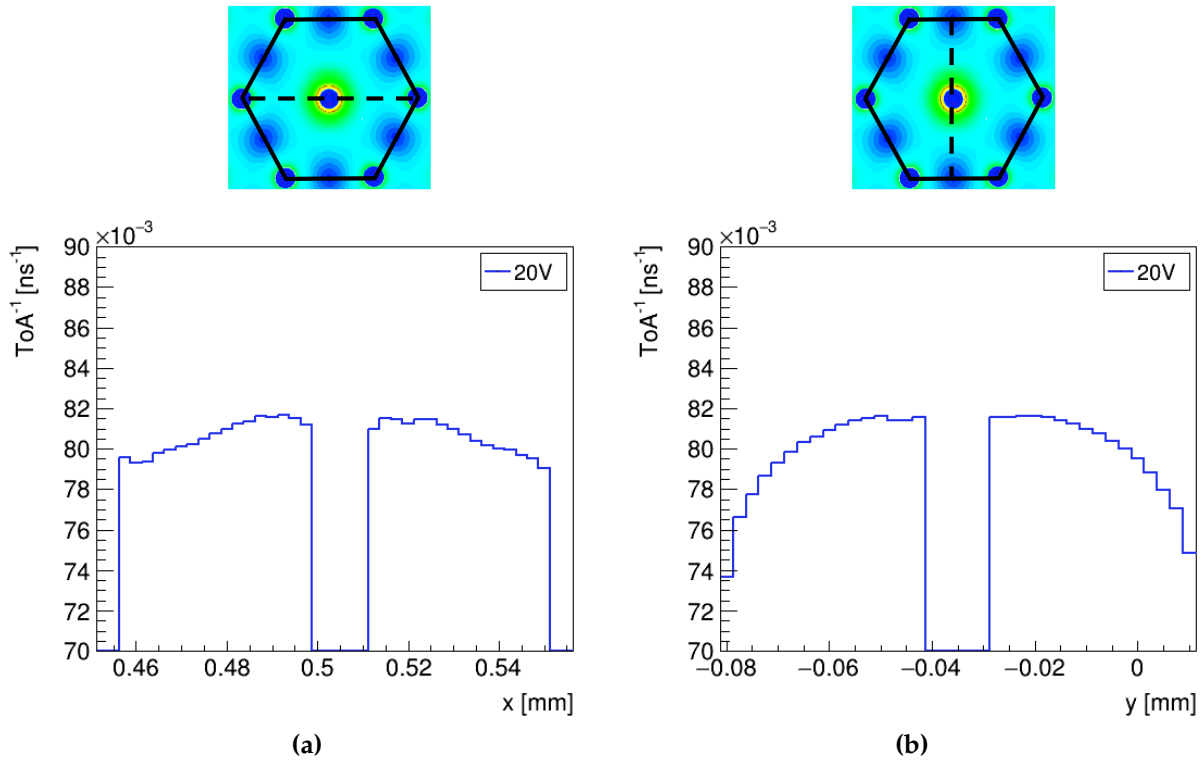


**Figure 5.16:** Inverse ToA profiles along (a) the horizontal and (b) the vertical axes of the hexagonal pixel cell at  $z_{Si} \approx 100 \mu m$  under a bias voltage of 20 V. These axes are indicated by black dashed lines in the electric field maps shown for reference.

To study the evolution of ToA with increasing electric field intensity, measurements were performed at  $z_{Si} \simeq 100 \mu\text{m}$  for bias voltages ranging from 2 V to 20 V. Figure 5.17 presents the MAD of the ToA distribution as a function of bias voltage, reaching 173 ps at 20 V. Unlike the square pixel layout, the hexagonal geometry exhibits a monotonic decrease in ToA spread with increasing bias voltage. Although a direct comparison at the same bias voltage is not meaningful—because the hexagonal and square pixel layouts differ in inter-electrode distance, leading to different electric field strengths and configurations—the MAD values in the hexagonal geometry remain consistently higher across the full voltage range.

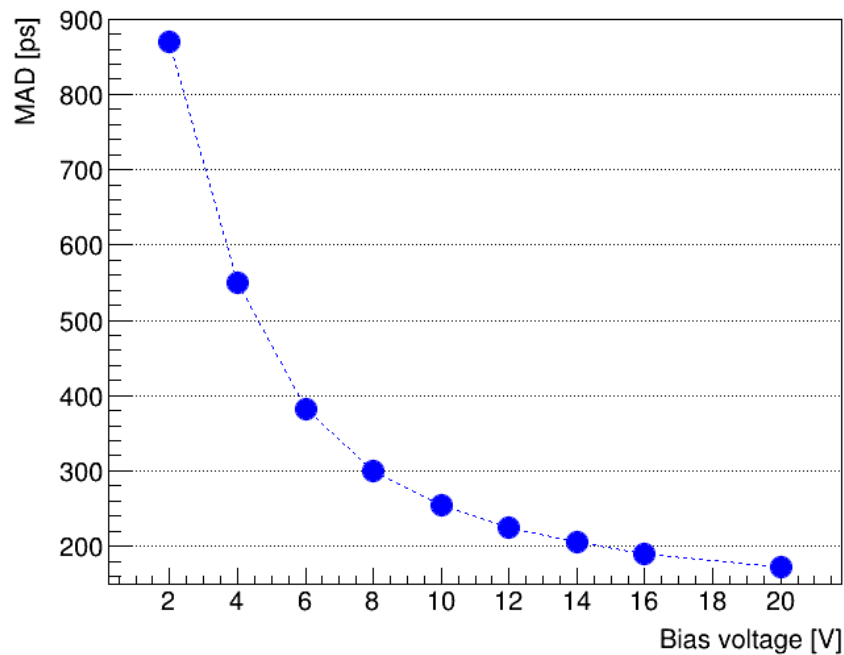


**Figure 5.17:** MAD of the ToA distribution across the hexagonal pixel cell as a function of bias voltage. Measurements were performed at  $z_{Si} \simeq 100 \mu\text{m}$ .

Figures 5.18a – 5.18c show the ToA distribution across one quarter of the hexagonal pixel cell at  $z_{Si} \simeq 100 \mu\text{m}$  for bias voltages of 4 V, 8 V and 14 V. These maps illustrate the progressive depletion of the pixel cell and the changes in electric field intensity with increasing bias voltage. Figures 5.18d – 5.18f present the corresponding one-dimensional ToA distributions, while Figures 5.18g – 5.18i and 5.18j – 5.18l show separate distributions for the inner and outer regions of the hexagonal pixel cell. As the bias voltage increases, the inner and outer distributions tend to converge, reflecting improved electric field uniformity.

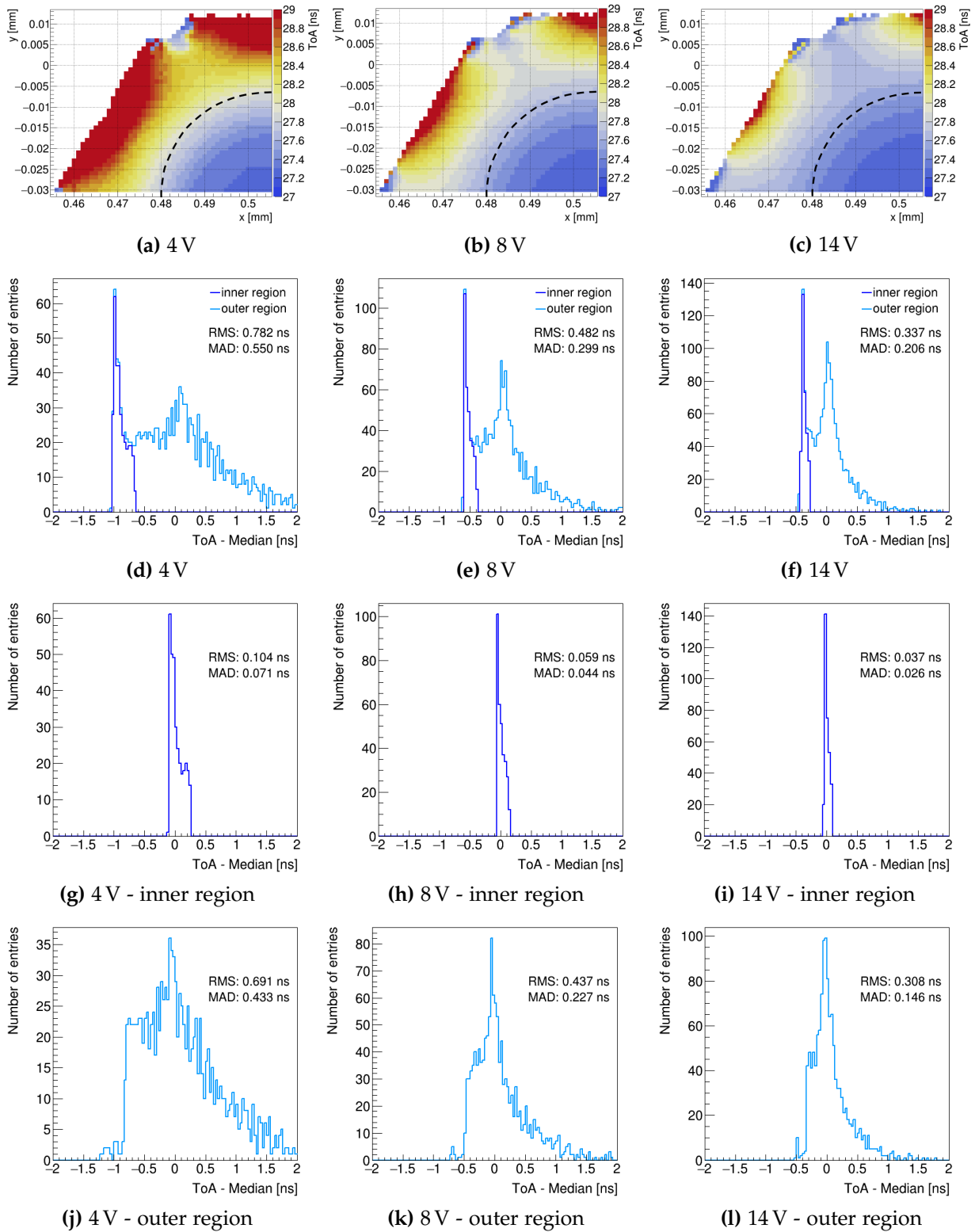


**Figure 5.18:** ToA across one quarter of the hexagonal pixel cell at  $z_{Si} \simeq 100 \mu m$ , for bias voltages of (a) 4 V, (b) 8 V, and (c) 14 V. The black dashed line marks the boundary between the inner and outer regions of the pixel cell. The corresponding one-dimensional ToA distributions are shown in (d)–(f), with histograms for each region stacked on top of one another. Separate distributions for the inner and outer regions are shown in (g)–(i) and (j)–(l), respectively. Each distribution is corrected by its respective median value.

The dependence of ToA on depth was also studied for the hexagonal sample, as shown in Figure 5.19. Measurements were performed at two different positions within the pixel cell at a bias voltage of 20 V. The profile in Figure 5.19a corresponds to a position approximately midway between the  $n^+$  electrode and one of the  $p^+$  electrodes, while Figure 5.19b corresponds to a position roughly midway between the central  $n^+$  column and the midpoint between two  $p^+$  electrodes. The resulting profiles differ near the frontside and backside of the sensor, where the  $p^+$  and  $n^+$  electrodes do not overlap. In the first position, the ToA increases near both the frontside and backside, indicating lower electric field strength in these regions. Conversely, in the second position, a valley near the frontside and a peak near the backside appear, corresponding to higher and lower electric field intensities, respectively.

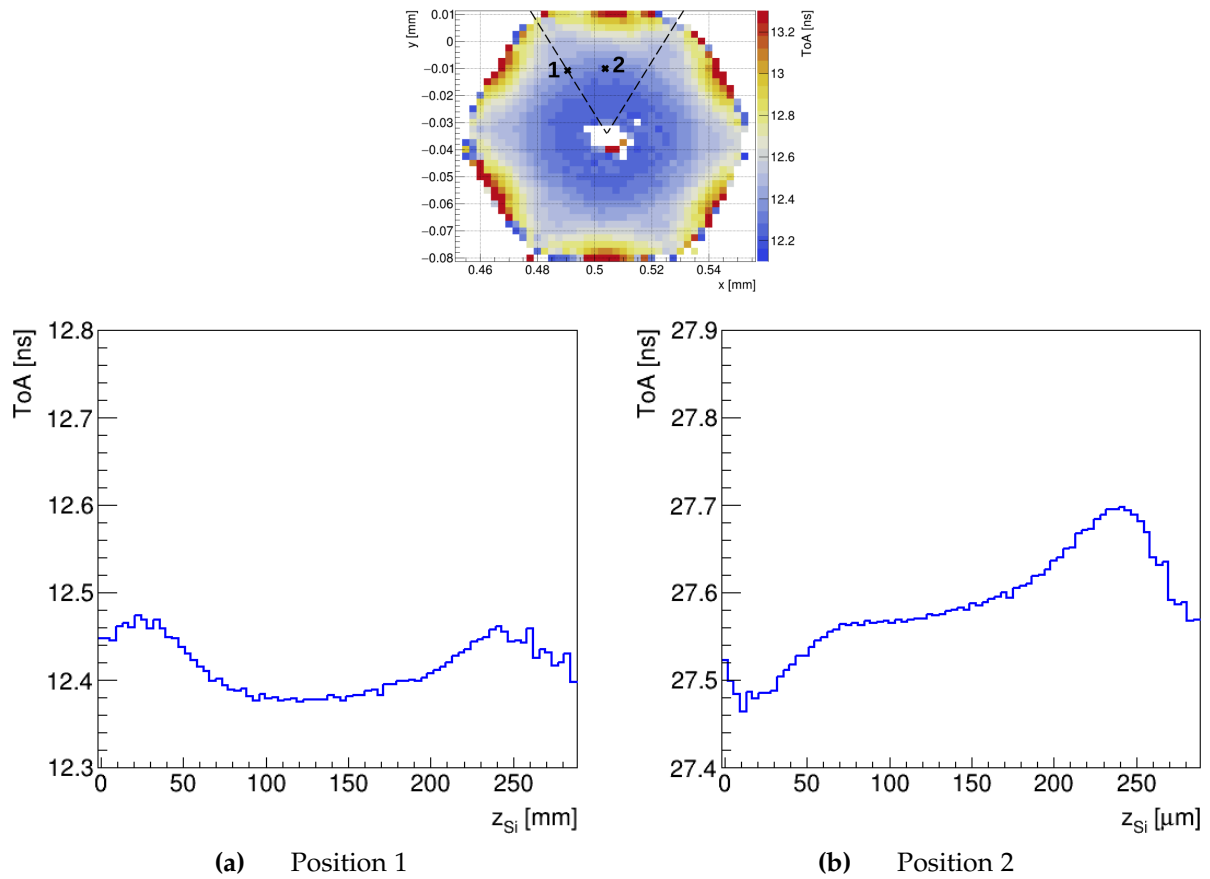


**Figure 5.19:** (a) and (b) show the ToA as a function of depth at two different positions within the hexagonal pixel cell. These positions are indicated in the ToA map shown for reference. Measurements were performed at a bias voltage of 20 V. The shift in the ToA magnitude is due to a change in the oscilloscope's time reference.

For the hexagonal sample, the sensor time jitter was evaluated following the procedure described in Section 5.3.2. The measurement was performed at  $z_{Si} \simeq 100 \mu\text{m}$ , at a position approximately halfway between the  $n^+$  electrode and one of the  $p^+$  electrodes.

This location corresponds to the first position indicated in Figure 5.19. The sensor was biased at 20 V, and the selected laser intensity resulted in a signal approximately equivalent to the charge deposited by 9.5 MIPs.

Figure 5.20a shows the average current transient from  $10^4$  measurements, each capturing two consecutive laser pulses. For each measurement, the ToA of both pulses was extracted using several CFD thresholds to evaluate the dependence of time jitter on the discriminating fraction. The resulting sensor time jitter as a function of CFD threshold is presented in Figure 5.20b. The best time jitter at the measured position—22 ps—was achieved using a 65% CFD threshold. The corresponding distribution of ToA differences between the two pulses is shown in Figure 5.20c, along with a Gaussian fit used to extract the time spread.

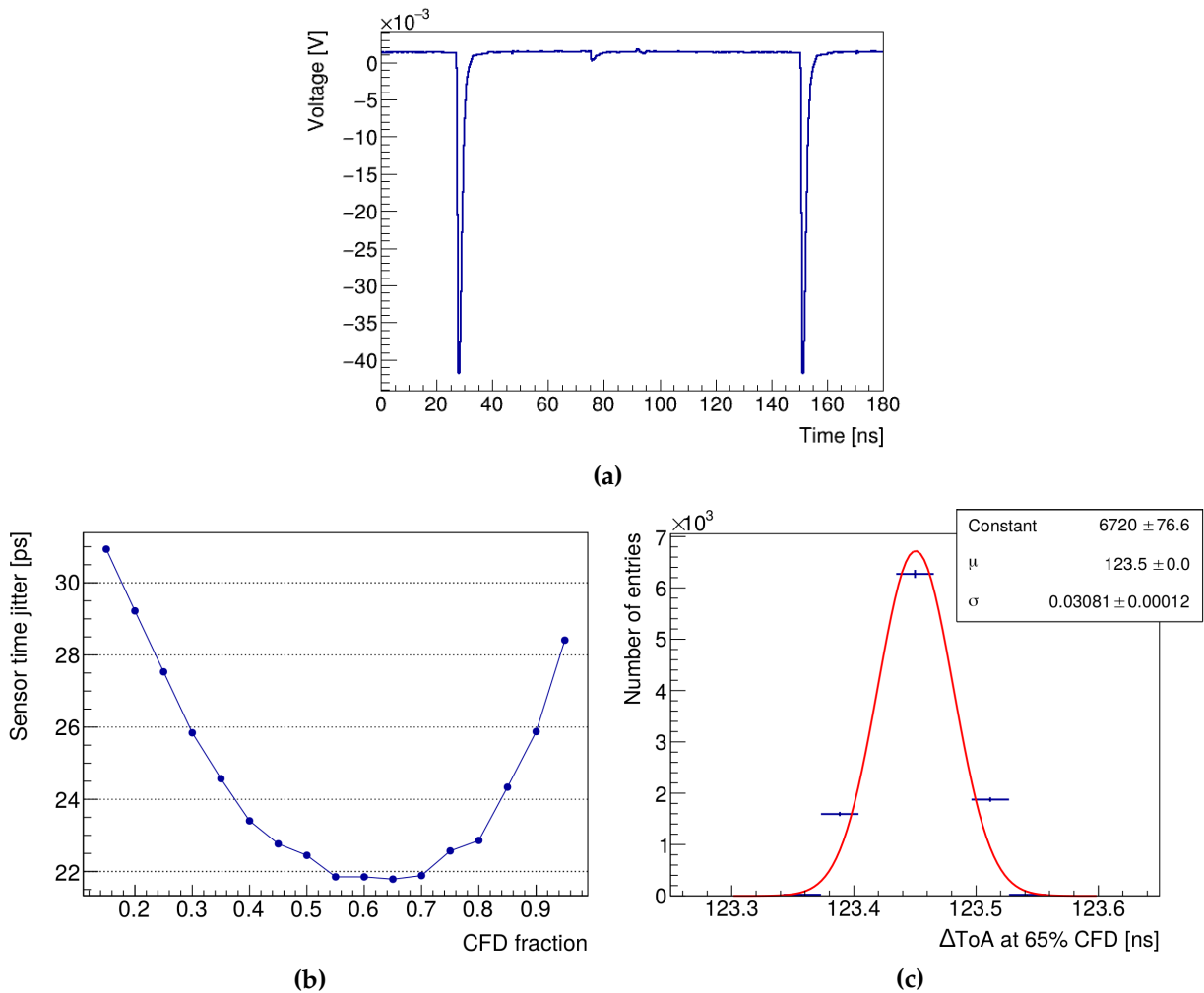


**Figure 5.20:** (a) Average current transient showing two pulses, obtained from  $10^4$  measurements. (b) Sensor time jitter as a function of CFD threshold used for ToA extraction. (c) Distribution of ToA differences between the two pulses at a 65% CFD threshold. A Gaussian fit is used to extract the time spread  $\sigma$ , from which the sensor time jitter is calculated as  $\sigma/\sqrt{2}$ .



## 5.4. Summary

The results presented in this chapter evaluate the influence of pixel cell layout on the timing performance of 3D pixel sensors. Samples with square and hexagonal pixel cells were characterized using the Two-Photon Absorption Transient Current Technique (TPA-TCT), which enables high-resolution, three-dimensional mapping of the timing response across the sensor volume. The level of spatial and temporal resolution in TPA-TCT surpasses what radioactive sources or standard Single-Photon Absorption TCT can achieve, highlighting the unique power of femtosecond infrared lasers for detailed studies in complex sensor geometries.

Measurements revealed a significant impact of pixel cell layout on timing performance, with the square geometry exhibiting a more uniform time-of-arrival (ToA) response. At the highest explored bias voltage of 20 V, ToA spreads of approximately 45 ps and 175 ps were measured across the square and hexagonal pixel cells, respectively. However, the larger distance between electrodes of opposite polarity in the hexagonal layout results in a weaker inter-electrode electric field, partially contributing to the larger ToA variation. Therefore, a direct comparison between the two geometries at the same bias voltage is not meaningful, as the internal field conditions are not comparable.

A novel method to estimate the sensor time jitter was also developed in the frame of this thesis, based on analyzing time differences between consecutive pulses in the TPA-TCT pulse train under identical conditions. This technique yielded sensor time jitter values as low as 22 ps in the hexagonal sample and provides a reliable and reproducible approach for detailed timing characterization.

Overall, these findings underline the importance of pixel design optimization for future 4D-tracking detectors and have been published in [145].

# Chapter 6

## Conclusions

Operation under the unprecedented radiation levels and collision rates foreseen during the high-luminosity phase of the CERN Large Hadron Collider (LHC) requires upgrades to several components of the Compact Muon Solenoid (CMS) experiment. In particular, the tracking system must be entirely replaced to maintain high performance under these more demanding conditions. The Inner Tracker (IT) requires sensors with high radiation tolerance, minimal power dissipation, increased granularity for improved spatial resolution, and high single-hit detection efficiency.

To meet these requirements, the final sensor design adopts *n-in-p* silicon technology with a thickness of  $150\text{ }\mu\text{m}$  and a pixel cell size of  $25 \times 100\text{ }\mu\text{m}^2$ . Planar pixel sensors will be installed throughout most of the IT, except in the layer closest to the interaction point. Thermal simulations of this region—considering both planar and 3D pixel sensors under various fluence and power consumption scenarios—have revealed thermal runaway issues with the planar pixel technology. As a result, 3D pixel sensors have been selected as the most suitable option for this layer, owing to their superior radiation hardness and lower power dissipation.

This thesis presents the characterization of 3D pixel detectors as part of a comprehensive R&D program aimed at their qualification for deployment in the innermost layer of the CMS IT. Two sensor manufacturers, Fondazione Bruno Kessler (FBK) and Centro Nacional de Microelectrónica (CNM), contributed to this effort. Sensors from both fabrication centers were bump-bonded to the full-scale readout chip prototype, developed by the RD53 Collaboration. Beam tests were conducted with single-chip 3D pixel modules to evaluate their performance before and after irradiation. The maximum tested fluence was  $1.6 \times 10^{16}\text{ n}_{\text{eq}}\text{cm}^{-2}$ , which is sufficient given the foreseen replacement of the innermost layer in the second half of HL-LHC operations.

Non-irradiated modules demonstrated excellent performance, achieving full depletion at bias voltages below 10 V, hit detection efficiency above 97%, and spatial resolution

down to  $2.5\text{ }\mu\text{m}$ . Moreover, the inefficiency introduced by the columnar electrodes is not expected to impact the overall detector performance once integrated into the CMS experiment, where particles will traverse the sensors at a wide range of incidence angles. After irradiation to  $1 \times 10^{16}\text{ n}_{\text{eq}}\text{cm}^{-2}$ , the modules maintained 97% efficiency at normal incidence across an operational range of 60 V, with fewer than 2% of masked pixels. The spatial resolution remained as low as  $3.5\text{ }\mu\text{m}$ , indicating only modest degradation. Even at the maximum tested fluence of  $1.6 \times 10^{16}\text{ n}_{\text{eq}}\text{cm}^{-2}$ , 96% efficiency was achieved at normal incidence within an operational range of 30 V, again with a low fraction of masked pixels. This ability to maintain high performance across a broad range of bias voltages ensures compatibility with the serial powering scheme planned for the IT.

In addition to test beam characterization, system-level tests with single-chip modules were conducted to assess robustness under the IT power distribution scheme. Module performance was found to remain stable across a serial-power chain, despite variations in effective bias voltage. Further tests also verified key functionalities of the readout electronics, demonstrating that the system can tolerate an open-circuit failure in one of the chips without compromising the operation of the remaining chips or increasing the total current demand.

Overall, the performance of 3D pixel detectors, both before and after irradiation, meets the CMS specifications for the innermost layer of the IT. With sensor production at FBK and module assembly at designated centers underway, full system integration and commissioning are scheduled to begin by the end of 2026.

Following this successful qualification program, an essential step during module assembly is the verification of connectivity between the sensors and the readout electronics to prevent performance degradation caused by defective bump-bonds. In preparation for the module production phase at one of the designated assembly centers, initial tests were performed with single-chip modules to commission the setups and validate the quality control procedures, which demonstrated excellent effectiveness.

Beyond the high-luminosity LHC upgrade, 3D pixel sensors are also being explored for timing applications in next-generation experiments, where extreme radiation environments are expected. Detectors in these experiments must provide precise timing information to reliably reconstruct particle trajectories. A key challenge for 3D pixel technology in this context is the non-uniformity of its electric and weighting fields, which introduces position-dependent variations in signal detection time and affects the overall time resolution.

This thesis presents a detailed timing characterization of 3D columnar-electrode pixel sensors with square and hexagonal cell geometries, focusing on the spatial dependence of signal detection time and the influence of pixel cell layout on timing performance.

The sensors were studied using the Two-Photon Absorption Transient Current Technique, which enables high-resolution, three-dimensional mapping of the timing response across the sensor volume. The measurements revealed a significant impact of pixel cell geometry, highlighting the importance of pixel design optimization for future 4D-tracking detectors, where both spatial and temporal resolution will be essential.

# References

- [1] R.L. Workman et al. *Review of Particle Physics: 2022*. Vol. 2022. Note. Oxford: Oxford University Press, 2022. DOI: [10.1093/ptep/ptac097](https://doi.org/10.1093/ptep/ptac097). URL: <https://cds.cern.ch/record/2836514>.
- [2] A.B. Arbuzov. “Quantum Field Theory and the Electroweak Standard Model”. In: (2018). 35 pages, pp. 1–34. DOI: [10.23730/CYRSP-2017-004.1](https://doi.org/10.23730/CYRSP-2017-004.1). arXiv: [1801.05670](https://arxiv.org/abs/1801.05670). URL: <https://cds.cern.ch/record/2315477>.
- [3] FCC - Future Circular Collider. Accessed: 2025-03-19. URL: <https://fcc.web.cern.ch/>.
- [4] The CEPC Study Group. *CEPC Technical Design Report – Accelerator (v2)*. 2024. arXiv: [2312.14363](https://arxiv.org/abs/2312.14363) [physics.acc-ph]. URL: <https://arxiv.org/abs/2312.14363>.
- [5] Philip Bambade et al. *The International Linear Collider: A Global Project*. 2019. arXiv: [1903.01629](https://arxiv.org/abs/1903.01629) [hep-ex]. URL: <https://arxiv.org/abs/1903.01629>.
- [6] Lyndon Evans and Philip Bryant. “LHC Machine”. In: *Journal of Instrumentation* 3.08 (2008), S08001. DOI: [10.1088/1748-0221/3/08/S08001](https://doi.org/10.1088/1748-0221/3/08/S08001). URL: <https://dx.doi.org/10.1088/1748-0221/3/08/S08001>.
- [7] Michael Benedikt et al. *LHC Design Report*. CERN Yellow Reports: Monographs. Geneva: CERN, 2004. DOI: [10.5170/CERN-2004-003-V-3](https://doi.org/10.5170/CERN-2004-003-V-3). URL: <https://cds.cern.ch/record/823808>.
- [8] M Meddahi et al. “Chapter 21: Beam from Injectors: The LHC Injectors Upgrade (LIU) Project”. In: *Adv. Ser. Direct. High Energy Phys.* 31 (2024), pp. 457–473. DOI: [10.1142/9789811278952\\_0021](https://doi.org/10.1142/9789811278952_0021). URL: <https://cds.cern.ch/record/2906395>.
- [9] Ewa Lopienska. “The CERN accelerator complex, layout in 2022. Complexe des accélérateurs du CERN en janvier 2022”. In: (2022). General Photo. URL: <https://cds.cern.ch/record/2800984>.
- [10] J Bernhard et al. *CERN Proton Synchrotron East Area Facility: Upgrades and renovation during Long Shutdown 2*. Ed. by J Bernhard. Vol. 4/2021. CERN Yellow Reports: Monographs. Geneva: CERN, 2021. DOI: [10.23731/CYRM-2021-004](https://doi.org/10.23731/CYRM-2021-004). URL: <https://cds.cern.ch/record/2792490>.
- [11] Dipanwita Banerjee et al. “The North Experimental Area at the Cern Super Proton Synchrotron”. In: (2021). Dedicated to Giorgio Brianti on the 50th an-

- niversary of his founding the SPS Experimental Areas Group of CERN-Lab II and hence initiating the present Enterprise. DOI: 10.17181/CERN.GP3K.OS1Y. URL: <https://cds.cern.ch/record/2774716>.
- [12] The ATLAS Collaboration et al. "The ATLAS Experiment at the CERN Large Hadron Collider". In: *Journal of Instrumentation* 3.08 (2008), S08003. DOI: 10.1088/1748-0221/3/08/S08003. URL: <https://dx.doi.org/10.1088/1748-0221/3/08/S08003>.
- [13] The CMS Collaboration et al. "The CMS experiment at the CERN LHC". In: *Journal of Instrumentation* 3.08 (2008), S08004. DOI: 10.1088/1748-0221/3/08/S08004. URL: <https://dx.doi.org/10.1088/1748-0221/3/08/S08004>.
- [14] The ALICE Collaboration et al. "The ALICE experiment at the CERN LHC". In: *Journal of Instrumentation* 3.08 (2008), S08002. DOI: 10.1088/1748-0221/3/08/S08002. URL: <https://dx.doi.org/10.1088/1748-0221/3/08/S08002>.
- [15] The LHCb Collaboration et al. "The LHCb Detector at the LHC". In: *Journal of Instrumentation* 3.08 (2008), S08005. DOI: 10.1088/1748-0221/3/08/S08005. URL: <https://dx.doi.org/10.1088/1748-0221/3/08/S08005>.
- [16] Maximilien Brice, Michael Hoch, and Joseph Gobin. "View of the CMS Detector before closure". 2008. URL: <https://cds.cern.ch/record/1133594>.
- [17] Claudia Marcelloni. "Different angles of the LHCb cavern on August 2008". 2008. URL: <https://cds.cern.ch/record/1144048>.
- [18] Maximilien Brice. "Installing the ATLAS calorimeter. Vue centrale du détecteur ATLAS avec ses huit toroides entourant le calorimètre avant son déplacement au centre du détecteur". 2005. URL: <http://cds.cern.ch/record/910381>.
- [19] Julien Ordan. "Inside ALICE detector empty skeleton". In: (2019). General Photo. URL: <https://cds.cern.ch/record/2665476>.
- [20] CMS Collaboration. "CMS Luminosity - Public results". In: (2024). Accessed: 2025-03-10. URL: <https://twiki.cern.ch/twiki/bin/view/CMSPublic/LumiPublicResults>.
- [21] Werner Herr and B Muratori. "Concept of luminosity". In: (2006). DOI: 10.5170/CERN-2006-002.361. URL: <https://cds.cern.ch/record/941318>.
- [22] O. Aberle et al. *High-Luminosity Large Hadron Collider (HL-LHC): Technical design report*. CERN Yellow Reports: Monographs. Geneva: CERN, 2020. DOI: 10.23731/CYRM-2020-0010. URL: <https://cds.cern.ch/record/2749422>.
- [23] *LHC/HL-LHC Plan*. Accessed: 2025-02-24. URL: <https://hilumilhc.web.cern.ch/content/hl-lhc-project>.
- [24] CMS Collaboration. *Technical proposal for the upgrade of the CMS detector through 2020*. Tech. rep. 2011. URL: <http://cds.cern.ch/record/1355706>.
- [25] Tai Sakuma. "Cutaway diagrams of CMS detector". In: (2019). URL: <http://cds.cern.ch/record/2665537>.

- [26] V Karimäki et al. *The CMS tracker system project: Technical Design Report*. Technical design report. CMS. Geneva: CERN, 1997. URL: <https://cds.cern.ch/record/368412>.
- [27] The Tracker Group of the CMS Collaboration. *The CMS Phase-1 Pixel Detector Upgrade*. Tech. rep. Geneva: CERN, 2020. URL: <https://cds.cern.ch/record/2745805>.
- [28] *The Phase-2 Upgrade of the CMS Tracker*. Tech. rep. Geneva: CERN, 2017. DOI: 10.17181/CERN.QZ28.FLHW. URL: <https://cds.cern.ch/record/2272264>.
- [29] *The CMS electromagnetic calorimeter project: Technical Design Report*. Technical design report. CMS. Geneva: CERN, 1997. URL: <https://cds.cern.ch/record/349375>.
- [30] *The CMS hadron calorimeter project: Technical Design Report*. Technical design report. CMS. Geneva: CERN, 1997. URL: <https://cds.cern.ch/record/357153>.
- [31] Candan Isik. *Phase 1 Upgrade of the CMS Hadron Calorimeter*. Tech. rep. Geneva: CERN, 2022. DOI: 10.1016/j.nima.2022.167389. URL: <https://cds.cern.ch/record/2810162>.
- [32] *The CMS magnet project: Technical Design Report*. Technical design report. CMS. Geneva: CERN, 1997. DOI: 10.17181/CERN.6ZU0.V4T9. URL: <http://cds.cern.ch/record/331056>.
- [33] J. G. Layter. *The CMS muon project: Technical Design Report*. Technical design report. CMS. Geneva: CERN, 1997. URL: <https://cds.cern.ch/record/343814>.
- [34] Antonello Pellecchia and on behalf of the CMS Muon group. “The upgrade of the CMS muon system for the high luminosity LHC”. In: *Journal of Instrumentation* 19.02 (2024), p. C02077. DOI: 10.1088/1748-0221/19/02/C02077. URL: <https://dx.doi.org/10.1088/1748-0221/19/02/C02077>.
- [35] Efe Yigitbasi. “New CMS Trigger Strategies for the Run 3 of the LHC”. In: *PoS EPS-HEP2023* (2024), p. 464. DOI: 10.22323/1.449.0464.
- [36] G L Bayatian et al. *CMS Physics: Technical Design Report Volume 1: Detector Performance and Software*. Technical design report. CMS. There is an error on cover due to a technical problem for some items. Geneva: CERN, 2006. URL: <http://cds.cern.ch/record/922757>.
- [37] S. Agostinelli et al. “Geant4—a simulation toolkit”. In: *Nuclear Instruments and Methods in Physics Research Section A: Accelerators, Spectrometers, Detectors and Associated Equipment* 506.3 (2003), pp. 250–303. ISSN: 0168-9002. DOI: [https://doi.org/10.1016/S0168-9002\(03\)01368-8](https://doi.org/10.1016/S0168-9002(03)01368-8). URL: <https://www.sciencedirect.com/science/article/pii/S0168900203013688>.
- [38] D Contardo et al. *Technical Proposal for the Phase-II Upgrade of the CMS Detector*. Tech. rep. Upgrade Project Leader Deputies: Lucia Silvestris (INFN-Bari), Jeremy Mans (University of Minnesota) Additional contacts: Lucia.Silvestris@cern.ch,



- Jeremy.Mans@cern.ch. Geneva, 2015. DOI: 10.17181/CERN.VU8I.D59J. URL: <https://cds.cern.ch/record/2020886>.
- [39] “FLUKA Simulations for Radiation Levels in Tracker and ECAL Regions for Phase II”. In: (2024). URL: <http://cds.cern.ch/record/2916743>.
- [40] *Layout of the Phase2 CMS Tracker for operation during the HL-LHC period*. Layout name: OT806.IT741. URL: <https://cms-tklayout.web.cern.ch/cms-tklayout/layouts-work/recent-layouts/>. Accessed: 2025-04-24.
- [41] *The Phase-2 Upgrade of the CMS Endcap Calorimeter*. Tech. rep. Geneva: CERN, 2017. DOI: 10.17181/CERN.IV8M.1JY2. URL: <http://cds.cern.ch/record/2293646>.
- [42] Collaboration CMS. *A MIP Timing Detector for the CMS Phase-2 Upgrade*. Tech. rep. Geneva: CERN, 2019. URL: <https://cds.cern.ch/record/2667167>.
- [43] D.A. Neamen. *Semiconductor Physics And Devices: Basic Principles*. 4th ed. McGraw-Hill international edition. McGraw-Hill, 2012. ISBN: 9780071089029.
- [44] V. Alex, S. Finkbeiner, and J. Weber. “Temperature dependence of the indirect energy gap in crystalline silicon”. In: *Journal of Applied Physics* 79.9 (May 1996), pp. 6943–6946. ISSN: 0021-8979. DOI: 10.1063/1.362447. eprint: [https://pubs.aip.org/aip/jap/article-pdf/79/9/6943/18685042/6943\\\_1\\\_online.pdf](https://pubs.aip.org/aip/jap/article-pdf/79/9/6943/18685042/6943\_1\_online.pdf). URL: <https://doi.org/10.1063/1.362447>.
- [45] C. Jacoboni et al. “A review of some charge transport properties of silicon”. In: *Solid-State Electronics* 20.2 (1977), pp. 77–89. ISSN: 0038-1101. DOI: [https://doi.org/10.1016/0038-1101\(77\)90054-5](https://doi.org/10.1016/0038-1101(77)90054-5). URL: <https://www.sciencedirect.com/science/article/pii/0038110177900545>.
- [46] D.M. Caughey and R.E. Thomas. “Carrier mobilities in silicon empirically related to doping and field”. In: *Proceedings of the IEEE* 55.12 (1967), pp. 2192–2193. DOI: 10.1109/PROC.1967.6123.
- [47] Daniel Hynds. “Silicon Zoology”. In: *7th Barcelona Techno Week - Course on semiconductor radiation detectors*. July 2023.
- [48] S.M. Sze and K.K. Ng. *Physics of Semiconductor Devices*. 3rd ed. Wiley, 2006. ISBN: 9780470068304.
- [49] *Characteristic IV curve - PN junction diode*. Accessed: 2025-04-03. URL: <https://testbook.com/physics/pn-junction-diode>.
- [50] A Chilingarov. “Temperature dependence of the current generated in Si bulk”. In: *Journal of Instrumentation* 8.10 (2013), P10003. DOI: 10.1088/1748-0221/8/10/P10003. URL: <https://dx.doi.org/10.1088/1748-0221/8/10/P10003>.
- [51] C. Patrignani. “Review of Particle Physics”. In: *Chinese Physics C* 40.10 (2016), p. 100001. DOI: 10.1088/1674-1137/40/10/100001. URL: <https://dx.doi.org/10.1088/1674-1137/40/10/100001>.
- [52] J Beringer et al. “Review of Particle Physics, 2012-2013”. In: *Phys. Rev. D* 86.1 (2012). The 2012 edition of Review of Particle Physics is published for the

- Particle Data Group as article 010001 in volume 86 of Physical Review D. This edition should be cited as: J. Beringer et al. (Particle Data Group), Phys. Rev. D 86, 010001 (2012)., p. 010001. DOI: [10.1103/PhysRevD.86.010001](https://doi.org/10.1103/PhysRevD.86.010001). URL: <http://cds.cern.ch/record/1481544>.
- [53] William R Leo. *Techniques for nuclear and particle physics experiments: a how-to approach; 2nd ed.* Berlin: Springer, 1994. DOI: [10.1007/978-3-642-57920-2](https://doi.org/10.1007/978-3-642-57920-2). URL: <https://cds.cern.ch/record/302344>.
- [54] Frank Hartmann. *Evolution of Silicon Sensor Technology in Particle Physics*. Vol. 275. Springer Tracts in Modern Physics. Springer, 2017. ISBN: 978-3-319-64434-9, 978-3-319-64436-3. DOI: [10.1007/978-3-319-64436-3](https://doi.org/10.1007/978-3-319-64436-3).
- [55] *Photon interaction mechanisms*. Accessed: 2025-03-28. URL: <https://www.flickr.com/photos/mitopencourseware/3706466731/in/photostream/>.
- [56] Martin A. Green. “Improved silicon optical parameters at 25°C, 295 K and 300 K including temperature coefficients”. In: *Progress in Photovoltaics: Research and Applications* 30.2 (2022), pp. 164–179. DOI: <https://doi.org/10.1002/pip.3474>. eprint: <https://onlinelibrary.wiley.com/doi/pdf/10.1002/pip.3474>. URL: <https://onlinelibrary.wiley.com/doi/abs/10.1002/pip.3474>.
- [57] Helmuth Spieler. *Semiconductor Detector Systems*. Vol. v.12. Semiconductor Science and Technology. Oxford: Oxford University Press, 2005. ISBN: 978-0-19-852784-8.
- [58] Leonardo Rossi et al. *Pixel detectors: from fundamentals to applications*. Particle acceleration and detection. Berlin: Springer, 2006. DOI: [10.1007/3-540-28333-1](https://doi.org/10.1007/3-540-28333-1). URL: <https://cds.cern.ch/record/976471>.
- [59] Michael Moll. “Displacement Damage in Silicon Detectors for High Energy Physics”. In: *IEEE Transactions on Nuclear Science* 65.8 (2018), pp. 1561–1582. DOI: [10.1109/TNS.2018.2819506](https://doi.org/10.1109/TNS.2018.2819506).
- [60] V Eremin, E Verbitskaya, and Z Li. “The origin of double peak electric field distribution in heavily irradiated silicon detectors”. In: *Nuclear Instruments and Methods in Physics Research Section A: Accelerators, Spectrometers, Detectors and Associated Equipment* 476.3 (2002). Proc. of the 3rd Int. Conf. on Radiation Effects on Semiconductor Materials, Detectors and Devices, pp. 556–564. ISSN: 0168-9002. DOI: [https://doi.org/10.1016/S0168-9002\(01\)01642-4](https://doi.org/10.1016/S0168-9002(01)01642-4). URL: <https://www.sciencedirect.com/science/article/pii/S0168900201016424>.
- [61] CMS Collaboration. *The Phase-2 Upgrade of the CMS Beam Radiation Instrumentation and Luminosity Detectors*. Tech. rep. This is the final version, approved by the LHCC. Geneva: CERN, 2021. URL: <https://cds.cern.ch/record/2759074>.
- [62] I. Arnquist et al. “The DAMIC-M Low Background Chamber”. In: *Journal of Instrumentation* 19.11 (2024), T11010. DOI: [10.1088/1748-0221/19/11/T11010](https://doi.org/10.1088/1748-0221/19/11/T11010). URL: <https://dx.doi.org/10.1088/1748-0221/19/11/T11010>.

- [63] M. Aguilar et al. “First Result from the Alpha Magnetic Spectrometer on the International Space Station: Precision Measurement of the Positron Fraction in Primary Cosmic Rays of 0.5–350 GeV”. In: *Phys. Rev. Lett.* 110 (14 2013), p. 141102. DOI: [10.1103/PhysRevLett.110.141102](https://doi.org/10.1103/PhysRevLett.110.141102). URL: <https://link.aps.org/doi/10.1103/PhysRevLett.110.141102>.
- [64] M. Turala. “Silicon tracking detectors—historical overview”. In: *Nuclear Instruments and Methods in Physics Research Section A: Accelerators, Spectrometers, Detectors and Associated Equipment* 541.1 (2005). Development and Application of Semiconductor Tracking Detectors, pp. 1–14. ISSN: 0168-9002. DOI: <https://doi.org/10.1016/j.nima.2005.01.032>. URL: <https://www.sciencedirect.com/science/article/pii/S0168900205000446>.
- [65] Ivan Perić et al. “The FEI3 readout chip for the ATLAS pixel detector”. In: *Nuclear Instruments and Methods in Physics Research Section A: Accelerators, Spectrometers, Detectors and Associated Equipment* 565.1 (2006). Proceedings of the International Workshop on Semiconductor Pixel Detectors for Particles and Imaging, pp. 178–187. ISSN: 0168-9002. DOI: <https://doi.org/10.1016/j.nima.2006.05.032>. URL: <https://www.sciencedirect.com/science/article/pii/S0168900206007649>.
- [66] M. Garcia-Sciveres et al. “The FE-I4 pixel readout integrated circuit”. In: *Nuclear Instruments and Methods in Physics Research Section A: Accelerators, Spectrometers, Detectors and Associated Equipment* 636.1, Supplement (2011). 7th International “Hiroshima” Symposium on the Development and Application of Semiconductor Tracking Detectors, S155–S159. ISSN: 0168-9002. DOI: <https://doi.org/10.1016/j.nima.2010.04.101>. URL: <https://www.sciencedirect.com/science/article/pii/S0168900210009551>.
- [67] *PSI46dig readout chip - External specification*. Accessed: 2025-10-09. URL: <https://www.cmspixel.phys.ethz.ch/docs/psi46-readout-chip/psi46v2.pdf>.
- [68] A. Starodumov, P. Berger, and M. Meinhard. “High rate capability and radiation tolerance of the PROC600 readout chip for the CMS pixel detector”. In: *Journal of Instrumentation* 12.01 (2017), p. C01078. DOI: [10.1088/1748-0221/12/01/C01078](https://doi.org/10.1088/1748-0221/12/01/C01078). URL: <https://doi.org/10.1088/1748-0221/12/01/C01078>.
- [69] F. Loddo et al. “RD53 pixel chips for the ATLAS and CMS Phase-2 upgrades at HL-LHC”. In: *Nuclear Instruments and Methods in Physics Research Section A: Accelerators, Spectrometers, Detectors and Associated Equipment* 1067 (2024), p. 169682. ISSN: 0168-9002. DOI: <https://doi.org/10.1016/j.nima.2024.169682>. URL: <https://www.sciencedirect.com/science/article/pii/S0168900224006089>.
- [70] The Tracker Group of the CMS Collaboration. “Evaluation of planar silicon pixel sensors with the RD53A readout chip for the Phase 2 Upgrade of the CMS Inner Tracker”. In: *JINST* 18.11 (Nov. 2023), P11015. DOI: [10.1088/1748-0221/18/11/P11015](https://doi.org/10.1088/1748-0221/18/11/P11015). URL: <https://dx.doi.org/10.1088/1748-0221/18/11/P11015>.

- [71] S.I. Parker, C.J. Kenney, and J. Segal. “3D — A proposed new architecture for solid-state radiation detectors”. In: *Nuclear Instruments and Methods in Physics Research Section A: Accelerators, Spectrometers, Detectors and Associated Equipment* 395.3 (1997). Proceedings of the Third International Workshop on Semiconductor Pixel Detectors for Particles and X-rays, pp. 328–343. ISSN: 0168-9002. DOI: [https://doi.org/10.1016/S0168-9002\(97\)00694-3](https://doi.org/10.1016/S0168-9002(97)00694-3). URL: <https://www.sciencedirect.com/science/article/pii/S0168900297006943>.
- [72] A. Loi, A. Contu, and A. Lai. “Timing optimisation and analysis in the design of 3D silicon sensors: the TCoDe simulator”. In: *Journal of Instrumentation* 16.02 (Feb. 2021), P02011. DOI: [10.1088/1748-0221/16/02/P02011](https://doi.org/10.1088/1748-0221/16/02/P02011). URL: <https://dx.doi.org/10.1088/1748-0221/16/02/P02011>.
- [73] G. Aad et al. “Sensor response and radiation damage effects for 3D pixels in the ATLAS IBL Detector”. In: *Journal of Instrumentation* 19.10 (Oct. 2024), P10008. ISSN: 1748-0221. DOI: [10.1088/1748-0221/19/10/p10008](https://doi.org/10.1088/1748-0221/19/10/p10008). URL: <http://dx.doi.org/10.1088/1748-0221/19/10/P10008>.
- [74] M Albrow et al. *CMS-TOTEM Precision Proton Spectrometer*. Tech. rep. 2014. URL: <https://cds.cern.ch/record/1753795>.
- [75] L Adamczyk et al. *Technical Design Report for the ATLAS Forward Proton Detector*. Tech. rep. 2015. URL: <http://cds.cern.ch/record/2017378>.
- [76] Fabio Ravera. “3D silicon pixel detectors for the CT-PPS tracking system”. Presented 16 Jun 2017. Turin U., 2017. URL: <http://cds.cern.ch/record/2682003>.
- [77] Stefano Terzo et al. “Novel 3D Pixel Sensors for the Upgrade of the ATLAS Inner Tracker”. In: *Frontiers in Physics* 9 (Apr. 2021), p. 624668. DOI: [10.3389/fphy.2021.624668](https://doi.org/10.3389/fphy.2021.624668).
- [78] A. Lai et al. “First results of the TIMESPOT project on developments on fast sensors for future vertex detectors”. In: *Nuclear Instruments and Methods in Physics Research Section A: Accelerators, Spectrometers, Detectors and Associated Equipment* 981 (2020), p. 164491. ISSN: 0168-9002. DOI: <https://doi.org/10.1016/j.nima.2020.164491>. URL: <https://www.sciencedirect.com/science/article/pii/S0168900220308883>.
- [79] F. Borgato et al. “Characterisation of highly irradiated 3D trench silicon pixel sensors for 4D tracking with 10 ps timing accuracy”. In: *Frontiers in Physics* Volume 12 - 2024 (2024). ISSN: 2296-424X. DOI: [10.3389/fphy.2024.1393019](https://doi.org/10.3389/fphy.2024.1393019). URL: <https://www.frontiersin.org/journals/physics/articles/10.3389/fphy.2024.1393019>.
- [80] A Fernández Prieto. “The LHCb VELO Upgrade II: design and development of the readout electronics”. In: *JINST* 19.05 (2024), p. C05011. DOI: [10.1088/1748-0221/19/05/C05011](https://doi.org/10.1088/1748-0221/19/05/C05011). URL: <https://cds.cern.ch/record/2914039>.

- [81] V.A.K. Temple. “Increased avalanche breakdown voltage and controlled surface electric fields using a junction termination extension (JTE) technique”. In: *IEEE Transactions on Electron Devices* 30.8 (1983), pp. 954–957. DOI: [10.1109/T-ED.1983.21243](https://doi.org/10.1109/T-ED.1983.21243).
- [82] Lazar Markovic. “Progress on characterization of LGAD sensors for the CMS ETL”. In: *PoS BPU11* (2023), p. 095. DOI: [10.22323/1.427.0095](https://doi.org/10.22323/1.427.0095). URL: <http://cds.cern.ch/record/2883835>.
- [83] C. Agapopoulou et al. *Performance of a front-end prototype ASIC for the ATLAS High Granularity Timing Detector*. 2023. arXiv: 2306.08949 [physics.ins-det]. URL: <https://arxiv.org/abs/2306.08949>.
- [84] C. Agapopoulou et al. “Performance in beam tests of irradiated Low Gain Avalanche Detectors for the ATLAS High Granularity Timing Detector”. In: *Journal of Instrumentation* 17.09 (Sept. 2022), P09026. DOI: [10.1088/1748-0221/17/09/P09026](https://doi.org/10.1088/1748-0221/17/09/P09026). URL: <https://dx.doi.org/10.1088/1748-0221/17/09/P09026>.
- [85] Matteo Centis Vignali and Giovanni Paternoster. “Low gain avalanche diodes for photon science applications”. In: *Frontiers in Physics* (2024). DOI: [10.3389/fphy.2024.1359179](https://doi.org/10.3389/fphy.2024.1359179).
- [86] *Medipix Collaboration webpage*. Accessed: 2025-05-04. URL: <https://medipix.web.cern.ch/home>.
- [87] Jan Dudak. “High-resolution X-ray imaging applications of hybrid-pixel photon counting detectors Timepix”. In: *Radiation Measurements* 137 (2020), p. 106409. ISSN: 1350-4487. DOI: <https://doi.org/10.1016/j.radmeas.2020.106409>. URL: <https://www.sciencedirect.com/science/article/pii/S1350448720301888>.
- [88] R. Ballabriga et al. “The Timepix4 analog front-end design: Lessons learnt on fundamental limits to noise and time resolution in highly segmented hybrid pixel detectors”. In: *Nuclear Instruments and Methods in Physics Research Section A: Accelerators, Spectrometers, Detectors and Associated Equipment* 1045 (2023), p. 167489. ISSN: 0168-9002. DOI: <https://doi.org/10.1016/j.nima.2022.167489>. URL: <https://www.sciencedirect.com/science/article/pii/S0168900222007811>.
- [89] J. Baudot et al. “First test results of MIMOSA-26, a fast CMOS sensor with integrated zero suppression and digitized output”. In: *2009 IEEE Nuclear Science Symposium Conference Record (NSS/MIC)*. 2009, pp. 1169–1173. DOI: [10.1109/NSSMIC.2009.5402399](https://doi.org/10.1109/NSSMIC.2009.5402399).
- [90] M. Mager. “ALPIDE, the Monolithic Active Pixel Sensor for the ALICE ITS upgrade”. In: *Nuclear Instruments and Methods in Physics Research Section A: Accelerators, Spectrometers, Detectors and Associated Equipment* 824 (2016). Frontier Detectors for Frontier Physics: Proceedings of the 13th Pisa Meeting on Advanced Detectors, pp. 434–438. ISSN: 0168-9002. DOI: <https://doi.org/10.1016/j.nima.2015.09.057>. URL: <https://www.sciencedirect.com/science/article/pii/S0168900215011122>.



- [91] T.H. Pham et al. “Design of the OBELIX monolithic CMOS pixel sensor for an upgrade of the Belle II vertex detector”. In: *Journal of Instrumentation* 19.04 (Apr. 2024), p. C04020. DOI: [10.1088/1748-0221/19/04/C04020](https://dx.doi.org/10.1088/1748-0221/19/04/C04020). URL: <https://dx.doi.org/10.1088/1748-0221/19/04/C04020>.
- [92] ALICE collaboration The. *Technical Design report for the ALICE Inner Tracking System 3 - ITS3 ; A bent wafer-scale monolithic pixel detector*. Tech. rep. Co-project Manager: Magnus Mager, [magnus.mager@cern.ch](mailto:magnus.mager@cern.ch). Geneva: CERN, 2024. URL: <https://cds.cern.ch/record/2890181>.
- [93] Hans-Günther Moser. “The Belle II DEPFET pixel detector”. In: *Nuclear Instruments and Methods in Physics Research Section A: Accelerators, Spectrometers, Detectors and Associated Equipment* 831 (2016). Proceedings of the 10th International “Hiroshima” Symposium on the Development and Application of Semiconductor Tracking Detectors, pp. 85–87. ISSN: 0168-9002. DOI: <https://doi.org/10.1016/j.nima.2016.02.078>. URL: <https://www.sciencedirect.com/science/article/pii/S0168900216002540>.
- [94] R. Bugiel et al. “High spatial resolution monolithic pixel detector in SOI technology”. In: *Nuclear Instruments and Methods in Physics Research Section A: Accelerators, Spectrometers, Detectors and Associated Equipment* 988 (2021), p. 164897. ISSN: 0168-9002. DOI: <https://doi.org/10.1016/j.nima.2020.164897>. URL: <https://www.sciencedirect.com/science/article/pii/S0168900220312948>.
- [95] Maurice Garcia-Sciveres. *The RD53A Integrated Circuit*. Tech. rep. Geneva: CERN, 2017. URL: <https://cds.cern.ch/record/2287593>.
- [96] W. Adam et al. “Comparative evaluation of analogue front-end designs for the CMS Inner Tracker at the High Luminosity LHC”. In: *JINST* 16.12 (2021). 31 pages, 26 figures, prepared for submission to JINST, P12014. DOI: [10.1088/1748-0221/16/12/P12014](https://doi.org/10.1088/1748-0221/16/12/P12014). arXiv: 2105.00070. URL: <https://cds.cern.ch/record/2765909>.
- [97] Maurice Garcia-Sciveres, Flavio Loddo, and Jorgen Christiansen. *The RD53B-CMS Pixel Readout Chip Manual*. Tech. rep. Geneva: CERN, 2019. URL: <https://cds.cern.ch/record/2665301>.
- [98] Dinardo, Mauro Emanuele. “The CMS Inner Tracker DAQ system for the High Luminosity upgrade of LHC: From single-chip testing, to large-scale assembly qualification”. In: *EPJ Web of Conf.* 295 (2024), p. 02028. DOI: [10.1051/epjconf/202429502028](https://doi.org/10.1051/epjconf/202429502028). URL: <https://doi.org/10.1051/epjconf/202429502028>.
- [99] CMS Tracker Group. *Ph2\_ACF: Phase-2 Acquisition & Control Framework*. [https://gitlab.cern.ch/cms\\_tk\\_ph2/Ph2\\_ACF](https://gitlab.cern.ch/cms_tk_ph2/Ph2_ACF). Accessed: 2025-06-16.
- [100] Centro Nacional de Microelectrónica (CNM). URL: <http://www.cnm.es>.
- [101] Fondazione Bruno Kessler (FBK). URL: <https://sd.fbk.eu>.
- [102] Stefano Terzo et al. “Novel 3D Pixel Sensors for the Upgrade of the ATLAS Inner Tracker”. In: *Frontiers in Physics Volume 9 - 2021* (2021). ISSN: 2296-424X. DOI:

- 10.3389/fphy.2021.624668. URL: <https://www.frontiersin.org/journals/physics/articles/10.3389/fphy.2021.624668>.
- [103] Marco Meschini et al. "Pixel Detector Developments for Tracker Upgrades of the High Luminosity LHC: Volume 2". In: Aug. 2018, pp. 349–355. ISBN: 978-981-13-1315-8. DOI: 10.1007/978-981-13-1316-5\_65.
- [104] Jordi Duarte-Campderros. "Pixelated 3D sensors for tracking in radiation harsh environments". In: *JPS Conf. Proc.* 34 (2021). Proceedings of the The 29th International Workshop on Vertex Detectors (VERTEX2020), p. 010005. DOI: 10.7566/JPSCP.34.010005. arXiv: 2101.06019. URL: <https://cds.cern.ch/record/2749997>.
- [105] Karlsruhe Irradiation Facility. Accessed: 2025-06-03. URL: [https://www.etp.kit.edu/english/irradiation\\_center.php](https://www.etp.kit.edu/english/irradiation_center.php).
- [106] CERN Irradiation Facility. Accessed: 2025-06-03. URL: <https://ps-irrad.web.cern.ch/ps-irrad/>.
- [107] A. Papadopoulos and on behalf of the CMS Tracker Group. "Analog performance of the CROCv1 pixel readout chip for the CMS Phase-2 Tracker Upgrade". In: *Journal of Instrumentation* 18.01 (Jan. 2023), p. C01068. DOI: 10.1088/1748-0221/18/01/C01068. URL: <https://dx.doi.org/10.1088/1748-0221/18/01/C01068>.
- [108] P. Allport et al. "Experimental determination of proton hardness factors at several irradiation facilities". In: *Journal of Instrumentation* 14.12 (Dec. 2019), P12004. DOI: 10.1088/1748-0221/14/12/P12004. URL: <https://dx.doi.org/10.1088/1748-0221/14/12/P12004>.
- [109] R. Diener et al. "The DESY II test beam facility". In: *Nuclear Instruments and Methods in Physics Research Section A: Accelerators, Spectrometers, Detectors and Associated Equipment* 922 (2019), pp. 265–286. ISSN: 0168-9002. DOI: <https://doi.org/10.1016/j.nima.2018.11.133>.
- [110] Hendrik Jansen et al. "Performance of the EUDET-type beam telescopes". In: *EPJ Techniques and Instrumentation* 3.1 (Oct. 2016). ISSN: 2195-7045. DOI: 10.1140/epjti/s40485-016-0033-2. URL: <http://dx.doi.org/10.1140/epjti/s40485-016-0033-2>.
- [111] D. Cussans. *A Trigger/Timing Logic Unit (TLU) for AIDAinnova (New TLU Poduced)*. Tech. rep. June 2025. DOI: 10.5281/zenodo.15672112. URL: <https://doi.org/10.5281/zenodo.15672112>.
- [112] Yi Liu. *EUDAQ2 User Manual*. Tech. rep. Geneva: CERN, 2018. URL: <https://cds.cern.ch/record/2314266>.
- [113] D. Dannheim et al. "Corryvreckan: a modular 4D track reconstruction and analysis software for test beam data". In: *Journal of Instrumentation* 16.03 (Mar. 2021), P03008. DOI: 10.1088/1748-0221/16/03/P03008. URL: <https://dx.doi.org/10.1088/1748-0221/16/03/P03008>.



- [114] S. Spannagel J. Kröger and M. Williams. *Corryvreckan User Manual (latest version)*. <http://cern.ch/go/db9Z>. Accessed: 2025-06-17.
- [115] *Corryvreckan: The Maelstrom for Your Test Beam Data*. <https://gitlab.cern.ch/corryvreckan/corryvreckan>. Accessed: 2025-09-10.
- [116] R. Turchetta. “Spatial resolution of silicon microstrip detectors”. In: *Nucl. Instrum. Meth. A* 335 (1993), pp. 44–58. doi: 10.1016/0168-9002(93)90255-G.
- [117] M Swartz et al. “A new technique for the reconstruction, validation, and simulation of hits in the CMS Pixel Detector”. In: *PoS Vertex 2007* (2007), p. 035. doi: 10.22323/1.057.0035. URL: <https://cds.cern.ch/record/1073691>.
- [118] V. Blobel. “A new fast track-fit algorithm based on broken lines”. In: *Nuclear Instruments and Methods in Physics Research Section A: Accelerators, Spectrometers, Detectors and Associated Equipment* 566.1 (2006). TIME 2005, pp. 14–17. ISSN: 0168-9002. doi: <https://doi.org/10.1016/j.nima.2006.05.156>. URL: <https://www.sciencedirect.com/science/article/pii/S0168900206007996>.
- [119] Claus Kleinwort. “General broken lines as advanced track fitting method”. In: *Nuclear Instruments and Methods in Physics Research Section A: Accelerators, Spectrometers, Detectors and Associated Equipment* 673 (2012), pp. 107–110. ISSN: 0168-9002. doi: <https://doi.org/10.1016/j.nima.2012.01.024>. URL: <https://www.sciencedirect.com/science/article/pii/S0168900212000642>.
- [120] F and James. “MINUIT: Function Minimization and Error Analysis Reference Manual”. In: (1998). CERN Program Library Long Writeups. URL: <https://cds.cern.ch/record/2296388>.
- [121] V. Blobel. “Software alignment for tracking detectors”. In: *Nuclear Instruments and Methods in Physics Research Section A: Accelerators, Spectrometers, Detectors and Associated Equipment* 566.1 (2006). TIME 2005, pp. 5–13. ISSN: 0168-9002. doi: <https://doi.org/10.1016/j.nima.2006.05.157>. URL: <https://www.sciencedirect.com/science/article/pii/S0168900206007984>.
- [122] Clara Lasaosa Garcia. *Implementation of the 3D pixel sensor response into CMSSW*. 2020. URL: <http://hdl.handle.net/10261/231575>.
- [123] Morris Swartz. *A Detailed Simulation of the CMS Pixel Sensor*. Tech. rep. Geneva: CERN, 2002. URL: <https://cds.cern.ch/record/687440>.
- [124] Tamas Almos Vami and Morris Swartz. *Simulated performance and calibration of CMS Phase-2 Upgrade Inner Tracker sensors*. 2023. arXiv: 2301.13815 [physics.ins-det]. URL: <https://arxiv.org/abs/2301.13815>.
- [125] Clara Lasaosa Garcia and Davide Zuolo. *Evaluation of 3D pixel silicon sensors for the CMS Phase-2 Inner Tracker*. Tech. rep. Geneva: CERN, 2024. URL: <https://cds.cern.ch/record/2940830>.
- [126] Marcelo O. Pereira et al. “Development of a methodology for low-energy X-ray absorption correction in biological samples using radiation scattering techniques”. In: (2009). URL: <https://inis.iaea.org/records/bdryz-q7a98>.

- [127] Panagiotis Assiouras. *Qualification of Bump Bonding in CMS Inner Tracker Pixel Modules for the Phase-2 Upgrade*. Tech. rep. 07. Geneva: CERN, 2025. DOI: [10.1088/1748-0221/20/07/C07003](https://doi.org/10.1088/1748-0221/20/07/C07003). arXiv: 2505.06752. URL: <https://cds.cern.ch/record/2931989>.
- [128] A. Cassese. “Powering of the CMS Phase-2 Upgraded Tracker”. In: *PoS TWEPP2019* (2020), p. 066. DOI: [10.22323/1.370.0066](https://doi.org/10.22323/1.370.0066).
- [129] A. Cassese, on behalf of the CMS Tracker Group. *Serial powering for the CMS Inner Tracker detector at High Luminosity LHC*. Presented at the 18th Trento Workshop on Advanced Silicon Radiation Detectors [https://indico.cern.ch/event/1223972/contributions/5262006/attachments/2601137/4491323/Cassese\\_Serial\\_Powering\\_CMS\\_IT\\_Upgrade.pdf](https://indico.cern.ch/event/1223972/contributions/5262006/attachments/2601137/4491323/Cassese_Serial_Powering_CMS_IT_Upgrade.pdf). 2023.
- [130] Dominik Koukola. *Serial Powering for the Tracker Phase-2 Upgrade*. Tech. rep. Geneva: CERN, 2019. DOI: [10.22323/1.373.0039](https://doi.org/10.22323/1.373.0039). URL: <https://cds.cern.ch/record/2712278>.
- [131] *RD53B users guide*. Tech. rep. Geneva: CERN, 2020. URL: <https://cds.cern.ch/record/2754251>.
- [132] G. Kramberger et al. “Timing performance of small cell 3D silicon detectors”. In: *Nuclear Instruments and Methods in Physics Research Section A: Accelerators, Spectrometers, Detectors and Associated Equipment* 934 (2019), pp. 26–32. ISSN: 0168-9002. DOI: <https://doi.org/10.1016/j.nima.2019.04.088>. URL: <https://www.sciencedirect.com/science/article/pii/S0168900219305704>.
- [133] Leena Diehl et al. “Evaluation of 3D sensors for fast timing applications”. In: *Nuclear Instruments and Methods in Physics Research Section A: Accelerators, Spectrometers, Detectors and Associated Equipment* 1065 (2024), p. 169517. ISSN: 0168-9002. DOI: <https://doi.org/10.1016/j.nima.2024.169517>. URL: <https://www.sciencedirect.com/science/article/pii/S0168900224004431>.
- [134] Matthew Addison et al. “Position-resolved timing characterisation tests of hexagonal and trench 3D silicon detectors”. In: *Nuclear Instruments and Methods in Physics Research Section A: Accelerators, Spectrometers, Detectors and Associated Equipment* 1054 (2023), p. 168392. ISSN: 0168-9002. DOI: <https://doi.org/10.1016/j.nima.2023.168392>. URL: <https://www.sciencedirect.com/science/article/pii/S0168900223003820>.
- [135] A. Loi, A. Contu, and A. Lai. “Timing optimisation and analysis in the design of 3D silicon sensors: the TCoDe simulator”. In: *Journal of Instrumentation* 16.02 (Feb. 2021), P02011. DOI: [10.1088/1748-0221/16/02/P02011](https://doi.org/10.1088/1748-0221/16/02/P02011). URL: <https://dx.doi.org/10.1088/1748-0221/16/02/P02011>.
- [136] A. Loi on behalf of the TIMESPOT project. *Design of 3D silicon sensors for high resolution time measurements*. Presented at the 13th Trento Workshop on Advanced Silicon Radiation Detectors <https://indico.cern.ch/event/666427/>

- [contributions/2880558/attachments/1602555/2541602/3D\\_silicon\\_detector\\_Angelo\\_Loi.pdf](#). 2018.
- [137] I. Vila et al. “A novel Transient-Current-Technique based on the Two Photon Absorption process”. In: *25th Workshop of Radiation Hard Semiconductor Devices for Very High Luminosity Colliders (RD50)*. Zenodo, Nov. 2014. DOI: [10.5281/zenodo.14493775](#). URL: <https://doi.org/10.5281/zenodo.14493775>.
- [138] V. Eremin et al. “Development of transient current and charge techniques for the measurement of effective net concentration of ionized charges (Neff) in the space charge region of p-n junction detectors”. In: *Nuclear Instruments and Methods in Physics Research Section A: Accelerators, Spectrometers, Detectors and Associated Equipment* 372.3 (1996), pp. 388–398. ISSN: 0168-9002. DOI: [https://doi.org/10.1016/0168-9002\(95\)01295-8](https://doi.org/10.1016/0168-9002(95)01295-8). URL: <https://www.sciencedirect.com/science/article/pii/0168900295012958>.
- [139] Gregor Kramberger. “Advanced Transient Current Technique Systems”. In: *PoS Vertex2014* (2015), p. 032. DOI: [10.22323/1.227.0032](#).
- [140] Mariacristina Rumi and Joseph Perry. “Two-photon absorption: an overview of measurements and principles”. In: *Advances in Optics and Photonics* 2 (Aug. 2010), pp. 451–518. DOI: [10.1364/AOP.2.000451](#).
- [141] Moritz Oliver Wiehe. “Development of a two-photon absorption - TCT system and study of radiation damage in silicon detectors”. PhD thesis. Freiburg U., Freiburg U., 2021. DOI: [10.6094/UNIFR/223092](#).
- [142] Sebastian Pape. “Characterisation of Silicon Detectors Using the Two Photon Absorption – Transient Current Technique”. Presented 29 Jan 2024. PhD thesis. Tech. U., Dortmund (main), 2024. URL: <https://cds.cern.ch/record/2889325>.
- [143] Moritz Wiehe et al. “Development of a Tabletop Setup for the Transient Current Technique Using Two-Photon Absorption in Silicon Particle Detectors”. In: *IEEE Transactions on Nuclear Science* 68.2 (2021), pp. 220–228. DOI: [10.1109/TNS.2020.3044489](#).
- [144] David Pennicard. “3D Detectors for Synchrotron Applications”. PhD thesis. University of Glasgow, 2009. URL: <https://repository.cern/records/vvd8f-kyq17>.
- [145] C. Lasaosa et al. “The influence of pixel cell layout on the timing performance of 3D sensors”. In: *Journal of Instrumentation* 20.06 (June 2025), p. C06080. DOI: [10.1088/1748-0221/20/06/C06080](#). URL: <https://dx.doi.org/10.1088/1748-0221/20/06/C06080>.

# Appendix

## A.1. Test beam measurements across a multi-pixel grid

In addition to the single-pixel cell maps presented in Chapter 3, the observables measured in test beam experiments to evaluate detector performance can also be visualized across multiple pixel cells. Mapping these observables over a  $2 \times 2$  pixel grid, as shown in Figure 3.5d, provides additional insight and can help identify subtle performance variations or asymmetries between odd and even rows in the sensor matrix.

It is important to note that the values shown in these maps represent average values over all pixel cells in the matrix that registered a hit within a  $2 \times 2$  grid arrangement. Representative results for both non-irradiated and irradiated modules are presented below. Details of the devices under test can be found in Tables 3.6 and 3.7.

### A.1.1. Performance of non-irradiated devices

Figure A.1 shows the hit detection efficiency at normal beam incidence across a  $2 \times 2$  pixel grid for CNM and FBK sensors with  $25 \times 100 \mu\text{m}^2$  pixels, measured at various bias voltages. For completeness, results from a CNM sensor with a  $50 \mu\text{m}$  pitch are also included. All modules were tuned to an average pixel threshold of 1000 electrons.

The cluster charge MPV for the same FBK sensor, biased at 30 V, is shown in Figure A.2. Figure A.3 presents the average cluster size maps for the above-mentioned devices under the same beam conditions and at different bias voltages. Additionally, Figure A.4 shows cluster size distributions at several rotation angles for another FBK sensor, tuned to an average pixel threshold of 1200 electrons and biased at 50 V.

Overall, the results obtained across the  $2 \times 2$  pixel grid are consistent with those from the single-pixel cell maps discussed in Section 3.3.3, and no significant asymmetries are observed across the matrix prior to irradiation.

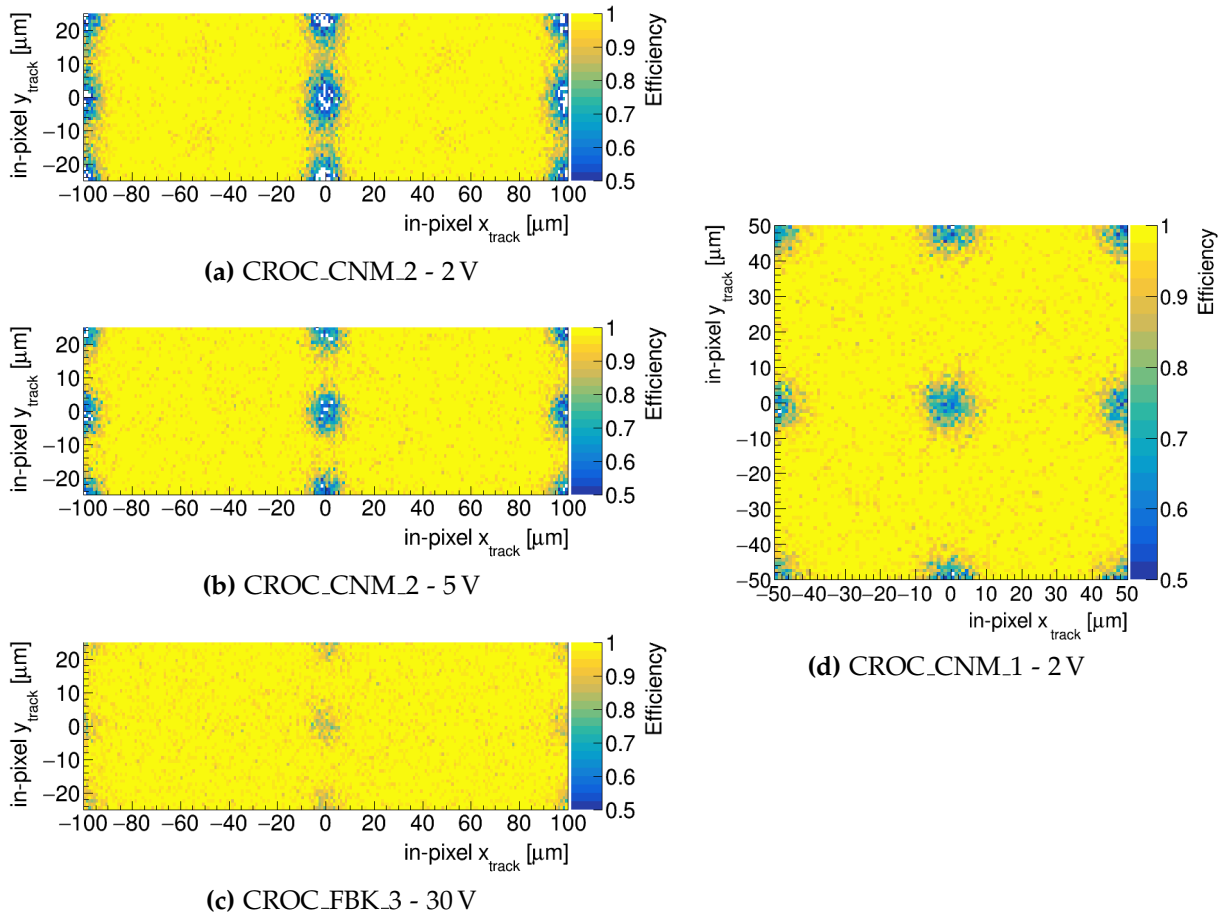


**Figure A.1:** Hit detection efficiency maps for a  $2 \times 2$  pixel grid from several non-irradiated modules at normal beam incidence: the CNM sensor with  $25 \times 100 \mu\text{m}^2$  pixels biased at (a) 2 V and (b) 5 V; one of the FBK sensors biased at (c) 30 V; and the CNM sensor with  $50 \mu\text{m}$  pitch biased at (d) 2 V. White regions indicate an efficiency below 0.5.

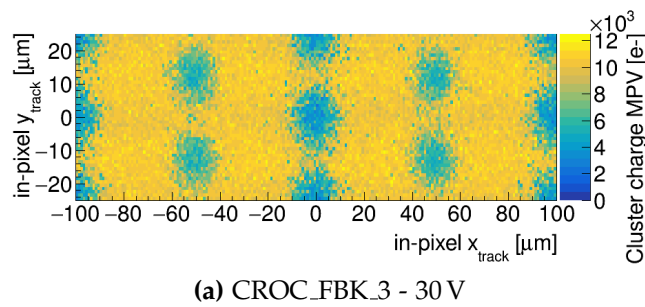


**Figure A.2:** Cluster charge MPV map for a  $2 \times 2$  grid from a non-irradiated FBK sensor biased at 30 V. Measurements were taken at normal beam incidence.



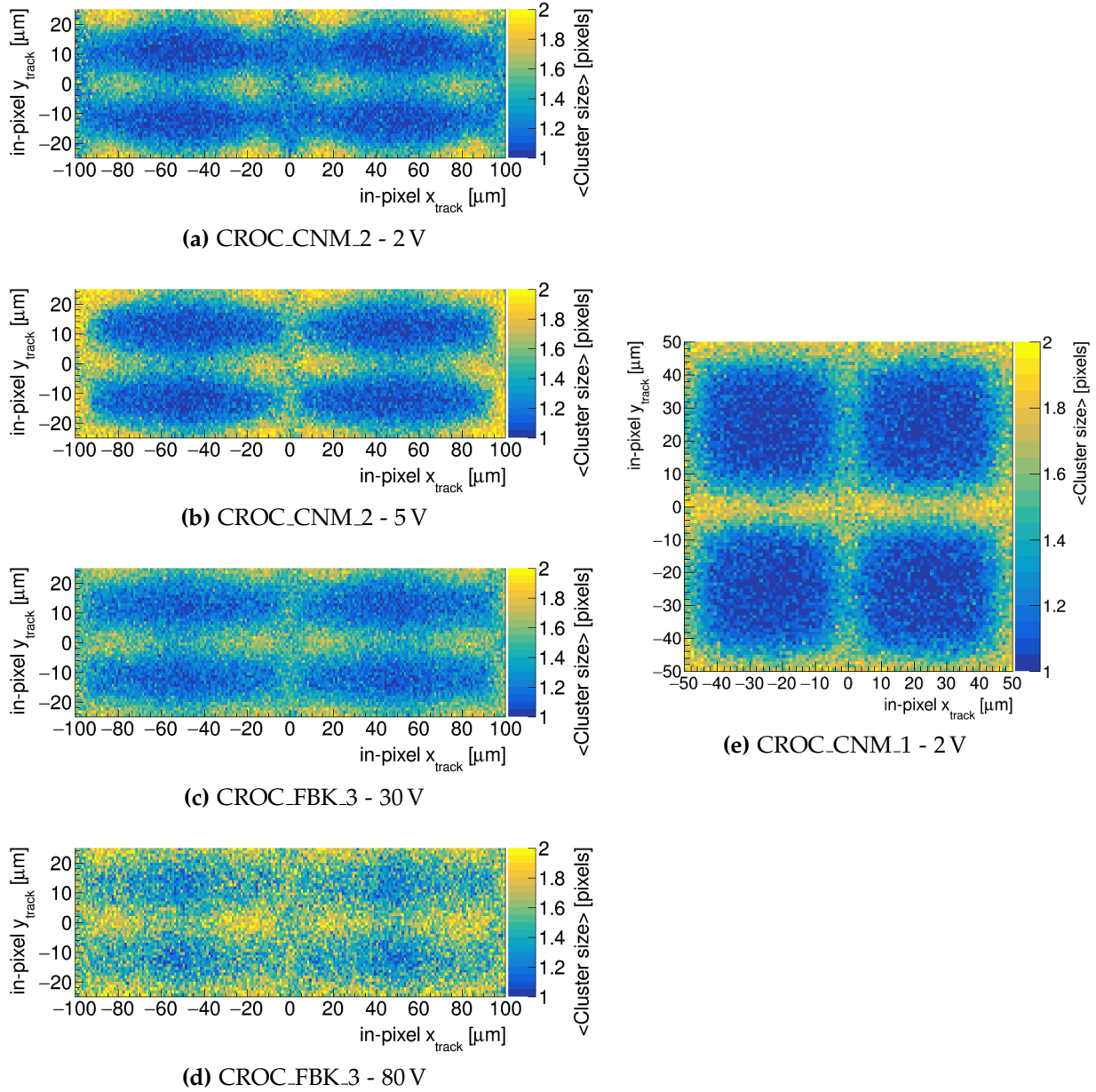


**Figure A.3:** Cluster size maps for a  $2 \times 2$  pixel grid from several non-irradiated modules at normal beam incidence: the CNM sensor with  $25 \times 100 \mu\text{m}^2$  pixels biased at (a) 2 V and (b) 5 V; one of the FBK sensors biased at (c) 30 V and (d) 80 V; and the CNM sensor with  $50 \mu\text{m}$  pitch biased at (e) 2 V.

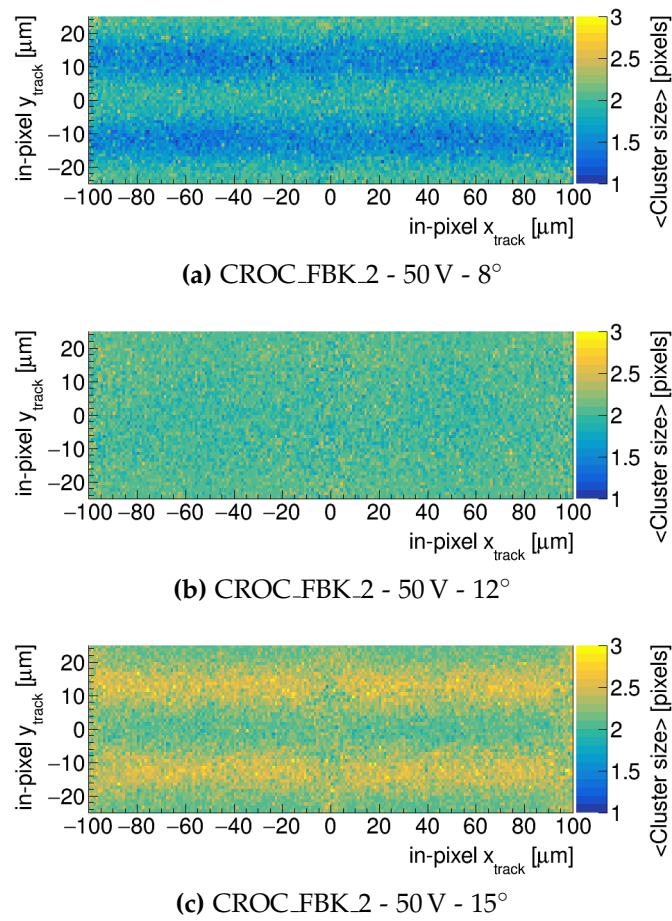


**Figure A.4:** Cluster size maps for a  $2 \times 2$  pixel grid from a non-irradiated FBK sensor biased at 50 V and rotated by (a)  $8^\circ$ , (b)  $12^\circ$ , and (c)  $15^\circ$ .

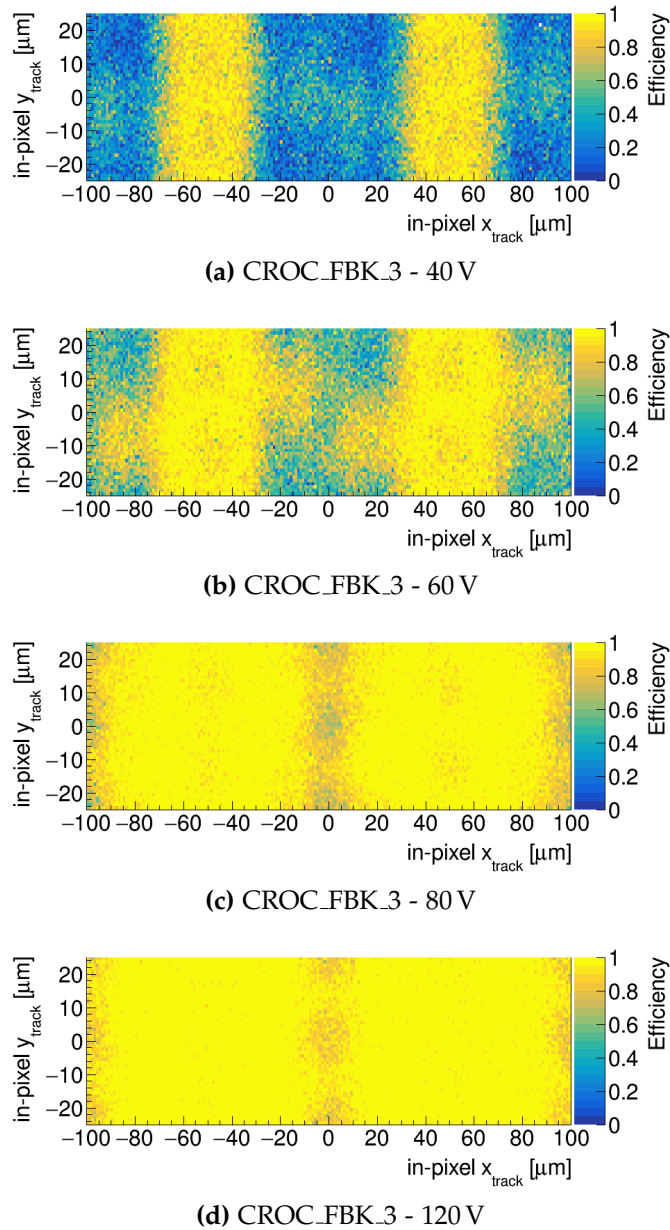
### A.1.2. Performance of irradiated devices

Figure A.5 shows the hit detection efficiency across a  $2 \times 2$  pixel grid for an FBK module irradiated to  $1 \times 10^{16} \text{ n}_{\text{eq}}\text{cm}^{-2}$  and tuned to an average pixel threshold of 1000 electrons. Measurements were performed at various bias voltages under normal beam incidence.

At bias voltages well below full depletion, such as 40 V and 60 V, an asymmetry is observed between even and odd sensor rows. The efficiency is enhanced near the bump-bond pads: in the right half of the pixel cell for even rows and in the left half for odd rows. This behavior is attributed to a spurious signal induction mechanism: particles traversing a pixel near its bump-bond pad can induce an additional signal on top of the one generated by charge carriers drifting to the collecting electrode. This unintended contribution can cause the total signal to exceed the threshold more frequently, leading to a localized increase in efficiency. At higher bias voltages, once the sensor is fully depleted, the efficiency becomes more uniform across the pixel cell



and the asymmetry disappears.



**Figure A.5:** Hit detection efficiency maps for a  $2 \times 2$  pixel grid from an FBK module irradiated to  $1 \times 10^{16} \text{ n}_{\text{eq}} \text{ cm}^{-2}$  at normal beam incidence and a bias voltage of (a) 40 V, (b) 60 V, (c) 80 V, and (d) 120 V.

The average cluster size across a  $2 \times 2$  pixel grid for the same FBK sensor, biased at 120 V and rotated by different angles, is presented in Figure A.6. An asymmetry between even and odd rows persists even above full depletion and is observed at all rotation angles. The cluster size increases near the bump-bond pads, but with a reversed pattern compared to the efficiency maps: in the left half of the pixel cell for even rows and in the right half for odd rows.

This effect is attributed to cross-talk with neighboring pixels. When a particle traverses a pixel close to the bump-bond pad of an adjacent pixel, it may induce a signal in that neighbor. If the induced signal exceeds the threshold, the neighboring pixel is added to the cluster, increasing its overall size.

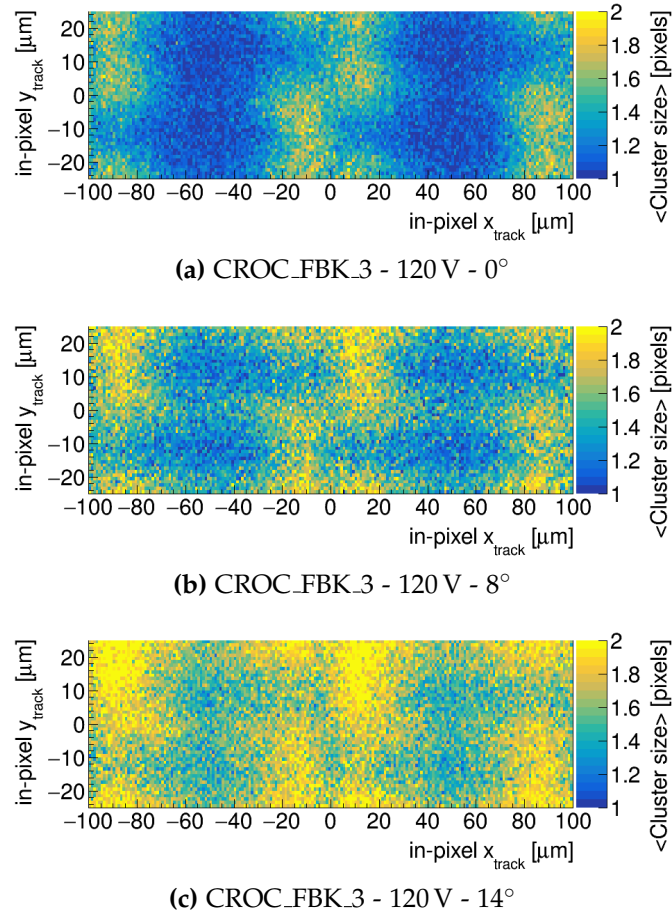
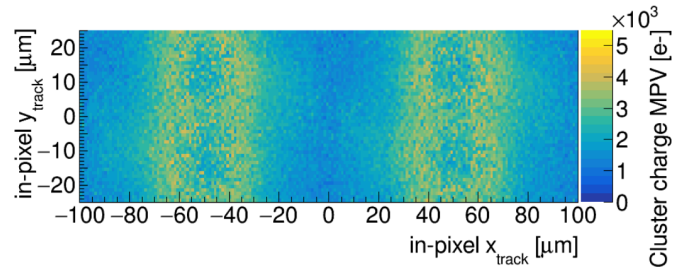
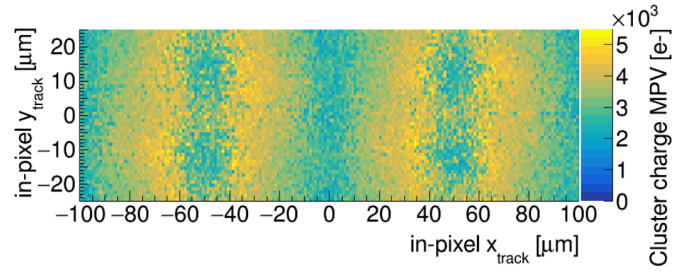


**Figure A.6:** Cluster size maps for a  $2 \times 2$  pixel grid from an FBK module irradiated to  $1 \times 10^{16} \text{ n}_{\text{eq}} \text{ cm}^{-2}$ . The maps correspond to rotation angles of (a)  $0^\circ$  or normal beam incidence, (b)  $8^\circ$ , and (c)  $14^\circ$ . All measurements were performed at a bias voltage of 120 V.

Figure A.7 shows the cluster charge MPV for the same FBK module at normal beam incidence and two different bias voltages. In contrast to the previous observables, the results are consistent with those from the single-pixel cell maps discussed in Section 3.3.4, and no significant asymmetries are observed. This may be due to the superposition of the two effects described for the efficiency and cluster size, which appear to be spatially complementary and may give rise to a symmetric distribution of cluster charge.



(a) CROC\_FBK\_3 - 90 V



(b) CROC\_FBK\_3 - 120 V

**Figure A.7:** Cluster charge MPV maps for a  $2 \times 2$  grid from an FBK module irradiated to  $1 \times 10^{16} \text{ n}_{\text{eq}} \text{ cm}^{-2}$  and biased at (a) 90 V and (b) 120 V. Measurements were taken at normal beam incidence.